

NICKEL-CHROMIUM-LAYERED DOUBLE HYDROXIDE
HYBRIDIZED WITH POLYOXOMETALATE ANIONS
AND GRAPHENE OXIDE NANOSHEETS FOR
SUPERCAPACITOR APPLICATION

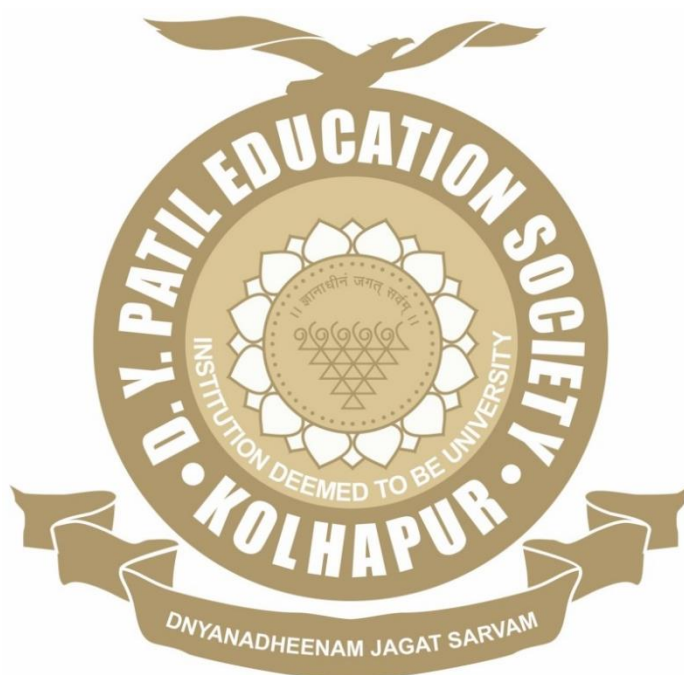
By

Mr. NAVNATH S. PADALKAR

Under the Supervision of

Dr. JAYAVANT L. GUNJAKAR

Thesis Submitted to



For the Degree of

Doctor of Philosophy

2021

**NICKEL-CHROMIUM-LAYERED DOUBLE HYDROXIDE
HYBRIDIZED WITH POLYOXOMETALATE ANIONS AND
GRAPHENE OXIDE NANOSHEETS FOR SUPERCAPACITOR
APPLICATION**

**A THESIS SUBMITTED TO
D. Y. PATIL EDUCATION SOCIETY
(DEEMED TO BE UNIVERSITY), KOLHAPUR**



**FOR THE DEGREE OF
DOCTOR OF PHILOSOPHY
IN
PHYSICS
UNDER THE FACULTY OF
INTERDISCIPLINARY STUDIES**

**BY
Mr. NAVNATH SHANKAR PADALKAR**

M.Sc.

UNDER THE SUPERVISION OF

Dr. J. L. GUNJAKAR

M.Sc., Ph.D.

**RAMANUJAN FELLOW,
CENTRE FOR INTERDISCIPLINARY RESEARCH,
D. Y. PATIL EDUCATION SOCIETY (DEEMED TO BE UNIVERSITY),
KOLHAPUR- 416 006, MAHARASHTRA, (INDIA)**

(2021)

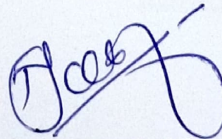
DECLARATION

I hereby declare that the thesis **"NICKEL-CHROMIUM-LAYERED DOUBLE HYDROXIDE HYBRIDIZED WITH POLYOXOMETALATE ANIONS AND GRAPHENE OXIDE NANOSHEETS FOR SUPERCAPACITOR APPLICATION"** submitted for the degree of **Doctor of Philosophy in Physics** under the faculty of **Centre for Interdisciplinary Research** of the **D. Y. Patil Education Society (Deemed to be University), Kolhapur** is completed and written by me, has not before made the basis for the award of any other higher education institute in India or any other country to the best of my knowledge. Further, I declare that, I have not violated any of the provisions under Copyright and Piracy/ Cyber/ IPR Act amended from time to time.

Place: Kolhapur

Date: 31-12-2021

Research student



Mr. Navnath Shankar Padalkar

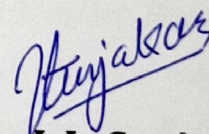
CERTIFICATE

This is to certify that the thesis entitled "**NICKEL-CHROMIUM-LAYERED DOUBLE HYDROXIDE HYBRIDIZED WITH POLYOXOMETALATE ANIONS AND GRAPHENE OXIDE NANOSHEETS FOR SUPERCAPACITOR APPLICATION**" which is being submitted herewith for the award of the Degree of **Doctor of Philosophy** in **Physics** of **D. Y. Patil Education Society (Deemed to be University), Kolhapur**, is the result of the original research work completed by **Mr. Navnath Shankar Padalkar** under my supervision and guidance and to the best of my knowledge and belief the work embodied in this thesis has not formed earlier the basis for the award of any degree or similar title of this or any other University or examining body.

Place: Kolhapur

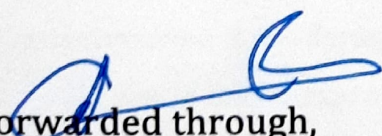
Date: 31/12/2021

Research Guide



Dr. J. L. Gunjekar
Ramanujan Fellow

Dr. J. L. Gunjekar
Ramanujan Fellow
Centre for Interdisciplinary Research
D.Y.Patil Education Society
(Deemed University),
Kolhapur-416 006 (India)



Forwarded through,
Prof. C. D. Lokhande
Dean and Research Director,
Centre for Interdisciplinary Research

Prof. C. D. LOKHANDE
Dean

Centre For Interdisciplinary Studies
D. Y. Patil Education Society
(Institution Deemed to be University)
869, 'E', Kasaba Bawada
KOLHAPUR- 416006

ACKNOWLEDGEMENT

A journey is easier when you travel together. Interdependence is certainly more valuable than independence. This thesis is the result of work where I have been accompanied and supported by many peoples.

*At the completion of my Ph.D. thesis, I would like to express my sincere gratitude towards my advisor, **Dr. J. L. Gunjekar** (Ramanujan Fellow, D. Y. Patil Education Society) for the continuous support during my Ph.D. study and related research, for his motivation, and immense knowledge. I thank him not only for the guidance he rendered in the field of research but also for enlightening the path of my life with a deep love for science. With his support, I could overcome my personal and scientific problems on writing scientific papers including this Ph.D. thesis and this work could not have been completed without his inspiring guidance and constant encouragement during the course of research tenure.*

*I sincerely acknowledge the whole hearted help, valuable discussions, guidance and suggestions provided by **Prof. C. D. Lokhande**, Head and Research Director, Centre for Interdisciplinary Research (CIR). He provided a very fruitful discussion and helpful guidance for time management regarding my Ph.D. progress.*

*I would like to express my sincere thanks to Vice-Chancellor **Prof. R. K. Mudgal**, Pro-Vice Chancellor **Dr. Shimpa Sharma** and Registrar **Dr. V. V. Bhosale** for the inspiration and support. I thank **Dr. U. M. Patil**, **Dr. Vishwajeet Khot** and **Dr. Meghanand Joshi** who helped me to analyze the results with all their empathy and cooperative mind. I also thank **Dr. A. C. Lokhande**, **H. M. Pathan**, **Dr. S. D. Sartale**, **Dr. R. N. Bulakhe** and **Dr. V. G. Parale**, for providing me very important sample characterization data, during entire research work.*

*I would like to express sincere thanks to my seniors **Dr. R. B. Pujari**, **Dr. P. K. Katkar**, **Dr. T. T. Ghogare**, **Dr. S. B. Kale**, and **Dr. S. J. Marje** for insightful guidelines, scientific discussions and valuable suggestions on the present work.*

*I am thankful to my uncle **Dr. D. S. Dhawale**, Scientist, Commonwealth Scientific and Industrial Research Organisation, Australia, for his good wishes, encouragement and support throughout my academic career.*

*I own a word of thanks to all my friends and research colleague from CIR department viz. **Shrikant Sadavar, Rohini Shinde, Vikas Magdum, Yogesh Chitare, Shirin Kulkarni, Akash patil, Vikas Mane, Shivaji Ubale, Sachin Pujari, Suraj Khalate, Satish Jadhav, Dhanaji Malavekar, Priti Bagawade, Vinod Patil, Ranjit Nikam, Sambhaji Kumbhar, Shraddha Bhosale and Sambhaji Khot.** Thanks for being the ultimate lab-neighbors, providing a great work environment, and for help and discussions. I am also thankful non-teaching staff of the CIR Department for their kind co-operation during my research work.*

*I am overwhelmed by the constant happiness, love and support given by my friends **Vikas Sule, Sudhir Narale, Vivek More, Jayshri Shingade, Sachin Gorad, Manoj Jamadade and Arvind Patil.***

*My heartfelt gratitude goes out to my late Father **Shankar (Tatya)**, Mother **Laxmibai (Aai)**, Sisters **Suvarna, Sarika, and Ujjwala**, as well as all of my family members for their constant support, encouragement and their love affection towards me to cruise through the difficulties to bring me at this position.*

~Navnath Padalkar

Place: Kolhapur

SUMMARY OF RESEARCH WORK

A) Published (Indian) Patents:

- 1) Jayavant L. Gunjekar, Chandrakant D. Lokhande, Saji T. Kochuveedu, Shrikant V. Sadavar, **Navnath S. Padalkar**, Vishwanath V. Bhosale, "A method of polyoxovanadate intercalation into layered copper hydroxide", (2018), Application No.-201821018926.
- 2) Jayavant L. Gunjekar, **Navnath S. Padalkar**, Shrikant V. Sadavar, Rohini B. Shinde, Chandrakant D. Lokhande, Vishwanath V. Bhosale, "A method of preparation of an electrode based on nickel-chromium-layered double hydroxide intercalated with polyoxovanadate for supercapacitor application", (2020), Application No.- 202021001507.
- 3) Jayavant L. Gunjekar, Shrikant V. Sadavar, **Navnath S. Padalkar**, Rohini B. Shinde, Ravindra N. Bulakhe, Chandrakant D. Lokhande, Vishwanath V. Bhosale, "A method of preparation of an supercapacitor electrode based on cobalt chromium layered double hydroxide pillared with polyoxovanadate" (2020), Application No.- 202021005460.
- 4) Jayavant L. Gunjekar, Rohini B. Shinde, **Navnath S. Padalkar**, Shrikant V. Sadavar, Akash S. Patil, Chandrakant D. Lokhande, Vishwanath V. Bhosale, "A method of preparation of thin films of zinc chromium layered double hydroxide nanotubes with porous walls" (2020), Application No.- 202021039044.

B) Papers Published/Submitted at International Journals:

- 1) **Navnath S. Padalkar**, Shrikant V. Sadavar, Rohini B. Shinde, Akash S. Patil, Umakant M. Patil, Dattatray S. Dhawale, Habib M. Pathan, Shrikrishna D. Sartale, Vinayak G. Parale Ajayan Vinu, Chandrakant D. Lokhande, Jayavant L. Gunjekar, "Mesoporous nanohybrids of 2D Ni-Cr-layered double hydroxide nanosheets pillared with polyoxovanadate anions for high-performance hybrid supercapacitor", Adv. Mater. Interfaces, (2021) 2101216, Wiley VCH, I.F.- 6.14.
- 2) Rohini B. Shinde, Akash S. Patil, Shrikant V. Sadavar, Yogesh M. Chitare, Vikas V. Magdum, **Navnath S. Padalkar**, Umakant M. Patil, Saji T. Kochuveedu, Vinayak G. Parale, Hyung-Ho. Park, Chandrakant D. Lokhande, Jayavant L. Gunjekar, "Polyoxotungstate intercalated self-assembled nanohybrids of Zn-Cr-LDH for

- room temperature Cl_2 sensing”, *Sensors and Actuators B: Chemical*, 352 (2022) 131046 Elsevier, I.F.- 7.46.
- 3) Akash S. Patil, Jayavant L. Gunjekar, Chandrakant D. Lokhande, Umakant M. Patil, Shrikant V. Sadavar, **Navnath S. Padalkar**, Rohini B. Shinde, Mahesh M. Wagh, Jaydeep S. Bagi, “Nanocrystalline copper-chromium-layered double hydroxide with tunable interlayer anions for electrochemical capacitor application”, *Synthetic Metals*, 264 (2020) 116371, Elsevier, I.F.- 3.28.
- 4) Shrikant V. Sadavar, **Navnath S. Padalkar**, Rohini B. Shinde, Saji T. Kochuveedu, Umakant M. Patil, Akash S. Patil, Ravindra N. Bulakhe, Chandrakant D. Lokhande, Insik In, Jayavant L. Gunjekar, Rahul R. Salunkhe, “Mesoporous nanohybrids of 2-D cobalt–chromium layered double hydroxide and polyoxovanadate anions for high performance hybrid asymmetric supercapacitors”, *Journal of Power Sources*, Elsevier, I.F.- 9.12 (Revision submitted).
- 5) **Navnath S. Padalkar**, Shrikant V. Sadavar, Rohini B. Shinde, Akash S. Patil, Umakant M. Patil, Dattatray S. Dhawale, Ravindra N. Bulakhe, Hyungsang Kim, Hyunsik Im, Ajayan Vinu, Chandrakant D. Lokhande, Jayavant L. Gunjekar, “Layer-by-Layer nanohybrids of Ni-Cr-LDH intercalated with 0D polyoxotungstate for highly efficient hybrid supercapacitor”, *Journal of Colloid and Interface Science*, Elsevier, I.F.- 8.12 (Under review).
- 6) **Navnath S. Padalkar**, Shrikant V. Sadavar, Rohini B. Shinde, Akash S. Patil, Umakant M. Patil, Vikas V. Magdum, Yogesh M. Chitare, Shirin P. Kulkarni, Ravindra N. Bulakhe, Vinayk G. Parale, Jayavant L. Gunjekar, “2D-2D nanohybrids of Ni-Cr-layered double hydroxide wrapped with graphene oxide nanosheets: electrode for hybrid asymmetric supercapacitors”, *Advanced Sustainable Systems*, Wiley VCH, I.F.- 6.27 (Under review).
- 7) Shrikant. V. Sadavar, **Navnath. S. Padalkar**, Rohini. B. Shinde, Akash S. Patil, Umakant M. Patil, Vikas V. Magdum, Yogesh M. Chitare, Shirin P. Kulkarni, Ravindra. N. Bulakhe, Saji T. Kochuveedu, Jayavant L. Gunjekar, “Lattice engineering exfoliation-restacking route for 2D layered double hydroxide hybridized with 0D polyoxotungstate anions: Cathode for hybrid asymmetric supercapacitors”, *Energy Storage Materials*, Elsevier, I.F.- 17.78 (Required revision).

- 8) Shrikant. V. Sadavar, **Navnath. S. Padalkar**, Rohini. B. Shinde, Akash S. Patil, Umakant M. Patil, Vikas V. Magdum, Yogesh M. Chitare, Shirin P. Kulkarni, Ravindra. N. Bulakhe, Vinayak G. Parale , Jayavant L. Gunjekar, "Graphene oxide an efficient hybridization matrix for exploring electrochemical activity of 2D cobalt-chromium-layered double hydroxide based nanohybrids", ACS Applied Energy Materials, American Chemical Society, I.F.- 6.02 (Required revision).
- 9) Rohini B. Shinde, **Navnath S. Padalkar**, Shrikant V. Sadavar, Akash S. Patil, Shital B. Kale, Vikas V. Magdum, Yogesh M. Chitare, Shirin P. Kulkarni, Umakant M. Patil, Vinayak G. Parale, Jayavant L. Gunjekar, "Lattice engineering route for self-assembled nanohybrids of 2D layered double hydroxide with 0D isopolyoxovanadate: Chemiresistive SO₂ sensor", Materials Today Chemistry, Elsevier, I.F.- 8.30 (Required revision).
- 10) Rohini B. Shinde, **Navnath S. Padalkar**, Shrikant V. Sadavar, Shital B. Kale, Vikas V. Magdum, Yogesh M. Chitare, Shirin P. Kulkarni, Umakant M. Patil, Vinayak G. Parale, Jayavant L. Gunjekar, "2D-2D Lattice engineering route for intimately coupled nanohybrids of layered double hydroxide and potassium hexaniobate: chemiresistive SO₂ Sensor", Journal of Hazardous Materials, Elsevier, I.F.- 10.58 (Submitted).

C) Poster Presented at National/International Conferences:

- 1) **Navnath S. Padalkar**, Shrikant V. Sadavar, Rohini B. Shinde, Akash S. Patil, Chandrakant D. Lokhande, Jayavant L. Gunjekar, "Preparation of Ni-Cr-layered double hydroxide nanosheets and its use in electrochemical energy storage" AMSCA-2018, Savitribai Phule Pune University, Pune.
- 2) **Navnath S. Padalkar**, Shrikant V. Sadavar, Rohini B. Shinde, Akash S. Patil, Chandrakant D. Lokhande, Jayavant L. Gunjekar, "Simplified synthesis Ni-Cr-layered double hydroxide for supercapacitor", 4th ICPM-MDF-2019, Shivaji University, Kolhapur.
- 3) **Navnath S. Padalkar**, Shrikant V. Sadavar, Rohini B. Shinde, Akash S. Patil, Chandrakant D. Lokhande, Jayavant L. Gunjekar, "Synthesis of Ni-Cr-layered double hydroxide for supercapacitor application", MAS-2019, K. N. Bhise Arts, Commerce and Vinayakrao Patil Science College, Bhosare (Kurduwadi), Solapur.

List of Abbreviations

Energy density	ED	Layered metal oxides	LMO
Power density	PD	Layer-by-layer	LBL
Electrochemical energy storage	EES	Electrophoretic mobility	μ_e
Supercapacitor	SC	Zeta potential	ζ
Equivalent series resistance	ESR	Full width at half maximum	FWHM
Direct current	DC	Charge-coupled device	CCD
Maximum power	P_{max}	Brunauer-Emmette-Teller	BET
Electrochemical capacitor	EC	Barrett-Joyner-Halenda	BJH
Electric double layer capacitor	EDLC	Cyclic voltammetry	CV
Specific capacitance	C_s	Solution resistance	R_s
Electric double layer	EDL	Charge transfer resistance	R_{ct}
Diffusion region capacitance	C_d	Double distilled water	DDW
Compact double layer capacitance	C_c	Polyvinylidene fluoride	PVDF
Hybrid supercapacitor	HSC	N-methylpyrrolidone	NMP
Nanosheets	NSs	Stainless steel	SS
Graphene oxide	GO	Selected area electron diffraction	SAED
Reduced graphene oxide	rGO	Carbon nanotubes	CNTs
Polyaniline, and	PANI	Potassium hydroxide	KOH
Poly-(3,4-ethylenedioxythiophene)	PEDOT	Polyoxometalate	POM
Polypyrrole	PPy	Polyoxotungatate	POW
Polythiophene	PTh	Acetylene black	AB
Chemical bath deposition method	CBD	Metal-organic framework	MOF
Layered double hydroxide	LDH	Layered transition metal dichalcogenides	LTMDCs
Carbon nanoparticles	CNPs	Transition metal dichalcogenide	TMDC
Nickel foam	NF	Transition metal oxides	TMO
Polyoxovanadate	POV	Transition metal chalcogenides	TMCs
X-ray diffraction	XRD	Binding energy	BE
Fourier-transform infrared	FTIR	Zero-dimensional	0D
High-resolution transmission electron microscopy	HRTM	Two-dimensional	2D
X-ray Photoelectron spectroscopy	XPS	Pinnacle research institute	PRI
Cyclic voltammetry	CV	Charge-coupled device	CCD
Galvanostatic charge- discharge	GCD	Chemical vapor deposition	CVD
Electrochemical impedance spectroscopy	EIS	Activated carbon	AC

CONTENTS

Chapter No.	Title	Page No.
1	General introduction and literature survey	1-37
2	Theoretical background of material synthesis process and characterization technique	39-75
3	Synthesis, characterization and electrochemical performance evaluation of Ni-Cr-LDH and rGO	77-100
4	Synthesis, characterization and electrochemical performance evaluation of Ni-Cr-LDH hybridized with POV anions and HSC	101-134
5	Synthesis, characterization and electrochemical performance evaluation of Ni-Cr-LDH hybridized with POW anions and HSC	135-167
6	Synthesis, characterization and electrochemical performance evaluation of Ni-Cr-LDH hybridized with GO and HSC	169-200
7	Summary and conclusions	201-205
8	80-Recommendation	207-212



CHAPTER - 1

General Introduction and Literature Survey

CHAPTER 1

General Introduction and Literature Survey

Sr. No.	Title		Page No.
1.1	General Introduction		1
	1.1.1	<i>Electrochemical energy storage and conversion systems</i>	1-4
	1.1.2	<i>Historical background and current status of supercapacitors</i>	4-6
	1.1.3	<i>Basic principle, classification and salient feature of supercapacitor</i>	6-12
		1.1.3.1 <i>Electric double layer capacitors (EDLCs)</i>	7-9
		1.1.3.2 <i>Pseudocapacitors</i>	9-10
		1.1.3.3 <i>Hybrid capacitors</i>	10
	1.1.4	<i>Electrode materials for supercapacitor</i>	12-18
		1.1.4.1 <i>Carbon based material</i>	14-15
		1.1.4.2 <i>Conducting polymers</i>	16
		1.1.4.3 <i>Metal oxides</i>	16
		1.1.4.4 <i>Layered double hydroxides</i>	16-17
		1.1.4.5 <i>2D nanosheets based hybrids</i>	18
1.2	Literature Survey		18-29
	1.2.1	<i>Literature survey of LDH for supercapacitor</i>	18-20
	1.2.2	<i>Literature survey of LDH based hybrids for supercapacitor</i>	20-24
1.3	Orientation and purpose of the dissertation		30-32
1.4	References		32-37

1.1 General Introduction

1.1.1 Electrochemical energy storage and conversion systems

The rapid development of the global economy and growth in the world population demands more energy. Presently, fossil fuels are the main energy resources to fulfill this major energy demand. However, the consistently rising cost of fossil fuels has emerged as a global energy crisis. In addition, the rapid depletion of fossil fuels and the environmental issues caused by their combustion has received much research attention for exploring renewable energy sources which can generate clean and efficient energy with low production costs.

In this context, many researchers are currently working in the field of solar cell to convert solar energy into electrical energy. Wind energy is also a potential renewable energy source. However, the seasonal occurrence of sunlight on the earth's surface and uncertain wind flow at different places at different times fluctuate the overall output of these sources. Therefore, efficient energy storage devices need to be developed to store the generated electrical energy, allowing the user to utilize the stored energy as per requirement during any time and season. Also, these kinds of devices are highly essential for the applications like power tools, electric vehicles, smart appliances, portable electronics including mobile phones and laptops, advanced electrical appliances, and wherever stored energy is required. Many of these applications need special characteristics from energy storage devices. For example, electric vehicles require high power as well as high energy; smart phones require batteries with high energy to function for a longer time; power drilling tools require high power for their efficient function. Therefore, it is of utmost importance to develop an energy storage system capable of storing high energy density (ED) and delivering high power density (PD) [1-5].

Presently electrochemical energy storage (EES) devices like batteries, capacitors and supercapacitor (SC) systems are attracting more attention to store electrical energy. The energy storage and conversion mechanism of each EES device are different. Various EES devices are working on different principles. The ionic liquid electrolyte is necessary for charge storage through an electrochemical reaction in a fuel cell. A major limitation in the fuel cell is the requirement of a continuous supply of H_2 as a fuel. Batteries are a type of galvanic cell that consists of two (either identical or dissimilar) charge-carrying electrodes kept in a

conducting electrolyte. Generally, the liquid electrolyte is used in traditional batteries, while recent development allows solid electrolyte. Different types of batteries have been developed for different applications over the last decades, such as lead-acid batteries, metal hydride batteries, Ni-metal batteries, and Li-ion batteries. Nowadays, Li-ion batteries are widely used in cell phones, laptops, auto vehicles, power backup, electronic gadgets etc. Though Li-batteries possesses high ED, it suffers from low PD and limited cycle life due to its high equivalent series resistance (ESR). Therefore, batteries are not useful in many applications where high power delivering systems are needed [6-7].

Capacitors are the devices that provide a mode of quick electrical energy storage and delivery, often complementary to batteries. When the capacitor is connected to direct current (DC) source, the potential difference developed between two plates is 'V', the charge stored at the conducting plates is 'Q' ($Q = |Q_+| + |Q_-|$), then the capacitance is stated as

$$C = \frac{Q}{V} \quad (1.1)$$

The capacitor's maximum power (P_{max}) or the rate of energy delivery per unit time can be computed using the following relation

$$P_{max} = \frac{E}{T} = \frac{V^2}{4R} \quad (1.2)$$

Where, E is enegy, T is time, V is potential difference and R is expressed in terms of the resistance of the electrolyte in both the electrode material or in the separator . Traditional parallel plate capacitors possess low ED than batteries. Also the stored energy in capacitors depletes due to internal leakage current. This drawback does not make the capacitor a preferable choice for high energy storage. Consequently, SCs are receiving high research attention due to their large storage capacity (energy) than conventional capacitors. In addition, the higher PD and reasonable ED are advantageous for their application in diverse fields, including smart appliances, portable electronics, etc. Likewise, other fascinating features of SCs, including higher operating potential window, the flexibility of devices, and compactness, allow their use in hybrid vehicles, telecommunication devices (remote communication, cell phones, walkie-talkies, satellites, etc.), solar devices, memory backup system, pace- makers, etc [8, 9].

The comparison of the fuel cells, batteries, capacitors, and SCs to ED and PD is illustrated using the Ragone plot in Fig.1.1. With the continuous advancement in research and development, the SC has achieved an intermediate position in the Ragone plot with higher ED than a conventional capacitor and higher PD than batteries [10]. As shown in Fig.1.1, SCs play a crucial role in applications where high ED and PD are required.

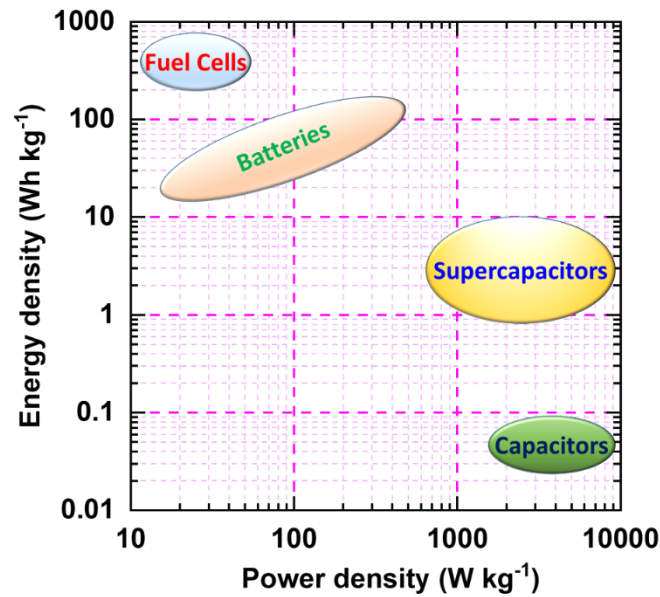


Fig. 1.1: Ragone plot for comparing the fuel cells, batteries, capacitors, and SCs with respect to their ED and PD [11].

Table 1.1: Comparison of battery, capacitor, and SC.

Parameters	Batteries	Conventional Capacitors	SCs
ED (Wh kg ⁻¹)	10 to 100	0.01 to 0.1	5 to 10
PD (W kg ⁻¹)	<100	<100000	<10000
Charging time (s)	1800 to 10800	10 ⁻⁶ to 10 ⁻³	0.3 to 30
Discharging time (s)	3600 to 1800	10 ⁻⁶ to 10 ⁻³	0.3 to 30
Cycle life	500 to 2000	>500000	> 100000
Coulombic efficiency (%)	70 - 85	>95	90 to 95

Moreover, SCs have a longer life cycle than batteries, high capacitance and low ESR than the ordinary conventional capacitors [11, 12]. SCs propose a viable solution for meeting the rising power demands of some applications that require

high ED and PD energy storage devices [13, 14]. The comparative characteristics of batteries, conventional capacitors and SCs are presented in Table 1.1. [15-19].

1.1.2 Historical background and current status of supercapacitors

The double-layer formation at the solid-electrolyte interface has been a known phenomenon since 1879, first predicted by Hermann von Helmholtz. Using this principle, Becker developed carbon-based electrolytic capacitors at the General Electric Corporation in 1957. [20]. This device was not commercialized because of its impracticable design in which both the electrodes were needed to dip in an electrolyte container. In 1966, the Standard Oil Company of Ohio corporation developed energy storage devices by utilizing high surface area carbon electrodes in non-aqueous electrolytes [21]. This device also failed to commercialize. In 1978, the Nippon Electric Company (Japanese) marketed the double layer capacitor technology as SC for the memory back up in computers and later various consumer appliances under the license of SOHIO.

B. E. Conway presented a new charge storage idea in 1975-1981, in which quick and reversible redox reactions occur on or near the electrode-electrolyte interface. Then, pseudocapacitor is the name given to this class of SC. The first pseudocapacitor was developed using ruthenium oxide (RuO_2) as an electrode [22-24]. At present, the capacitors available in the market contain high surface area carbonaceous (activated carbon) and highly redox-active RuO_2 electrodes [25]. By the 1980's several companies were producing electrochemical capacitor (EC). In 1978, Matsushita Electric Industrial Co. (often known as Panasonic in the West) developed the "gold capacitor" [26]. Under the brand name 'Dynacap,' ELNA began manufacturing its own double-layer capacitor in 1987 [27]. Pinnacle research institute (PRI) invented the first high-power double-layer capacitors. Metal oxide electrodes were used in the PRI ultracapacitor, which was invented in 1982 [28]. In 1990, the whole research field in SCs became more concerned with developing high-performance devices. Consequently, in 1992, the US department of energy started a study on hybrid electric vehicles and initiated the department of energy ultracapacitor development program at Maxwell laboratories [27]. Up to now, researchers have done substantial work on both electric double layer capacitor (EDLC) and pseudocapacitor electrode materials, using various types of metal oxides, composites and conducting polymers.

Table 1.2: Overview of world-wide commercially available SC [29].

Company	Country	Product Name	Voltage Range (V)	Capacitance Range (F)
AVX	US	Bestcap	3.6-16	0.010-1
Cooper	US	Powerstor	2.5-5.5	0.07-100
IOXUS	US	Ultracapacitor Cell	2.3-16	58-5000
Maxwell	US	Boostcap	2.2-125	1-3000
Evans	US	Capattery	5.5, 11	0.47-1.5
IOXUS	US	Hybrid Capacitor	1-2.3	220-1000
SAFT-ESMA	France	Soft Nickel Capacitor	7-29	500-1200
Cornell Dubilier	UK	CDE	2.1-5.5	0.022-70
Cap-XX	Australia	SC	2.3-5.5	0.09-120
Tarvima	Canada	ESCap	14-300	2-160
WIMA	Germany	Supercap	2.5-2.7	110-6500
Cellergy	Israel	Cellery	2.1-12	0.01-0.12
Nichicon	Japan	Evercap	2.5-2.7	0.47-4000
NEC-Tokin	Japan	SC	2.7-12	0.01-100
Panasonic	Japan	Gold Capacitor	2.1-5.5	0.015-70
Elna	Japan	Dynacap	2.5-5.5	0.047-100
VINATECH	Korea	HY-CAP	2.3-5.4	0.75-800
Nesscap	Korea	EDLC	2.3-2.7	5-60
Nesscap	Korea	Pseudocapacitor	2.3	50-300

Currently, a number of different companies, such as Maxwell Technologies Boost-cap (U.S.A.), Nippon Chemi-Con Corporation (Japan), CAP-XX (Australia), ELTON SC (Russia), NessCap (Republic of Korea) have financed the development of SCs devices for commercial activity. Further, several vendors provided SCs as per global demand from 1999 to 2013, which was much higher than the market growth value. In 2013, forty companies were involved in the production of carbon-based SCs worldwide [30]. The details of companies producing composite-based

hybrid SCs with their product name, voltage range and capacitance range are listed in table.1.2.

Recently, Saft-ESMA and IOXUS are trying to commercialize hybrid (asymmetric) capacitors, demonstrating their capacity to compete with the presently available Li-ion hybrids and asymmetric nickel-carbon-based SCs [31].

1.1.3 Basic principle, classification and salient features of supercapacitors

Basic principle of supercapacitor

As shown in Fig.1.2, SCs store electric charge in an electric double layer (EDL) generated at the between electrolyte-electrode interface. ECs work on the same principles as conventional electrostatic capacitors, with the exception that an electrolyte is always present to form a double layer. In an EC, electrochemically active materials are coated onto metallic current collectors to act as cathode and anode separated by an electrolyte.

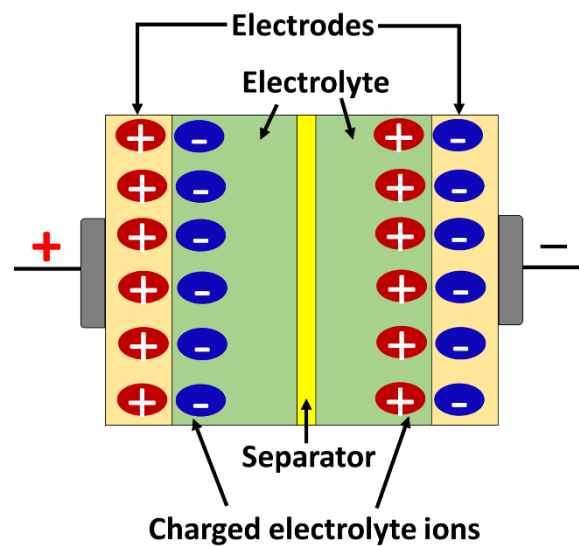


Fig. 1.2: Schematic diagram of EC.

The specific capacitance (C_s) of the SC device depends upon the size, specific surface area of respective electrode plates, and the spacing of the conducting plates. The capacitance of an EC is calculated as,

$$C_s = \frac{\epsilon_r \epsilon_0 S}{D} \quad (1.3)$$

where, ' C_s ' is the specific capacitance of the EC, ' S ' is the specific surface area of the active electrodes, ' ϵ_0 ' is the dielectric constant of the vacuum, and ' D ' is the distance between electrolyte ions and the electrode.

Classification of supercapacitors and electrode materials

Based on the charge storage mechanism and electrode materials, SCs are classified into three major categories: EDLCs, pseudocapacitors, and hybrid type capacitors [34-36]. They utilize Faradaic, non-Faradaic and a combination of these two processes for the charge storage. The taxonomy of SCs is summarized in chart 1.1.

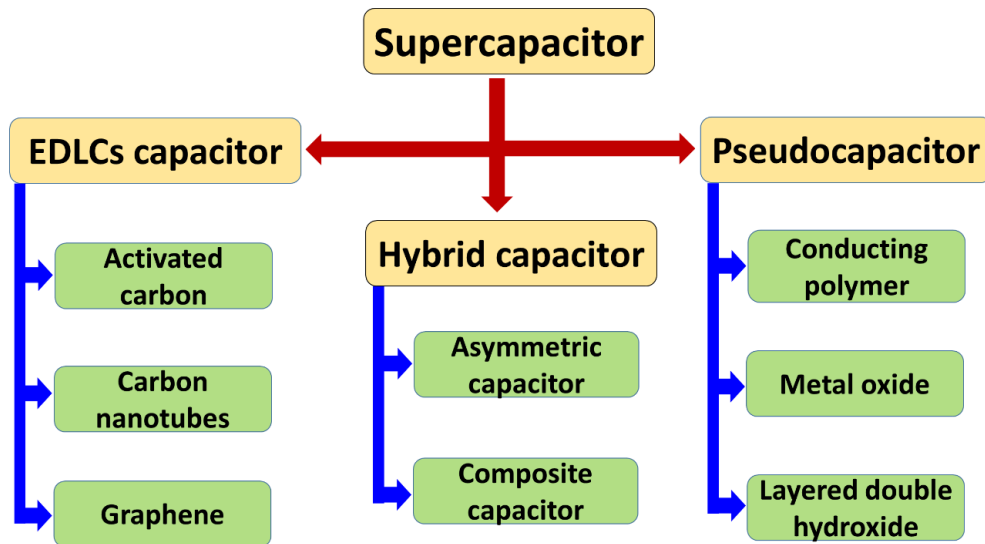


Chart 1.1: Taxonomy of SCs.

1.1.3.1 Electrochemical double layer capacitors

In EDLCs, charges can be stored electrostatically or through non-Faradic processes, in which no charge is transferred between the electrode-electrolyte interface. The EDLCs can be constructed using two carbonaceous material electrodes separated by separator and electrolytes [37].

In EDLCs, there is no transfer of charge, means it stores a charge by reversible adsorption of ions between electrode and electrolyte interface. This process is pictorially presented in Fig.1.5. Von Helmholtz was the first to identify the concept of EDL in a SC in 1879. The formation of double-layer due to strong interactions between the ions or molecules at the electrode-electrolyte interface is depicted in Fig. 1.3(a). This system's differential capacitance is calculated by following equation [38],

$$C_c = \frac{\varepsilon}{4\pi\delta} \quad (1.4)$$

Where, ϵ is the permittivity of solution, δ is the separation of the electrode surface and the centre of the ion. This model predicts a constant capacitance, but the Helmholtz theory failed to show the effect of surface potential or electrolyte concentration on the capacitance of EDLCs. Moreover, Gouy and Chapman modified the EDL principle and displayed the effect of electrolyte concentration and potential on the capacitance of the EDLCs (Fig. 1.3(b)). The charge is assumed to reside in a diffuse layer in the Gouy-Chapman model, resulting in a capacitance defined by equation.

$$C_d = \frac{\epsilon K}{4\pi} \cosh \frac{Z}{2} \quad (1.5)$$

The valence of the ions is denoted by z , while the reciprocal Debye-Hückel length is denoted by ϵ .

Further, Sterns model, which combines the Helmholtz and Gouy-Chapman models, clearly distinguishes two regions of ion distribution: the inner region, known as the Stern layer or compact layer, and the diffuse layer, as shown in Fig. 1.3(c). The electrode is heavily adsorbed by electrolyte ions (usually hydrated), forming the compact inner Helmholtz plane (IHP) followed by diffused layer separated by the outer Helmholtz plane (OHP) [39]. The total capacitance (C) in the EDLC can be calculated as the sum of capacitances from two regions: diffusion region capacitance (C_d) and stern type compact double layer capacitance (C_c). As a result, the equation for 'C' can be rewritten as (38).

$$\frac{1}{C} = \frac{1}{C_c} + \frac{1}{C_d} \quad (1.6)$$

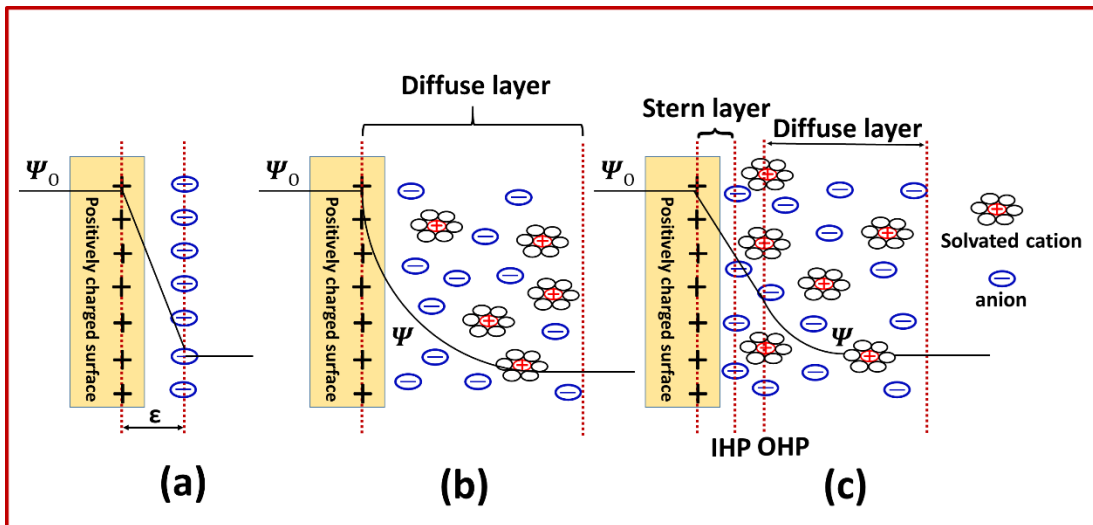


Fig. 1.3: EDL formation at a positively charged surface using the (a) Helmholtz, (b) Gouy Chapman, and (c) Stern models [38].

The carbon-based electrodes are electrochemically inert at all working potentials, thus useful for the EDLC electrodes. The electrolyte decomposition potential determines the operating potential range of EDLCs. Accordingly, the ED of EDLC depends on the type of electrolytes (aqueous or non-aqueous) used. The ionic conductivity of the aqueous electrolyte is high as compared to a non-aqueous electrolyte that increases the PD of the EDLC. The carbon-based electrode materials like carbon nanotubes, activated carbon, carbon aerogel, graphene and reduced graphene oxides are typically used as electrodes in EDLCs [40].

1.1.3.2 Pseudocapacitors

In contrast to EDLC, pseudocapacitors store charges Faradaically via transferring charge between electrode-electrolyte. The typical current response for EDLC and pseudocapacitor with potential are displayed in Fig. 1.4. The Cs of pseudocapacitor is dependent on the characteristics of electrode materials (high surface area and conductivity). .

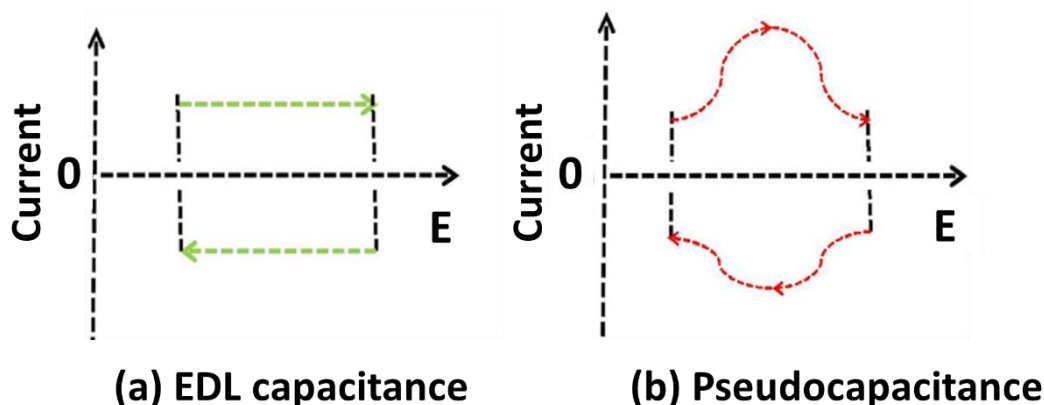


Fig. 1.4: Difference in (a) EDL capacitance and (b) pseudocapacitance.

The charge storing mechanism of pseudocapacitors is indirect and similar to the charging and discharging principle in batteries to some extent. In Faradic process, the charge transformation occurs through the double layer instead of forming a static double layer. Pseudocapacitors may be able to reach higher capacitances and ED than EDLCs due to Faradaic processes.

However, many factors influence the performance of pseudocapacitors e.g., the conductivity, porosity, surface area and particle sizes of electrode material, packing, type of electrolyte, and cell design. The metal oxides, metal phosphates,

conducting polymers, and sulphides are commonly employed as pseudocapacitor electrode materials [41-45]. However, the pseudocapacitors suffer from poor cycling stability due to phase transformation of electrode material or electrochemical leaching through redox reactions. Among the various materials, layered double hydroxides are attracted wide attention as a pseudocapacitive electrode material because of their special layered structure, tunable chemical composition, and ability to hybridize with other materials [46].

1.1.3.3 Hybrid supercapacitors

In order to achieve simultaneous improvement in ED and PD of SC devices, features of EDLC and pseudocapacitor electrodes are brought together to develop a new kind of hybrid supercapacitor (HSC) cell. Thus, HSCs can store charges by Faradaic and non-Faradaic reactions. The high-surface-area carbon-based materials are useful as an EDLCs-type charge storage electrode. While expanded surface area metal oxide/hydroxide-based materials are useful as a pseudocapacitive charge storage electrode.

Recently, the battery-type hybrid capacitor was developed, consisting of one battery type (energy source) and another is a capacitive type (power source) electrode. This device shows the features of the capacitor and a battery by delivering high ED and PD. However, the performnace of such HSC can not meet the desired demand of ED and PD. Also, the limited cycle life of pseudocapacitive electrodes hinders its long-term application. Fig.1.5. shows the schematic diagram of electric charge storage mechanisms of (a) EDLCs, (b) pseudocapacitor, and HSC

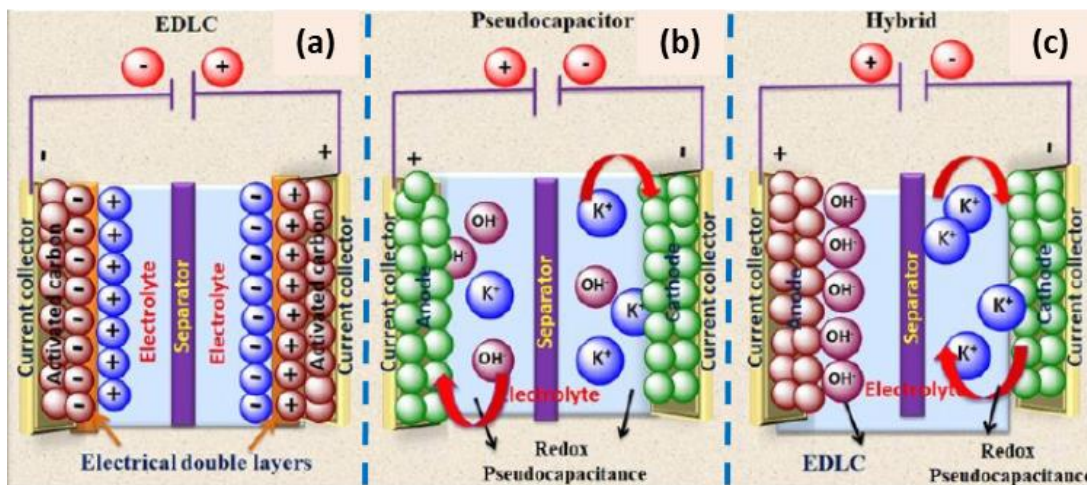


Fig. 1.5: Schematic diagram of electric charge storage mechanisms: (a) EDLCs, (b) pseudocapacitor, and HSC [47].

Salient features of supercapacitors

The following describes the salient features of the SC.

High PD:

SC can deliver high PD due to its unique principle of charge storage. As non-faradic or reversible faradic reactions are fast, the SC can deliver quick delivery charges, leading to high PD. This feature makes them highly applicable in hybrid electric vehicles, transportation, cranes, and power tools.

high coulombic efficiency:

The coulombic efficiency is defined as the ratio of discharging and charging time at same current densities. This feature reflects the long-term application of SC as no chemical reaction occurs without any electrode phase transformation.

Wide range of voltage (high ED):

Wide range of voltage is a direct impact on energy storage capacity. The aqueous electrolytes can operate upto ~ 1.23 V, whereas organic electrolytes can operate up to 3V. SC cells can work with aqueous as well as organic electrolytes. Consequently, SC can show wide operating potential leading to considerably high ED.

Wide range of operating temperature:

The working temperature range for military applications is -40 to 85 °C. Automotive applications have essentially the same temperature range. The working temperature range for a general-purpose consumer battery is ~ 0 - 40 °C, with storage temperatures ranging from -20 to 85 °C. When utilising automobiles and hand-held gadgets in the winter in northern places, and in the scorching summer sun in southern areas, these temperatures range are encountered. Therefore, considering the above point, the SC operating temperature range is very important and beneficial for various appliances. Also, SC have wide range of operating temperature i.e. -40°C to $+85^{\circ}\text{C}$.

Easy integration:

Every day brings new technological innovation, and the need for smaller, more compact, and more functional gadgets produce. This puts force on design and development of EES devices. The SC is one of them easily integrate and solve an aspect of above mentioned.

Long cycle life:

SC stores charges via EDLC (non-Faradic) or pseudocapacitive (reversible redox reactions) mechanism. Ideally, these processes do not lead to any phase change or electrochemical corrosion. Thus, SCs can be charged and discharged almost an infinite number of times. The performance of the SCs changes little after prolonged cycling (500,000 to 1 million times), and the internal resistance and capacity are dropped by 10% to 20%.

Ease of maintenance:

The SC has excellent charge-discharge efficacy, has a definite tolerance for overcharging and discharging. Once fabricated, SCs do not require any maintenance, as electrode and electrolyte are remained intact during the SCs operation.

Green and environmental protection:

Electrodes and electrolytes comprising SCs do not use heavy metals and other toxic compounds. Moreover, SCs have a long lifespan. Therefore, they are considered as a new type of green environmental protection power supply. All these features of SCs make them highly promising energy storage devices [1].

1.1.4 Electrode material for supercapacitor

SC mainly composed of four elements i.e., electrolyte, separator, current collector, and electrodes. Each element has its own importance and characteristic for the efficient working of SC.

Characteristics of electrolyte

High conductivity: The electrolyte in all SCs requires high conductivity to gain fast ionic movements in the charging-discharging process and deliver optimum power.

Solubility: Electrolytes for SCs should have high solubility of solute salt to enhance conductivity.

Ion-pairing: Electrolyte for SCs should have minimum ion-pairing at given practical solute salt concentrations to enhance conductivity.

Viscosity: Electrolyte for SCs should have low viscosity of the solution or solvent in order to enhance ionic mobility and resultant conductance.

Dielectric permittivity: Optimal dielectric permittivity or donor number of solvents to increase salt solubility and decrease ion pairing.

Characteristics of separator

In a SC, the separator acts as a sandwich between two electrodes. Separator materials' primary tasks are to prevent short circuits, store electrolyte in their pores, and let ions to pass through during charging and discharging processes.

Ionic conductivity: Separator material should have high ionic conductivity. The ionic conductivity of the separator affects the ED and PD.

Electrical insulation: The separator should have good electrical insulation to avoid short circuits.

High mechanical strength: The separator should have a high mechanical strength to prevent electrical shorting between electrodes.

High porosity: The pore density of the separator must be sufficient to hold liquid electrolytes and allow ions to pass between the electrodes.

Small pore size: The pore size must be less than the particle size of the electrode component, including the active material and conductive additives. The pores should ideally be equally distributed and have a tortuous shape. This maintains a consistent ionic current distribution throughout the separator.

High thermal stability: The separator must have high-temperature stability to sustain a wide operating temperature range of SCs.

Characteristics of the current collector

High flexibility: The current collectors desire to have high flexibility to fabricate flexible SC devices.

High geometrical surface area: The current collectors should have a high geometrical surface area to stabilize a large amount of active material that can accumulate a large number of ions to enhance the specific capacity of the SCs.

High conductivity: The current collectors should have good conductivity to transport the stored charges from active material to external connections.

High chemical stability: The current collectors should have high chemical stability to avoid corrosion and remain intact during electrochemical cycling.

Characteristics of electrode

The properties and performance of SCs mainly depend on the electrode materials. Hence to further improve the performance of electrode materials, the following features must be taken into consideration.

High surface area: The electrode in SCs should possess a high surface area. This can be achieved by synthesizing nanostructured electrode materials. Also, electrode material must have optimum pore structure for the easy percolation of charge storing ions. The high surface area electrodes allow the number of active sites available to store charge.

High electrical and thermal conductivity: The electrode must have high conductivity to transport stored charges to the current collector. The high conductivity of electrode material can enhance the rate capability and PD of SCs.

Long-term stability: The charge-discharge mechanism of pseudocapacitors or redox capacitors includes the transfer of electric charge between the phases without any bulk phase transformation. Accordingly, material for SCs should be stable upon multiple electrochemical cycling.

High cyclability: The electrode material for SCs should have high cyclability. The charge-discharge processes in batteries often involve irreversible inter-conversions of the chemicals and electrodes. Conversely, charge-discharge processes in SCs do not involve any irreversible inter-conversions of the chemicals and electrodes. Thus, the electrode material for SCs must have a suitable chemical composition that enables reversible redox reactions for charge storage. As a result, SCs electrode recyclability is nearly limitless, with a typical range of 10^5 to 10^6 times.

On these backdrops, a variety of materials are used as electrode materials for SCs they are broadly classified as (i) carbonaceous materials, (ii) conducting polymers, (iii) metal oxides, (iv) layered double hydroxide (LDH), and (v) 2D nanosheets (NSs) based hybrids.

1.4.1.1. Carbon-based materials

Carbon materials are typically used as EDLC materials. They can offer wide distribution of porosity, corrosion resistance, high surface area, excellent electric conductivity, high chemical stability, and wide availability in different structural forms by tuning and selecting appropriate synthesis protocols [2-4, 18]. Different forms of carbonaceous materials can be used as a SC electrode material that includes carbon nanofibers, carbon nanotubes, activated carbon, carbon aerogel, and graphene [48-53,18].

Activated carbon (AC)

AC is less expensive and possesses a higher surface area ($>1000 \text{ m}^2\text{g}^{-1}$); hence, it is the most useful electrode material in EDLCs. ACs are widely used in commercial SCs because of their low cost, feasible and scalable synthesis [48]. ACs can be produced from different biomass precursors like wood, coconut, coal, and other agricultural waste. The surface area and porosity of carbon is significantly increased by an activation process that improves the SCs capacitive performance [18].

Carbon nanotubes (CNTs):

CNTs are nothing but an allotrope of carbon arranged in a cylindrical hollow nanostructure. CNTs offer many advantages like small pore size distribution, High conductivity, high surface area, and high stability. These characteristics make them a potential candidate for SCs electrodes. Furthermore, due to their high surface area and chemical stability, there is a growing research interest in using CNTs as substrates for the growth of other nanomaterials. Pure CNTs demonstrated a specific surface area of $\sim 120\text{--}500 \text{ m}^2 \text{ g}^{-1}$ and a Cs of $2\text{--}200 \text{ F g}^{-1}$ [49,50].

Two types of CNTs are available (i) multi-walled carbon nanotubes (MWCNT) and (ii) single walled carbon nanotubes (SWCNT). Also, CNTs can be highly useful as conductivity enhancer additives in electrode materials that can alter carbon black.

Graphene

Graphene contains a layer of sp^2 carbon atoms tightly packed into a 2D honeycomb structure. In the view of electrode material for EDLCs it can offers interesting properties like good electronic conductivity, large surface area, high mobility of charge carriers, suitable pore size distribution, high mechanical strength, thermal and chemical stability [51]. Graphene can be prepared using epitaxial growth, micromechanical cleavage, chemical vapour deposition and exfoliation of graphene oxide (GO). Among these methods, exfoliation of GO is one of the simple methods for the scalable production of GO NS. Modified hummer's approach is generally used for the production of GO NSs by exfoliation of graphite oxide [52].

Moreover, reduced graphene oxide (rGO) can be prepared by reducing GO NSs and finds advantages over GO NS due to its higher conductivity [52].

1.1.4.2 Conducting polymer

Conducting polymers like polyaniline (PANI), poly-(3,4-ethylenedioxythiophene) (PEDOT), polypyrrole (PPy), and derivatives of polythiophene (PTh), have attracted attention as SC electrodes due to their relatively high capacitance values and supererious conductivity. Conducting polymers, store and release charge through redox processes. However, the weak stability of conducting polymers for electrochemical cycling leads to a non-conducting phase of polymer and limits their uses as SCs electrodes. The Cs reported for PANI, PPy, and PTh are 750, 620 and 485 F g⁻¹, respectively [53]. Hryniewicz et al. [54] prepared the PPy nanotubes by direct electro-synthesis method on flexible mesh electrode and reported the Cs of 423 F g⁻¹. Patil et al. [55] synthesized the PTh thin film through the chemical bath deposition (CBD) method and achieved Cs of 300 F g⁻¹. The PANI electrode was prepared through the microwave-assisted CBD method and demonstrated Cs of 753 F g⁻¹ [56].

1.1.4.3 Metal oxides

Metal oxides SC electrodes show superior energy storage capability over traditional materials and long-cycle performance compared to conducting polymers. In the same phase, metal oxides possess two or more oxidation states; this fact is highly beneficial for enhancing the SCs performance. The transition metal oxides like MnO₂ [57], NiO [58] RuO₂ [59], Co₃O₄ [60], Fe₂O₃ [61], WO₃ [62], and V₂O₅ [63] are explored as SCs electrode materials. Among these transition metal oxides, RuO₂ performs exceptionally well due to its high theoretical Cs, low ESR and high electrical conductivity [64- 67]. However, the toxic nature and high cost of RuO₂ precursors limit its further commercial use. In metal oxides-based SC electrodes, charging-discharging processes involve reversible/irreversible redox transitions. Thus, there is a possibility of a phase change of electrode material. Due to phase change, the metal oxide-based SC electrode suffers from limited cycling performance. Therefore lots of efforts are put forward to increase the specific capacity and cycle life of transition metal oxides-based SCs electrodes.

1.1.4.4 Layered double hydroxides

LDH is a unique class of layered material with many applications like photocatalysis, flame retardant, CO₂ adsorbent, drug delivery, and so on. The

unique layered structure of LDH comprising stacking of brucite like structure with the general formula $[M^{2+}_{1-x} M^{3+}_x (OH)_2]^{x+} [A^{n-}/n]^{x-} \cdot mH_2O$ in which divalent and trivalent metal ions within the brucite like layers and A^{n-} are interlayer anions; typically x is usually between 0.2 to 0.4 [68]. Due to partial substitution of M^{2+} by M^{3+} , the individual monolayer of LDH acquires a positive electrostatic charge on them. This excess positive charge is compensated by anions like CO_3^{2-} , Cl^- , SO_4^{2-} , NO_3^- , etc. and water molecules which are intercalated between the hydroxide sheets as shown in Fig. 1.6.

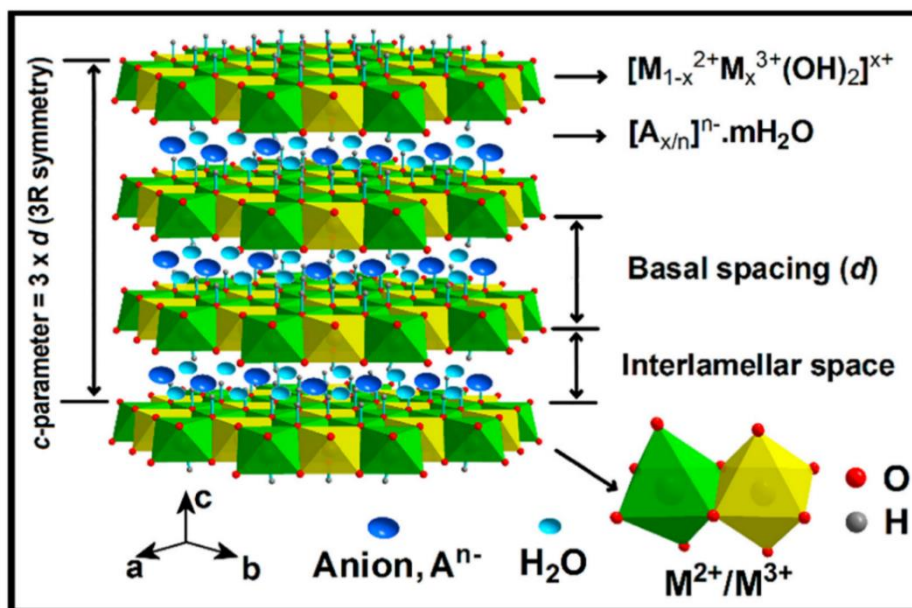


Fig. 1.6: Schematic representation of the LDH structure [69].

The LDHs demonstrated huge potential as SCs electrodes due to their tunable chemical composition, special anions intercalated structure and multiple redox states of constituent elements. Apart from these properties, LDHs show characteristic exfoliation in various solvents leading to the individual monolayer of LDH, which is commonly known as LDH NS [69]. Hence, due to the unique structure, porous morphology, good ion exchange properties, and low synthesis cost of LDHs, these materials are regarded as excellent candidates for SCs [70]. Although, on many instances, M-Al-LDH (M: Divalent metal ions) are amply exploited for SC applications. Their performance is limited by electrochemically inactive amphoteric Al^{+3} and restricted gallery space. Consequently, attempts were made to hybridize LDH with various guest nanostructures like conducting carbon, CNT, polymer, etc [71].

1.4.1.5 2D nanosheet based hybrids

2D NSs have recently sparked intense research interest as building blocks for the synthesis of hybrid electrodes due to their unique structure, high surface area, and versatile physicochemical characteristics. Compared to 1D and 3D structures, 2D structure permits easy transportation of electrons or ions due to their unique 2D shape [72]. The 2D NSs prepared by the exfoliation process of layered materials are highly anisotropic as compared to other nanostructure shapes. Moreover, the facile exfoliation of 2D crystals into monolayer NSs and easy chemical modification makes them suitable for synthesizing nanohybrid electrodes. In this approach, the layered structures formed by stacking of 2D NSs create 2D voids within consecutive monolayers that allow functional guest species to intercalate between these expandable interlayer spacings. The various guest nanostructure species like organic, inorganic, polymeric, and biological are useful for the hybridization with 2D NSs [73]. Due to these features provided by the inorganic NSs, hybrid materials on demand can be possible by the permutation and combination of practically unlimited guest species. 2D nanosheets based hybrids have more flexible capabilities and a wider range of applications in EES devices than other pure nanohybrids [74]. Also, these hybrid materials possess highly porous structure with expanded surface area that is highly beneficial for electrode material in EES device. Especially 2D NS-based nanohybrids derived from redoxable layered material such as layered metal oxide, layered metal chalcogenide, and LDH can be useful candidates for SCs electrode material [75]. During hybridization, a strong electronic connection between redoxable 2D NSs and guest species causes an alteration in electronic conductivity that is extremely advantageous for electrode functionality. Recent research has been concentrated on the production of 2D hybrid material based on graphene, mxenes, LDH, and metal oxide NSs, which can offer improved electrochemical performance compared to their bulk material due to the synergistic effect between the hybridized components.

1.2 Literature survey

1.2.1 Literature survey of LDH for supercapacitor

Various LDHs were synthesized using different methods such as hydrothermal, co-precipitation, electrodeposition, and solvothermal. LDH material with their synthesis protocol and corresponding electrochemical performance is summarized in table 1.3. Su et al. [76] synthesized well-crystalline thin platelets of Co-Al-LDH by coprecipitation method. The Co-Al-LDH showed enhanced capacitive performance with a Cs up to 145 F g⁻¹ at a 2 A g⁻¹. Gao et. al. [77] prepared NiCo₂Al-LDH nanowire-NSs structure via a hydrothermal method, which delivered Cs of 1137 F g⁻¹ at 0.5 A g⁻¹. The increased electrochemical performance of the NiCo₂Al-LDH was assigned to the nanowire-NS morphology. Zhai et. al. [78] prepared a unique hierarchical Co-Al-LDH structure using a simple hydrothermal method and reported Cs of 838 F g⁻¹ at 1 A g⁻¹ with excellent capacitive retention of 95% over 20000 cycles. Xiao et. al. [79] prepared hierarchical Ni/Co-LDH microspheres using a coprecipitation method and delivered a Cs of 1652 F g⁻¹ at 1 A g⁻¹ with excellent stability (100 %) over 2000 cycles. Hierarchical Ni-Co-LDH cages structures were synthesized by Jian et. al. [80] via reflux method, which offered maximum Cs of 1203 F g⁻¹ at 1 A g⁻¹ with 90.2% capacitive retention after 1000 cycles. Wang et al. [81] prepared platelet-like particles of Ni/Al LDH coated on the nickel foam (NF) via a hydrothermal method. Ni/Al LDH electrode demonstrated pseudocapacitive behavior with maximum Cs of 701 F g⁻¹ at 10 mA cm⁻². Ni-Co-LDH ultrathin NSs were synthesized by Chen et. al. [82] via hydrothermal technique that offered maximum Cs of 2682 F g⁻¹ at 3 A g⁻¹. Wang et. al. [83] prepared a petal-like Ni-Al-LDH on NF by hydrothermal method followed by a CBD method. This method can effectively avoid the accumulation of LDH sheets on Ni foam. Ni-Al-LDH delivered Cs of 795 F g⁻¹ at a current density of 0.5 A g⁻¹ with better cycling stability (80 %) over 1000 cycles. The NiCoDH nanoflakes were synthesized by Jin et. al. [84], which showed a maximum Cs of 1372 F g⁻¹ at 1 A g⁻¹. Li et. al. [85] prepared 3D flower-like Ni/Co-LDH microspheres via the co-precipitation method, which delivered an excellent Cs of 2228 F g⁻¹ at 1 A g⁻¹. Zhao et. al. [86] synthesized monolayer Ni-Co-LDH by simple hydrothermal technique. This unique monolayer structure efficiently raises exposed electroactive sites and facilitates surface-dependent electrochemical reaction processes, resulting in a Cs of 2266 F g⁻¹ at 0.5 A g⁻¹. Ni-Mn-LDH NSs were prepared by Sim et. al. [87] on NF and delivered the highest Cs of 881 F g⁻¹ at 0.5 A g⁻¹ with better stability (88 %). Co_{0.5}Ni_{0.5}(OH)₂ nanodiscs

uniformly coated on graphene sheets were successfully synthesized via coprecipitation method by Cheng et al. [88] and delivered Cs of 2660 F g⁻¹ at 0.5 A g⁻¹. Tao et al. [89] synthesized microspheres of Ni-Co-DHM by in situ method and reported a Cs of 2275.5 F g⁻¹ at 1 A g⁻¹ in an aqueous 6M KOH electrolyte with 92.9% capacitive retention over 5000 cycles. Also, Song et al. [90] prepared Ni-Co-LDH NSs via hydrothermal technique and investigated the electrochemical characteristics of NiCo-LDH. The Ni-Co-LDH NSs demonstrated Cs of 2242 F g⁻¹ at 1 A g⁻¹. Chen et al. [91] studied the capacitive performance of flowers-like binary Ni_{0.32}Co_{0.68}(OH)₂ electrodes prepared via a coprecipitation method. The Ni_{0.32}Co_{0.68}(OH)₂ exhibit the highest Cs of 1000 F g⁻¹ at 5 mV s⁻¹. Pu et al. [92] synthesized Ni-Co-LDHs NSs by hydrothermal technique, showings a high Cs of 1734 F g⁻¹ at 6 A g⁻¹. The capacitance retention of the Ni-Co LDHs in GCD test after 1000 cycles was 86%. Sun et al. [93] successfully synthesized nanosheet, nanoplate and nanosphere morphologies of Ni-Co-LDHs by CBD. CBD synthesized Ni-Co-LDHs demonstrated Cs of 1030 F g⁻¹ at 3 A g⁻¹. Jagadale et al. [94] prepared ultrathin nanoflakes-like morphology of Co-Mn-LDHs via electrodeposition method, which showed Cs of 1062 F g⁻¹ at 0.7 A cm⁻² in 1M LiOH electrolyte and excellent cycle life (96.3 % cyclic stability over 5000 cycles). The Ni-Cr-LDH has been prepared onto NF via chemical precipitation method by Chen et al. [95] and reported Cs of 1525 F g⁻¹ at 2 A g⁻¹. Patil et al. [96] synthesized nanocrystalline Cu-Cr-LDH by coprecipitation method and demonstrated Cs of 843 F g⁻¹ at 1 A g⁻¹. Liang et al. [97] prepared Ni-Co-LDH nanowires array using the hydrothermal method. The Ni-Co-LDH nanowires array electrode showed a Cs of 995.4 F g⁻¹ at 1 A g⁻¹.

1.2.2 Literature survey on LDH based nanohybrids

In recent years, the research on the LDH based nanohybrids for SC is accelerated due to their higher ED compared to the carbonaceous material and higher electrochemical stability compared to the conducting polymer. The fast and reversible Faradic reactions at the electrode-electrolyte interface are responsible for higher ED. Electrochemical performance of LDH based nanohybrids for SC is summarized in table 1.4.

Zhao et al. [98] reported the CoNi-LDH/PEDOT:PSS[Poly (3,4-ethylene dioxythiophene): poly(styrene sulfonate) hybrid structure by self-assembly process. CoNi-LDH/PEDOT:PSS shows the Cs of 960 F g⁻¹ at 2 A g⁻¹ and 93.7%

capacitance retention after 1000 cycles. Wu et al. [99] synthesized porous Co-Al-LDH NSs (GSP-LDH) electrode by electrostatic self-assembly. GSP-LDH showed a high Cs of 1043 F g⁻¹ at 1 A g⁻¹ with 88% capacitive retention after 3000 cycles. Li et al. [100] synthesized the unique core-shell structure of Ni-Co-LDH@CNT/NF by the electrodeposition method. The Ni-Co-LDH@CNT/NF electrode delivered a maximum Cs of 2046 F g⁻¹ at 1 A g⁻¹. It showed capacity retention of 78% after 1200 cycles. Wang et al. [101] prepared the Co-Ni-Fe-LDH/CNFs NSs using a hydrothermal approach. The Co-Ni-Fe-LDH/CNFs-0.5 composite showed a high surface area with Cs of 1203 F g⁻¹ at 1 A g⁻¹. Zhao et al. [71] prepared Ni-Mn-LDH/CNPs(carbon nano particles) electrode, which delivers a high Cs of 2960 F g⁻¹ at 1.5 A g⁻¹ with good capacitive retention of 79.5% at 30 A g⁻¹. Ni-Al-LDH@carbon nanoparticles were prepared by Liu et al. [102], and this hybrid electrode exhibited a Cs of 478 F g⁻¹ at 200 mVs⁻¹. CoAl-LDHs@PEDOT core/shell narrow platelet array on NF was prepared by Han et al. [103] and exhibited the highest Cs of 672 F g⁻¹ at 1 A g⁻¹. The improved electrochemical performance of LDH@PEDOT electrode was attributed to the synergistic effect of its constituent components. Furthermore, the device shows outstanding rate capability with an ED of 39.4 Wh kg⁻¹ at 40 A g⁻¹ and a superior cyclic lifespan with 93% capacity retention after 5000 cycles. Co-Mn-LDH/CF synthesized by Zhao et al. [104] via coprecipitation method delivered maximum Cs of 1079 F g⁻¹ at 2.1 A g⁻¹ with 81% capacitance retention after 6000 cycles. Zhang et al. [105] prepared GNS/CoAl-LDHs by simple reflux method and the obtained hybrid exhibited Cs of 712 F g⁻¹ at 1 A g⁻¹. Furthermore, the GNS/CoAl-LDHs hybrids displayed capacitance retention of 81% after 2000 cycles at 10 A g⁻¹. Ni-Co-Al-LDH nanoplates coupled with Ni-Co-carbonate hydroxide (Ni-Co-CH) nanowires grown on graphite paper via hydrothermal method by Yang et al. [106] Ni-Co-CH showed Cs of 1297 F g⁻¹ at 1 A g⁻¹. Yu et al. [107] synthesized polyhedral-like Ni-Mn-LDH/PC composites electrode by hydrothermal method and obtained Cs of 1634 F g⁻¹ at 1 A g⁻¹. Further, Ni-Mn-LDH/PC electrode can retain 84.58% of original Cs after 3000 cycles at 15 A g⁻¹. The Co-Al-LDHs/rGO composites were prepared by hydrothermal method and Cs of 1492 F g⁻¹ at 1 A g⁻¹ was reported by Li et al. [108]. Zhong et al. [109] were synthesized orderly lamellar structured rGO/Co-Al-LDHs via a one-step hydrothermal method. The rGO/Co-Al-LDHs composite containing 12.0 wt% rGO delivered a maximum Cs of

825 F g⁻¹ at 1 A g⁻¹. Face-to-face self-assembling between positively charged Co-Al-LDH-NS and negatively charged rGO NSs can avoid the self-agglomeration of CoAl-LDH. The NiCo₂O₄@NiFe-LDHs core/shell nanowires array was synthesized via electrodeposition method by Luo et al. [110] and obtained a maximum Cs of 1160 F g⁻¹ at 1 A g⁻¹. The Ni-Mn-LDH NS arrays on KCu₇S₄ microwires (KCu₇S₄@NiMn LDHs) were synthesized by hydrothermal method and showed maximum Cs up to 733.8 F g⁻¹ (1 A g⁻¹) was reported by Guo et al. [111]. Guan et al. [112] prepared the CoSx/Ni-Co-LDHs nanocages with rhombic dodecahedral structure and showed excellent Cs of 1562 F g⁻¹ at 1 A g⁻¹. Liu et al. [113] synthesized hierarchal NiO/Ni-Mn-LDH NSs array on NF. NiO/Ni-Mn-LDH displayed a high Cs of 937 F g⁻¹ at 0.5 A g⁻¹ in redox-active 3M KOH electrolyte. Yang et al. [114] synthesized Ni-Co-LDHs/Go by reflux method and reported Cs of 1137 F g⁻¹ at 0.5 A g⁻¹. Gunjekar et al. [115] prepared a mesoporous nanoplate network of 2D Ni(OH)₂ intercalated with polyoxovanadate (POV) anions via a chemical solution deposition. The obtained thin film electrode exhibited high Cs of 1440 F g⁻¹ at 1 A g⁻¹ and cyclic stability up to 2000 cycles with a good capacitive retention (85%). The sandwich-like RGO@Mg-Al-LDH nanohybrid was synthesized via solvothermal method by Hatui et al. [116] and obtained Cs of 1334 F g⁻¹ at 1 A g⁻¹ current density. Lai et al. [117] prepared Cellulose@Ni-Co-LDH composite via a solution deposition technique and composite electrodes exhibited significantly enhanced Cs of 1949.5 F g⁻¹ at 1 A g⁻¹ with capacitive retention of 54% at high current density of 10 A g⁻¹. Li et al. [118] synthesized Co-Mn-LDH/rGO hybrid electrode via co-precipitation method, which showed a high Cs of 1635 F g⁻¹ at 1 A g⁻¹. The incorporation of rGO can boost the Cs and improve cyclic stability of the Co-Mn-LDH/rGO hybrids. Wu et al. [119] prepared the 1D core-shell architecture composed of silver nanowire@hierarchical Ni-Al-LDH via a hydrothermal method, which showed high Cs of 1246.8 F g⁻¹ at 1 A g⁻¹. Wang et al. [120] prepared three-dimensional porous MXene/Ni-Al-LDH composite by liquid-phase deposition method and reported Cs of 1061 F g⁻¹ at 1 A g⁻¹. The Ni-Al-LDH platelets homogeneously anchored on the MXene sheets allow excellent Faradaic utilization of the electro-active surface and facile electrolyte penetration that enhance the electrochemical performance. The Ni-Co-LDH/PANI/BC electrode reported by Wu et al. [121] showed a high Cs of 1690 F g⁻¹ at 1 A g⁻¹, and

remarkable cycling stability performance of 83.2% capacitance retention over 5000 cycles was. Jagadale et.al. [122] prepared binder-free thin films of Co-Al-LDH on carbon fibers by electrodeposition method. The binder-free Co-Al-LDH thin films showed maximum Cs of 634.3 F g⁻¹ and better stability. Zhang et al. [123] prepared 3D porous Ni-Al-LDH/GNS composite using a liquid-phase deposition method that showed high Cs of 1255.8 F g⁻¹ at 1 A g⁻¹. Yu et al. [124] synthesized LDH-CNT/RGO nanohybrid by chemical coprecipitation method. The LDH-CNT/RGO nanohybrids showed the maximum Cs of 1188 F g⁻¹ at 1 A g⁻¹ and 850 F g⁻¹ at 10 A g⁻¹ with a capacitance retention of 72%. The excellent rate capability of LDH-CNT/RGO was attributed to the synergistic effect of NiCoAl-LDHs, RGO, and CNTs. Ma et al. prepared Co-Ni-LDH/graphene super lattice composite by self-assembly strategy and obtained Cs value 650 F g⁻¹ in 1M KOH [125]. Synthesis of a sandwich-type three-dimensional Ni-Al-LDH/rGO composite was reported by Xu et al. [126] via hydrothermal method followed by LBL technique. Ni-Al LDH/rGO composite delivered a maximum Cs of 1329 F g⁻¹ at 3.57 A g⁻¹ in 6M KOH. Wang et al. reported hierarchical structured Ni-Al-LDHs/MWCNT/NF composites using a hydrothermal technique followed by a chemical vapor deposition (CVD) route. Ni-Al-LDHs/MWCNT/NF composites showed a Cs of 1293 F g⁻¹ at 5 mA cm⁻² in 1M KOH [127]. Gao et al. reported a capacitance value of 782 F g⁻¹ at 5 mV s⁻¹ for hydrothermally fabricated GNS/NiAl-LDHs in 6M KOH electrolyte [128]. Li et al. [129] synthesized flower-like of Fe₃O₄@C@Ni-Al LDHs composite by hydrothermal method. The Fe₃O₄@C@Ni-Al LDHs composite exhibited a significantly improved electrochemical performance of 768 F g⁻¹ at 1 A g⁻¹ and good capacitive retention 92.3 %. He et al. [130] prepared Ni-Al-LDHs/CNFs composite by hydrothermal method. The Ni-Al-LDHs/CNFs hybrid electrode delivered an excellent Cs of 1613 F g⁻¹ at 1 A g⁻¹ and superior capacitive retention of 80 % over 1000 cycles. Ning et al. [131] prepared Co₃O₄@NiAl-LDHs core/shell hierarchical nanowire arrays by hydrothermal method and obtained Cs of 1772 F g⁻¹ at 2 A g⁻¹ current density in 6M KOH. Chen et al. [132] prepared Co_{0.4}Ni_{0.6}(OH)₂ LDHs/CNT using a chemical precipitation method and reported a Cs of 1843 F g⁻¹ at 0.5 A g⁻¹. Also, Co_{0.4}Ni_{0.6}(OH)₂ LDHs/CNT delivered high ED and PD of 51 Wh kg⁻¹ and 3.3 k W kg⁻¹, respectively. Ma et al. [133] synthesized Ni-Co-OH/rGO hybrid nanolayers through one-pot hydrothermal method. The obtained Ni-Co-

OH/rGO hybrid showed superior Cs of 1316 F g⁻¹ at a 0.5 A g⁻¹. Cai et al. [134] reported porous Ni-Co-LDH NSs decorated on RGO using the solvothermal method and delivered Cs of 1911 F g⁻¹ at 2 A g⁻¹ discharge rate. Huang et al. [135] prepared sandwich-like RGO@CoNiAl-LDHs via hydrothermal process and obtained a Cs of 1866 F g⁻¹ at 1 A g⁻¹ in 3M KOH electrolyte. Yang et al. [136] reported a Cs of 1035 F g⁻¹ at 1 A g⁻¹ for NiCoAl-LDHs-MWCNT on Ni foam substrate prepared by reflux method. Trang et al. [137] prepared ZnONF/NiCoLDHs composite by hydrothermal method. A maximum Cs of 1624 F g⁻¹ at 10 A g⁻¹ was obtained in 1 M LiOH electrolyte. Also, it delivered ED and PD of 68.2 Wh kg⁻¹ and 27 k W kg⁻¹, respectively. Wang et al. [138] reported a Cs of 1805 F g⁻¹ at 0.5 1 A g⁻¹ for Ni-Co-LDHs-ZTO hybrid material prepared by an electrochemical deposition method. Li et al. [139] reported Ni-Co-hydroxide nanoflakes decorated on the surface of CNTs by a CBD process and it delivered maximum Cs of 1151 F g⁻¹ at 1 A g⁻¹. Co-Al-LDHs/GF nanohybrid was synthesized by Masikhwa et al. [140] via the hydrothermal method and showed maximum Cs of 600 F g⁻¹ at of 1 A g⁻¹ with ED of 28.0 Wh kg⁻¹. Vialat et. al. [141] prepared Co^{II}Co^{III}-CO₃ LDHs by simple coprecipitation method. The nano composite showed a maximum Cs of 1490 F g⁻¹ at 0.5 A g⁻¹ in 1 M KOH electrolyte. The hierarchical structured LDHs@CoS composite was synthesized by Dou et. al. [142] via hydrothermal technique, and it showed Cs of 1205 F g⁻¹ at 1 A g⁻¹. Xu et. al. [143] prepared N-C@LDHs hollow microspheres via hydrothermal technique. The N-C@LDHs exhibited maximum Cs of 1712 F g⁻¹ at 1 A g⁻¹ in 1 M KOH electrolyte. The activation cotton T-shirt (ACT)/CoAl-LDHs was prepared by Gao et. al. [144] via in situ hydrothermal process and showed Cs of 977 F g⁻¹ at 2.5 A g⁻¹ with 88 % capacitive retention after 2000 cycles. Abushrenta et. al. [145] prepared hierarchical microstructured Co(OH)₂@Co-Al LDH (PLDHs) nanocomposite via hydrothermal approach, which delivered Cs of 1734 F g⁻¹ at 5 mA cm⁻² with 85 % capacitive retention over 500 cycles. A core-shell nano wire array structured Ppy@LDHs prepared by shao et al. [146] via electrosynthesis method and delivered Cs of 2342 F g⁻¹ at 1 A g⁻¹ with excellent stability (115%) over 20000 cycles.

Table 1.3: Comparative literature survey of electrochemical capacitive performance of LDH.

Sr. No.	Material	Method of preparation	Electrolyte	Capacitance (F g^{-1}) at current density	Cycles	Stability (%)	Ref.
1	CoAl-LDH	Solvothermal	6M KOH	145 (2 A g^{-1})	-	-	76
2	NiCoAl-LDHs	Hydrothermal	1M KOH	1137 (0.5 A g^{-1})	12000	-	77
3	CoAl-LDHs	Hydrothermal	2M KOH	838 (1 A g^{-1})	20000	95	78
4	Ni/Co-LDH	Coprecipitation	1M KOH	1652 (1 A g^{-1})	2000	100	79
5	LDH nanocage	Reflux	1M KOH	1203 (1 A g^{-1})	1000	90.2	80
6	NiAl-LDH	Hydrothermal	6M KOH	701 (10 mA cm^{-2})	400	94	81
7	NiCo-LDH	Hydrothermal	1M KOH	2682 (3 A g^{-1})	-	-	82
8	NiAl-LDHs	CBD and Hydrothermal	1M KOH	795 (0.5 A g^{-1})	1000	80	83
9	NiCoDH	Hydrothermal	-	1372 (1 A g^{-1})	2000	94.3	84
10	Ni/Co LDHs	Coprecipitation	6M KOH	2228 (1 A g^{-1})	-	-	85
11	NiCo-LDHs	Hydrothermal	6M KOH	2266 (0.5 A g^{-1})	-	-	86
12	NiMn-LDHs	Hydrothermal	1M KOH	881 (0.5 A g^{-1})	-	88	87
13	$\text{Co}_{0.5}\text{Ni}_{0.5}(\text{OH})_2$	Coprecipitation	2M KOH	2360 (0.5 A g^{-1})	-	86	88
14	NiCo-DHM	Hydrothermal	6M KOH	2275.5 (1 A g^{-1})	5000	92.9	89

15	NiCo-DH	Hydrothermal	1M KOH	2442 (1 A g ⁻¹)	-	83.5	90
16	Ni _{0.32} Co _{0.68} (OH) ₂	Coprecipitation	1M KOH	1000 (5 mV s ⁻¹)	1000	100	91
17	NiCoLDHs	Hydrothermal	3M KOH	1734 (6 A g ⁻¹)	1000	86	92
18	NiCo-LDHs	Coprecipitation and Oil Bath	1M KOH	1030 (3 A g ⁻¹)	1000	97.3	93
19	CoMnLDHs	Electrodeposition	1M LiOH	1062 (0.7 A cm ⁻²)	5000	96.3	94
20	Ni-Cr LDH	Coprecipitation	6M KOH	1525 (2 A g ⁻¹)	1000	86	95
21	Cu-Cr-LDH	Coprecipitation	2M KOH	843 (1 A g ⁻¹)	1500	85	96
22	NiCo-LDH	Hydrothermal	6M KOH	995.4 (1 A g ⁻¹)	-	-	97

Table 1.4: Literature survey of LDH based nanohybrids for SC.

Sr. No.	Material	Method of preparation	Electrolyte	Capacitance at current density	Cycles	Stability	Ref.
1	CoNi-LDH/PEDOT:PSS	Coprecipitation	1M KOH	960 (2 A g ⁻¹)	1000	93.7	98
2	GSP-LDH	Hydrothermal	6M KOH	1043 (1 A g ⁻¹)	3000	88	99
3	NiCo-LDH@CNT/ NF	Hydrothermal	2M KOH	2046 (1 A g ⁻¹)	1200	78	100
4	CoNiFe-LDH/CNFs-0.5	Chemical precipitation	6M KOH	1203 (1 A g ⁻¹)	2000	82.7	101

5	NiMn-LDH/CNT	Hydrothermal	1M KOH	2960 (1.5 A g^{-1})	2000	99.1	71
6	NiAl-LDH@carbon nanoparticles	Green- precipitate	1M KOH	478 (20 mV s^{-1})	2000	88.9	102
7	CoAl-LDH@PEDOT	Hydrothermal	6M KOH	649 (2 mV s^{-1})	5000	92.5	103
8	CoMn-LDH/CF	Chemical precipitation	1M LiOH	1079 (2.1 A g^{-1})	6000	81	104
9	CoAl-LDH/GNS	Chemical precipitation	6M KOH	711.5 (1 A g^{-1})	2000	81	105
10	NiCoAl- LDH-NPs/CH-NWs	Hydrothermal	6M NaOH	1297 (1 A g^{-1})	-	-	106
11	NiMn-LDHs/PC	Hydrothermal	6M KOH	1634 (1 A g^{-1})	3000	84.58	107
12	CoAl-LDHs/rGO	Hydrothermal	6M KOH	1492 (1 A g^{-1})	5000	94.3	108
13	rGO/CoAl-LDHs	Hydrothermal	6M KOH	825 (1 A g^{-1})	4000	89.3	109
14	NiCo ₂ O ₄ @NiFe-LDHs	Electrodeposition	2M KOH	1160 (1 A g^{-1})	1000	79	110
15	KCu ₇ S ₄ @NiMn LDHs	Hydrothermal	1M KOH	733.8 (1 A g^{-1})	-	-	111
16	CoS _x /Ni-Co LDHs	Hydrothermal	2M KOH	1562 (1 A g^{-1})	5000	76.62	112
17	NiO/NiMn-LDHs	Hydrothermal	3M KOH	937 (0.5 A g^{-1})	1000	91	113
18	NiCo-LDHs/Go	reflux	6M KOH	1137 (0.5 A g^{-1})	5000	80	114
19	NiMn-LDHs@ Ni foam	Hydrothermal	1M KOH	1511 (2.5 A g^{-1})	3000	92.8	115
20	RGO@MgAl LDH	Hydrothermal	1M KOH	1334 (1 A g^{-1})	-		116
21	Cellulose@NiCo-LDH	Solution deposition	6M KOH	1949.5 (1 A g^{-1})	5000	74.4	117

22	Co-Mn LDH-rGO	Coprecipitation	2M KOH	1635 (1 A g ⁻¹)	-		118
23	Ag NW@NiAl LDH	Hydrothermal	6M LiCl	1246.8 (1 A g ⁻¹)	5000	80.3	119
24	MXene/Ni-Al LDH/ by	Hydrothermal	6M KOH	1061 (1 A g ⁻¹)	4000	70	120
25	NiCo-LDH/PANI/BC	CBD	2M KOH	1690 (1 A g ⁻¹)	5000	83.2	121
26	CoAl LDH@CF	Electrodeposition	2M KOH	634.3 (1 A g ⁻¹)	4000	94	122
27	NiAl-LDH/GNS	Hydrothermal	6M KOH	1255.8 (1 A g ⁻¹)	1500	106	123
28	LDH-CNT/RGO	Coprecipitation	1M KOH	501 (10 A g ⁻¹)	1000	91	124
29	CoNi-LDH/graphene	Self-assembly	1M KOH	650 (5 A g ⁻¹)	2000	97	125
30	rGO/NiAl-LDHs	Hydrothermal	6M KOH	1329 (3.57 A g ⁻¹)	500	91	126
31	NiAl-LDHs/MWCNT/NF	Hydrothermal & CVD	1M KOH	1293 (5 mA cm ⁻²)	1000	83	127
32	GNS/NiAl-LDHs	Hydrothermal	6M KOH	782 (5 mV s ⁻¹)	200	123	128
33	Fe ₃ O ₄ @C@Ni-Al LDHs	Hydrothermal	6M KOH	768 (1 A g ⁻¹)	1000	92	129
34	NiAl-LDHs/CNFs	Hydrothermal	6M KOH	1613 (1 A g ⁻¹)	1000	83	130
35	Co ₃ O ₄ @NiAl-LDHs	Hydrothermal	6M KOH	1772 (2 A g ⁻¹)	2000	88	131
36	Co _{0.4} Ni _{0.6} (OH) ₂ LDHs/CNT	Chemical precipitation	6M KOH	1843 (0.5 A g ⁻¹)	1000	100	132
37	NiCo-OH/rGO	Hydrothermal	6M KOH	1316 (0.5 A g ⁻¹)	17000	80	133
38	NiCo-LDHs/RGO	Solvothermal	1M KOH	1911 (2 A g ⁻¹)	1000	74	134

39	RGO(25)@CoNiAl-LDHs	Hydrothermal	3M KOH	1866 (1 A g^{-1})	5000	100	135
40	NiCoAl-LDHs-MWCNT	precipitation	1M KOH	1035 (1 A g^{-1})	1000	83	136
41	ZnONF/NiCoLDHs	Hydrothermal	1M LiOH	1624 (10 A g^{-1})	2000	93	137
42	NiCoLDHs-ZTO	Hydrothermal	1M KOH	1805 (0.5 A g^{-1})	5000	92.7	138
43	NiCoLDHs/CNTs	CBD	1M KOH	1151 (1 A g^{-1})	1000)	77	139
44	CoAl-LDHs/GF	Hydrothermal	1M KOH	600 (1 A g^{-1})	5000	100	140
45	$\text{Co}^{\text{II}}\text{Co}^{\text{III}}\text{-CO}_3\text{LDHs}$	Copecipitation	0.1M KOH	1490 (0.5 A g^{-1})	300	85	141
46	LDHs@CoS	Hydrothermal	-	1205 (1 A g^{-1})	2000	89	142
47	N-C@LDHs	Hydrothermal	6M KOH	1712 (1 A g^{-1})	500	95	143
48	ACT/CoAl-LDHs	Hydrothermal	6M KOH	977 (2.5 A g^{-1})	2000	88	144
49	$\text{Co(OH)}_2\text{@CoAlLDH (PLDHs)}$	Hydrothermal	2M KOH	1734 (5 mA cm^{-2})	5000	85	145
50	PPY@LDHs	Electrosynthesis	1M KOH	2342 (1 A g^{-1})	20000	115	146

1.3 Orientation and purpose of the dissertation

The SC is one of the highly important EES devices which possess properties like higher specific power, higher cycle life, fast charge-discharge and high cyclic efficiencies. SCs cell mainly comprising electrode, electrolyte and separator cascade in as suitable leak-proof container. The Cs, ED, PD, and long cycle life characteristics of SCs significantly rely on the properties of electrode materials; thus, it is crucial to optimize the properties of electrode materials.

The electrical conductivity, well-defined redox states, pore size distribution, and surface area are the significant properties that must be taken under consideration to design efficient SC electrode material. Previously carbon-based composite, conductive polymers and metal oxides have been commonly used as electrode materials for EES devices. However, these materials suffer from low charge storage capacity limitations and limited cycle life, hindering their use in a commercial application. Thus lots of efforts are escalated to improve the electrode performance of SC. Such efforts include doping, nanostructuring and hybridization with conducting species.

Recently invented 2D inorganic NSs are unique building blocks for the synthesis of nanohybrid materials. 2D NSs possess characteristics of large surface area, high morphological anisotropy, tunable chemical composition, and multiple redox active sites. Thus, 2D NSs-based nanohybrids have increased much attention as prospective candidates for SC electrodes.

Among the various electrode materials, LDHs are potential electrode materials due to their unique anion intercalated structure, 2D morphology and tunable chemical composition. However, this class suffers from low Cs and limited stability due to its poor conductivity, compact structure, and low surface area. Thus, various strategies are applied to improve the electrochemical performance of LDH-based electrodes.

Though LDH materials are explored as an SC electrode material, this class suffers from low electrochemical performance due to their densely packed gallery space by charge compensating anions with a high charge-to-size fraction. To circumvent the issue of compact structure, LDHs with expanded gallery space has been successfully attempted via intercalation of bulky organic/inorganic anions or hybridized with low dimensional biomolecules/nanostructures.

A polyoxometalate (POM) anions possess diversified electrochemically active metal elements and negative charges, making them excellent functional components for intercalation in LDHs. It has long been considered the ideal LDHs pillaring agent due to its well-defined ionic size, robust structure, redox properties, and variable charge density useful to tune LDHs gallery height. Taking into account the fact that exfoliation of nitrate intercalated LDHs gives rise to cationic LDH nanosheets, the self-assembly between cationic LDH NSs and POM anions leads to highly porous structure with unusually expanded surface area, gallery height and ordered pillared structure via the formation of self-assembled intercalative structure. This type of pillared LDH-POM hybridization can be the best way to achieve the high capacity and rate capability for energy storage due to their fast and reversible multi-electron redox reactions. Also, hybridization of LDH with conducting GO NSs can enable high conductivity of LDH.

Thus, the present work focuses on preparing highly porous Ni-Cr-LDH-POM and Ni-Cr-LDH-GO nanohybrids SC electrodes using an exfoliation-restacking strategy. The mesoporous layer-by-layer self-assembled LDH-POM nanohybrids are synthesized by electrostatically induced self-assembly between the Ni-Cr-LDH monolayer NSs and POM anions. Moreover, LDH-GO nanohybrids are synthesized by electrostatically induced self-assembly between the Ni-Cr-LDH monolayer and GO nanosheets.

Various characterizations techniques are used to study the physicochemical properties of nanohybrid materials. Zeta potential measurement is performed to monitor the surface charge of 2D NSs. The crystalline structure (phase identification) of the pristine LDH and nanohybrids is studied using the powder X-ray diffraction (XRD) technique. Fourier-transform infrared (FTIR) and Micro-Raman spectroscopic studies are executed to analyze the chemical bonding nature of the present nanohybrids. The surface morphology and stacking structure between pristine LDH and POM are evaluated by field emission scanning electron microscopy (FESEM) and high-resolution transmission electron microscopy (HRTEM) techniques.

The elemental composition and distribution of the nanohybrids are examined with energy d EDS-elemental mapping analysis. The specific surface area, pore size distribution and pore structure of the nanohybrids are studied by

measuring the N₂ adsorption-desorption isotherms at a temperature of -196.15 °C using a gas sorption analyzer. Nanohybrid materials' oxidation states and chemical composition are probed using X-ray photoelectron spectroscopy (XPS) technique. The electrochemical performance of the prepared nanohybrid materials for EES is examined with cyclic voltammetry (CV), galvanostatic charge-discharge (GCD), and electrochemical impedance spectroscopy (EIS) technique. Three electrode system is used for the electrochemical study of single electrodes in 2 M aqueous KOH electrolyte.

The activity and usefulness of Ni-Cr-LDH-POM and Ni-Cr-LDH-GO nanohybrid electrodes are further tested by fabricating an aqueous hybrid supercapacitor (HSC). The performance of these devices is studied in terms of capacitance, ED and PD, and cyclic stability. The HSC is fabricated with Ni-Cr-LDH-POM or Ni-Cr-LDH-GO nanohybrid and rGO NSs as a battery (cathode) and capacitive type (anode) electrodes, respectively. Finally, conclusions are assessed on the basis of the performance of 2D LDH based nanohybrid devices.

1.4 References

- [1] G. Wang, L. Zhang, J. Zhang, *Chem. Soc. Rev.* 41 (2012) 797-828.
- [2] J. Tao, N. Liu, W. Ma, L. Ding, L. Li, J. Su, Y. Gao, *Sci. Rep.* 3 (2013) 2286-2292.
- [3] Y. Tao, X. Xie, W. Lv, D. M. Tang, D. Kong, Z. Huang, H. Nishihara, T. Ishii, B. Li, D. Golberg, F. Kang, T. Kyotani, Q. H. Yang, *Sci. Rep.* 3 (2013) 2975-2982.
- [4] J. H. Kim, K. H. Lee, L. J. Overzet, G. S. Lee, *Nano Lett.* 11(2011) 2611-2617.
- [5] M. H. Braga, N. S. Grundish, A. J. Murchison, J. B., Goodenough, *Energy Environ. Sci.* 10 (2017) 331-336.
- [6] M. V. Reddy, G. V. Subba Rao, B. V. R. Chowdari, *Chem. Rev.* 113(2013) 5364-5457.
- [7] J. Lu, Q. Peng, W. Wang, C. Nan, L. Li, Y. Li., *J. Am. Chem. Soc.* 135 (2013) 1649-1652.
- [8] C. Zhou, Y. Zhang, Y. Li, J. Liu, *Nano Lett.* 13 (2013) 2078-2085.
- [9] W. Lu, R. Hartman, L. Qu, L. Dai, *J. Phys. Chem. Lett.* 2 (2011) 655-660.
- [10] P. Simon, Y. Gogotsi, *Nat. Mater.* 7 (2008) 845-854.
- [11] S. Zhang, N. Pan, *Adv. Energy Mater.* 5 (2015) 1401401.
- [12] D. Xu, C. Mu, J. Xiang, F. Wen, C. Su, C. Hao, W. Hu, Y. Tang, Z. Liu, *Electrochim. Acta* 220 (2016) 322-330.
- [13] J. Xu, D. Zhang, *Electrochim. Acta* 224 (2017) 105-112.
- [14] K. Kotz, M. Carlen, *Electrochim. Acta* 45 (2000) 2483-2498.
- [15] M. V. Kiamahalleh, S. H. S. Zein, G. Najafpour, S. A. Sata, S. Buniran, *Nano* 7 (2012) 1-27.

- [16] M. Hashemi, M. S. Rahmanifar, M. F. El-Kady, A. Noori, M. F. Mousavi, R. B. Kaner, *Nano Energy* 44 (2018) 489-498.
- [17] T. C. Mendes, F. Zhou, A. J. Barlow, M. Forsyth, P. C. Howlett, D. R. MacFarlane, *Sustain. Energy Fuels*, 2 (2018) 763-771.
- [18] A. G. Pandolfo, A. F. Hollenkamp, *J. Power Sources*, 157 (2006) 11-27.
- [19] L. Ren, G. Zhang, J. Lei, Y. Wang, D. Hu, *J. Colloid Interf. Sci.* 512 (2018) 300-307
- [20] H. I. Becker, Low voltage electrolytic capacitors. U.S. Patent 2800616 (1957).
- [21] R. A. Rightmire, Electrical energy storage apparatus. U.S. Patent 3288641 (1966).
- [22] S. Hadzi-Jordanov, H. Angerstein-Kozłowska, M. Vuković, B. E. Conway, *J. Electrochem. Soc.* 125 (1978) 1471-1480.
- [23] S. Trasatti, G. Buzzanca, *J. Electroanal. Chem. Interf. Electrochem.* 29 (1971) A1-A5.
- [24] D. Galizzioli, F. Tantardini, S. Trasatti, *Appl. Electrochem.* 5 (1975) 203-214.
- [25] C. C. Hu, K. H. Chang, M. C. Lin, Y. T. Wu, *Nano Lett.* 6 (2006) 2690-2695.
- [26] A. Yoshida, K. Imoto, H. Yoneda, A. Nishimo, *IEEE*, 15 (1992) 133-138.
- [27] http://services.eng.uts.edu.au/cempe/subjects_JGZ/eet/SuperCap_1_11_05.pdf, J. G. Zhu, (2012) Supercapacitors.
- [28] G. L. Bullard, H. B. Sierra-Alcazar, H. L. Lee, J. L., *IEEE Transactions on Magnetics*, 25 (1989) 102-106.
- [29] M. Y. Ho, Transition metal oxide and phosphate-based/carbon composites as supercapacitor electrodes. PhD thesis, University of Nottingham (2017).
- [30] D. M. Zogbi, Supercapacitors the Myth, the Potential and the Reality.
- [31] J. Ledge, Saft and ESMA to cooperate on supercapacitor development, production and commercialisation, Saft Press Release (2009).
- [32] S. Huang, X. Zhu, S. Sarkar, Y. Zhao, *APL Mater.* 7 (2019) 1-9.
- [33] A. Davies, A. Yu, *Can J. Chem. Eng.* 89 (2011) 1342-1357.
- [34] I. Shakir, M. Nadeem, M. Shahid, D. J. Kang, *Electrochim Acta* 118 (2014) 138-142.
- [35] X. Lang, A. Hirata, T. Fujita, M. Chen, *Nat. Nanotechnol.* 6 (2011) 232-236.
- [36] D. Pech, M. Brunet, P. Huang, H. Durou, V. Mochalin, Y. Gogotsi, P. L. Taberna, P. Simon, *Nat. Nanotechnol.* 5 (2010) 651-654.
- [37] S. H. Kwon, E. Lee, B. S. Kim, S. G. Kim, B. J. Lee, M. S. Kim, J. C. Jung, *Curr. Appl. Phys.* 14 (2014) 603-607.
- [38] B. E. Conway, "Electrochemical Supercapacitors", Kluwer-Plenum, New York, (1999).
- [39] <http://en.wikipedia.org/wiki/Supercapacitor/>.
- [40] E. Frackowiak, E. Beguin, *Carbon* 39 (2001) 937-950.
- [41] Z. Wen, W. She, Y. Li, R. Che, *J. Mater. Chem. A* 2 (2014) 20729-20738.
- [42] L. L. Xing, K. J. Huang, L. X. Fang, *Dalton Trans.* 45 (2016) 17439-17446.
- [43] J. Xu, T. Xiao, X. Tan, P. Xiang, L. Jiang, D. Wu, J. Li, S. Wang, *J. Alloys Compd.* 706 (2017) 351-357.
- [44] W. Chen, R. B. Rakhi, H. N. Alshareef, *Nanoscale* 5 (2013) 4134-4138.

- [45] S. Lyu, H. Chang, F. Fu, L. Hu, J. Huang, S. Wang, J. Power Sources 327 (2016) 438-446.
- [46] T-H. Gu, N. H. Kwon, K-G. Lee, X. Jin, S-J. Hwang, Coord. Chem. Rev. 421 (2020) 213439-213468.
- [47] B. Pal, S. Yang, S. Ramesh, V. Thangadurai, R. Jose, Nanoscale Adv. 1(2019) 3807-3835.
- [48] Dodevskia, B. Jankovic, M. Stojmenovic, S. Krstic, J. Popovic, M. C. Pagnacco, M. Popovic, S. Pasalic, Colloids Surf. A 522 (2017) 83-96.
- [49] Z. Yang, J. Ren, Z. Zhang, et al., Chem. Rev. 115 (2015) 5159-5223.
- [50] K. Jurewicz, S. Delpeux, V. Bertagna, F. Béguin, E. Frackowiak, Chem. Phys. Lett. 347 (2001) 36-40.
- [51] K. S. Novoselov, A. K. Geim, S. V. Morozov, D. Jiang, Y. Zhang, S. V. Dubonos, I. V. Grigorieva, A. A. Firsov, Science 306 (2004) 666-669.
- [52] S. J. Marje, P. K. Katkar, S. S. Pujari, S. A. Khalate, A. C. Lokhande, U. M. Patil, Synth. Met. 259 (2020) 1-11.
- [53] G. A. Snook, P. Kao, A. S. Best, J. Power Sources 196 (2011) 1-12.
- [54] B. M. Hryniewicz, R. V. Lima, F. Wolfart, M. Vidotti, Electrochim. Acta 293 (2019) 447-457.
- [55] B. H. Patil, S. J. Patil, C. D. Lokhande, Electroanalysis 26 (2014) 2023-2032.
- [56] P. R. Deshmukh, S. N. Pusawale, V. S. Jamadade, U. M. Patil, C. D. Lokhande, J. Alloys Compd. 509 (2011) 5064-5069.
- [57] V. J. Mane, D. B. Malavekar, S. B. Ubale, V. C. Lokhande, C. D. Lokhande, Inorg. Chem. Commun. 115 (2020) 1-17.
- [58] U. M. Patil R. R. Salunkhe, K. V. Gurav, C. D. Lokhande, Appl. Surf. Sci. 255 (2008) 2603-2607.
- [59] U. M. Patil, S. B. Kulkarni, V. S. Jamadade, C. D. Lokhande, J. Alloys Compd. 509 (2011) 1677-1682.
- [60] A. D. Jagadale, V. S. Kumbhar, R. N. Bulakhe, C. D. Lokhande, Energy J. 64 (2014) 234-241.
- [61] P. M. Kulal, D. P. Dubal, C. D. Lokhande, V. J. Fulari, J. Alloys Compd. 509 (2011) 2567-2571.
- [62] K. K. Upadhyaya, M. Altomare, S. Eugenio, P. Schmuki, T. M. Silva, M. F. Montemor, Electrochim. Acta 232 (2017) 192.
- [63] G. Yilmaz, C. X. Guo, X. Lu, ChemElectroChem 3 (2016) 158.
- [64] S. Jeon, J. H. Jeong, H. Yoo, H. K. Yu, B. H. Kim, M. H. Kim, ACS Appl. Nano Mater. 3 (2020) 3847-3858.
- [65] B. Y. Fugare, B. J. Lokhande, Mater. Sci. Semicond. Process 71 (2017) 121-127.
- [66] Ten Elshof, J. E.; Yuan, H.; Rodriguez, P. G. Adv. Energy Mater. 6 (2016) 1-5.
- [67] S. R. Ede, S. Anantharaj, K. T. Kumaran, S. Mishra, S. Kundu, RSC Adv. 7 (2017) 5898-5911.
- [68] Q. Wang, D. O'Hare, Chem. Rev. 112(2012,) 4124-4155.
- [69] T. Li, H. N. Miras, Y.-F. Song, Catalysts 7 (2017) 260.
- [70] M. Shao, R. Zhang, Z. Li, M. Wei, D. G. Evans, X. Duan, Chem. Commun. 51 (2015) 15880-15893.

- [71] J. Zhao, J. Chen, S. Xu, M. Shao, Q. Zhang, F. Wei, J. Ma, M. Wei, D. G. Evans, X. Duan, *Adv. Funct. Mater.* 24 (2014) 2938-2946.
- [72] M. Xu, T. Liang, M. Shi, H. Chen, *Chem. Rev.* 113(2013) 3766-3798.
- [73] M. A. Bizeto, A. L. Shiguehara, V. R. Constantino, *J Mater Chem.* 19 (2009) 2512-2525.
- [74] E. R. Hitzky P. Aranda, M. Dardera, G. Rytwo, *J Mater Chem.* 20 (2010) 9306-9321.
- [75] R. Ma, T. Sasaki, *Adv Mater* 22 (2010) 5082-5104.
- [76] L. H. Su, X. G. Zhang, *J. Power Sources* 172(2007) 999-1006.
- [77] X. Gao, X. Liu, D. Wu, B. Qian, Z. Kou, Z. Pan, Y. Pang, L. Miao, J. Wang, *Adv. Funct. Mater.* 29 (2019) 1-12.
- [78] J. Zai, Y. Liu, X. Li, Z. F. Ma, R. Qi, X. Qian, *Nano-Micro Lett.* 9 (2017) 1-9.
- [79] Z. Xiao, Y. Mei, S. Yuan, H. Mei, B. Xu, Y. Bao, L. Fan, W. Kang, F. Dai, R. Wang, L. Wang, S. Hu, D. Sun, H-C. Zhou, *ACS Nano* 13 (2019) 7024-7030.
- [80] Z. Jiang, Z. Li, Z. Qin, H. Sun, X. Jiao, D. Chen, *Nanoscale* 5 (2013) 11770-11775.
- [81] J. Wang, Y. Song, Z. Li, Q. Liu, J. Zhou, X. Jing, M. Zhang, Z. Jiang, *Energy Fuels* 24 (2010) 6463-6467.
- [82] H. Chen, L. Hu, M. Chen, Y. Yan, L. Wu, *Adv. Funct. Mater.* 24 (2014) 934.
- [83] B. Wang, Q. Liu, Z. Qian, X. Zhang, J. Wang, Z. Li, H. Yan, Z. Gao, F. Zhao, L. Liu, *J. Power Sources* 246 (2014) 747-753.
- [84] M. Jing, H. Hou, C. E. Banks, Y. Yang, Y. Zhang, X. Ji, *ACS Appl Mater Interfaces* 7 (2015) 22741-22744.
- [85] T. Li, G. H. Li, L. H. Li, L. Liu, Y. Xu, H. Y. Ding, T. Zhang, *ACS Appl Mater Interfaces* 8 (2016) 2562-2572.
- [86] Y. F. Zhao, H. N. Ma, S. F. Huang, X. J. Zhang, M. R. Xia, Y. F. Tang, Z. F. Ma, *ACS Appl Mater Interfaces* 8 (2016) 22997-23005.
- [87] H. Sim, C. Jo, T. Yu, E. Lim, S. Yoon, J. H. Lee, J. Yoo, J. Lee, B. Lim, *Chem. Eur. J.* 20 (2014) 1-6.
- [88] Y. Cheng, H. Zhang, C. V. Varanasi, J. Liu, *Energ. Environ. Sci.* 6 (2013) 3314-3321.
- [89] Y. Tao, L. Zaijun, L. Ruiyi, N. Qi, K. Hui, N. Yulian, L. Junkang, *J. Mater. Chem.* 22 (2012) 23587-35592.
- [90] Y. Song, X. Cai, X. Xu, X.-X. Liu, *J. Mater. Chem. A* 3 (2015) 14712-14720.
- [91] J. -C. Chen, C. -T. Hsu, C. -C. Hu, *J. Power Sources* 253 (2014) 205-213.
- [92] J. Pu, Y. Tong, S. Wang, E. Sheng, Z. Wang, *J. Power Sources* 250 (2014) 250-256.
- [93] X. Sun, G. Wang, H. Sun, F. Lu, M. Yu, J. Lian, *J. Power Sources* 238 (2013) 150-156.
- [94] A. D. Jagadale, G. Q. Guan, X. M. Li, X. Du, X. L. Ma, X. G. Hao, A. Abudula, *J. Power Sources* 306 (2016) 526-534.
- [95] Z. Chen, H. Deng, M. Zhang, Z. Yang, D. Hu, Y. Wanga, K. Yan, *Nanoscale Adv.* 2(2020) 2099-2105.
- [96] A. S. Patil, J. L. Gunjekar, C. D. Lokhande, U. M. Patil, S. V. Sadavar, N. S. Padalkar, R. B. Shinde, M. M. Wagha, J. S. Bagi, *Synth. Met.* 264 (2020) 1-9.

- [97] H. Liang, H. Jia, T. Lin, Z. Wang, C. Li, S. Chen, J. Qi, J. Cao, W. Fei, J. Feng, *J. Colloid Interf. Sci.* 554 (2019) 59-65.
- [98] J. Zhao, S. Xu, K. Tschulik, R. G Compton, M. Wei, D. O'Hare, G. Evans, X. Duan, *Adv. Funct. Mater.* 25 (2015) 2745-2753.
- [99] X. Wu, L. Jiang, C Long, T. Wei, Z. Fan, *Adv. Funct. Mater.* 25 (2015) 1-8.
- [100] X. Li, J. Shen, W. Sun, X. Hong, R. Wang, X. Zhao, X. Yan, *J. Mater. Chem. A* 3 (2015) 13244-13253.
- [101] F. Wang, S. Sun, Y. Xu, T. Wang, R. Yu, H. Li, *Sci. Rep.* 4707 (2017) 1-11.
- [102] X. Liu, C. Wang, Y. Dou, A. Zhou, T. Pan, J. Han, M. Wei, *J. Mater. Chem. A* 2 (2014) 1682-1685.
- [103] J. Han, Y. Dou, J. Zhao, M. Wei, D. G. Evans, X. Duan, *Small* 9 (2013) 98-106.
- [104] J. Zhao, J. Chen, S. Xu, M. Shao, D. Yan, M. Wei, D. G. Evans, X. Duan, *J. Mater. Chem. A* 1 (2013) 8836-8843.
- [105] L. Zhang, X. Zhang, L. Shen, B. Gao, L. Hao, X. Lu, F. Zhang, B. Ding, C. Yuan, *J. Power Sources*, 199 (2012) 395-401.
- [106] J. Yang, C. Yu, X. Fan, J. Qiu, *Adv. Energy Mater.* 4(2014) 1-8.
- [107] M. Yu, R. Liu, J. Liu, S. Li, Y. Ma, *Small* 13 (2017) 1-9.
- [108] J. Li, P. Zhang, X. Zhao, L. Chen, J. Shen, M. Li, B. Ji, L. Song, Y. Wu, D. Liu, *J. Colloid Interface Sci.* 549 (2019) 236-245.
- [109] Y. Zhong, Y. Liao, A. Gao, J. Hao, D. Shu, Y. Huang, J. Zhong, C. He, R. Zeng, *J. Alloys Compd.* 669 (2016) 146-155.
- [110] G. Luo, K. S. Teh, Y. Xia, Z. Li, Y. Luo, L. Zhao, Z. Jiang, *J. Alloys Compd.*, 767 (2018) 1126-1132.
- [111] X. L. Guo, J. M. Zhang, W. N. Xu, C. G. Hu, L. Sun, Y. X. Zhang, *J. Mater. Chem. A* 5 (2017) 20579-20587.
- [112] X. Guan, M. Huang, L. Yang, G. Wang, X. Guan, *Chem. Eng. J.* 372 (2019) 151-162.
- [113] P. F. Liu, J. J. Zhou, G. C. Li, M. K. Wu, K. Tao, F. Y. Yi, W. N. Zhao, L. Han, *Dalton Trans.* 46 (2017) 7388-7391.
- [114] J. Yang, C. Yu, C. Hu, M. Wang, S. Li, H. Huang, K. Bustillo, X. Han, C. Zhao, W. Guo, Z. Zeng, H. Zheng, J. Qiu, *Adv. Funct. Mater.* 28 (2018) 1-11.
- [115] J. L. Gunjekar, A. I. Inamdar, B. H. Hou, S. Cha, S. M. Pawar, A. A. Talha, H. S. Chavan, J. Kim, S. Cho, S. Lee, Y. Jo, H. Kim, H. Im, *Nanoscale* 10 (2018) 8953-8961.
- [116] G. Hatui, G. C. Nayak, G. Udayabhanu, *Electrochim. Acta.* 219 (2016) 214-226.
- [117] F. Lai, Y-E. Miao, L. Zuo, H. Lu, Y. Huang, T. Liu, *Small* 12 (2016) 3235-3244.
- [118] M. Li, J. P. Cheng, J. Wang, F. Liu, X. B. Zhang, *Electrochim. Acta* 206 (2016) 108-115.
- [119] S. X. Wu, K. S. Hui, K. N. Hui, *J. Phys. Chem. C* 119 (2015) 23358-23365.
- [120] Y. Wang, H. Dou, J. Wang, B. Ding, Y. Xu, Z. Chang, X. Hao, *J. Power Sources* 327 (2016) 221-228.

- [121] H. Wu, Y. Zhang, W. Yuan, Y. Zhao, S. Luo, X. Yuan, L. Zheng, L. Cheng, *J. Mater. Chem. A* 6 (2018) 16617-16626.
- [122] A. D. Jagadale, G. Guan, X. Li, X. Du, X. Ma, X. Hao, A. Abudula, *Energy Technol.* 4 (2016) 1-9.
- [123] L. Zhang, J. Wang, J. Zhu, X. Zhang, K. S. Hui, K. N. Hui, *J. Mater. Chem. A* 1 (2013) 9046.
- [124] C. Yu, J. Yang, C. Zhao, X. Fan, G. Wang, J. Qiu, *Nanoscale* 6(2014) 3097-3104.
- [125] R. Ma, X. Liu, J. Liang, Y. Bando, T. Sasaki, *Adv. Mater.* 26 (2014) 4173.
- [126] J. Xu, S. Gai, F. He, N. Niu, P. Gao, Y. Chen, P. Yang, *J. Mater. Chem. A* 2 (2014) 1022-1031.
- [127] B. Wang, G. R. Williams, Z. Chang, M. Jiang, J. Liu, X. Lei, X. Sun, *ACS Appl Mater Interfaces* 6 (2014) 16304-16311.
- [128] Z. Gao, J. Wang, Z. Li, W. Yang, B. Wang, M. Hou, Y. He, Q. Liu, T. Mann, P. Yang, M. Zhang, L. Liu, *Chem. Mater.* 23(2011) 3509-3516.
- [129] L. Li, R. Li, S. Gai, F. He, P. Yang, *J. Mater. Chem. A* 2 (2014) 8758-8765.
- [130] F. He, Z. Hu, K. Liu, S. Zhang, H. Liu, S. Sang, *J. Power Sources* 267(2014) 188-196.
- [131] F. Ning, M. Shao, C. Zhang, S. Xu, M. Wei, X. Duan, *Nano Energy* 7 (2014) 134-142.
- [132] H. Chen, F. Cai, Y. Kang, S. Zeng, M. Chen, Q. Li, *ACS Appl Mater Interfaces* 6 (2014) 19630-19637.
- [133] H. N. Ma, J. He, D. B. Xiong, J. S. Wu, Q. Q. Li, V. Dravid, Y. F. Zhao, *ACS Appl Mater Interfaces* 8 (2016) 1992-2000.
- [134] X. Cai, X. Shen, L. Ma, Z. Ji, C. Xu, A. Yuan, *Chem. Eng. J.* 268 (2015) 251-259.
- [135] P. Huang, C. Cao, Y. Sun, S. Yang, F. Wei, W. Song, *J. Mater. Chem. A* 3 (2015) 10858-10863.
- [136] J. Yang, C. Yu, X. Fan, Z. Ling, J. Qiu, Y. Gogotsi, *J. Mater. Chem. A* 1 (2013) 1963-1968.
- [137] N. T. Trang, H. V. Ngoc, N. Lingappan, D. J. Kang, *Nanoscale* 6 (2014) 2434-2439.
- [138] X. Wang, A. Sumboja, M. Lin, J. Yan, P. S. Lee, *Nanoscale* 4 (2012) 7266-7272.
- [139] M. Li, K. Y. Ma, J. P. Cheng, D. Lv, X. B. Zhang, *J. Power Sources* 286 (2015) 438-444.
- [140] T. M. Masikhwa, M. J. Madito, D. Y. Momodu, J. K. Dangbegnon, O. Guellati, A. Harat, M. Guerioune, F. Barzegar, N. Manyala, *RSC Adv.* 6 (2016) 46723-46732.
- [141] P. Vialat, C. Mousty, C. Taviot-Gueho, G. Renaudin, H. Martinez, J. C. Dupin, E. Elkaim, F. Leroux, *Adv. Funct. Mater.* 24 (2014) 4831-4842.
- [142] Y. B. Dou, J. Zhou, F. Yang, M. J. Zhao, Z. R. Nie, J. R. Li, *J. Mater. Chem. A* 4 (2016) 12526-12534.
- [143] J. Xu, F. He, S. Gai, S. Zhang, L. Li, P. Yang, *Nanoscale* 6 (2014) 10887-10895.
- [144] Z. Gao, C. Bumgardner, N. Song, Y. Zhang, J. Li, X. Li, *Nat Commun* 7 (2016) 11586.
- [145] N. Abushrenta, X. Wu, J. Wang, J. Liu, X. Sun, *Sci Rep.* 5 (2015) 13082.
- [146] M. Shao, Z. Li, R. Zhang, F. Ning, M. Wei, D. G. Evans, X. Duan, *Small* 11(2015) 3530-3538.



CHAPTER-2

Theoretical Background of Synthesis Process and Characterization Techniques

CHAPTER 2

Theoretical Background of Synthesis Process and Characterization Techniques

Sr. No.	Title	Page No.
2.1	Introduction	39-41
2.2	Synthesis of 2D nanosheets	41-49
	2.2.1 <i>Bottom-up approach</i>	41-43
	2.2.2 <i>Top-down approach</i>	43-49
2.3	<i>Synthetic strategies for 2D nanosheet-based hybrids</i>	49-52
	2.3.1 <i>Exfoliation-reassembly</i>	49-50
	2.3.2 <i>Anchored assembly</i>	50-51
	2.3.3 <i>Layer by layer</i>	51-52
2.4	Characterization techniques	52-65
	2.4.1 <i>Zeta potential</i>	52-54
	2.4.2 <i>X-ray diffraction (XRD)</i>	54-56
	2.4.3 <i>Fourier transform-infrared spectroscopy (FTIR)</i>	56-57
	2.4.4 <i>Micro- Raman spectroscopy</i>	57-59
	2.4.5 <i>Field emission-scanning electron microscopy (FESEM) and energy dispersive X-ray spectroscopy (EDS)</i>	59-61
	2.4.6 <i>High Resolution-transmission electron microscopy (HRTEM)</i>	61-63
	2.4.7 <i>Brunauer-Emmettt-Teller (BET)</i>	63-64
	2.4.8 <i>X-ray photoelectron spectroscopy (XPS)</i>	64-65
2.5	Electrochemical techniques	65-69
	2.5.1 <i>Cyclic voltammetry (CV)</i>	66-67
	2.5.2 <i>Galvanostatic charge-discharge (GCD)</i>	67-68
	2.5.3 <i>Electrochemical impedance spectroscopy (EIS)</i>	68-69
2.6	References	69-75

2.1 Introduction

Layered materials with well-arranged voids and surfaces provide beneficial features for addressing today's energy and environmental issues. EES systems such as SCs and batteries have garnered intense research interest in recent decades [1-4] as the demand for reliable and environmentally friendly energy resources has grown, promoting the development and optimization of new high-performance materials. A HSC with a higher power capability than batteries offers a promising approach to meet the high power and ED demand of energy storage systems. The development of HSCs are attracting high research attention due to their usefulness as high power and environmentally friendly EES systems [5]. In HSC devices, several aspects must be optimized to achieve high power and ED. High charge storage, specific capacity, stability, economic feasibility, and safety are crucial to achieving desired HSC performance. The performance of HSCs is highly dependent on electrode material; thus, recent research efforts have been devoted to finding advanced electrode materials. These electrode materials most often involve carbon-based materials [6], metal oxides [7], conducting polymers [8], metal phosphate [9], LDH and their hybrids [10,11]. Recently, 2D nanostructured materials with enhanced surface areas and reduced crystal sizes have emerged as efficient electrode alternatives for HSC [12]. Also, 2D nanostructured materials proved their usefulness in various applications. Fig. 2.1 displays different areas of applications of 2D NSs.

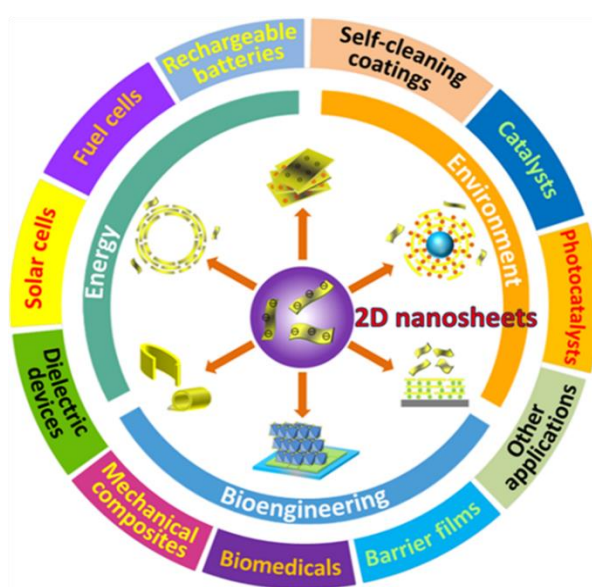


Fig. 2.1: Different applications of 2D NSs [13].

The advantages of 2D materials include unique morphological anisotropy, enlarged bifacial 2D surface area, short carrier ion diffusion path, tailorable electronic structure, well-defined surface structure, and tailorable chemical compositions [14, 15]. These advantages of 2D NSs have sparked intense research interest as electrode materials in HSC devices. The advantages of 2D NSs are illustrated in Fig. 2.2

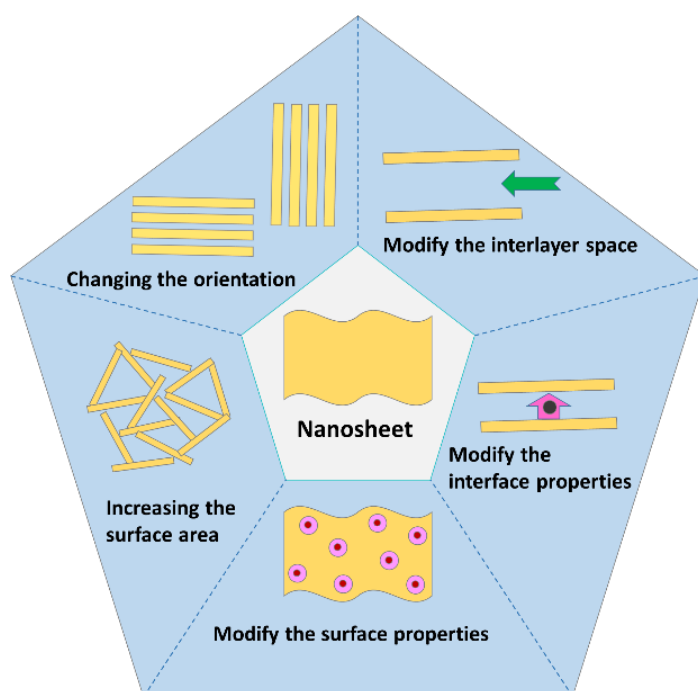


Fig. 2.2: The advantages of 2D NSs [16].

Hybridization of 2D NSs with other nanostructured species has attracted a lot of research interest because of its effectiveness in controlling the physicochemical characteristics of each component and creating unexpected functionality via an interfacial electronic coupling between hybridized components [17–19]. Furthermore, the hybridization of 2D NSs with foreign species (polyoxometalate, GO, biomolecules, etc.) typically results in highly porous hierarchical structures [20, 21]. In 2D NS-based hybrid materials, microporosity originates from the restacking structure, while mesopores can originate from the interconnected stacking structure of the NS. Due to these attractive physicochemical properties of 2D NS-based hybrids, these materials demonstrated huge potential as electrode candidates for HSC devices.

This chapter presents brief information regarding the structure, synthesis processes of various 2D NS and their hybrids with several modification strategies

and most recent breakthroughs in different sectors, particularly in HSC and other applications.

2.2 Synthesis of 2D NSs

Various synthesis strategies are developed for the synthesis of 2D NS. The synthetic technique of 2D NS has a substantial impact on their physicochemical characteristics and electrode functionalities. The synthetic routes of 2D NSs are generally divided into two branches: top-down and bottom-up approaches. In the top-down approach, single-layered NSs are obtained by delaminating the pristine layered solids or crystals. This approach is of much interest due to its high processability, low synthesis cost, high yield, and fascinating features of exfoliated NSs. Furthermore, this approach is more accessible than the bottom-up approach and can be applied to synthesize a variety of 2D NS.

2.2.1 Bottom-up approach

For the direct synthesis of 2D inorganic NSs, many bottom-up approaches have been developed, mainly depending on certain precursor's chemical reactions at given specific experimental conditions. 2D NS of non-layered materials can be synthesized by various bottom-up processes such as hot-injection, solution-based crystal growth, hydrothermal, and CVD methods.

Chemical vapor deposition method

CVD is a process whereby solid materials are deposited from a vapor phase chemical reaction occurring on or in the vicinity of the heated substrate surface. The schematic diagram of the CVD method is shown in Fig.2.3

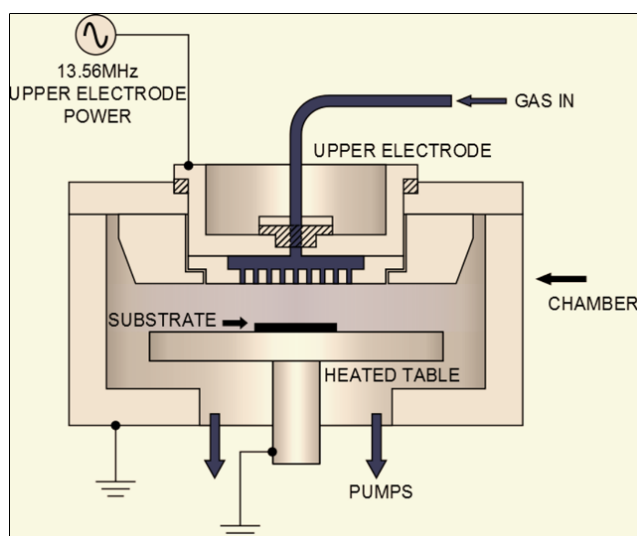


Fig. 2.3: Schematic diagram of CVD method [22].

By the fine-control of synthetic condition, the CVD allows to prepare variety of highly crystalline few-layered or monolayered inorganic NSs of transition metal dichalcogenides (TMDCs: MoSe_2 , MoS_2 , ReS_2 , WS_2 , SnS_2 , MoTe_2) [23], transition metal oxides (TMOs: ZnO , TiO_2 , SnO_2 , Co_3O_4 etc) [24], and transition metal chalcogenides (TMCs: ZnSe , ZnS , Co_9Se_8 , etc) [25]. Also, CVD is effectively used to synthesize graphene [26, 27].

Advantages: Offers direct growth of material in thin-film form; controlled growth rate; thick coating layers are produced; multiple layers are deposited at the same time; high purity can be obtained.

Disadvantages: Requires high processing temperature; the possibility of evolution of toxic and corrosive gases; high cost; relatively low yield.

Hydrothermal method

The hydrothermal method is a typical phenomenon of a solvothermal chemical reaction that occurs in an aqueous solvent at temperatures beyond the solvent's boiling point and at a high pressure above 1 bar [28]. Fig. 2.4 represents the schematic diagram for the hydrothermal method.

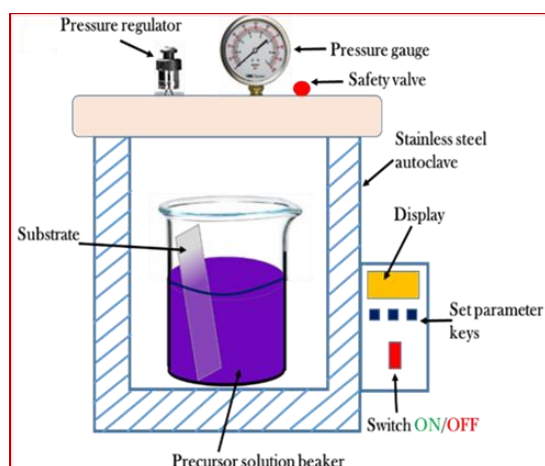


Fig. 2.4: Schematic diagram of hydrothermal process [29].

In the hydrothermal process, 2D NS can be grown directly onto the other heterogeneous surfaces like stainless steel, NF, carbon cloth, carbon paper, etc. The hydrothermal method is useful for synthesizing novel heterostructure and binder-free electrodes [30, 31]. Various 2D NSs of TMO, TMDC, metal-organic framework (MOF) and LDH synthesized by the hydrothermal method are reported [32–38]. The hydrothermal synthesis method offers several benefits over other methods, which are listed below: [39, 40]

Advantages: By controlling various preparative parameters desired material properties can be achieved, e.g. by optimizing hydrothermal temperature and pressure, different crystalline or amorphous phases and morphology can be achieved; it is possible to control the particle size and shape of highly anisotropic 2D NS by hydrothermal method; in the hydrothermal method, it is possible to prepare thermodynamically metastable phases; it can be combined with other methods like optical radiation, microwave, ultrasound, mechano-chemistry and hot-pressing, to improve the reaction kinetics and to produce a variety of nanomaterials; it doesn't need any external seeds and catalyst at any stage, so it is beneficial for bulk powder production and also for the synthesis of material in thin-film form; this method is more environmentally friendly as compared to CVD method; better product yield than CVD method.

Disadvantages: It is challenging to control size distribution; requirement of high-pressure reactor with high-temperature control; time consuming process.

2.2.2 Top-down approaches

In top-down approaches, single-layered NSs are obtained by exfoliating layered inorganic solids or crystals. This approach is easier than the bottom-up approach and can produce many kinds of 2D inorganic NS. Various top-down exfoliation techniques are suitable for synthesizing mono-layered NSs [41-50].

Scotch tape method

A simple method to prepare inorganic 2D NSs is to peel off monolayer from bulk layered compounds using scotch tape, where mechanical force is applied through the scotch tape to weaken the interlayer Van Der Waals forces without breaking inplane chemical bonds [41]. Schematic diagram of the scotch tape technique is shown in Fig. 2.5.

This method was firstly reported for graphene [51]. After the success of graphene, this method has been commonly used for the production of inorganic 2D NS of WS₂, MoSe₂, MoS₂, etc. [52], antimonene [53], and metal phosphorous trichalcogenides[54].

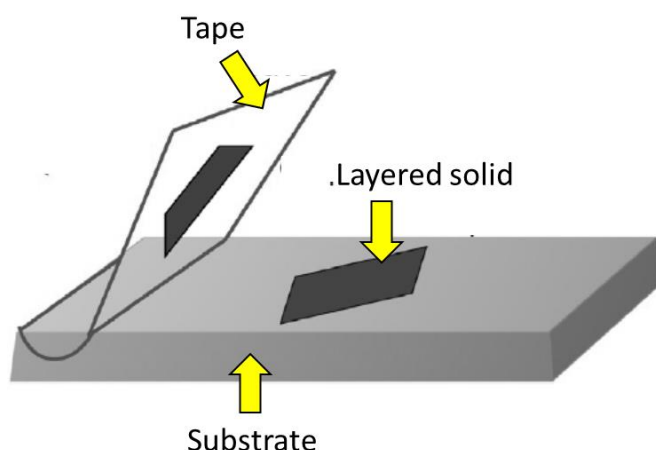


Fig. 2.5: Schematic diagram of scotch tape technique.

Advantages: The monolayers achieved with this process are typical of high purity since no chemicals or chemical reactions involve in the process; this technique is a safe and simple process; in this process, chances of impurities are less as compared to the chemical process; it is cost-effective process.

Disadvantages: Meager yield obtained, which does not meet the requirement of bulk production; limited to bulk layered material; it is not scalable for integration into new technologies.

Ultrasonication method

Applying ultrasonication to the layered material dispersion in a suitable polar solvent can induce effective exfoliation of bulk layered material (Fig. 2.6) [55].

Ultrasonic irradiation, as a new technology, has been widely used in chemical reactions. Ultrasonication simultaneously produces pressure waves in liquids and short-living microbubbles. This phenomenon leads to cavitation and causes high-speed impinging liquid jets and strong hydrodynamic shear forces on dispersant particles. When these bubbles collapse vigorously during high sonication cycles, microjets and shock waves pass through the layered compounds, which creates tensile stress in the layered compound and eventually leads to the exfoliation of layered crystals into a few-layered NSs [45, 48].

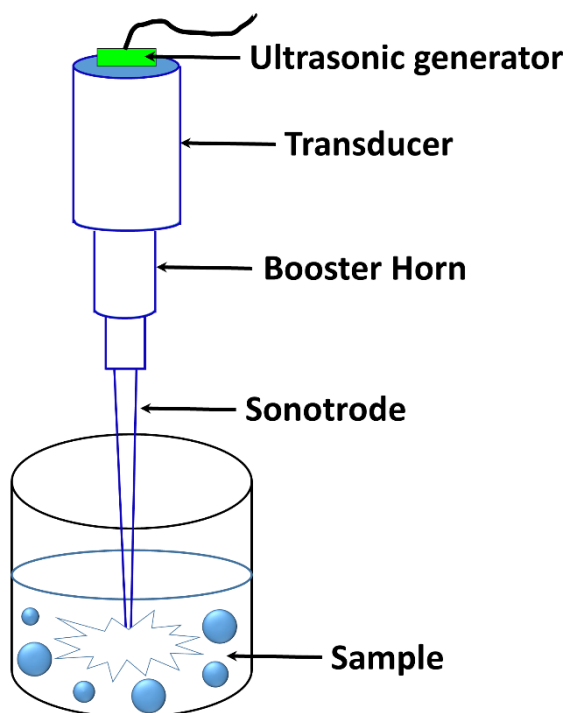


Fig. 2.6: Schematic diagram of ultrasonication.

This method has been generally used for delamination of inorganic layered materials like TMOs (WO_3 , MoO_3 etc.) [56], LDH ($\text{NiCo}(\text{OH})_2$, $\text{NiFe}(\text{OH})_2$) [57], TMDCs (WS_2 , NbSe_2 , MoS_2 , TaSe_2 and WS_2 etc.) [45,58], antimonene [59,60].

Advantages: The number of layers and size of delaminated NSs can be controlled by tuning the nature of solvent with control of parameters of time and power; the high power of sonication results in the delamination of small-sized NSs with considerable defect formation; it is an inexpensive, simple and efficient technique; ultrasonication method does not produce thermal, electric and chemical abnormal surface impurities; large-scale production and high yield are possible.

Disadvantages: Unnecessary large grain size cause defect; ultrasonication method is not suitable to machine soft and ductile materials; the temperature of the bath is not constant; very high size distribution; it is suitable for the synthesis of monolayer NSs.

Though this method proves its advantages for various applications, its use is limited to special devices and research purposes due to the high size distribution of the NSs. Thus, efforts are put forward to synthesize monolayered NSs. In this context, solution exfoliation techniques are explored to achieve monolayers of the

inorganic layered crystals. The ion exchange-exfoliation, infinite solvation, and Li intercalation-hydroxylation are representative solution exfoliation techniques.

Ion-exchange exfoliation

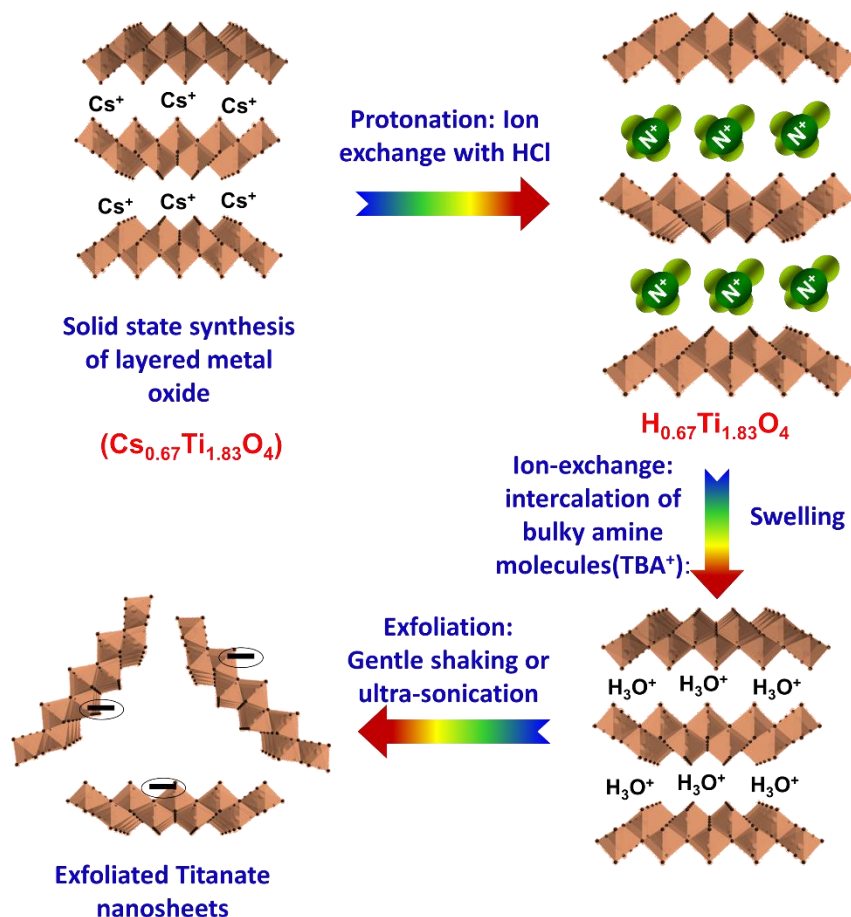


Fig. 2.7: Schematic model of the synthesis and exfoliation of LMO.

Up to now, various ways have been explored to exfoliate layered crystals. Various layered materials such as perovskite structure ($\text{KSr}_2\text{Nb}_3\text{O}_{10}$, $\text{KCa}_2\text{Nb}_3\text{O}_{10}$, and $\text{KSr}_2\text{Ta}_3\text{O}_{10}$, etc.), Ruddlesden-Popper phase ($\text{K}_2\text{La}_2\text{Ti}_3\text{O}_{10}$), or aurivillius phase ($\text{SrBi}_4\text{Ti}_4\text{O}_{15}$), rocksalt-type structure ($\text{K}_{0.45}\text{MnO}_2$ and LiCoO_2), lepidocrocite-type structure ($\text{Cs}_x\text{Ti}_{2-x/4}\square_{x/4}\text{O}_4$; \square =vacancy) pukered titanoniobate structure (KTi_2NbO_7 , KTiNbO_5 , and $\text{K}_3\text{Ti}_5\text{NbO}_{14}$, etc.) can be exfoliated into monolayered NSs by this method [61-71].

The exfoliation of layered metal oxides (LMO) can be attained by the intercalation of bulky amine molecules into protonated derivatives of LMO. Initially, the protonated derivatives of LMO can be achieved by replacing interlayer alkali metal ions with proton or hydronium ions using acid treatment [72, 73].

Then the protonated material is reacted with the aqueous solution of bulky organic cations, which replace the protons/ hydronium ions with the larger cations. During the ion exchange process, the automatic solvation reaction between the host material and bulky organic cation results in the swelling of the host lattice. Further weakening the interlayer interaction between the host layer and bulky organic cation, which in turn exfoliates the host material into individual NSs under gentle shaking or ultrasonication as depicted in Fig.2.7 [67,72,74]. Fig. 2.7 depicts the example of exfoliated LMO NSs.

LDH infinite solvation

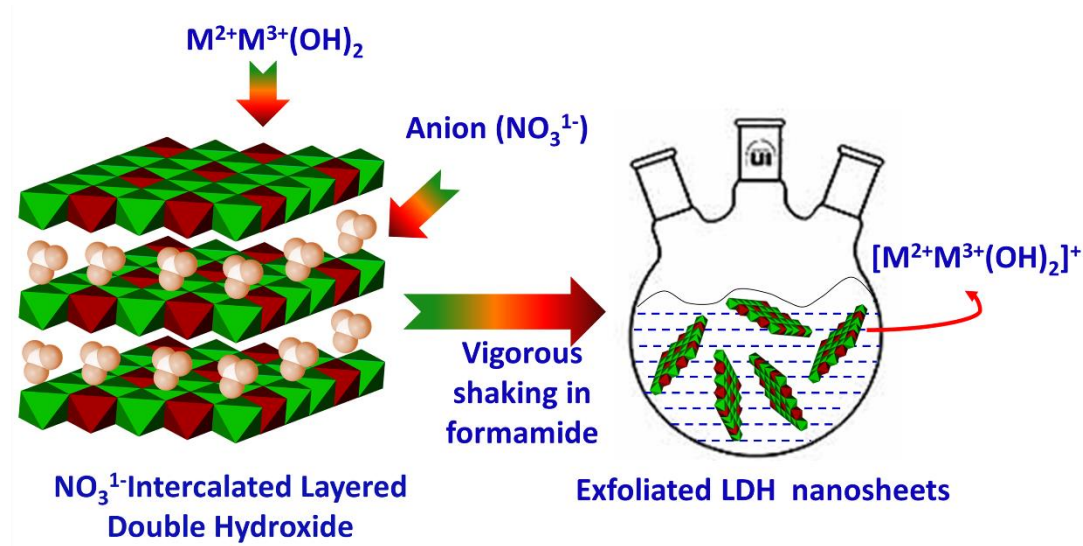


Fig. 2.8: Schematic processes of the LDH exfoliation in formamide.

LDHs consist of positively charged brucite-type octahedral sheets alternately arranged with interlayer charge balancing anions (CO_3^{2-} , NO_3^- , Cl^- etc.). Among the various anions, carbonate anions have a high affinity towards LDH gallery space due to their high charge-to-size ratio. Also, synthesis processes of LDH comprise aqueous solutions and basic pH; thus, carbonate anions are readily available for intercalation at these synthesis conditions due to the atmospheric dissolution of CO_2 . The carbonate intercalated LDHs are difficult to exfoliate due to the high attraction between LDH layers and carbonate anions. Alternatively, nitrate anions intercalated LDH demonstrated exfoliation behavior in formamide. In this approach, the strong hydrogen bonding between the intercalated anions and polar solvent as well as between the solvent molecules themselves could lead to the

penetration of large amounts of solvent between the layers and hence facilitate exfoliation. Fig. 2.8 shows schematic processes of the LDH exfoliation in formamide

Adachi-Pagano and co-workers first reported the complete exfoliation of LDH by refluxing [Zn-Al-DS] (DS: dodecyl sulphate) in 1999. LDH dispersed in butanol at 120°C for 16 hours resulted in translucent colloidal solution, which is an indication of exfoliation[75]. Venugopal et al. studied the exfoliation behaviour of a number of surfactant-intercalated LDHs under sonication/heating/stirring conditions, confirms that these LDHs were rarely exfoliated in non-polar solvents, while they were exfoliated best in alcohols [76]. Later on, Hibino and Jones [77] first reported the LDHs exfoliation in formamide (HCONH_2). The most practical way for exfoliating LDH material is an infinite swelling of the LDH layers in formamide solvent, which does not require any surfactant/organophilic anions or heat treatment [78]. In formamide, the exfoliation appeared to occur instantly and spontaneously. The nitrate form of the LDH materials is commonly employed for the efficient exfoliation process [78-80].

Li-ion intercalation and hydroxylation

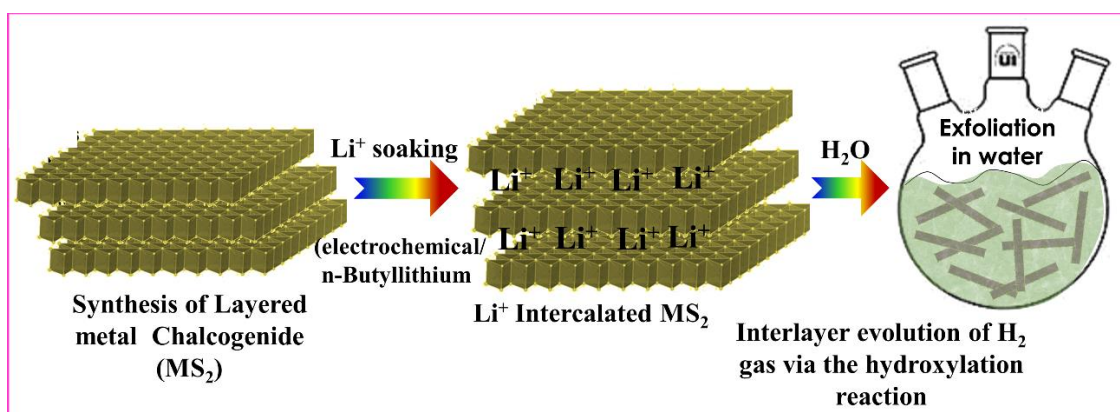


Fig. 2.9: Schematic model of the exfoliation of LTMDs.

A layered transition metal dichalcogenides (LTMDs) are represented by general chemical formula MX_2 , which consists of a transition-metal (M: Ti, Hf, Zr, Mo, V, Nb, W, Ta, Tc, Pt, Re, Pd, etc.) and chalcogen atoms (X: Se, S, and Te,) [81,82]. MX_2 is one of the most explored parent materials for the exfoliation process. The MX_2 layered structures consist of strong in-plane bonds (covalent) and weak out-of-plane bonds (van der Waals), forming a various 3D LTMDs crystal structures. The interlayer evolution of H_2 gas via the hydroxylation of tiny intercalated cations such as Na^+ , K^+ , and Li^+ , is one of the successful strategies for the exfoliation of

layered materials. The schematic model of the exfoliation of LTMDs is as shown in Fig. 2.9. The chemical intercalation using organolithium reactant has been typically used to intercalate Li^+ ion [83]. However, controlling Li^+ ion intercalation via this process is difficult because insufficient or excessive Li^+ ion intercalation frequently occurs. So, the electrochemical route can provide a more efficient way for the exfoliation and intercalation of TMDCs than the chemical route. In this technique, using electrical potential, both anionic and cationic guest species can be intercalated into bulk TMDCs materials [84].

2.3 Synthetic strategies for 2D NS-based hybrids

Exfoliated 2D NSs have been widely used as building blocks for the synthesis of novel hybrid structures due to their unique physicochemical characteristics. The hybrid structure can be applicable for many applications such as hybrid electrodes for EES devices, fuel cells, CO_2 adsorption, dye degradation [16,85,86].

In this section, typical synthesis strategies for 2D NS-based hybrids are briefly discussed, including exfoliation-reassembly, anchored assembly, and layer-by-layer deposition.

2.3.1 Exfoliation-reassembly

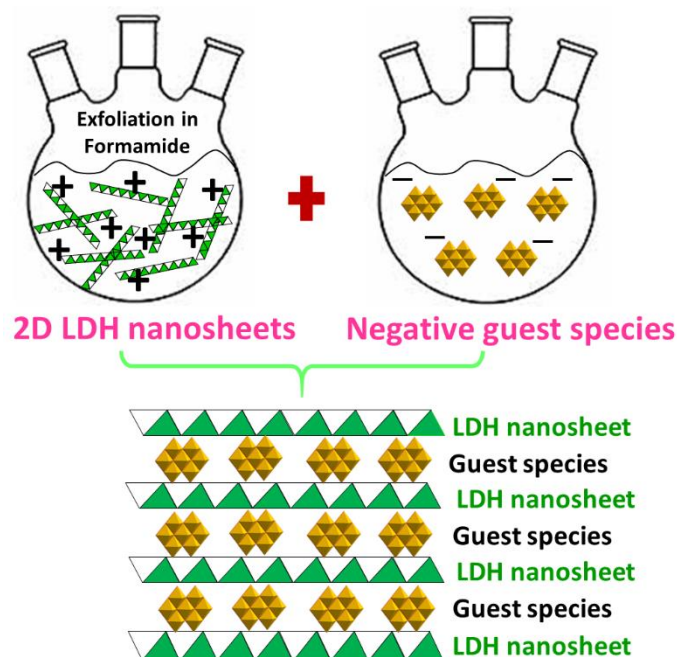


Fig. 2.10: Schematic of exfoliation-reassembly with stacking structure of LDH-based hybrid.

The ions intercalative route is generally used to synthesize 2D-based heterolayered nanohybrid. This method has a number of limitations, like the

requirement of the high mobility of guest species and the uncontrolled formation of intercalated materials. These limitations of the intercalative route can be avoided by using the exfoliation-reassembly process. In this approach, oppositely charged host NSs and the guest species are freely reassembled from initially separated colloidal states. This strategy can precisely control the chemical composition and restacking pattern of 2D NS-based hybrids. In this method, high diffusivity of guest species is not required, which enables wide opportunity to hybridize various couples of host and guest species [87-90].

The exfoliation-reassembling process between exfoliated host 2D NS and other nanostructured guest species demonstrated unique features like high surface area, mesoporous structure, intimate coupling of hybridized components, etc.[91]. Different types of crystal shapes like interstratified, hollow, core-shell and pillared were designed by this method [92]. Gunjekar et al. prepared 2D Zn-Cr-LDH NS-based hybrids of Zn-Cr-LDH-POM, Zn-Cr-LDH-titanate NSs and Zn-Cr-LDH-GO [93-95]. Fig.2.10 shows the schematic diagram of exfoliation-reassembly with stacking structure of LDH-based hybrid. MgAl-LDH-POM hybrids were prepared by exfoliation-reassembling and used for the CO₂ adsorption [96]. The exfoliation-reassembly route was used to design the CdS-ZnCr-LDH hybrids. The CdS-ZnCr-LDH hybrids were highly active photocatalysts for the H₂ production [97]. On the basis of exfoliation-reassembly strategy, hybrids of MoS₂ with variety of LDHs (like NiFe-LDH, CoFe-LDH, NiCo-LDH etc.) were prepared [98,99].

2.3.2 Anchored assembly

As 2D NSs are derived from their highly crystalline layered solid crystals with lateral size in the range of few to several micrometers, thus can acts as a 2D platform for either anchoring or growth of various functional foreign species like NSs, nanoparticles and nanoclusters. For the direct growth of functional nanoparticles, exfoliated 2D NSs are capable of providing nucleation and surface anchoring sites. The anchoring of functional foreign species occurs via either homogeneous adsorption or direct growth of nanoparticles on the surface of 2D NSs. For synthesis of NSs based nanohybrids via anchored assemblies, controlled adsorption, stability of NSs and growth of guest species (nanoparticles) on the 2D NSs platform are the significant parameters that must be taken into consideration [100]. 2D NSs-based nanohybrid electrodes made by anchoring leads to

homogeneous and uniform growth of electrode material on the 2D NSs without self-aggregation, which is quite useful in avoiding huge volume change during the electrochemical cycling. GO/rGO prepared by the exfoliation of graphite has proved to be a unique candidate as a platform for the anchoring of various nanostructures [101]. Recently, NSs based anchored assemblies of RGO-ZnCr-LDH, RuO₂-xH₂O@MXene, Ag₃PO₃-RuO₂, PANI-MoS₂, Ru-calcium niobate NSs, Ru-hexaniobate NSs, Au-WS₂, Au-MoS₂, Fe₂O₃-MoS₂, MnO₂-RGO, were investigated for multifunctional applications [102-105]. The schematic representation of 2D LDH anchored on GO NSs is shown in Fig. 2.11.

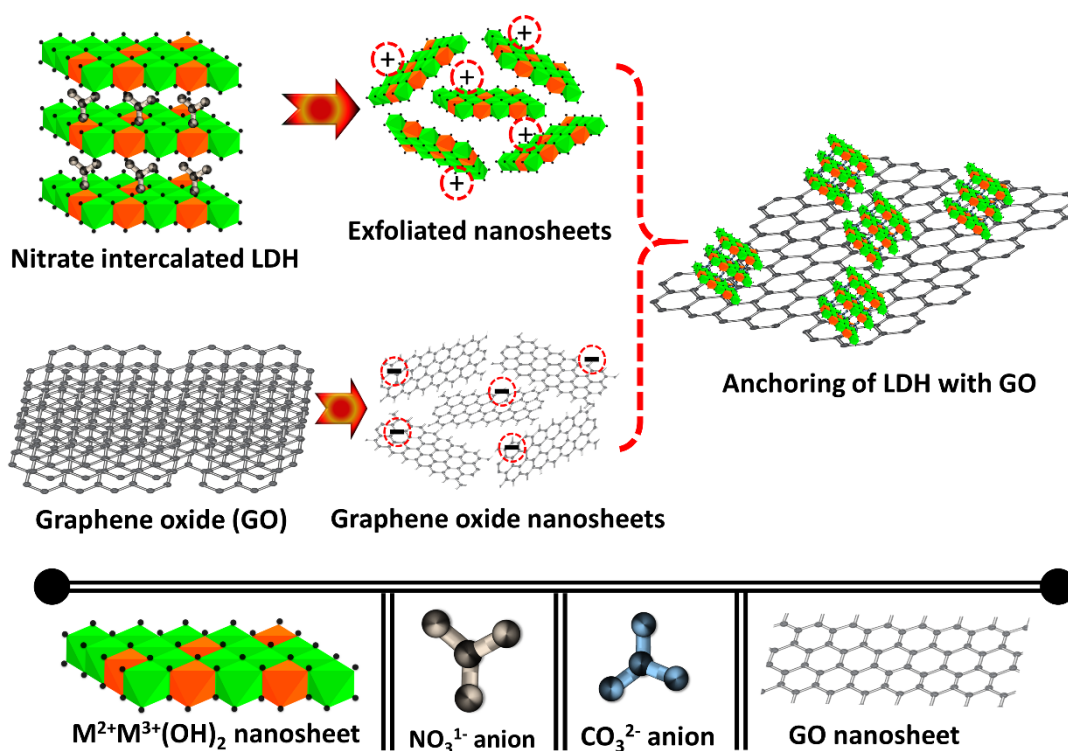


Fig. 2.11: Schematic representation of 2D LDH anchored on GO NSs.

2.3.3 Layer-by-layer (LBL) assembly

The NS-based hybridization strategies are not only limited to the synthesis of bulk/powder form but also can be applied for the deposition of high-quality NSs based thin films by LBL. The principle of LBL deposition is based on the exfoliated 2D NS that carries electrostatic charges and can be adsorbed onto substrates with opposite charges. Thus exfoliated 2D NSs can be readily applicable as effective building blocks for the successive LBL coating of multi-layered hybrid NS based film fabrication [106].

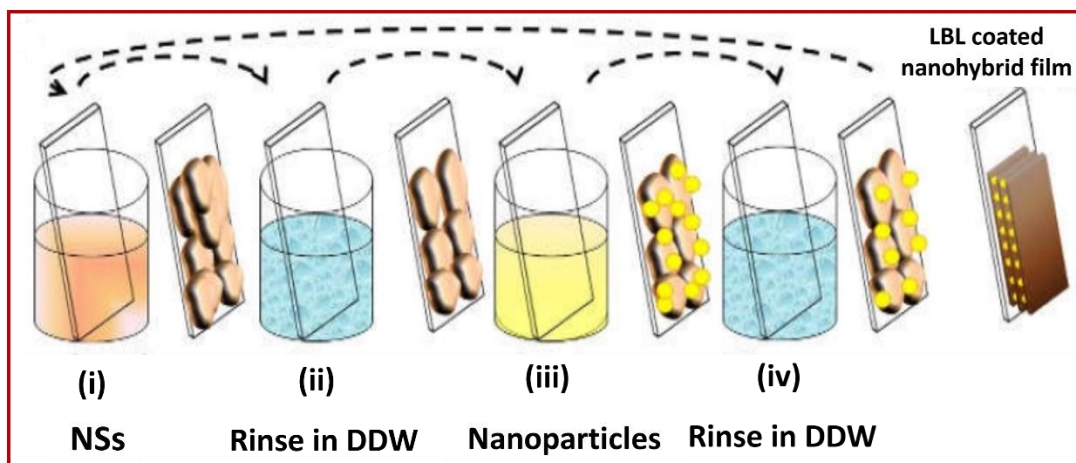


Fig. 2.12: synthesis of nanohybrid films using LBL coating.

This method can be used to precisely control the stacking sequence of the NS-based LBL film and optimize its functionality. The LBL assembly depends on the charge compensation mechanism between guest species and host NSs (Fig.2.12) [107,108]. Therefore, this method allows controlling the stacking sequence of NSs and guest species at the nanometre scale. A wide range of hybrid materials, including multi-component hybrid films, hybrid hollow spheres, and hybrid freestanding membrane, were reported by this method [109-111]. In some examples, LBL assembly is used to deposit thin films of $\text{Ca}_2\text{Nb}_3\text{O}_{10}$ -Mg-Al-LDH and TiO_2 -Mg-Al-LDH with precise control over its thickness [112].

2.4 Characterization Techniques

2.4.1 Zeta potential

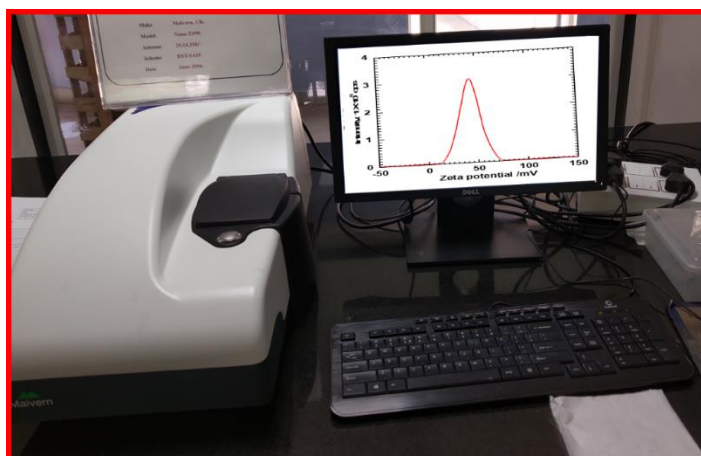


Fig. 2.13: Photograph of malvern zeta potential analyser.

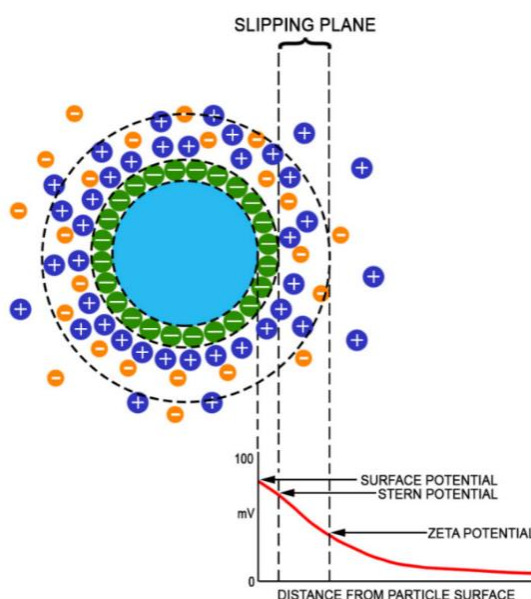


Fig. 2.14: Schematic representation of zeta potential [113].

The net charge on the particle surface is measured indirectly using zeta potential technique. The photograph of malvern zeta potential analyser is displayed in Fig.2.13. Among various techniques to characterize the superficial properties of particle in solution (liquid state), zeta potential measurement technique is one of the utmost accessible. Zeta potential is a scientific term for electrokinetic potential in colloidal suspension, generally indicated by Greek letter zeta (ζ). The electric potential at the boundary of the double layer is called as the Zeta potential of the particle, and it typically ranges from -100mV to +100 mV. Zeta potential is nothing but the potential observed at the shear plane and is defined as the potential difference between the shear plane and the electroneutral region of the solution. It can be significantly affected by factors like pH of the solution, concentration, and the electric double layer thickness. The zeta potential of dispersion can be measured via the electrophoresis process by applying an electric field across the dispersion. During zeta potential measurements, an electrical field is applied across the sample, inducing the movement of charged particles. Electrophoretic mobility μ_e is velocity of a particle in a unit electric field. Further, μ_e is measured and converted to the zeta potential (ζ) using Henry equation:

$$\mu_e = \frac{2 \times \epsilon \times \zeta \times f(k.a)}{3\eta} \quad (2.1)$$

where, η and ϵ are the absolute zero-shear viscosity and dielectric constant of the medium, respectively [113-115]. $f(k.a)$ is known as the Henry's function, where k

is a Debye parameter often taken as a measure of the "thickness" of EDL, and α is a radius of the particle (see Fig. 2.14). electrophoretic determinations of zeta potential are commonly estimated in aqueous media and moderate electrolyte concentrations.

Advantages: Different particles can be analyzed; useful for macromolecules; small sample concentration is required; simple and fast measurements are possible; this technique provides quantitative measurement.

Disadvantages: Poor resolution; large particles can change the measurement; particle over shadowing; significant dilution is required; polydispersity can cause complications.

2.4.2 X-ray diffraction

Basic principle

When monochromatic X-rays are incident on a crystalline material at an angle ' θ ', the rays are diffracted by parallel lattice planes separated by basal spacing ' d '. The diffraction pattern is obtained by measuring the intensity of diffracted X-rays as a function of scattering angle. According to Braggs condition, when the path difference equals the integral multiple of the X-rays wavelength, constructive interference occurs (Fig. 2.16).

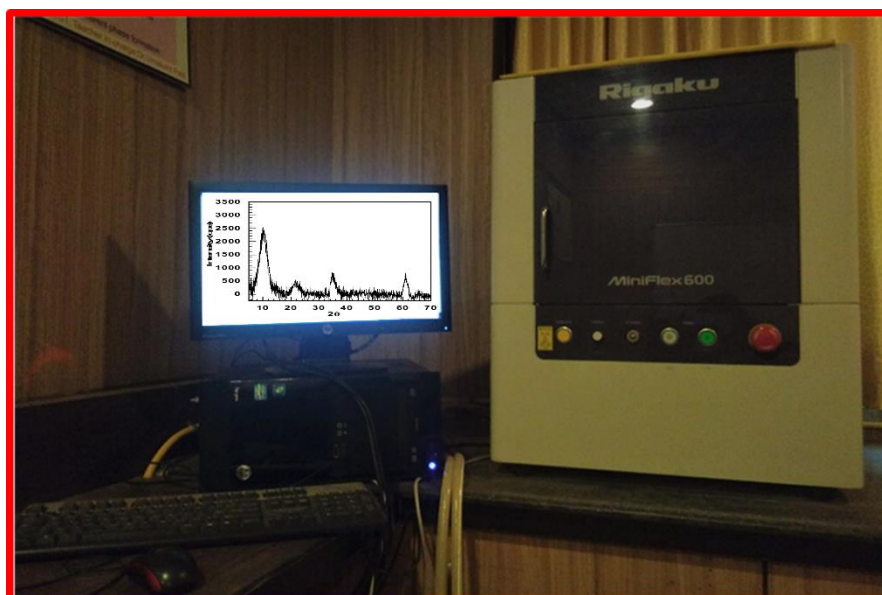


Fig. 2.15: Photograph of Rigaku miniflex-600 X-Ray diffractometer.

The basic phenomenon of XRD can be considered as the diffraction of X-rays from the crystallographic planes of the material and is directed by the Braggs equation [116];

$$2d_{hkl}\sin\theta = n\lambda \quad (2.2)$$

where, d_{hkl} , λ , θ , and n are the basal spacing, wavelength of X-ray, diffraction angle, and order of diffraction ($n = 1$), respectively. The photograph of Rigaku Miniflex-600 X-Ray diffractometer is displayed in Fig. 2.15. The schematic model of XRD diffractometer is presented in Fig. 2.16.

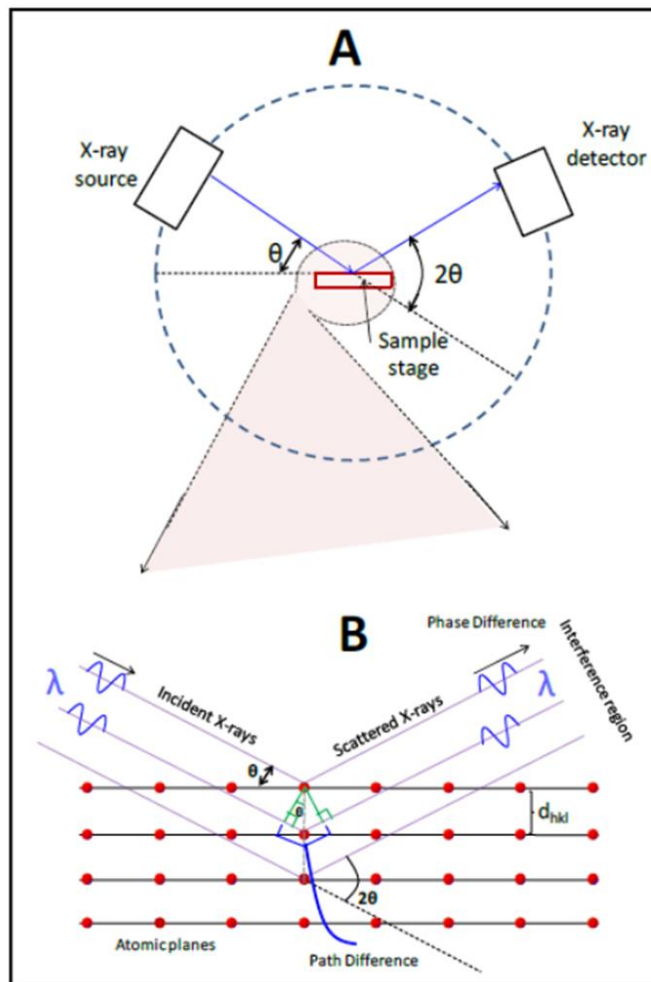


Fig. 2.16: (A) Schematic representation of XRD diffractometer and (B) X-ray diffraction condition using the Bragg's law [117].

Scherrer's equation is used to calculate the particle size from the full width at half maximum (FWHM) of the highly intense diffraction peak [117].

$$D = \frac{k\lambda}{\beta \cos\theta} \quad (2.3)$$

where, D = particle size, k = constant, β = FWHM, λ = wavelength of X-rays, and θ = diffraction angle.

Advantages: Commonly used method to determine the crystal structure; least expensive and most convenient; the best method for phase analysis; X-rays are not absorbed very much by air, so the sample need not be in an evacuated chamber.

Disadvantages: X-rays do not interact very strongly with lighter elements; This technique is not useful to analyze chemical composition; XRD method does not give information regarding the chemical bonding nature.

The present study applies the powder XRD technique to investigate the crystal structure, lattice dimensions, and crystallite size of nanohybrids materials.

2.4.3 Fourier transform infrared spectroscopy

Working principle

FTIR is a powerful analytical tool for identifying functional groups of a compound based on vibrational spectroscopy of the bonds. The spontaneous orientation of the dipole moment in materials is studied by the non-destructive tool using infrared spectroscopy that can provide information about inter-atomic forces within the crystal lattice. There are six different ways in which organic/inorganic compound can vibrate: symmetrical and anti-symmetrical stretching, wagging, rocking, scissoring, and twisting [118]. The FTIR spectrometer; (Alpha (II) Bruker model) was used for sample characterization. The digital photograph and ray diagram of the FTIR is presented in Fig. 2.17 (a) and (b), respectively.

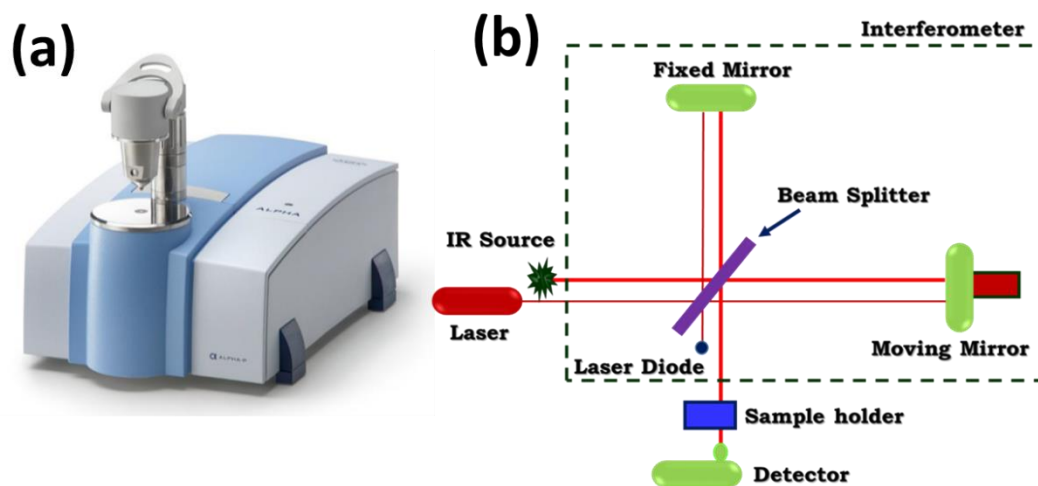


Fig. 2.17: (a) Digital photograph of FTIR Spectrometer and (b) basic ray diagram of FTIR spectrometer [118].

The infrared vibrational frequencies and inter-atomic forces are correlated and so to examine functional groups present in the material. According to the

Planck-Einstein relation, energy transfer between different energy states of molecules can be written as the following equation,

$$\Delta E = h\nu \quad (2.4)$$

In this equation, positive and negative values of ΔE corresponds to the absorption and emission of energy by molecules, respectively. When the above equation (2.4) is satisfied, a unique spectrum is originated, characteristic of the molecule. The spectrum is a plot of the transmittance versus frequencies where peaks are observed when the condition is satisfied. Different spectra are raised by molecules or atoms based on the energy level involved in the transitions in the atom. The transition between different allowed levels for the orbital electron signifies absorption, and the whole molecule vibrates or rotates when atoms vibrate within the molecule. Hence, the total energy (E_{tot}) contribution can be denoted by the following equation [118],

$$E_{tot} = E_{elect} + E_{vib} + E_{rot} + E_{trans} \quad (2.5)$$

Where, E_{elect} is electronic energy, E_{vib} is vibrational energy, E_{rot} is rotational energy, and E_{trans} is translational energy.

Advantages: It is a universal technique; it is relatively inexpensive and gives reach information; elimination of stray light and emission contribution; highly sensitive to any molecules that contain chemical bonds; powerful data station; it is easy, fast and highly sensitive.

Disadvantages: Atoms or monoatomic ions detection is impossible because single atomic entities contain no chemical bonds; cannot detect symmetric molecules like N_2 or O_2 ; aqueous solutions are very challenging to study because water is a significant IR absorber.

In the present study, the FTIR technique is used to investigate the functional group, chemical bonding nature and water content of nanohybrid materials.

2.4.4 Micro-Raman spectroscopy

Working principle

Raman spectroscopic technique is based on inelastic scattering of monochromatic light called Raman scattering. When incident monochromatic light interacts with matter, photons interact with the electron cloud of the functional groups bonds, which excite an electron into a virtual state. This process leads to a

change in wavelength of incident photons (red or blue shifted) detected as Stokes Raman scattering. These Stokes Raman lines are characteristics of the functional group, the structure of the molecule to which it is attached, the types of atoms in that molecule and the molecule's environment. The ray diagram of the Raman spectrometer is shown in Fig.2.18.

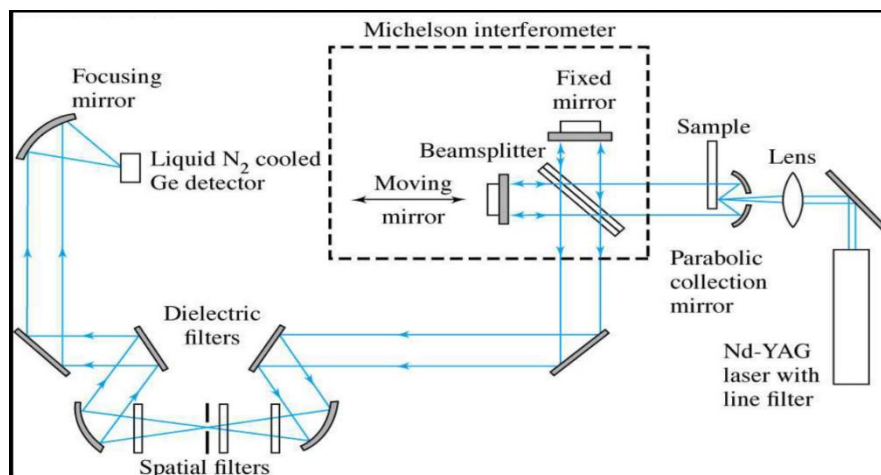


Fig. 2.18: Ray diagram of Raman spectrometer [119].

The energy shift can be used to determine the system's vibrational modes. Initially, a laser beam is used to illuminate a sample, and light from the corresponding illuminated spot is captured with a lens and sent through a monochromator. The wavelength close to the laser line due to the elastic scattering is filtered out while the rest of the collected light is dispersed onto a detector. Furthermore, the atomic arrangement, chemical bonds and masses of the atoms in the molecule are more important for finding the Raman spectrum of the molecule [120]. The Raman spectral features demonstrates the chemical interaction existed in sample which is an important supplement to the FTIR result.

Advantages: It is non-destructive technique; in this technique, a single recording can cover the range from 50 cm^{-1} to 4000 cm^{-1} ; for Raman analysis various organic and inorganic materials are used and these can be liquids, solids, vapors or polymers, etc.; this technique is a highly specific like a chemical fingerprint of a material; Raman spectra can be obtained from a relatively small volume ($< 1\text{ }\mu\text{m}$ in diameter); generally, water has no effect on it; Raman spectrum is acquired quickly within second.

Disadvantages: This technique cannot be used for alloys or metals; a sensitive and well-optimized equipment is required for the sample detection; the Raman effect

is very weak; when the sample is irradiated with a laser beam, several substances shows fluorescence; the Raman spectrum might be hidden by the fluorescence of contaminants or the sample itself; sample heating caused by powerful laser light has the potential to damage the sample or obscure the Raman spectrum.

In the present study, the micro-Raman spectroscopy technique is used to investigate the chemical bonding nature of nanohybrid materials and complimentary to the FTIR results.

2.4.5 Field emission-scanning electron microscopy

Working principle

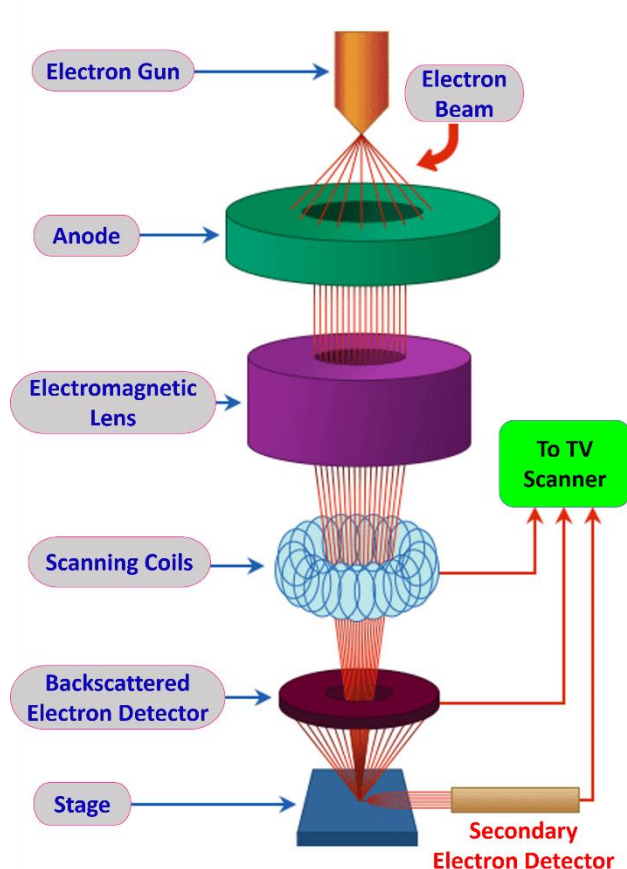


Fig. 2.19: Ray diagram of FESEM [121].

In FESEM, high-energy electrons (also called primary electrons) are generated by heating a thin and sharp tungsten needle (cathode). The voltage difference between anode and cathode allows; the generated electrons to accelerate towards the sample. The electromagnetic lenses focus the electron beam in a tiny sharp spot. The precoated sample is mounted on the special holder and inserted onto the high vacuum part of the microscope through a sample exchange chamber. The schematic diagram of the FESEM instrument is shown in Fig. 2.19.

The FESEM is always performed in a high vacuum to avoid the interaction of high-energy electrons with gas molecules in order to obtain high resolution. Once the focused electron beam bombards the surface of the sample, it penetrates the sample up to a few microns and interacts in different ways. After the interaction, primary electrons lose their energy inside the sample. Due to this, different types of emissions are observed, as shown in Fig. 2.20 [122]. The scattering and interaction of electrons on the surface depending on the surface elements (atomic number), the concentration of atoms, and the energy of primary electrons. The high energy of primary electrons increases the interaction volume and scattering process. In contrast, the high concentration of atoms and the atomic number will decrease the interaction volume and scattering.

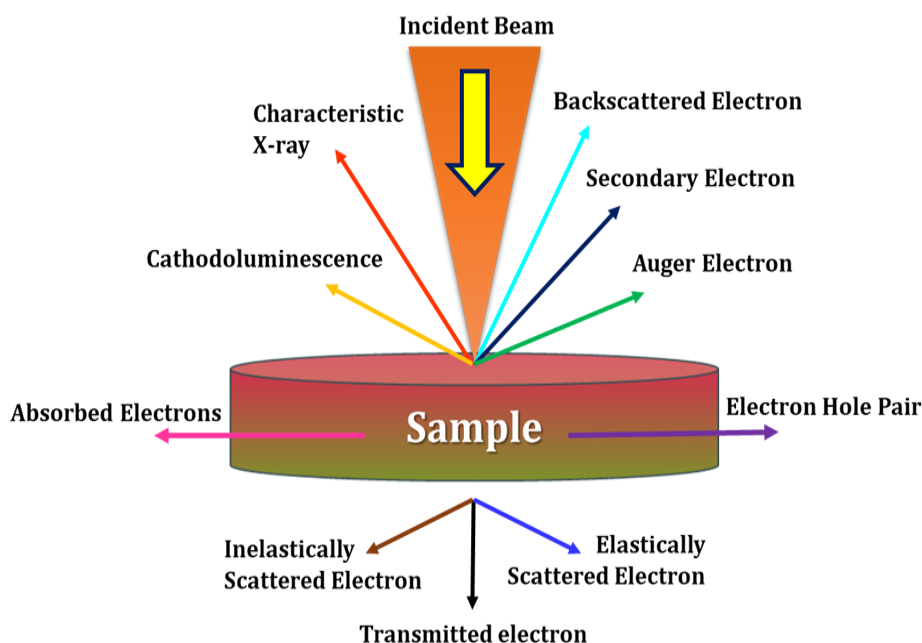


Fig. 2.20: Ray diagram of the emission of diverse forms of electrons during scanning [122].

All these signals are gathered at a detector and separated based on their energy values. The backscattered and secondary electrons are used for the creation of a sample image by amplifying and transforming the signals. When primary electrons interact with electrons at the inner shell and knock it out, the electron from a higher energy level jumps to lower energy by losing some energy. This extra energy is emitted in the form of X-rays. Therefore, each element in the sample produces a characteristic X-ray. All these characteristic X-rays from all elements

are used to identify the elemental composition of the sample by energy-dispersive X-ray spectroscopy (EDX) coupled to the FESEM instrument.

Advantages: It is possible to study a larger depth of field; this technique, magnifies objects more than 500000X; most of the samples just necessitate a few steps of preparation; data generated in a digital format.

Disadvantages: This tool is expensive; this instrument needs a very large space and is operated in special rooms; artifacts can occur during the sample preparation process; this technique is limited to solid samples; small risk of radiation exposure associated with the electrons that scatter from beneath the sample surface; affected by magnetic fields.

In the present study, the FESEM technique is used to analyze the surface morphology, thickness, and pore size of the nanohybrids. this technique is also used to analyze the elemental composition of nanohybrid materials.

2.4.6 High resolution transmission microscopy

HRTEM is another important technique used as a materials characterization tool that involves passing an electron beam through the sample. The main difference between FESEM and HRTEM is the speed of primary electrons. The electrons in HRTEM have a much higher speed than in FESEM. Also, the electrons in the case of FESEM bounce off the sample, while in HRTEM, they get transmitted through the sample.

Working principle

The high-speed electrons travel in a vacuum chamber and pass through the ultra-thin sample cast on a TEM grid and stricken on a phosphor screen where a charge-coupled device (CCD) camera is focused for imaging.

The HRTEM enables the imaging of material at an atomic scale. The general construction of TEM consists of several parts, including electron gun for thermionic emission, a high vacuum system to minimize the contamination, electromagnetic lenses to direct the electron beam, a high voltage source to emit thermally accelerated electrons, computer coupled recording devices along with required electronic components. The microscope setup is maintained at a very high vacuum to avoid electron scattering. TEM microscopy uses a focused electron beam bombarded onto the sample specimen, which forms an electronic image of the morphology and achieves compositional information present on the surface of the

sample. The darker region in the image is due to less transmitted electrons, which illustrates a dense or thick portion of the sample. Conversely, the lighter region in the image is due to the higher transmitted electrons, which indicates the thinner portion of the sample. The ray diagram of the TEM is shown in Fig. 2.21.

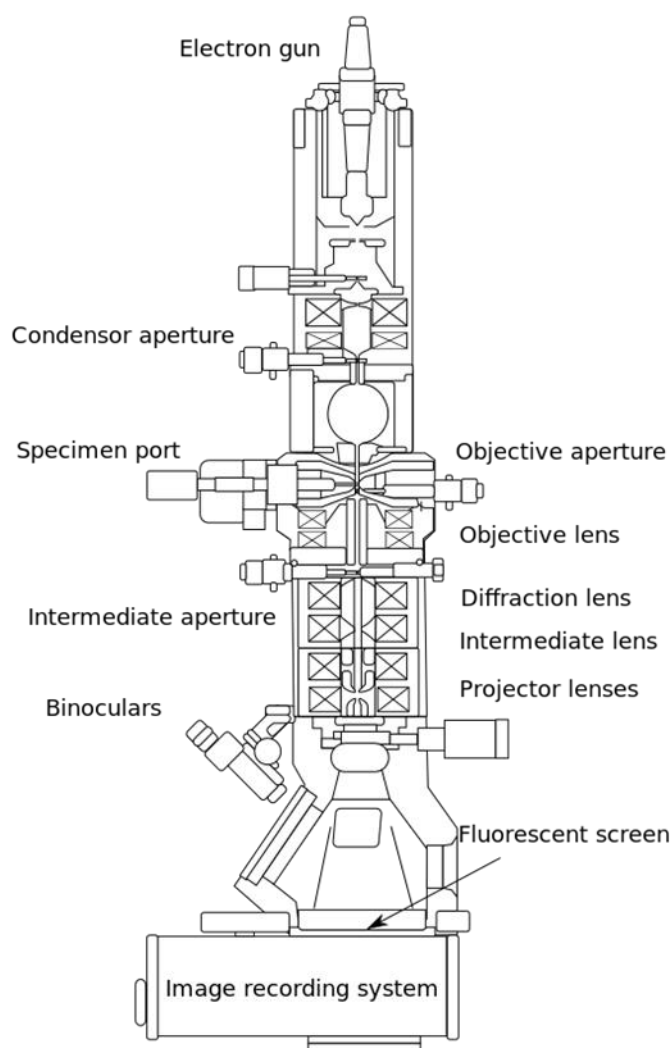


Fig. 2.21: Ray diagram of TEM [123].

Advantages: It has a broad range of applications and can be used in a variety of scientific, educational, and industrial fields; this technique provides the elemental and compound structure information; HRTEM provides both information such as real space (in the imaging mode) and reciprocal space (in the diffraction mode); this technique provides detailed and high-quality images.

Disadvantages: This instrument requires large space with special housing and maintenance; requires considerable time and effort for sample preparation; specialized trainee is required for operation and analysis; in this technique, only

electron transparent samples are allowed; this technique provides black and white images.

In the present study, this technique is used to probe morphology, particle size distribution, crystal structure, interplanar distance and elemental distribution of nanohybrids.

2.4.7 Brunauer-Emmette-Teller

Working principle

The BET method is based on the multilayer physical adsorption of gaseous molecules on the surface of solid using non-corrosive inert gases such as argon, nitrogen, etc. [124], and the amount of adsorbed gas gives a specific surface area of a prepared sample. The gas adsorbs on the solid surface and in the pores of the specimen. At a given pressure, the amount of condensed or adsorbed gas on the surface of a solid at a constant temperature gives information about the pore structure. The schematic diagram of the dynamic flow method apparatus used for measuring specific surface area is shown in Fig. 2.22.

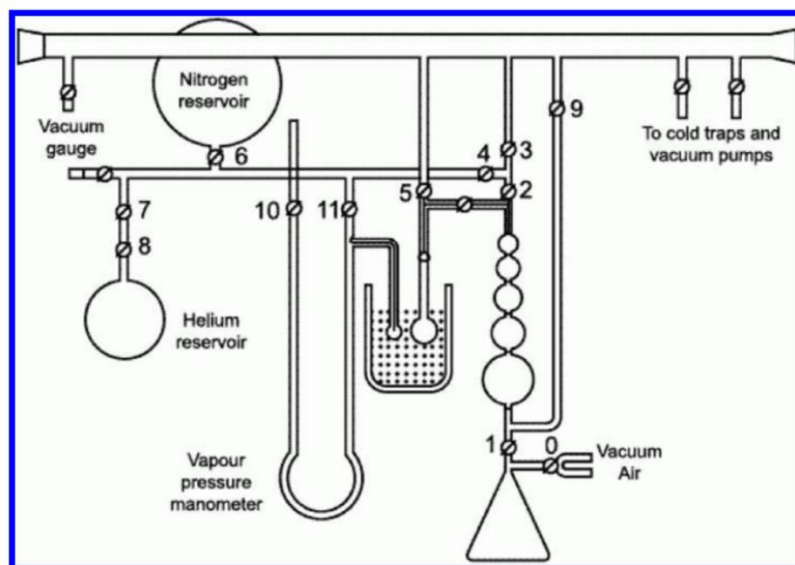


Fig. 2.22: Schematic illustration of the dynamic flow method apparatus [125].

The total surface area (S_t) and a specific surface area (S_{BET}) are calculated by using equations 2.6 and 2.7.

$$S_t = \frac{N_s v_m}{V} \quad (2.6)$$

$$S_{BET} = \frac{S_{total}}{a} \quad (2.7)$$

where, 'S' is the adsorption cross-section of the adsorbing species, ' v_m ' is the molar volume of the adsorbate gas, 'N' is the Avogadro's number, and 'a' is the mass of the

adsorbent [126]. The Barrett–Joyner–Halenda (BJH) method is used to determine pore size and volume in the same technique.

Advantages: It can determine porosity up to the size of 0.4 to 50 nm; this method also allows the type, size, and form of porosity contained in the material.

Disadvantages: The measurement errors in this method are high; this method is a time-consuming method; not sufficient to measure low-level surfaces; this technique is not suitable for powder samples with micrometric particle size.

In the present study, the BET technique is used to analyze specific surface areas and pore structure of nanohybrids.

2.4.8 X-Ray photoelectron spectroscopy

Basic principle

When an incident X-ray has sufficient energy, it will be absorbed by an atom and by the phenomenon of the photoelectric effect, an inner shell electron will be ejected as demonstrated in Fig. 2.23. The kinetic energy of photoelectrons is collected. As the energy of an incident X-ray is known, the binding energy of photoelectron is calculated by the following formula:

$$KE = h\nu - B.E - \varphi_s \quad (2.8)$$

where, φ_s is a spectrometer work function of the element.

The composition of the sample and the various oxidation states of the elements present in it can be estimated by monitoring the count of photoelectrons as a function of binding energy.

In XPS, an X-ray source generates X-rays (typically $MgK\alpha$ and $AlK\alpha$) which are monochromatized using a monochromator in a high vacuum. These X-rays are then incident on the sample and excite the electrons inside the atoms present on the surface of the sample. These photoelectrons go to the electron detector where the detector counts the incoming electrons as well as the kinetic energy of these electrons. Finally, this kinetic energy is represented in the form of a spectrum where particular energy represents a specific element.

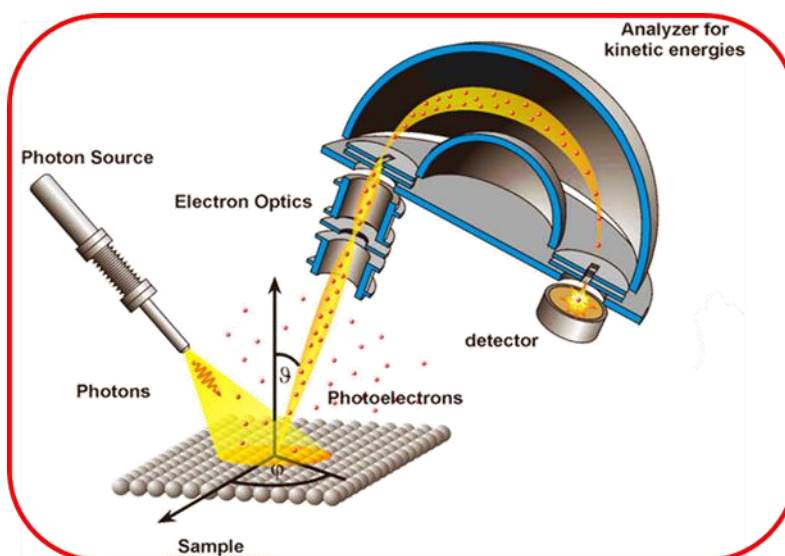


Fig.2.23: Ray diagram of XPS [127].

Advantages: This is a non-destructive technique; quantitative measurements are obtained; this technique is highly surface sensitive (10 to 100 Å); this technique provides information about chemical bonding and elemental mapping.

Disadvantages: Measurements cost is high; it is necessary to use a high vacuum; it requires a large-area analysis; slow processing technique (30 min to 8 hr per sample); in this technique, He and H cannot be identified; it gives poor lateral resolution.

In the present study, XPS is used to measure chemical composition, electronic configuration and chemical state of elements present in nanohybrids.

2.5 Electrochemical techniques

As discussed in chapter 1, SCs are divided into two groups, i.e. EDLCs (charge stored by non-faradaic mechanism) and pseudocapacitors (charge stored by faradaic mechanism). The following equation is used for the calculation of specific capacity, C_s , ED and PD of electrode. The electrochemical capacity and C_s were calculated from GCD profile using the following equation,

$$\text{Specific capacity} = \frac{i \times \Delta t}{m} \quad (\text{C g}^{-1}) \quad (2.9)$$

$$\text{Specific capacitance} = C_s = \frac{\text{specific capacity}}{\Delta V (\text{V})} \quad (\text{F g}^{-1}) \quad (2.10)$$

In equation (2.9) and (2.10), i , Δt , A , ΔV , m are applied current density (A g^{-1}), discharge time (s), active unit area of electrode (cm^{-2}), potential window of the

electrode and mass loading of the active material (g) respectively. For the Ragone plot, the ED (Wh kg^{-1}) as well as PD (W kg^{-1}) of the electrode is calculated by using equation (2.11) and (2.12),

$$ED = \frac{0.5 \times C_s \times (\Delta V)^2}{3.6} \quad \text{and,} \quad (2.11)$$

$$PD = \frac{E \times 3.6}{\Delta t} \quad (2.12)$$

The high ED with PD of SC is based on maximum capacitance value and large operating potential window of supercapacitor device. However, electrolyte and active electrode materials are responsible for high capacitance and large potential window of supercapacitor. Electrical charges accumulated in SC devices are shown as,

$$E_{s1} + E_{s2} + K^+ + A^- = E_{s1}^- // K^+ + E_{s2}^+ // A^- \quad (2.13)$$

where E_{s1} and E_{s2} are the specific surface areas corresponding to negative and positive electrodes, respectively. The symbol $//$ denotes charges accumulated on both electrodes, where K^+ and A^- are cations and anions present in the electrolyte, respectively. The electrochemical performance of working electrode is studied using CV, GCD and EIS techniques.

2.5.1 Cyclic voltammetry

The CV is generally used to study the electrochemical properties of a working electrode or analyte in the electrolyte. CV is a type of potentiodynamic electrochemical measurement in which the working electrode potential is ramped linearly versus time, as shown in Fig. 2.24. In this arrangement, potential is applied with respect to the reference electrode and working electrode, while Faradic current is measured through working and counter electrodes in a three-electrode cell [152, 153]. In CV, the potential is varied in a constant operating potential window with respect to time. After the set potential is reached in a CV experiment, the working electrode potential is ramped in the opposite direction to return the initial potential. The cyclic voltammogram trace is observed by plotting the current of the working electrode against the applied voltage, as shown in Fig. 2.25(a, b). The working potential of the electrode depends upon redox and electrolytes decomposition potential.

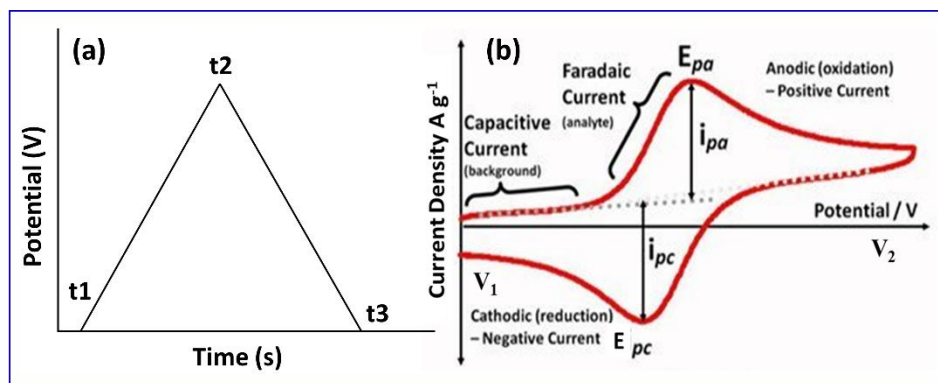


Fig. 2.24: (a) Ramping applied voltage with time frame (b) a typical CV for a reversible single electrode transfer reaction [154].

Fig 2.24(b) illustrates the typical CV curve for a reversible single electron transfer reaction occurred within the potential limit of ' V_2-V_1 ', however, i_{pc} and i_{pa} are the cathodic and anodic peak currents, and E_{pc} and E_{pa} are cathodic and anodic peak voltages of resulting voltammogram, respectively. During forward scan, potential increases from V_1 to V_2 , initially cathodic current increases and further decreases with decreasing concentration of a reduced analyte. In reverse scan, potential decreases from V_2 to V_1 , and reduced analyte will start to re-oxidized, which delivers reverse polarity current, called an anodic current. In CV measurement, the selection of potential limit is important due to the oxidation and reduction positions of CV curve and decomposition potential of electrolyte.

2.5.2 Galvanostatic Charge-Discharge

The GCD technique is very beneficial for the testing capacitive performance of SCs. In this technique, a constant current is applied to the working electrode and its potential is measured as a function of time with respect to the reference electrode. The schematic GCD curve is shown in Fig. 2.25. When a constant current is applied, initially, potential quickly develops because of internal resistance, and further, it develops gradually due to the exhaustion of reactant concentration at the electrode surface. Also, potential drop occurs while discharging due to ohmic drop (IR drop) and it is related to the electrode, solution resistance and connection interface. Constant current is used to achieve the required voltage during charge and discharge [155].

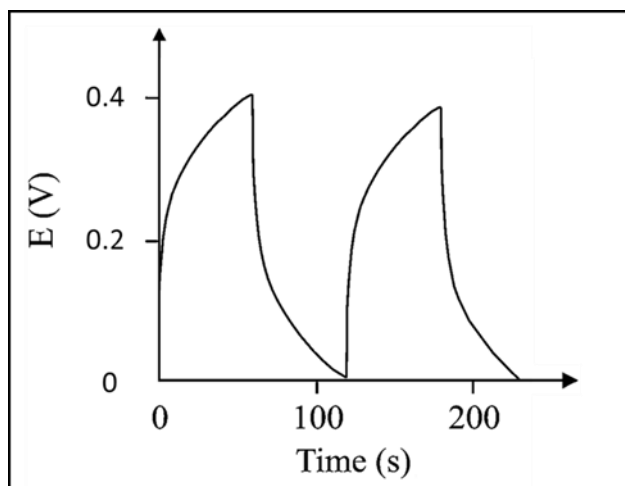


Fig. 2.25: Schematic of GCD curves [155].

By studying the nature of the GCD profile, one can confirm the possible type of charge storage mechanism of active electrode. Symmetric nature of charge-discharge profile indicates the EDL mechanism, and non-symmetric nature indicate pseudocapacitive charge storage mechanism [156].

2.5.3 Electrochemical Impedance Spectroscopy

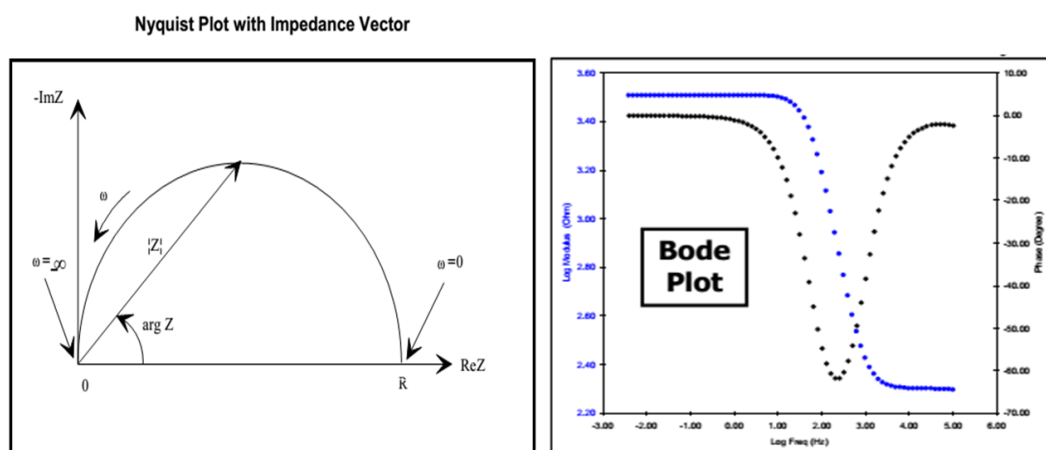


Fig. 2.26: Nyquist plot with Bode plot [157].

In the EIS technique, electrochemical impedance and current response are measured by applying a range of alternating current frequencies to a system. Impedance, an alternating current resistance of the cell comprises imaginary and real parts. Fig. 2.26 illustrates a typical Nyquist plot and Bode plots. In general, the electrochemical cell contains resistive, capacitive, and inductive properties. Capacitive and inductive properties contribute to the imaginary part, while resistive property is involved in the real part. The opening point of Nyquist plot

and diameter of extrapolated semicircle represents the solution resistance (R_s) and charge transfer resistance (R_{ct}), respectively. In the low-frequency region, the Nyquist plot displays a straight line correlated to the Warburg impedance for electrolyte ion diffusion through the electrodes. All these characterization techniques are used to find out ED, PD, working potential window, C_s , and cyclic stability of SC.

2.6 Reference:

- [1] T-H. Gu, N. H. Kwon, K-G. Lee, X. Jin, S-J. Hwang, *Coord. Chem. Rev.* 421 (2020) 213439-213468.
- [2] B. E. Conway, *J. Electrochem. Soc.* 138 (1991) 1539-1548.
- [3] B. E. Conway, *Electrochemical supercapacitors: scientific fundamentals and technological applications*, kluwer-plenum, New York, 1999, pp. 1-697.
- [4] B. E. Conway, V. I. Birss, J. Wojtowicz, *J. Power Sources*, 66 (1997) 1-14.
- [5] N. R. Chodankar, H. D. Pham, A. K. Nanjundan, J. F. S. Fernando, K. Jayaramulu, D. Golberg, Y-K. Han, D. P. Dubal, *Small*, 16 (2020) 1-35.
- [6] X. Ge, C. Gu, Z. Yin, X. Wang, J. Tu, J. Li, *Nano Energy*, 20 (2016) 185-193.
- [7] B. Liu, J. Hou, T. Zhang, C. Xu, H. Liu, *J. Mater. Chem. A*, 7 (2019) 16222-16230.
- [8] B. M. Hryniewicz, R. V. Lima, F. Wolfart, M. Vidotti, B. M. Hryniewicz, R. V. Lima, F. Wolfart, M. Vidotti, *Electrochim. Acta*, 293 (2019) 447-457.
- [9] Z. Xiao, Y. Bao, Z. Li, X. Huai, M. Wang, P. Liu, L. Wang, *ACS Appl. Energy Mater.* 2 (2019) 1086-1092.
- [10] L. Zhang, H. Yao, Z. Li, P. Sun, F. Liu, C. Dong, J. Wang, Z. Li, M. Wu, C. Zhang and B. Zhao, *J. Alloys Compd.*, 711 (2017) 31-41.
- [11] X. Ge, C. Gu, Z. Yin, X. Wang, J. Tu, J. Li, *Nano Energy*, 20 (2016) 185-193.
- [12] A. S. Aricò, P. Bruce, B. Scrosati, J.-M. Tarascon and W. Van Schalkwijk, *Nat. Mater.* 4 (2005) 366-377.
- [13] L. Wang, T. Sasaki, *Chem Rev.* 114 (2014) 9455-9486.
- [14] E. Pomerantseva, Y. Gogotsi, *Nat. Energy*. 2 (2017), 1-6.
- [15] C. Tan, X. Cao, X.-J. Wu, Q. He, J. Yang, X. Zhang, J. Chen, W. Zhao, S. Han, G.-H. Nam, M. Sindoro, H. Zhang, *Chem. Rev.* 117 (2017) 6225- 6331.
- [16] S. M. Oh, S-J. Hwang, *J. Korean Ceram. Soc.* 57 (2020) 119-134.
- [17] J. -H. Choy, *J. Phys. Chem. Solids*, 65 (2004) 373-383.
- [18] E. Ruiz-Hitzky, P. Aranda, M. Darder, G. Rytwo, *J. Mater. Chem.* 20 (2010) 9306-9321.
- [19] D. -H. Park, S. -J. Hwang, J. -M. Oh, J. -H. Yang, J. -H. Choy, *Prog. Polym. Sci.* 38 (2013) 1442-1486.

- [20] F. Kooli, W. Jones, *Inorg. Chem.* 34 (1995) 6237–6238.
- [21] C. Xu, D. Liu, K. Li, X. Liu, B. Dong, F. Dong, Y. Zhang, *J. Energy Chem.* (2021) 218–227.
- [22] <https://plasma.oxinst.com/technology/pecvd>.
- [23] a) J. Yang, D. Voiry, S. J. Ahn, D. Kang, A. Y. Kim, M. Chhowalla, H. S. Shin, *Angew. Chem. Int. Ed.* 52, 13751–13754; b) J. Xie, H. Zhang, S. Li, R. Wang, X. Sun, M. Zhou, J. Zhou, X. W. Lou, Y. Xie, *Adv. Mater.* 25 (2013) 5807–5813; c) C. Zhai, N. Du, H. Z. D. Yang, *Chem. Commun.* 47 (2011) 1270–1272.
- [24] a) Z. Sun, T. Liao, Y. Dou, S. M. Hwang, M.-S. Park, L. Jiang, J. H. Kim, S. X. Dou, *Nat. Commun.* 5 (2014) 1–9; b) Y. Sun, F. Lei, S. Gao, B. Pan, J. Zhou, Y. Xie, *Angew. Chem. Int. Ed.* 52 (2013) 10569–10572.
- [25] a) X. Zhang, Q. Liu, L. Meng, H. Wang, W. Bi, Y. Peng, T. Yao, S. Wei and Y. Xie, *ACS Nano* 7 (2013) 1682–1688; b) Y. Sun, Z. Sun, S. Gao, H. Cheng, Q. Liu, J. Piao, T. Yao, C. Wu, S. Hu, S. Wei, Y. Xie, *Nat. Commun.* 3 (2012) 1057.
- [26] R. Muñoz, C. Gómez-Aleixandre, *Chem. Vap. Deposition* 19 (2013) 297–322.
- [27] A. M. Scaparro, V. Miseikis, C. Coletti, A. Notargiacomo, M. Pea, M. D. Seta, L. D. Gaspare, *ACS Appl. Mater. Interfaces* 8 (2016) 33083–33090.
- [28] M. Yoshimura, K. Byrappa, *J. Mater. Sci.* 43 (2008) 2085–2103.
- [29] P. K. Katkar, U M. Patil, Chemical synthesis of cobalt manganese phosphate thin films for supercapacitor application, 2021
- [30] H. Chen, L. Hu, M. Chen, Y. Yan, L. Wu, *Adv. Funct. Mater.* 24 (2014) 934–942.
- [31] B. Xu, L. Yu, M. Sun, F. Ye, Y. Zhong, G. Cheng, H. Wang, Y. Mai, *RSC Adv.* 7 (2017) 14910–14916.
- [32] A. Xia, W. Yu, J. Yi, G. Tan, H. Ren, C. Liu, *J. Electroanal. Chem.* 839 (2019) 25–31.
- [33] C. Cao, L. Xing, Y. Yang, Y. Tian, T. Ding, J. Zhang, T. Hu, L. Zheng, X. Li, *Appl. Surf. Sci.* 406 (2017) 245–253.
- [34] W. Bao, J. Wang, Q. Wang, D. O'Hare, Y. Wan, *Sci. Rep.* 6 (2016) 26738.
- [35] R. Yang, Y. Zhou, Y. Xing, D. Li, D. Jiang, M. Chen, W. Shi, S. Yuan, *Appl. Catal. B Environ.* 253 (2019) 131–139.
- [36] Y. Nakayasu, S. Bradley, H. Kobayashi, K. Nayuki, Y. Sasaki, T. Tomai, T. Nann, I. Honma, *Nanoscale Adv.*, 1 (2019) 3383–3387.
- [37] G. Murillo, E. Leon-Salguero, P. R. Martínez-Alanis, J. Esteve, J. Alvarado-Rivera, F. Güell, *Nano Energy* 60 (2019) 817–826.
- [38] Z. Hu, E. M. Mahdi, Y. Peng, Y. Qian, B. Zhang, N. Yan, D. Yuan, J.-C. Tan, D. Zhao, *J. Mater. Chem. A* 5 (2017) 8954–8963.
- [39] M. Shandilya, R. Rai, J. Singh, *Adv. Appl. Ceram.* 115 (2016) 354–376.
- [40] W. L. Suchanek, R. E. Riman, *Adv. Sci. Tech.* 45 (2006) 184–193.
- [41] S. M. Oh, S. B. Patil, X. Jin, S.-J. Hwang, *Chem. Eur. J.*, 24 (2018) 4757–4773.
- [42] V. Nicolosi, M. Chhowalla, M. G. Kanatzidis, M. S. Strano, J. N. Coleman, *Science* 331 (2011) 568–571.

- [43] T. Sasaki, M. Watanabe, *J. Am. Chem. Soc.* 120 (1998) 4682–4689.
- [44] T. W. Kim, E. J. Oh, S. T. Lim, D. H. Park, A. Y. Jee, M. Lee, S. H. Hyun, J. -H. Choy, S. -J. Hwang, *Chem. Eur. J.* 15 (2009) 10752–10761.
- [45] J. N. Coleman, M. Lotya, A. O'Neill, S. D. Bergin, P. J. King, U. Khan, K. Young, A. Gaucher, S. De, R. J. Smith, *Science* 331(2011) 568–571.
- [46] R. Ma, Z. Liu, L. Li, N.; Iyi, T. Sasaki, *J. Mater. Chem.* 16 (2006) 3809–3813.
- [47] T. Nakato, Y. Yamada, N. Miyamoto, *Clay. J. Phys. Chem. B* 113 (2009) 1323–1331.
- [48] L. Wang, P. Brazis, M. Rocci, C. R. Kannewurf, M. G. Kanatzidis, *Chem. Mater.* 10 (1998) 3298–3300.
- [49] C. C. Coleman, H. Goldwhite, W. Tikkanen, *Chem. Mater.* 10 (1998) 2794–2800.
- [50] M. Z. Hasan, C. L. Kane, *Rev. Mod. Phys.* 82 (2010) 3045–3067.
- [51] K. S. Novoselov, A. K. Geim, S. V. Morozov, D. Jiang, Y. Zhang, S. V. Dubonos, I. V. Grigorieva and A. A. Firsov, *Science* 306 (2004) 666–669.
- [52] a) H. Li, J. Wu, Z. Yin and H. Zhang, *Acc. Chem. Res.* , 47 (2014) 1067- 1075; b) S. Tongay, J. Zhou, C. Ataca, K. Lo, T. S. Matthews, J. Li, J. C. Grossman and J. Wu, *Nano Lett.*, 12 (2012) 5576-5580; c) Y. Li, A. Chernikov, X. Zhang, A. Rigosi, H. M. Hill, A. M. van der Zande, D. A. Chenet, E.-M. Shih, J. Hone and T. F. Heinz, *Phys. Rev. B*, 90(2014) 205422; d) H. Li, G. Lu, Y. Wang, Z. Yin, C. Cong, Q. He, L. Wang, F. Ding, T. Yu and H. Zhang, *Small*, 9 (2013) 1974-1981; e) N. E. Staley, J. Wu, P. Eklund, Y. Liu, L. Li, Z. Xu, *Phys. Rev. B*, 80 (2009) 184505; f) L. Li, W. Wang, Y. Chai, H. Li, M. Tian, T. Zhai, *Adv. Funct. Mater.* 27(2017) 1701011.
- [53] P. Ares, F. Aguilar-Galindo, D. Rodríguez-San-Miguel, D. A. Aldave, S. Díaz-Tendero, M. Alcamí, F. Martín, J. Gómez-Herrero and F. Zamora, Mechanical isolation of highly stable antimonene under ambient conditions, *Adv. Mater.* 28 (2016) 6332-6336, <https://doi.org/10.1002/adma.201602128>.
- [54] K.-Z. Du, X.-Z. Wang, Y. Liu, P. Hu, M. I. B. Utama, C. K. Gan, Q. Xiong, C. Kloc, *ACS Nano* 10 (2016) 1738-1743.
- [55] J. N. Coleman, M. Lotya, A. O'Neill, S. D. Bergin, P. J. King, U. Khan, K. Young, A. Gaucher, S. De, R. J. Smith, I. V. Shvets, S. K. Arora, G. Stanton, H. Y. Kim, K. Lee, G. T. Kim, G. S. Duesberg, T. Hallam, J. J. Boland, J. J. Wang, J. F. Donegan, J. C. Grunlan, G. Moriarty, A. Shmeliov, R. J. Nicholls, J. M. Perkins, E. M. Grievson, K. Theuvsen, D. W. McComb, P. D. Nellist and V. Nicolosi, *Science* 331 (2011) 568-571.
- [56] a) D. Hanlon, C. Backes, T. M. Higgins, M. Hughes, A. O'Neill, P. King, N. McEvoy, G. S. Duesberg, B. Mendoza Sanchez, H. Pettersson, V. Nicolosi and J. N. Coleman, *Chem. Mater.* 26(2014) 1751-1763; b) L. Liang, K. Li, C. Xiao, S. Fan, J. Liu, W. Zhang, W. Xu, W. Tong, J. Liao, Y. Zhou, B. Ye and Y. Xie, *J. Am. Chem. Soc.* 137(2015) 3102-3108.
- [57] A. Harvey, X. He, I. J. Godwin, C. Backes, D. McAteer, N. C. Berner, N. McEvoy, A. Ferguson, A. Shmeliov, M. E. G. Lyons, V. Nicolosi, G. S. Duesberg, J. F. Donegan and J. N. Coleman, *J. Mater. Chem. A* 4 (2016) 11046-11059.

- 58] a) J. Shen, Y. He, J. Wu, C. Gao, K. Keyshar, X. Zhang, Y. Yang, M. Ye, R. Vajtai, J. Lou and P. M. Ajayan, *Nano Lett.* 15 (2015) 5449-5454; b) J. Shen, J. Wu, M. Wang, P. Dong, J. Xu, X. Li, X. Zhang, J. Yuan, X. Wang, M. Ye, R. Vajtai, J. Lou and P. M. Ajayan, *Small* 12 (2016) 2741-2749.
- [59] C. Gibaja, D. Rodriguez-San-Miguel, P. Ares, J. Gómez-Herrero, M. Varela, R. Gillen, J. Maultzsch, F. Hauke, A. Hirsch, G. Abellán and F. Zamora, *Angew. Chem. Int. Ed.* 55 (2016) 14345-14349.
- [60] a) D. Hanlon, C. Backes, E. Doherty, C. S. Cucinotta, N. C. Berner, C. Boland, K. Lee, A. Harvey, P. Lynch, Z. Gholamvand, S. Zhang, K. Wang, G. Moynihan, A. Pokle, Q. M. Ramasse, N. McEvoy, W. J. Blau, J. Wang, G. Abellan, F. Hauke, A. Hirsch, S. Sanvito, D. D. O'Regan, G. S. Duesberg, V. Nicolosi and J. N. Coleman, *Nat. Commun.* 6 (2015) 8563; b) C. Hao, B. Yang, F. Wen, J. Xiang, L. Li, W. Wang, Z. Zeng, B. Xu, Z. Zhao, Z. Liu and Y. Tian, *Adv. Mater.* 28 (2016) 3194-3201.
- [61] Y. K. Jo, J. M. Lee, S. Son, S.-J. Hwang, *J. Photochem. Photobiol. C*, 40 (2019) 150-160.
- [62] M. Osada, T. Sasaki, *Int. J. Appl. Ceram. Technol.* 9 (2012) 29-36.
- [63] B.-W. Li, M. Osada, K. Akatsuka, Y. Ebina, T. C. Ozawa, T. Sasaki, *Jpn. J. Appl. Phys.* 50 (2011) 09NA10.
- [64] K. Toda, J. Watanabe, M. Sato, *Materials Research Bulletin*, 31 (1996) 1427-1435.
- [65] T. W. Kim, E. J. Oh, S. T. Lim, D. H. Park, A. Y. Jee, M. Lee, S. H. Hyun, J. -H. Choy, S. -J. Hwang, *Chem. Eur. J.* 15 (2009) 10752-10761.
- [66] E. -J. Oh, T. W. Kim, K. M. Lee, M. -S. Song, A. -Y. Jee, S. T. Lim, H. -W. Ha M. Lee, J. -H. Choy, S. -J. Hwang, *ACS Nano* 4 (2010) 4437-4444.
- [67] M. -S. Song, K. M. Lee, Y. R. Lee, I. Y. Kim, T. W. Kim, J. L. Gunjekar, S. -J. Hwang, *J. Phys. Chem. C*, 114 (2010) 22134-22140.
- [68] T. W. Kim, S. -J. Hwang, S. H. Jhung, J. -S. Chang, H. Park, W. Choi, J. -H. Choy, *Adv. Mater.* 20 (2008) 539-542.
- [69] I. Park, Y. S. Han, J. -H. Choy, *J. Nanosci. Nanotechnol.*, 9 (2009) 7190-7194.
- [70] A. Takagaki, T. Yoshida, D. Lu, J. N. Kondo, M. Hara, K. Domen, S. Hayashi, *J. Phys. Chem. B*, 108 (2004) 11549-11555.
- [71] T. Shibata, G. Takanashi, T. Nakamura, K. Fukuda, Y. Ebina, T. Sasaki, *Energy Environ. Sci.* 4 (2011) 535-542.
- [72] T. Sasaki, M. Watanabe, Osmotic swelling to exfoliation exceptionally high degrees of hydration of a layered titanate. *J. Am. Chem. Soc.* 120 (1998) 4682-4689.
- [73] T. W. Kim, E. J. Oh, S. T. Lim, D. H. Park, A. Y. Jee, M. Lee, S. H. Hyun, J. -H. Choy, S. -J. Hwang, *Chem. Eur. J.* 15 (2009) 10752-10761.
- [74] T. Sasaki, M. Watanabe, H. Hashizume, H. Yamada, H. Nakazawa, *J. Am. Chem. Soc.* 118 (1996) 8329-8335.
- [75] M. Adachi-Pagano, C. Forano, J.-P. Besse, *Chem. Commun.*, (2000) 91-92.
- [76] B. R. Venugopal, C. Shivakumara, M. Rajamathi, *J. Colloid Interface Sci.* 294 (2006) 234-239.

- [77] T. Hibino, W. Jones, *J. Mater. Chem.*, 11 (2001) 1321–1323.
- [78] L. Li, R. Ma, Y. Ebina, N. Iyi, T. Sasaki, *Chem. Mater.* 17 (2005) 4386–4391.
- [79] R. Ma, Z. Liu, L. Li, N. Iyi, T. Sasaki, *J. Mater. Chem.* 16 (2006) 3809–3813.
- [80] M. A. Woo, M. -S. Song, T. W. Kim, I. Y. Kim, J. Y. Joo, Y. S. Lee, S. J. Kim, J. -H. Choy, S. -J. Hwang, *J. Mater. Chem.* 21 (2011) 4286–4292.
- [81] S. Jeong, D. Yoo, , J. Jang M. Kim, J. Cheo, *J. Am. Chem. Soc.* 134 (2012) 18233–18236.
- [82] G. Cunningham, M. Lotya, C. S. Cucinotta, S. Sanvito, S. D. Bergin, R. Menzel, M. S. P. Shaffer, J. N. Coleman, *ACS Nano*, 6 (2012) 3468–3480.
- [83] C. Tan, X. Cao, X.-J. Wu, Q. He, J. Yang, X. Zhang, J. Chen, W. Zhao, S. Han, G.-H. Nam, M. Sindoro and H. Zhang, *Chem. Rev.* 117 (2017) 6225–6331.
- [84] L. Niu, J. N. Coleman, H. Zhang, H. Shin, M. Chhowalla, Z. Zheng, *Small*, 12(2016) 272–293.
- [85] S. M. Oh, S. B. Patil, X. Jin, S.-J. Hwang, *Chem. Eur. J.* 24 (2018) 4757–4773.
- [86] Y. Yang, X. Liu, Z. Zhu, Y. Zhong, Y. Bando, D. Golberg, J. Yao, X. Wang, *Joule* 2 (2018) 1075–1094.
- [87] J. -M. Oh, D. -H. Park, J. -H. Choy, *Chem. Soc. Rev.* 40 (2011) 583–595.
- [88] F. Leroux, J. -P. Besse, *Chem. Mater.* 13 (2001) 3507–3515.
- [89] Z. Huang, S. Wang, J. Wang, Y. Yu, J. Wen, R. Li, *Electrochimica Acta* 152 (2015) 117–125.
- [90] T. W. Kim, H. -W. Ha, M. -J. Paek, S. -H. Hyun, J. -H. Choy, S. -J. Hwang, *J. Mater. Chem.* 20(2010) 3238–3245.
- [91] T. W. Kim, I. Y. Kim, T. S. Jung, C. H. Ko, S.-J. Hwang, *Adv. Funct. Mater.* 23 (2013) 4377–4385.
- [92] J. L. Gunjekar, I. Y. Kim, J. M. Lee, Y. K. Jo, S. J. Hwang, *J Phys Chem C* 118 (2014) 3847–3863.
- [93] J. L. Gunjekar, T. W. Kim, H. N. Kim, I. Y. Kim, S. -J. Hwang, *J. Am. Chem. Soc.* 133 (2011) 14998–15007.
- [94] J. L. Gunjekar, I. Y. Kim, J. M. Lee, N-S Lee, S-J Hwang, *Energy Environ. Sci.* 6(2013) 1008–1017.
- [95] J. L. Gunjekar, T. W. Kim, I. Y. Kim, J. M. Lee, S. -J. Hwang, *Sci. Rep.* 3(2013) 2080.
- [96] J. L. Gunjekar, I. Y. Kim S. J. Hwang *Eur J Inorg Chem.* (2015) 1198–1202.
- [97] J. M. Lee, J. L. Gunjekar, Y. Ham, I. Y. Kim, K. Domen, S. J. Hwang, *Chem Eur J* 20 (2014) 17004–17010.
- [98] J. Hu, C. Zhang, L. Jiang, H. Lin, Y. An, D. Zhou, M. K. Leung, S. Yang, 1 (2017) 383–393.
- [99] M. S. Islam, M. Kim, X. Jin, S. M. Oh, N-S Lee, H. Kim, S-J Hwang, *ACS Energy Lett.* 3 (2018) 952–960.
- [100] J. L. Gunjekar, A. I. Inamdar, B. H. Hou, S. Cha, S. M. Pawar, A. A. Talha, H. S. Chavan, J. Kim, S. Cho, S. Lee, Y. Jo, H. Kim, H. Ima, *Nanoscale* 10 (2018) 8953–8961.
- [101] S. Bose, T. Kuila, A. K. Mishra, R. Rajasekar, N. H. Kim, J. H. Lee. *J. Mater. Chem.* 22 (2012) 767–784.
- [102] J. M. Lee, E. K. Mo, S. Lee, N. S. Lee, L. Debbichi, H. Kim, S. J. Hwang, *Angew Chem Int Ed.* 55 (2016) 8546–8550.

- [103] Q. Jiang N. Kurra M. Alhabeb, Y. Gogotsi, H. N. Alshareef, *Adv Energy Mater* 8 (2018) 1703043-1703053.
- [104] S. Yuan S. Y. Pang J. Hao, *Appl Phys Rev.* 7 (2020) 21304-21330.
- [105] J. Zhu, W. Sun, D. Yang, Y. Zhang, HH. Hoon, H. Zhang, Q. Yan, *Small*, 11 (2015) 4123-4129.
- [106] G. Decher, *Science*, 277 (1997) 1232-1237.
- [107] S. Bose, T. Kuila, A.K. Mishra, R. Rajasekar, N.H. Kim, J.H. Lee, *J. Mater. Chem.* 22 (2012) 767-784.
- [108] Y. Xiang, S. Lu, S. P. Jiang, *Chem. Soc. Rev.* 41 (2012) 7291-7321.
- [109] K. K. Manga, Y. Zhou, Y. Yan, K. P. Loh, *Adv. Funct. Mater.* 19 (2009) 3638-3643.
- [110] L. Wang, T. Sasaki, Y. Ebina, K. Kurashima, M. Watanabe, *Chem. Mater.* 14 (2002) 4827-4832.
- [111] L. Wang, Y. Omomo, N. Sakai, K. Fukuda, I. Nakai, Y. Ebina, K. Takada, M. Watanabe, T. Sasaki, *Chem. Mater.*, 15 (2003) 2873-2878.
- [112] L. Li, R. Ma, Y. Ebina, K. Fukuda, K. Takada, T. Sasaki, *J. Am Chem Soc.*, 129 (2012) 8000-8007.
- [113] a) J. Matusiak, E. Grządka, *Stability of colloidal systems-a review of the stability measurements methods*, *Annales Universitatis Mariae Curie-Skłodowska Lubin-Polonia* 72 (2017) 33-45; b) ISO 13099-2:2012, *Colloidal system- methods for zeta potential determination-part 2: Optical methods*, June 2012.
- [114] NCL method PCC-2, *Measuring zeta potential of nanoparticles*, April 2008, revised November 2009.
- [115] ASTM E2865-12, *Standard guide for measurement of electrophoretic mobility and zeta potential of nanosized biological materials*, ASTM International, West Conshohocken, PA, 2012, www.astm.org.
- [116] A. A. Bunaciu, E. gabriela Udriștioiu, H. Y. Aboul-Enein, *Crit. Rev. Anal. Chem*, 45 (2015) 289-299.
- [117] B. D. Cullity, *Elements of X-rays diffraction*, 2nd edition, Addison-Wesley, London, (1978).
- [118] J. Preudhomme, P. Tarte, *Infrared studies of spinels-III: The normal II-III spinels*, *Spectrochim Acta*, 27 (1971) 1817-1835.
- [119] M. Vallikkodi, *Synthesis, Growth and characterization of piperazinium p-aminobenzoate and piperazinium p-chlorobenzoate nonlinear optical single crystals*, Alagappa University, Karaikudi, India 2018.
- [120] *Raman spectroscopy*, Advanced Physics Laboratory (2006).
- [121] https://www.nanoimages.com/sem-technology-overview/sem_img2/, FE-SEM image.
- [122] <https://www.azom.com/article.aspx?ArticleID=16146>, *Interaction electron beam with sample*.
- [123] https://commons.m.wikimedia.org/wiki/File:Scheme_TEM_en.png.
- [124] http://en.wikipedia.org/wiki/BET_theory.

- [125] <http://particle.dk/methods-analytical-laboratory/surface-area-bet/surface-area-bet-theory>.
- [126] Y. F. Shi, Y. Meng, D. H. Chen, S. J. Cheng, P. Chen, T. F. Yang, Y. Wan, D. Y. Zhao, *Adv. Funct. Mater.* 16 (2006) 561-567.
- [127] <https://epm.univie.ac.at/research/low-dimensional-quantum-solids/methods/>, X-Ray Photoemission Spectroscopy.
- [128] N. S. Padalkar, S. V. Sadavar, R. B. Shinde, A. S. Patil, U. M. Patil, D. S. Dhawale, H. M. Pathan, S. D. Sartale, V. G. Parale, A. Vinu, C. D. Lokhande, J. L. Gunjekar, *Adv. Mater. Interfaces*, 2021, 2101216.

CHAPTER-3

**Synthesis, Characterization and
Electrochemical Performance
Evaluation of Nickel-Chromium-
Layer Double Hydroxide and rGO**

CHAPTER 3

Synthesis, Characterization and Electrochemical Performance Evaluation of Nickel-Chromium-Layer Double Hydroxide and rGO

Sr. No.	Title	Page No.
3.1	Introduction	77-78
3.2	Experimental details	78-79
	3.2.1 <i>Chemicals</i>	78
	3.2.2 <i>Synthesis of Ni-Cr-LDH</i>	78-79
	3.2.3 <i>Materials characterization</i>	79
3.3	Results and discussion	80-86
	3.3.1 <i>XRD study</i>	80
	3.3.2 <i>FTIR study</i>	80-81
	3.3.3 <i>Micro-Raman study</i>	81-82
	3.3.4 <i>FESEM study</i>	82-83
	3.3.5 <i>EDS study</i>	83
	3.3.6 <i>HRTEM study</i>	83-84
	3.3.7 <i>BET surface area study</i>	84-85
	3.3.8 <i>XPS study</i>	85-86
3.4	Conclusions	86
3.5	Electrochemical performance evaluation of Ni-Cr-LDH	87-88
	3.5.1 <i>Substrate and substrate cleaning</i>	87
	3.5.2 <i>Fabrication of Ni-Cr-LDH electrode</i>	87-88
3.6	Experimental setup for electrochemical studies	88-89
3.7	Results and discussion	89-92
	3.7.1 <i>CV study</i>	89
	3.7.2 <i>GCD study</i>	89-91
	3.7.3 <i>EIS study</i>	91
	3.7.4 <i>Stability study</i>	91-92
3.8	Conclusions	92
3.9	Synthesis, characterization and electrochemical performance evaluation of reduced graphene oxide (rGO)	92-97
3.9.1	Introduction	92-93
3.9.2	Experimental details	93
	3.9.2.1 <i>Chemicals</i>	93
	3.9.2.2 <i>Synthesis of GO</i>	93
	3.9.2.3 <i>Preparation of rGO</i>	93
3.9.3	Results and discussion	93-94
	3.9.3.1 <i>XRD study</i>	93-94

3.9.4	<i>Electrochemical performance of reduced graphene oxide electrode</i>		94-97
	<i>3.9.4.1</i>	<i>CV study</i>	94-95
	<i>3.9.4.2</i>	<i>GCD study</i>	95-96
	<i>3.9.4.3</i>	<i>EIS study</i>	96
	<i>3.9.4.4</i>	<i>Stability Study</i>	97
3.10.	Conclusions		98
3.11.	References		97-100

3.1 Introduction

The recent trend in energy storage applications is designing nanohybrid materials of different materials as electrodes, in which the two different components can work in synergy to deliver high capacity, stability and performance [1-4]. In the research of EES systems, electrode materials have a direct impact on their electrochemical properties. 2D LDH have been intensively studied in recent years because of their interesting properties, such as swelling and exfoliation behavior, intrinsically charged surface, easy tunability of cations in their host layers, effective utilization of homogeneously dispersed transition metal atoms, good anion exchange ability, and environmentally friendly nature and potential applications in energy storage devices [5-9]. Several methods are available to synthesize LDHs and can be engineered with desirable physical and chemical properties for various applications [10]. Most of them, the pristine LDH solid crystal can be prepared via a simple hydrolysis reaction of metal salts, in which the coprecipitation of two different metal ions occurs at controlled pH conditions [11]. LDHs consist of positively charged brucite-like layers that are intercalated with anions and water molecules in the interlayer space. The interlayers of LDH structures consist of various anions and water molecules. The anions can be generally preferred, such as CO_3^{2-} , NO_3^- , Cl^- , and so on [12]. However, the preparation of such materials with nitrate have been found to be very difficult because of the higher affinity for CO_3^{2-} anions which are ubiquitous in solution due to the presence of CO_2 in the atmosphere as well as in distilled water [13]. In addition, carbonate possesses a smaller ionic size as compared to nitrate ions which allows them to enter the interlayer gallery space of LDH sheets easily. Also, the higher charge on carbonate ions favors the intercalation of carbonate ions which ultimately makes the LDH structure densely packed [14]. Above all, once carbonate ion enters the LDH interplanar space, it becomes highly stable and cannot be easily exfoliated. In order to avoid the above disadvantages and to promote the intercalation of the desired anions, the preferred counter ions of cation salts are the nitrates or chlorides, which possess a low affinity towards the brucite layers. For the effective exfoliation process, the nitrate form of the LDH materials is generally used because the monovalent state of nitrate ions minimizes the interlayer interaction between the LDH layers and thus facilitates the

exfoliation into individual LDH monolayers [15-17]. To avoid the carbonate species it is always desirable to use decarbonized water instead of double distilled water (DDW).

In this section, we synthesized for the first time the nitrate form of the Ni-Cr-LDH via a facile coprecipitation method. The crystal structure, crystal morphology, chemical composition, and the nature of the chemical bonding in the pristine Ni-Cr-LDH were probed with a combination of several diffractions, microscopic and spectroscopic tools. The Ni-Cr-LDH material coated on SS substrate was applied as an SC electrode to examine its electrochemical activity.

3.2 Experimental details

3.2.1 Chemicals

The chemicals for synthesis such as nickel nitrate $[\text{Ni}(\text{NO}_3)_2 \cdot 3\text{H}_2\text{O}]$, chromium nitrate $[\text{Cr}(\text{NO}_3)_3 \cdot 9\text{H}_2\text{O}]$, sodium hydroxide $[\text{NaOH}]$, sodium nitrate $[\text{NaNO}_3]$, AC, polyvinylidene fluoride [PVDF] and N-methylpyrrolidone [NMP] were purchased from Sigma Aldrich chemical co. and used without further purification. Stainless steel (SS) foil was used as a current collector substrate for the fabrication of Ni-Cr-LDH based electrochemical capacitor electrodes. To avoid contamination of carbonate anions, decarbonated water was used throughout the synthesis of Ni-Cr-LDH samples.

3.2.2 Synthesis of nickel-chromium-layered double hydroxide (Ni-Cr-LDH)

The pristine Ni-Cr- NO_3 -LDH was synthesized via facile chemical coprecipitation method according to Reichle protocol (Fig. 3.1) [18]. The pristine NO_3^{1-} intercalated Ni-Cr-LDH sample was prepared by coprecipitation reaction of solutions A and B. Solution A was prepared by mixing 100 ml of aqueous solutions of 0.2 M $\text{Ni}(\text{NO}_3)_2 \cdot 6\text{H}_2\text{O}$ and 0.1 M $\text{Cr}(\text{NO}_3)_3 \cdot 9\text{H}_2\text{O}$. Solution B was prepared by mixing aqueous solutions of 1 M NaOH and 0.3 M NaNO_3 . Then, solutions A and B were simultaneously mixed (1 ml/min) together at room temperature and the pH of the resultant precipitate was adjusted at 8 ± 0.1 by controlling the addition of solution A. Resulting slurry mixture was aged at 338 K for 3 days with vigorous stirring. All the reaction courses were carried in N_2 atmosphere. After aging, the obtained sediment was centrifuged at 6000 rpm for 10 min and washed several

times with decarbonated water. The resulting product was freeze-dried for 20 h to ensure solid powder form of Ni-Cr-NO₃-LDH.

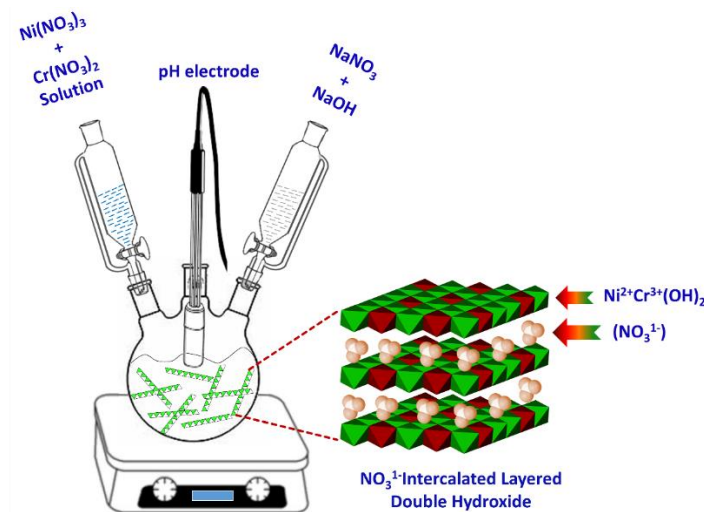


Fig. 3.1: Schematic presentation of Ni-Cr-LDH preparation by coprecipitation method.

3.2.3 Materials characterization

The powder XRD were obtained from Rigaku miniflex-600 with Cu K α ($\lambda = 0.15406$ nm) radiation, operated at 40 kV, with a scanning rate of 1° min^{-1} in the 2θ range from 5° to 70° . FTIR spectroscopy was recorded for the wavenumber range from 400 to 4000 cm^{-1} using by Alpha (II) Bruker unit and used to probe the functional groups of the present electrode. Micro-Raman spectroscopy was employed to characterize the nature of the chemical bonding in the nanohybrids using 532 nm laser excitation wavelength by 2.5 mW power and a 50 \times objective. To study the crystal morphology and layered structure of Ni-Cr-LDH, FESEM (Jeol JSM-6700F) and high-resolution transmission electron microscopy/selected area electron diffraction (HRTEM/SAED, JEOL JEM-2100F, accelerating voltage of 200 kV) techniques were used. The oxidation states of the component ions in the Ni-Cr-LDH were studied using XPS (Thermo, UK, Al K α). The N₂ adsorption-desorption isotherms of the Ni-Cr-LDH were obtained with the BET machine (BELSORP mini II, Japan). Prior to the measurement, the pore structures of the nanohybrid samples were activated at 413 K for 6 h under vacuum. The electrochemical measurements were carried out by Won Tech, ZIVE MP1 electrochemical workstation.

3.3 Results and discussion

3.3.1 XRD study

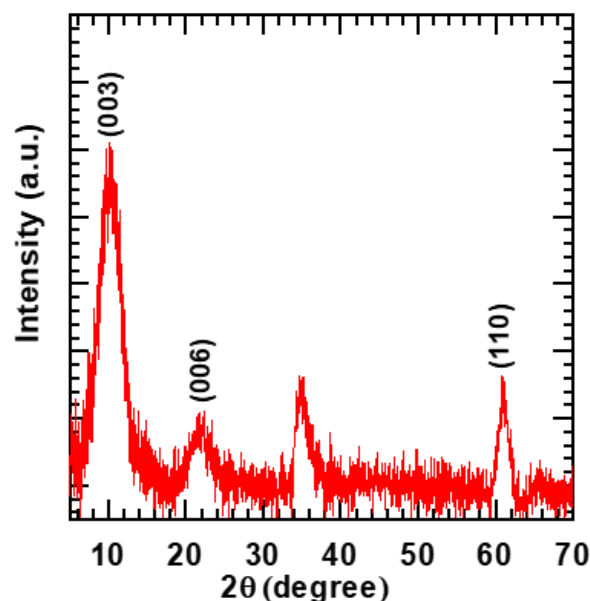


Fig. 3.2: XRD pattern of pristine Ni-Cr-LDH.

Fig. 3.2 represents the powder XRD pattern of Ni-Cr-LDH sample. The Ni-Cr-LDH display series of well-developed equally spaced ($00l$) Bragg's diffraction indicating layered hexagonal structure having R-3m rhombohedral symmetry (JCPDS 00-035-0965). The lattice parameters $a = 0.31$ nm and $c = 0.88$ nm for Ni-Cr-LDH sample are determined according to the least-squares fitting analysis, which is in good agreement with the lattice parameters of the nitrate intercalated Ni-Cr-LDH phase [14]. The crystallite size, according to Scherrer's calculation with the FWHM of (003) reflections for Ni-Cr-LDH is ~ 20 nm. Judging from the basal spacing of Ni-Cr-LDH, the gallery height of Ni-Cr-LDH is estimated as 0.40 nm. Ni-Cr-LDH sample shows an in-plane (110) peak and a broad hump at $2\theta = \sim 60.2$ and $2\theta = \sim 32$ to 44 , respectively, which are attributed to the development of in-plane hexagonal "turbostatic" crystal structure [19, 20]. These results provide strong evidence of effective synthesis of NO_3^{1-} intercalated Ni-Cr-LDH. The narrow and intense diffraction peaks demonstrated good crystallinity of Ni-Cr-LDH material which can be useful for synthesizing Ni-Cr-LDH NSs [21].

3.3.2 FTIR study

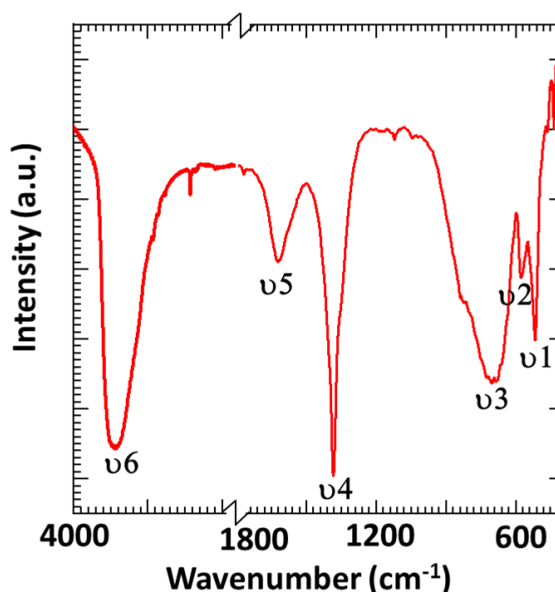


Fig. 3.3: FTIR spectrum of Ni-Cr-LDH.

The FTIR spectrum of Ni-Cr-LDH material is shown in Fig. 3.3. Ni-Cr-LDH displays the low-frequency absorption bands in $400\text{--}800\text{ cm}^{-1}$ (ν_1 (515 cm^{-1}), ν_2 (576 cm^{-1}), and ν_3 (670 cm^{-1})) that are associated with stretching and bending normal modes of metal-oxygen-hydrogen vibrations and oxygen-metal-oxygen of brucite-like Ni-Cr-LDH layers [22-24]. The strong and sharp peak at ν_4 (1384 cm^{-1}) can be assigned to the asymmetric stretching modes of NO_3^{1-} anions in the interlayer galleries of Ni-Cr-LDH [25]. The Ni-Cr-LDH shows broad bands ν_6 (3460 cm^{-1}) and sharp band ν_5 (1630 cm^{-1}) are attributed to the stretching vibration of the O-H groups and bending vibrational mode of water molecule entrapped in the Ni-Cr-LDH NSs, respectively [22, 25]. The present FTIR spectrum of Ni-Cr-LDH demonstrates distinct IR features of NO_3^{1-} anion intercalated in Ni-Cr-LDH. Also, the FTIR study confirms the structural water present in the prepared Ni-Cr-LDH.

3.3.3 Micro-Raman study

The microscopic structural bonding properties of the Ni-Cr-LDH were examined using Raman spectroscopy, as shown in Fig. 3.4. The Micro-Raman spectrum of the Ni-Cr-LDH shows the ν_1 (311 cm^{-1}) and ν_2 (464 cm^{-1}) peaks which are ascribed to the E_g and A_{1g} Raman-active vibrational modes of $\text{Ni}(\text{OH})_2$, respectively [26]. The broad and high-intensity peak ν_3 centered on 540 cm^{-1} which is attributed to the superposition of Cr-O-H bending mode of $\text{Cr}(\text{OH})_3$ at

530 cm^{-1} and second-order acoustic mode of $\text{Ni}(\text{OH})_2$ at 540 cm^{-1} [26, 27]. Moreover, Ni-Cr-LDH shows characteristic Raman bands at ν_4 (712 cm^{-1}) and ν_5 (1050 cm^{-1}) due to the symmetric stretching modes of NO_3^- anions [28]. The observation of these characteristic features underscores the intercalation of NO_3^{1-} anions in Ni-Cr-LDH interlayers.

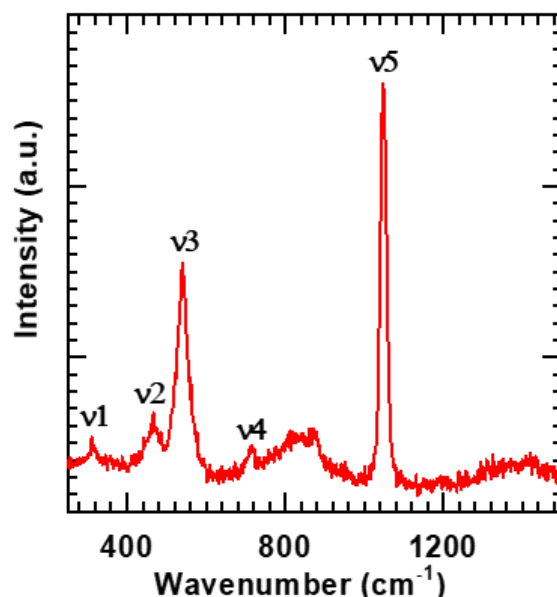


Fig. 3.4: Micro-Raman spectrum of the Ni-Cr-LDH.

3.3.4 FESEM study

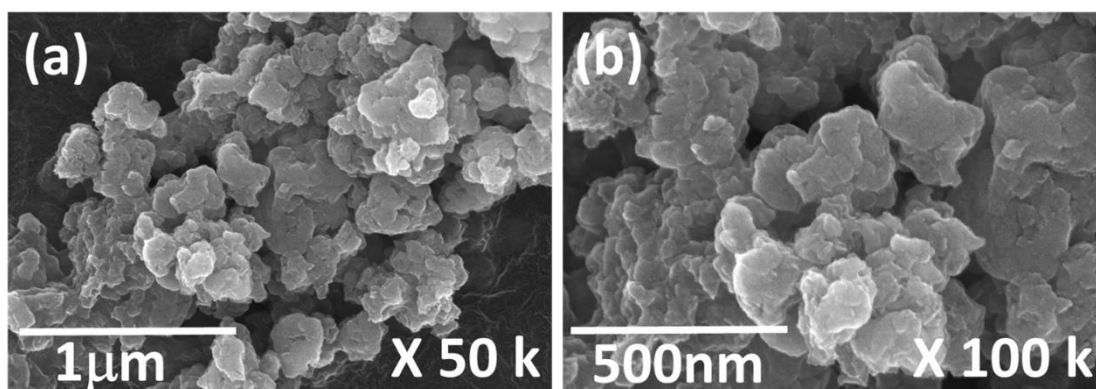


Fig. 3.5: FESEM micrographs of Ni-Cr-LDH.

The surface morphologies of the pristine Ni-Cr-LDH sample is studied using field FESEM. As displayed in Fig. 3.5 (a, b), the Ni-Cr-LDH sample displays clusters of sheets with compact morphology and negligible porosity. A careful topographical examination of micrographs at high magnification discloses that the average crystal size of the Ni-Cr-LDH sample is ~ 180 nm. Such a coarse particle

topography is common for co-precipitated hydroxide materials [17, 29-31]. The densely compact type of morphology is commonly observable for the pristine LDH materials synthesized by the coprecipitation method of 2D inorganic NSs [14].

3.3.5 EDS study

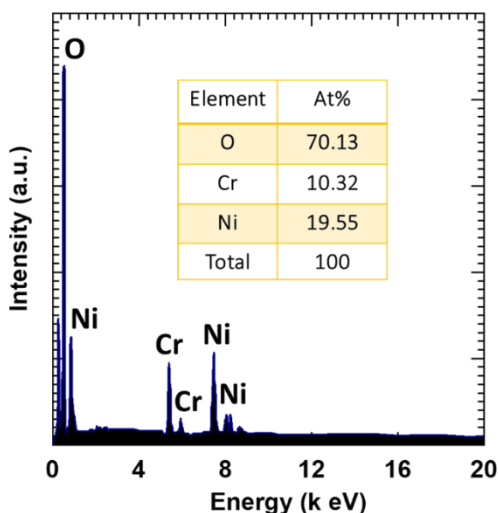


Fig. 3.6: The EDS spectrum of Ni-Cr-LDH.

The chemical composition of Ni-Cr-LDH is investigated by EDS and presented in Fig. 3.6. The EDS spectra confirm the presence of Ni, Cr, and O elements in a material without any other impurity. The observed Ni:Cr atomic ratio of 1.9:1 for pristine Ni-Cr-LDH is well matched experimental chemical compositions.

3.3.6 HRTEM study

The localized nanostructure, morphology, crystal shape and crystal structure of the pristine Ni-Cr-LDH were examined by the TEM, HRTEM, and the SAED analyses. As illustrated in Fig. 3.7 a and b, at a low magnification, the TEM images of pristine Ni-Cr-LDH show the aggregated plate-shaped dense clusters with lateral sizes ranging between 150 to 400 nm. As shown in Fig. 3.7 c and d, at a high resolution, the top-view HRTEM images demonstrate the set of equidistant lines separated by a spacing of 0.15 nm that are well-matched with (110) in-plane lattice fringes of Ni-Cr-LDH. These values are in good agreement with the lattice distances determined from the XRD analysis. The crystal structure of Ni-Cr-LDH is further confirmed using SAED analysis. The SAED pattern of Ni-Cr-LDH (Fig. 3.8) shows diffused diffraction rings which confirm the nanocrystalline nature [32, 33].

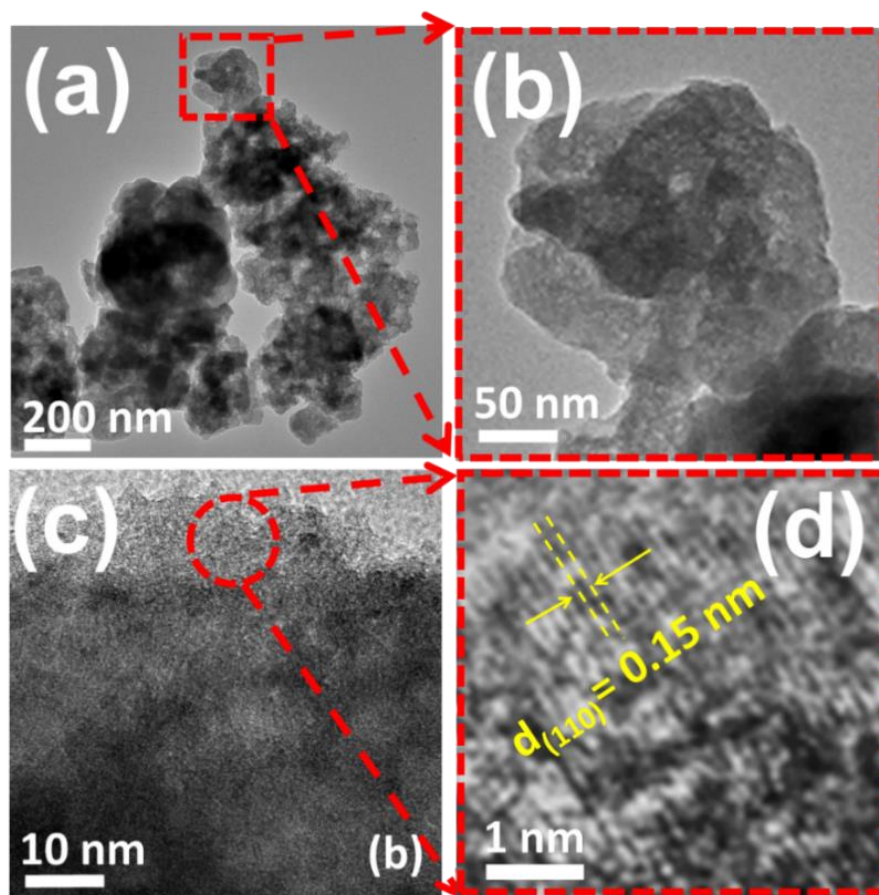


Fig. 3.7: (a, b) TEM and (c, d) HRTEM images of Ni-Cr-LDH.

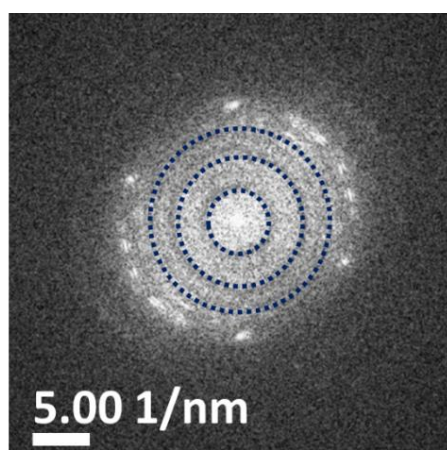


Fig. 3.8: SAED pattern of Ni-Cr-LDH.

3.3.7 Surface area analysis

The specific surface area and pore size distribution of the Ni-Cr-LDH sample was probed by N_2 adsorption-desorption analysis. Ni-Cr-LDH display specific surface areas of $14 \text{ m}^2 \text{ g}^{-1}$. As shown in Fig. 3.9, a hysteresis loop was not observed

in pristine Ni-Cr-LDH at $pp_0^{-1} > 0.45$, indicating the nonporous structure. The Ni-Cr-LDH shows a type-III isotherm, which is characteristic of nonporous, or possibly microporous materials [34]. According to the BJH method, the pore size distribution of the Ni-Cr-LDH shows wide distribution of the pores with an average diameter of 33 nm (shown in Fig. 3.9b). The obtained surface area for the Ni-Cr-LDH sample is comparable with the earlier LDH reports [35, 36]. For instance, Gunjekar et al. [37] obtained a specific surface area of $15 \text{ m}^2 \text{ g}^{-1}$ for Zn-Cr-LDH sample. BET result concluded that the pristine Ni-Cr-LDH is a nonporous structure.

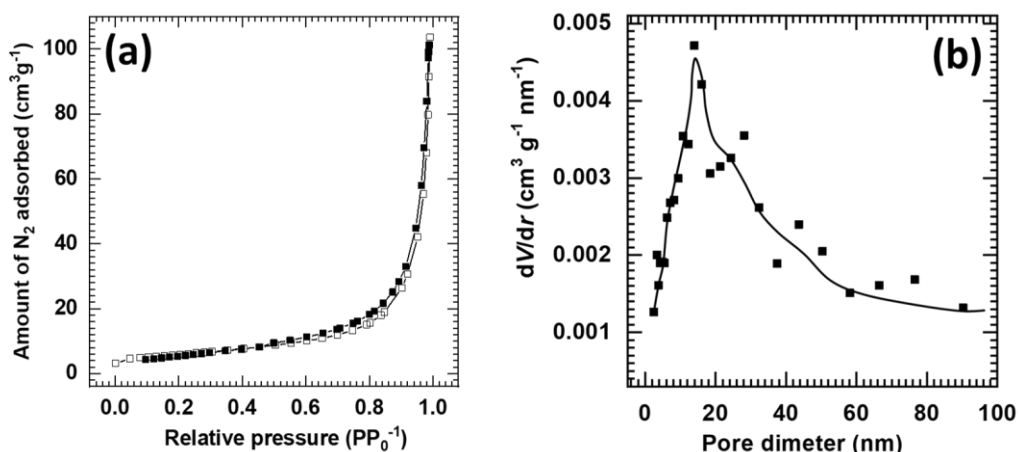


Fig. 3.9: (a) N_2 adsorption-desorption isotherms and (b) pore size distribution plots of the Ni-Cr-LDH.

3.3.8 XPS study

The chemical environment and valence state of the elements in the Ni-Cr-LDH were investigated by XPS analysis. The survey spectrum of XPS for sample Ni-Cr-LDH is shown in Fig. 3.10 (a). The survey spectrum confirms Ni, Cr, and O elements are present in the Ni-Cr-LDH. The Ni 2p spectrum in Fig. 3.10 (b) is fitted for two intense peaks at the binding energies of Ni 2p_{3/2} at 879.34 eV and Ni 2p_{1/2} at 855.9 eV along with two satellite peaks at 879.7 eV and 861.6 eV, respectively, which indicate Ni^{2+} oxidation state [38]. Fig. 3.10 (c) shows a high-resolution XPS spectrum of Cr 2p region, the two broad peak at 577.3 eV and 587 eV belong to spin-orbit splitting into Cr 2p_{1/2} and Cr 2p_{3/2}, respectively, indicating the trivalent oxidation state of the Cr [39]. Further, Fig. 3.10 (d) exhibits XPS spectrum of O 1s, the fitted peaks located at binding energies of 531.4 eV and 530.4 are assigned to the metal-oxygen species and OH group in Ni-Cr-LDH sample, respectively [40]. The XPS study highlighted divalent Ni and trivalent Cr states in Ni-Cr-LDH crystal.

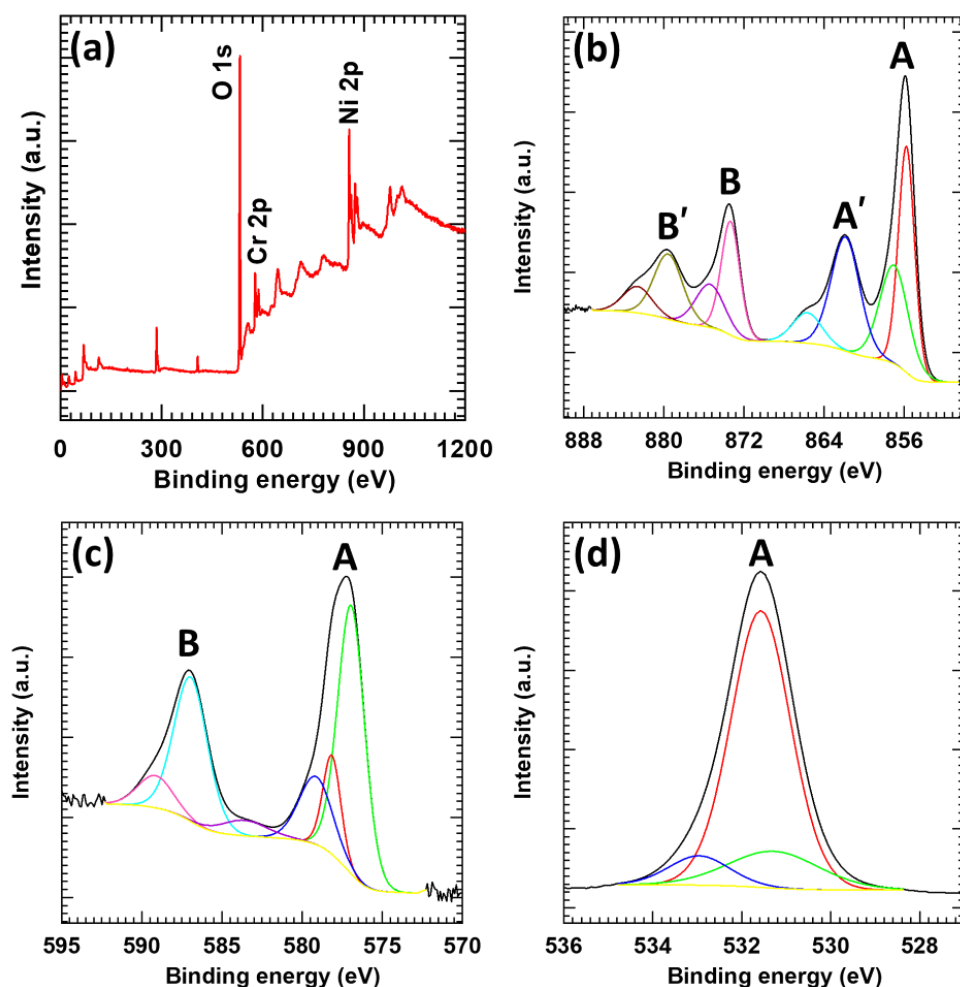


Fig. 3.10: (a) Survey, (b) Ni 2p, (c) Cr 2p and (d) O 1s XPS spectra of Ni-Cr-LDH.

3.4 Conclusions

In summary, pristine Ni-Cr-LDH was successfully prepared by a simple chemical coprecipitation method. PXRD analysis confirmed the successful formation of Ni-Cr-LDH. FTIR and Micro-Raman result confirmed presence of intercalated NO_3^{1-} ions in Ni-Cr-LDH. Surface morphological study revealed the compact sheet like structure. BET surface area analysis study indicates the nonporous structure of the Ni-Cr-LDH sample. The XPS analysis showed Ni, Cr and O elemental oxidation states. Also, the chemical composition (molar ratio of Ni and Cr element) of Ni-Cr-LDH was confirmed using EDS analysis. The above results complement each other and confirm the successful preparation of Ni-Cr-LDH material in nitrate form.

3.5 Electrochemical performance evaluation of Ni-Cr-LDH

3.5.1 Substrate and substrate cleaning

It is known that a good surface roughness helps the active material uniform coating on the substrate. Also, mechanical flexibility, high porosity, excellent conductivity, and high surface area of support substrates effectively increase the performances of the electrochemical device. Different substrates such as SS, carbon cloth, carbon-based paper, Ti foil, graphene sponge, NF, indium doped tin oxide, fluorine-doped tin oxide coated substrate, etc. act as a conductive backbone to support the active materials in SCs. In this investigation, SS substrate is employed as a current collector for loading active electrode material since SS substrate offers a 2D surface for coating material and does not participate in an electrochemical reaction.

Therefore, the SS substrate is suitable for electrochemical capacitor by the reason of its low cost, high conductivity, highly chemical stability (in KOH electrolyte). The 304 grade SS of dimension 5 X 1 cm² have been used as the substrates. The SS substrates were cleaned according to the following procedure;

- i] The SS substrate was mirror-polished using 1600 grade polish paper.
- ii] After that, substrates were ultrasonically cleaned in DDW for 15 min, and
- iii] Finally, the substrates were dried, degreased in AR grade ethanol, and were used for electrode fabrication.

3.5.2 Fabrication of Ni-Cr-LDH electrode

The electrochemical properties of the Ni-Cr-LDH electrode were investigated using a three-electrode electrochemical cell in 2 M KOH electrolyte solution. The working electrodes were prepared by mixing the as-synthesized Ni-Cr-LDH material, acetylene black (AB), and PVDF with the weight ratio of 80:15:5 in NMP to make a homogeneous slurry. The prepared slurry was uniformly painted on a well-polished SS substrate (1 × 1 cm²) and vacuum dried at 353 K for 10 h. The pristine Ni-Cr-LDH coated on SS substrate was directly used for further characterization. Photograph of Ni-Cr-LDH electrode is shown in Fig. 3.11



Fig. 3.11: Photograph of Ni-Cr-LDH electrode.

3.6 Experimental setup for electrochemical study

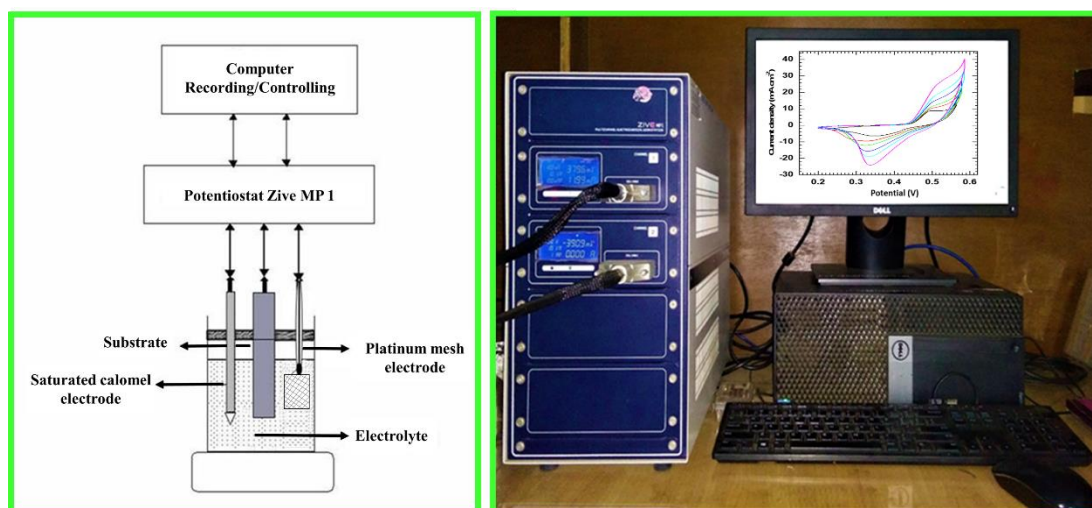


Fig. 3.12: (Left) schematic experimental setup for recording electrochemical study, (right) photograph of the electrochemical workstation.

Electrochemical analyses were conducted in the three-electrode configuration at room temperature. The Ni-Cr-LDH active material coated on SS strip (1 cm^2 area) and the platinum mesh were used as working and counter electrodes, respectively, and Hg/HgO was used as a reference electrode. The experiment setup for the electrochemical performance evaluation is shown in Fig. 3.12. The electrochemical studies are carried out using the ZIVE MP1 workstation. The electrochemical properties were measured by CV, GCD, and EIS techniques in aqueous 2M KOH electrolytes. CV is a powerful technique for deciding redox potentials and the types of redox reactions. Further, the GCD technique was used to calculate the electrochemical performance of electrode material in terms of

specific capacity, ED and PD of electrode. The electrochemical performance was calculated from GCD profile using the equation 2.9, 2.10, 2.11 and 2.12 .

3.7 Results and discussion

3.7.1 CV study

The CV curves of the NO_3^{1-} intercalated Ni-Cr-LDH electrode at different scan rates (4, 6, 8, 10, 15 and 20 mV s^{-1}) within a potential window of +0.2 to +0.6 V vs Hg/HgO are shown in Fig. 3.13. The tested electrodes showed pairs of redox peaks, suggesting the electrochemical charge storage involving both capacitive and diffusion-controlled battery-type of charge storage. The redox peaks are discernible between +0.45 to +0.55 V for the Ni-Cr-LDH. These redox peaks correspond to the following redox reaction,

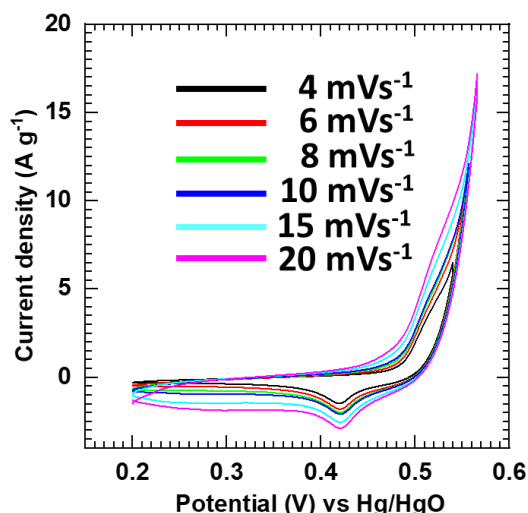
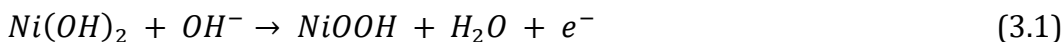


Fig. 3.13: The CV plots of Ni-Cr-LDH sample at a different scan rate of 4 to 20 mV s^{-1} .

The area under peak CV curves increases with scan rate indicating its hybrid behavior [44]. The observed asymmetry in area of oxidation and reduction in CV curves at high scan rate is a common phenomenon for LDH-based electrodes [45-49]. Present electrochemical behavior clearly highlight Ni-Cr-LDH electrodes as the potential electrode in HSC as a battery-type electrode [50,51].

3.7.2 GCD study

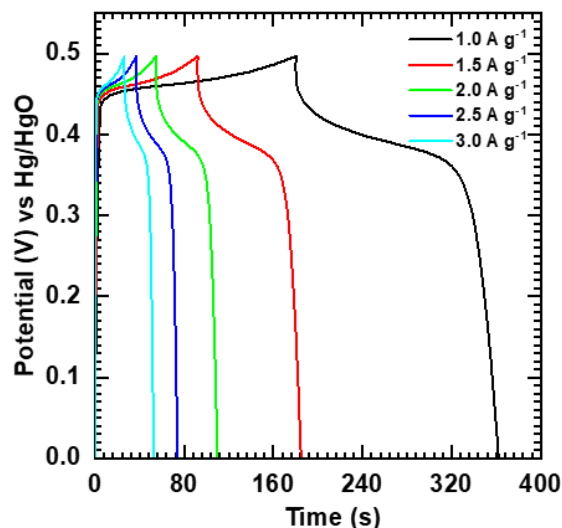


Fig. 3.14: The GCD curves of Ni-Cr-LDH at 1 to 3 A g⁻¹ current density.

The specific capacity of Ni-Cr-LDH electrodes was determined by the GCD technique. The corresponding GCD curves of Ni-Cr-LDH electrodes at different current densities (1 to 3 A g⁻¹), in a potential range of 0.0 to +0.5 V vs Hg/HgO (in 2M KOH electrolyte) are shown in Fig. 3.14. The non-linear behaviour including IR drop and prolonged voltage plateau of the GCD curves reveal the battery-type charge storage mechanism of the Ni-Cr-LDH electrode [52]. The specific capacity of the Ni-Cr-LDH electrode is determined from the GCD plots according to equation 2.9 are 356, 273, 216, 185, 156 C g⁻¹ at 1, 1.5, 2, 2.5 and 3 A g⁻¹ current density respectively. The calculated specific capacity values at different current densities are displayed in Fig. 3.15.

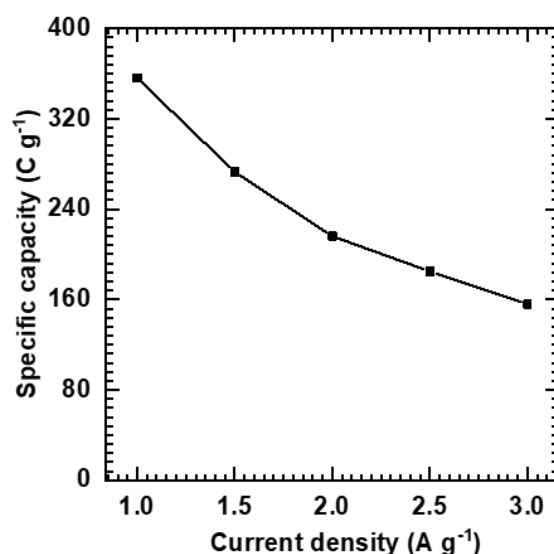


Fig. 3.15: The specific capacity of Ni-Cr-LDH at various current densities (1-3 A g⁻¹).

Moreover, the small potential drop in all the GCD curves observed for Ni-Cr-LDH electrode due to ESR. The GCD curves exhibit an increasing IR drop with increasing current density, which means the electrolyte ions could not fully access the active sites of the electrode materials during the electrochemical process. The decreasing trend of capacity with increasing GCD rate underlines that the inner electrode material is not utilized at a higher GCD rate.

3.7.3 EIS study

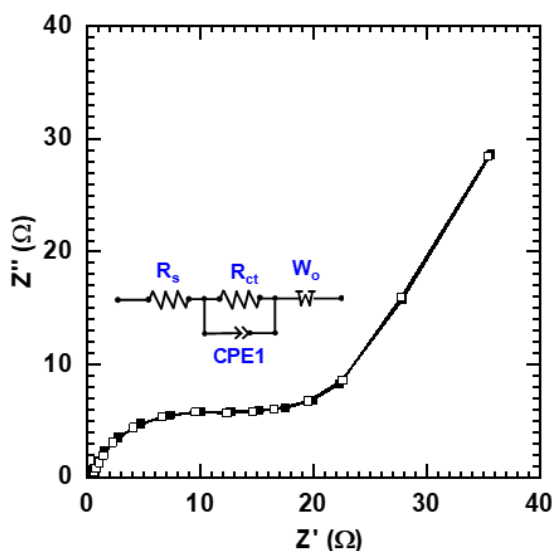


Fig. 3.16: Nyquist plot of Ni-Cr-LDH sample (Inset: fitted equivalent circuit).

The electrical conductivity was further investigated by EIS analysis and presented in Fig. 3.16. The EIS study was carried in the range of 10 mHz to 1MHz with an auternating current amplitude of 10 mV at open circuit potential. The electrochemical impedance spectral data is fitted with an equivalent electronic circuit which is shown in inset of Fig. 3.16. In these circuit, R_s is a solution (electrolyte) resistance, R_{ct} is a charge transfer resistance, W_o is a Warburg resistance of electrolytic ions, and CPE is a constant phase element to account for the capacitance [53, 54]. In the Nyquist plot, a vertical line appears in the low-frequency region and a semicircle appears in the high-frequency region. From fitting analysis, the values of R_s and R_{ct} are 0.36 Ω and 14 Ω , respectively. The low R_s and R_{ct} are attributed to the compatibility between the Ni-Cr-LDH electrode and KOH electrolyte.

3.7.4 Stability study

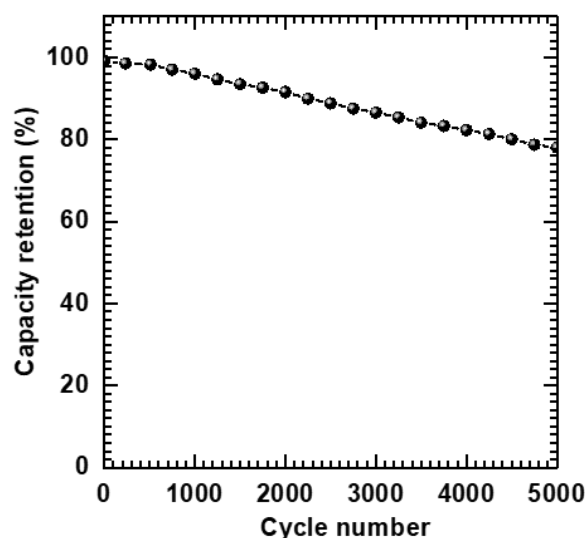


Fig. 3.17: The GCD stability graph of Ni-Cr-LDH electrode for 5000 cycles.

Another important requirement for electrochemical capacitor application is the long-term cyclic stability of the electrode material. Fig. 3.17 shows the cyclic stability of the Ni-Cr-LDH sample at 5 A g^{-1} current density within +0.0 to +0.5V. The Ni-Cr-LDH electrode shows excellent cyclic performance with 78% capacitance retention of over 5000 GCD cycles.

3.8 Conclusions

The electrochemical properties of Ni-Cr-LDH electrodes are investigated in 2 M KOH solution. The maximum specific capacity of 356 C g^{-1} at 1 A g^{-1} current density with capacity retention of 78 % (5000 GCD cycles) is observed for Ni-Cr-LDH electrodes. The low electrochemical performance of the Ni-Cr-LDH material is assigned to the compact nonporous plate-like morphology and limited gallery height.

3.9 Synthesis, characterization and electrochemical performance evaluation of reduced graphene oxide

3.9.1 Introduction

In recent, different types of carbon materials have been employed as a negative (anode) electrode for HSC and which include AC [52] carbon nanotubes (CNTs) [53] and rGO [54]. The carbon-based negative electrodes are used to make HSC devices because of their high PD, excellent electrical conductivity, strong

mechanical properties and good cycling stability [55, 56]. Among these materials, rGO provides the high specific surface area with high electric conductivity, strong mechanical strength, and good chemical stability [57, 58].

3.9.2 Experimental details

3.9.2.1 Chemicals

Graphite flakes, sodium nitrate (NaNO_3), were purchased from Sigma-Aldrich. Also, hydrogen peroxide (H_2O_2) and potassium hydroxide (KOH) were purchased from Alfa-Aesar. Sulfuric acid (H_2SO_4), potassium permanganate (KMnO_4) were purchased from Thomas baker. All the chemicals were AR grade and used without further purification.

3.9.2.2 Synthesis of graphene oxide

Modified Hummers approach was used to synthesize GO powder [59]. A mixed solution of 2.5 g of NaNO_3 and 120 ml H_2SO_4 was prepared first and then 5 g of graphite flakes were added with constant stirring. Then the mixture was put in an ice bath and 15 g of KMnO_4 was slowly added to it. Afterward, DDW (150 mL) and H_2O_2 (3mL) were slowly added to the mixture. To remove unwanted metal ions, the prepared solution was centrifuged, washed with 50 ml HCL and 500 ml DDW for several times. Further, the precipitate was washed with sufficient DDW to adjust pH nearly between 6 to 7. Finally, brownish sediment was collected and dried under a vacuum drying.

3.9.2.3 Preparation reduced graphene oxide

For the preparation of rGO, the well-dispersed 100 ml GO solution (8 mg ml^{-1}) was heated in the hydrothermal autoclave at 423K for 12h. The prepared rGO material was cooled using liquid nitrogen for solidification and freeze-dried for 60 h. Finally, the rGO foam was obtained and crushed into powder. Then, the slurry coating technique already mentioned (section 3.5.2) is followed to prepare rGO electrode (anode).

3.9.3 Results and discussion

3.9.3.1 XRD study

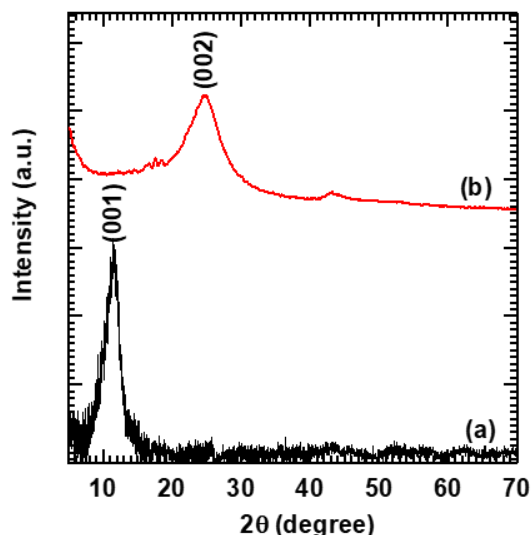


Fig. 3.18: Powder XRD patterns of (a) GO and (b) rGO.

The powder XRD patterns of (a) rGO and (b) GO are shown in Fig. 3.18. The intense characteristic peak at 11.2° corresponds to the (001) plane of GO confirming the successful preparation of GO [60]. The broad peak at 24.9° corresponds to the (002) plane observed in the XRD pattern of rGO, confirms the stacking of GO sheets due to the removal of oxygen-containing groups, and indicates the formation of multilayered rGO NSs [61]. A change in 2θ from 11.2 to 24.9° confirms the successful reduction of GO NSs to rGO nanostructure.

3.9.4 Electrochemical performance of reduced graphene oxide electrode

3.9.4.1 CV study

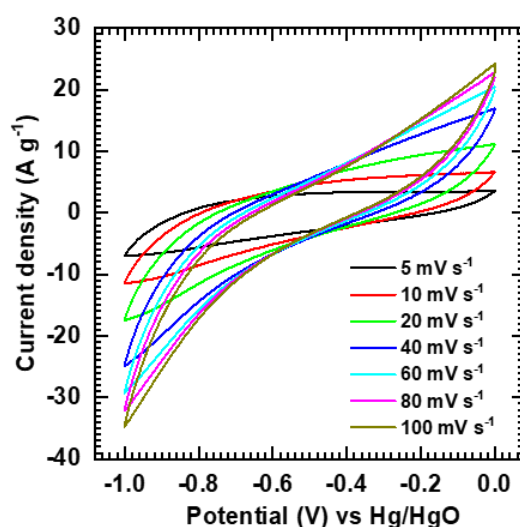


Fig. 3.19: The CV curves of rGO electrode at various scan rates.

The CV curves of rGO negative electrode within the potential range of 0 to –1.0 V vs Hg/HgO at different scan rates (5-100 mV s^{-1}) in 2.0 M KOH are shown in Fig. 3.19. The area under the CV curve increases with an increase in scan rate. The quasi-rectangular shape of CV curves confirms EDLC based capacitive behavior of the rGO electrode. Also, a large and symmetric current response in anodic and cathodic direction is observed, which represents EDLC capacitive behavior of rGO material.

3.9.4.2 GCD study

GCD plots of rGO electrode tested at current density 3 to 8 A g^{-1} in a potential window 0 to –1.0 V vs Hg/HgO and shown in Fig. 3.20. The nearly linear charge-discharge curves are obtained for rGO electrode, which shows its EDLC behavior. The maximum C_s of rGO electrode is found to be 258 F g^{-1} at 3 A g^{-1} and it decreased up to 104 F g^{-1} at 8 A g^{-1} , as shown in Fig. 3.21. The rGO displays the maximum C_s of 258 F g^{-1} (at 3 A g^{-1}), which is attributed to the more conducting channels for the charge transportation.

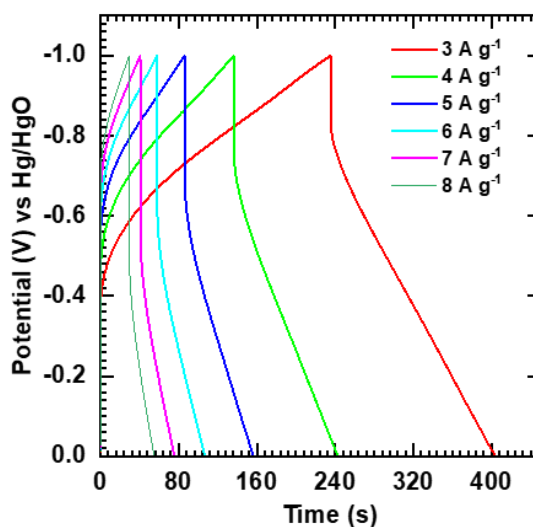


Fig. 3.20: The GCD curves of rGO electrode at various current densities (3–8 A g^{-1}).

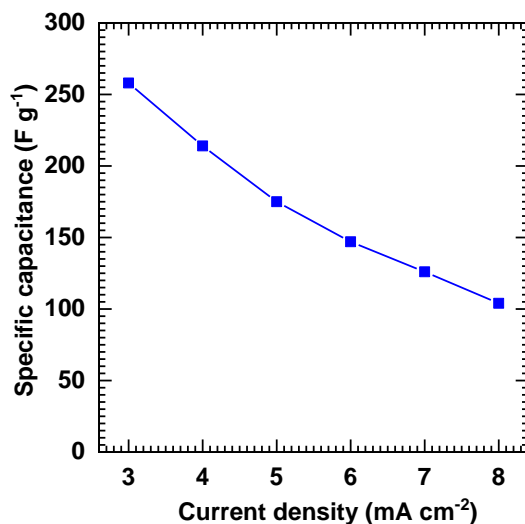


Fig. 3.21: The plot of C_s of rGO electrode at different current densities.

3.9.4.3 EIS study

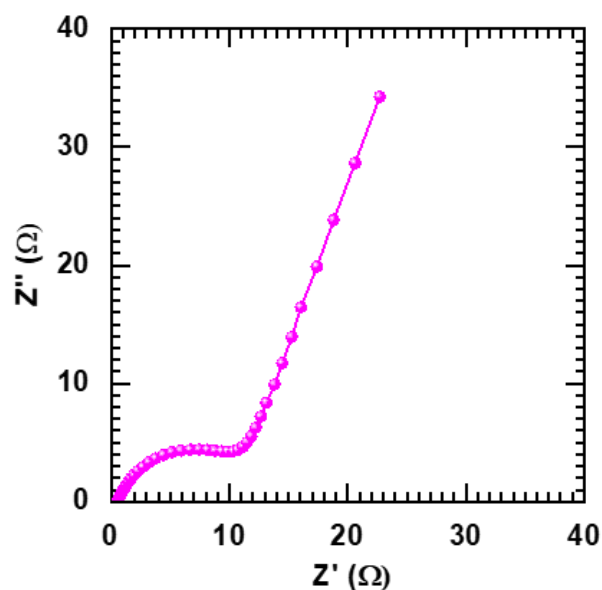


Fig. 3.22: Nyquist plot of rGO electrode.

Further, the EIS study of rGO electrode was performed to examine its electrochemical activity and conductivity. The Nyquist plot of the rGO electrode is depicted in Fig. 3.22. The R_s and R_{ct} of the rGO electrode calculated from the EIS result are 0.54Ω and 11.44Ω , respectively. The low values of R_s and R_{ct} indicate the high electrical conductivity and fast charge transfer kinetics of the rGO electrode in 2M KOH electrolyte.

3.9.4.4 Stability study

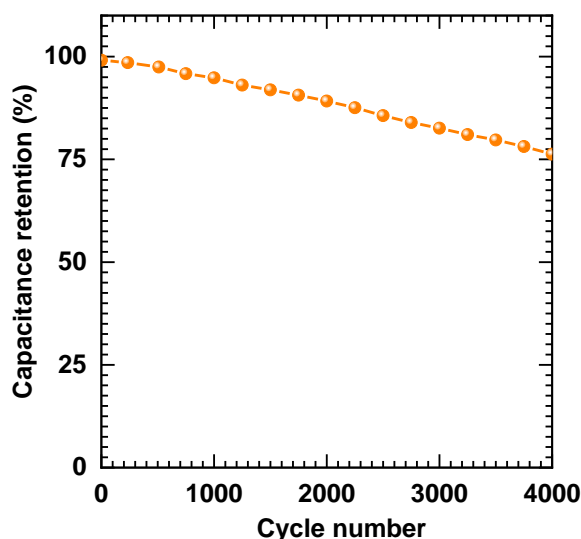


Fig. 3.23: Capacitance retention of rGO electrode at 5 A g⁻¹.

The electrochemical stability (in terms of capacitive retention) of rGO electrode tested by GCD analysis for 4000 cycles at 5 A g⁻¹ current density. As shown in Fig. 3.23, the rGO electrode shows 76 % capacitive retention after 4000 cycles. Moreover, the observed decrease in capacitance may be due to the depletion of minute active material during cycling.

3.10 Conclusions

In summary, rGO NSs were prepared via a modified Hummer's method followed by hydrothermal treatment. The reduction of GO to rGO was confirmed by XRD analyses. The rGO electrode showed excellent electrochemical performance with a maximum specific capacitance of 258 F g⁻¹ at a current density of 3 A g⁻¹. Also, it exhibited good cycling stability (76 %) over 4000 GCD cycles. The results suggested that rGO electrode is a promising candidate (anode) for HSC application.

3.11 References

- [1] M. Liang and L. Zhi, J. Mater. Chem. 19 (2009) 5871-5878.
- [2] G. Wang, L. Zhang, J. Zhang, Chem. Soc. Rev. 41 (2012) 797-828
- [3] Q. Wang, D. O'Hare, Chem. Rev. 112 (2012) 4124-4155.
- [4] L. Cao, F. Xu, Y-Y. Liang, H-L. Li, Adv. Mater. 16 (2004) 1853-1857.

- [5] K. S. Novoselov, A. K. Geim, S. V. Morozov, D. Jiang, M. I. Katsnelson, I. V. Grigorieva, S. V. Dubonos, A. A. Firsov, *Nature* 438 (2005) 197-200.
- [6] X. S. Zhou, L. J. Wan, Y. G. Guo, *Chem. Commun.* 49 (2013) 1838-1840.
- [7] X. Long, Z. Wang, S. Xiao, Y. An, S. Yang, *Mater. Today* 19 (2016) 213-226.
- [8] X. Li, D. Du, Y. Zhang, W. Xing, Q. Xue and Z. Yan, *J. Mater. Chem. A* 5 (2017) 15460-15485.
- [9] X. Deng, J. Huang, H. Wan, F. Chen, Y. Lin, X. Xua, R. Ma, T. Sasaki, *J. Energy Chem.* 32 (2019) 93-104.
- [10] T. L. P. Galvão, C. S. Neves, A. P. F. Caetano, F. Maia D. Mata, E. Malheiro, M. J. Ferreira, A. C. Bastos, A. N. Salak, J. R. B. Gomes, J. Tedim, M. G. S. Ferreira, *J. Colloid Interface Sci.* 468 (2016) 86-94.
- [11] T. W. Kim, E. J. Oh, S. T. Lim, D. H. Park, A. Y. Jee, M. Lee, S. H. Hyun, J. -H. Choy, S. -J. Hwang, *Chem. Eur. J.* 15(2009) 10752-10761.
- [12] V. Rives, *Layered double hydroxides: present and future*, nova sciences publications, Huntington, N.Y, 2001 ISBN: 1-59033-060-9.
- [13] J. Olanrewaju, B. L. Newalkar, C. Mancino, S. Komarneni, *Materials Letters* 45 (2000) 307-310.
- [14] A. S. Patil, J. L. Gunjekar, C. D. Lokhande, U. M. Patil, S. V. Sadavar, N. S. Padalkar, R. B. Shinde, M. M. Wagha, J. S. Bagi, *Synth. Met.* 264 (2020) 1-9.
- [15] R. Ma, Z. Liu, L. Li, N. Iyi, T. Sasaki, *J. Mater. Chem.* 16 (2006) 3809-3813.
- [16] L. Li, R. Ma, Y. Ebina, N. Iyi, T. Sasaki, *Chem. Mater.* 17(2005) 4386-4391.
- [17] M. A. Woo, M. -S. Song, T. W. Kim, I. Y. Kim, J. Y. Joo, Y. S. Lee, S. J. Kim, J. -H. Choy, S. -J. Hwang, *J. Mater. Chem.* 21 (2011) 4286-4292.
- [18] W.T. Reichle, *Solid State Ion.* 22 (1986) 135-141.
- [19] R. Ma, Z. Liu, L. Li, N. Iyi, T. Sasaki, *J. Mater. Chem.* 16 (2006) 3809-3813.
- [20] Z. Liu, R. Ma, Y. Ebina, N. Iyi, K. Takada, T. Sasaki, *Langmuir* 23 (2007) 861-867.
- [21] C. Wang, L. Yin, D. Xiang, Y. Qi, *ACS Appl. Mater. Interfaces* 4 (2012) 1636-1642.
- [22] S. Xia, T. Dai, Y. Meng, X. Zhou, G. Pan, X. Zhange, Z. Ni, *Phys. Chem. Chem. Phys.* 22 (2020) 12630-12643.
- [23] N. Baliarsingh, L. Mohapatra, K. Parida, *J. Mater. Chem. A* 1 (2013) 4236-4243.
- [24] R. A. Nyquist, R. O. Kagel, *Infrared spectra of inorganic compounds (3800-450cm⁻¹)*, Academic Press, New York, 1971.
- [25] L. Zhang, J. Wang, J. Zhu, X. Zhang, K. S. Huib, K. N. Huic, *J. Mater. Chem. A* 1 (2013) 9046-9053.
- [26] J. L. Gunjekar, A. I. Inamdar, B. Hou, S. Cha, S. M. Pawar, A. A. Abu Talha, H. S. Chavan, J. Kim, S. Cho, S. Lee, Y. Jo, H. Kim, H. Im, *Nanoscale* 10 (2018) 8953-8961.
- [27] L. Zhang, J. Wang, J. Zhu, X. Zhang, K. S. Huib, K. N. Huic, *J. Mater. Chem. A* 1 (2013) 9046-9053.
- [28] A. S. O. Gomes, N. Yaghini, A. Martinelli, E. J. Ahlberg, *J. Raman Spectrosc.* 48 (2017) 1256-126.

- [29] M. Shao, R. Zhang, Z. Li, M. Wei, D.G. Evans, X. Duan, *Chem. Commun.* 51 (2015) 15880-15893.
- [30] S. Ziegenheim, G. Varga, M. Szabados, P. Sipos, I. Palinko, *Chem. Pap.* 72 (2018) 897-902.
- [31] G. R. Williams, A. Clout, J. C. Burlay, *Phys. Chem. Chem. Phys.* 15 (2013) 8616-8628.
- [32] S. Mulkapuri, S. K. Kurapati, S. Mukhopadhyay, S. K. Das, *New J. Chem.* 43 (2019) 17670-17679.
- [33] M. Aureliano, C. A. Ohlin, M. O. Vieira, M. P. M. Marques, W. H. Casey, L. A. E. B. de Carvalho, *Dalton Trans.* 45 (2016) 7391-7399.
- [34] J. B. Condon, *Surface area and porosity determinations by physisorption: measurements and theory*, 1st ed. Elsevier, 2006, p 274.
- [35] M. Z. b. Hussein, T. K. Hwa, *J. Nanoparticle Res.* 2 (2000) 293-298.
- [36] S. Wang, T. Wang, X. Wang, Q. Deng, J. Yang, Y. Mao, G. Wang, *Int. J. Hydrog. Energy* 45 (2020) 12629-12640.
- [37] J. L. Gunjekar, T. W. Kim, H. N. Kim, I. Y. Kim, S-J. Hwang, *J. Am. Chem. Soc.* 133 (2011) 14998-15007.
- [38] W. Ye, X. Fang, X. Chen, D. Yan, *Nanoscale* 10 (2018) 19484-19491.
- [39] Y. Yang, L. Dang, M. J. Shearer, H. Sheng, W. Li, J. Chen, P. Xiao, Y. Zhang, R. J. Hamers, S. Jin, *Adv. Energy Mater* 8 (2018) 1-9.
- [40] T. Zhou, Z. Cao, P. Zhang, H. Ma, Z. Gao, H. Wang, Y. Lu, J. He, Y. Zhao, *Sci. Rep.* 7 (2017) 1-9.
- [41] S. J. Marje, P. K. Katkra, S. S. Pujari, S. A. Khalate, A. C. Lokhande, U. M. Patil, *Synth. Met.* 259 (2020) 1-11.
- [42] X. Guo, X. Liu, X. Hao, S. Zhu, F. Dong, Z. Wen, Y. Zhang, *Electrochim. Acta* 194 (2016) 17-186.
- [43] Z. Diao, Y. Zhang, X. Hao, Z. Wen, *Ceram. Int.* 40 (2014) 2115-2120.
- [44] Z. Jiang, Z. Li, Z. Qin, H. Sun, X. Jiao, D. Chen, *Nanoscale* 23 (2013) 11770-11775.
- [45] S. Li, P. Cheng, J. Luo, D. Zhou, W. Xu, J. Li, R. Li, D. Yuan, *Nano-Micro Lett.* 9 (2017) 1-10.
- [46] X. Liu, C. Wang, Y. Dou, A. Zhou, T. Pan, J. Han, M. Wei, *J. Mater. Chem. A* 6 (2014) 1682-1684.
- [47] A. Balducci, D. Belanger, T. Brousse, J. W. Long, W. Sugimoto, *J. Electrochem. Soc.* 164 (2017) A1487-A1488.
- [48] T. Brousse, D. Belanger, J.W. Long, *J. Electrochem. Soc.* 162 (2015) A5185-A5189.
- [49] H.Tian, K. Zhu, W. Li L. Wang, Z. Yu, Y. Lai, Y. He, *Electrochimica Acta* 377 (2021) 138087.
- [50] A. Paravannoor, S. V. Nair, P. Pattathil, M. Manca, A. Balakrishnan, *Chem. Commun.* 51 (2015) 6092-6095.
- [51] S. Hassan, M. Suzuki, S. Mori, A. A. El-Moneim, *RSC Adv.* 4 (2014) 20479-20488.
- [52] S. Subhadarshini, E. Pavitra, G. S. R. Raju, N. R. Chodankar, D. K. Goswami, Y-K. Han, Y. S. Huh, N. C. Das, *ACS Appl. Mater. Interfaces* 12 (2020), 29302-29315.

- [53] D. P. Dubal, N. R. Chodankar, Z. C. Huertas, F. Wolfart, M. Vidotti, R. Holze, C. D. Lokhande, P. G. Romero, J. Power Sources 308 (2016) 158-165.
- [54] P. K. Katkar, S. J. Marje, V. G. Parale, C. D. Lokhande, J. L. Gunjakar, H. Ho Park, U. M. Patil, Langmuir 37 (2021) 5260-5274.
- [55] L. Liu, Z. Niu, J. Chen, Chem. Soc. Rev. 45 (2016) 4340-4363.
- [56] Q. Wang, J. Yan, Z. Fan, Energy Environ. Sci. 9 (2016) 729-762.
- [57] H. Ma, J. He, D. B. Xiong, J. Wu, Q. Li, V. Dravid, Y. Zhao, ACS Appl. Mater. Inter. 8 (2016) 1992-2000.
- [58] X. Chen, R. Paul, L. Dai, Natl. Sci. Rev. 4 (2017) 453-489.
- [59] D. Marcano, D. Kosynkin, J. Berlin, A. Sinitskii, Z. Sun, A. Slesarev, L. Alemany, W. Lu, J. Tour, ACS Nano 4 (2010) 4806-4814.
- [60] J. Chen, Y. Li, L. Huang, C. Li, G. Shi, Carbon 81 (2015) 826-834.
- [61] M. J. S. Mohamed, D. K. Bhat, AIMS Mater. Sci. 4 (2017) 158-171.



CHAPTER-4

**Synthesis, Characterization and
Electrochemical Performance
Evaluation of Ni-Cr-LDH
Hybridized with POV Anions and
HSC Device**

CHAPTER 4

Synthesis, Characterization and Electrochemical Performance Evaluation of Ni-Cr-LDH Hybridized with POV Anions and HSC

Sr. No.	Title		Page No.
4.1	Introduction		101-102
4.2	Experimental details		102-105
	4.2.1	<i>Chemicals</i>	102
	4.2.2	<i>Exfoliation of Ni-Cr-LDH nanosheets</i>	103
	4.2.3	<i>Synthesis of Ni-Cr-LDH nanosheets hybridized with POV anions</i>	103-105
4.3	Results and discussion		105-115
	4.3.1	<i>XRD study</i>	105-106
	4.3.2	<i>FTIR study</i>	106-107
	4.3.3	<i>Micro-Raman study</i>	107-109
	4.3.4	<i>FESEM study</i>	109-110
	4.3.5	<i>HRTEM study</i>	110-111
	4.3.6	<i>BET surface area study</i>	112-113
	4.3.7	<i>XPS study</i>	113-115
4.4	Conclusions		115-116
4.5	Electrochemical performance evaluation of Ni-Cr-LDH nanosheets hybridized with POV anions		
4.5.1	Preparation of electrode		116
4.5.2	Results and discussion		116-124
	4.5.2.1	<i>CV study</i>	116-120
	4.5.2.2	<i>GCD study</i>	120-123
	4.5.2.3	<i>EIS study</i>	123-124
	4.5.2.4	<i>Stability study</i>	124
4.6	Electrochemical performance evaluation of NCV-2 rGO hybrid supercapacitor device		
	4.6.1	<i>Hybrid supercapacitor device fabrication</i>	124-126
	4.6.2	<i>CV study</i>	126-128

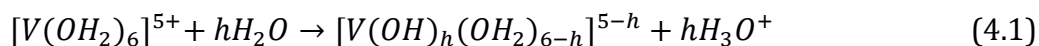
	4.6.3	<i>GCD study</i>	128-129
	4.6.4	<i>Ragone plot</i>	129-130
	4.6.5	<i>Stability study</i>	130
	4.6.6	<i>EIS study</i>	130-131
	4.6.7	<i>Practical demonstration of HSC</i>	131-132
4.7	Conclusions		132
4.8	References		133-134

4.1 Introduction

The portable electronic equipment in the mobiles, automobiles, defence, medical, transportation sectors needs energy storage devices with characteristic of high efficiency, capacity and power delivery [1-4]. SCs have emerged as the most promising portable EES devices among the available energy storage technologies. LDHs are the important type of layered materials that are composed of stacking of positively charged metal hydroxide layers and charge balancing interlayer anions with water molecules. LDHs demonstrated large potential as an electrochemical capacitor electrode owing to their promising properties like tunable chemical composition, better electrical conductivity, high ionic exchange capacity, and special layered structure with accessible interlayer gallery space for the energy storage/conversion [5, 6]. The transition metal LDHs particularly nickel, manganese, copper and cobalt-based LDHs are emerged as a battery-type HSC electrode materials due to their multiple redox properties and special layered structure that can accommodate large amount of charge storing ions [1, 7-11].

Though Ni-Cr-LDH materials showed as a battery-type HSC electrode material, this material suffers from low electrochemical performance due to their densely packed gallery space by charge-balancing anions with a high charge-to-size ratio. [11, 12]. To circumvent these type of issues, LDHs with expanded gallery space have been endeavored via intercalation of bulky organic/inorganic anions or hybridized with low dimensional biomolecules/ nanostructures [13-17]. 0D POV material from the polyoxometalate (POM) class consists of diversified electrochemically active metal elements and possesses negative charges, which make it one of the excellent functional components for intercalation in LDHs [1, 17].

Hydrolysis of the vanadium precursor produces a variety of POV anions with different structures. These POV anionic structures are dependent on their concentration and pH [18-20]. Considering polarising power and Lewis characteristics of V^{5+} and H_2O , some electrons migrate from the $3a_1$ orbital of the water molecule to the vacant 3d orbitals in V^{5+} , resulting in spontaneous acidification and deprotonation of the H_2O molecules, as shown by the hydrolysis reaction below,



The hydrolysis ratio, h , increases with pH in the aforementioned reaction, resulting in the formation of aquo, hydroxo, or oxo species. For a 0.1 M aqueous vanadate solution, these equilibria are $[VO_4]^{3-}$ at $pH > 13$, $[V_2O_7]^{4-}$ at $pH \sim 9-13$, $[V_4O_{12}]^{4-}$ at $pH \sim 6.7-9$, $[V_{10}O_{28}]^{6-}$ at $pH \sim 5.5-6.7$. POV anions have long been considered the ideal LDHs pillaring agent due to its well-defined ionic size, robust structure, redox properties, and variable charge density that is useful to tune LDHs gallery height [21]. Taking into account the fact that exfoliation of nitrate intercalated LDHs give rise to cationic LDH NSs, the self-assembly between cationic LDH NSs and POV anions leads to highly porous structure with unusually expanded surface area, gallery height and ordered pillared structure via the formation of self-assembled intercalative structure [22, 23]. This type of pillared LDH-POM hybridization can be the best way to achieve the high capacity and rate capability for energy storage due to their fast and reversible multi-electron redox reactions.

In this chapter, mesoporous layer-by-layer Ni-Cr-LDH-POV (NCV) nanohybrids are synthesized by the electrostatically-driven self-assembly of exfoliated Ni-Cr-LDH NSs and POV anions. The evolution of the electrochemical performance of Ni-Cr-LDH NSs upon the pillaring of POV anions is investigated with accompanying variations of crystal structural and physicochemical properties. The HSC device is fabricated with pillared NCV nanohybrid and rGO electrodes as a cathode and anode, respectively. To the best of our knowledge, this is the first kind of work on the exfoliation of Ni-Cr-LDH and pillared NCV nanohybrid and its use in HSC device.

4.2. Experimental details

4.2.1 Chemicals

Nickel nitrate hexahydrate ($Ni(NO_3)_2 \cdot 6H_2O$), chromium nitrate nonahydrate ($Cr(NO_3)_3 \cdot 9H_2O$), sodium nitrate ($NaNO_3$), sodium orthovanadate (Na_3VO_4), sodium hydroxide ($NaOH$), and formamide (CH_3NO) were purchased from Sigma-Aldrich. All chemical reagents were used without further purification. SS was used as a current collector to fabricate the Ni-Cr-LDH, NCV and rGO nanohybrids working electrodes.

4.2.2 Exfoliation of Ni-Cr-LDH nanosheets

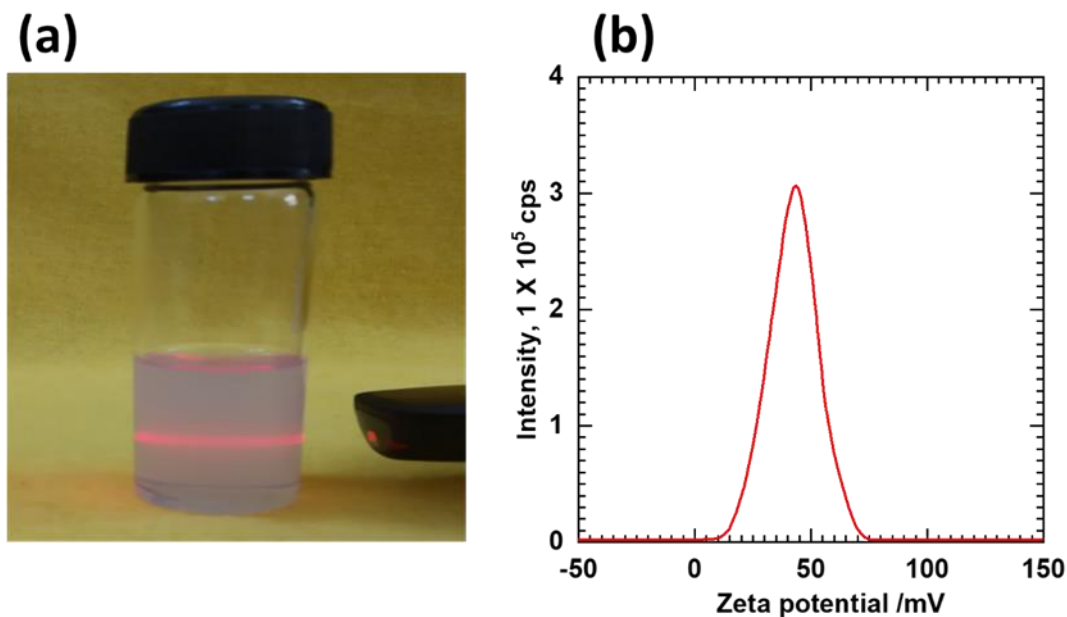


Fig. 4.1: (a) Photograph of a colloidal suspension of exfoliated Ni-Cr-LDH NSs, a laser beam is incident from the side to demonstrate the Tyndall effect and (b) Zeta potential curve of Ni-Cr-LDH sample.

As shown in Fig. 4.1(a), the formation of the colloidal suspension of exfoliated Ni-Cr-LDH NSs is evidenced by the observation of a clear Tyndall light scattering effect when irradiated with a laser beam. Moreover, the formation of positively charged Ni-Cr-LDH NSs is confirmed by the Zeta potential measurement (Fig.4.1(b)). The obtained Zeta potential of +43 mV indicated the good stability of exfoliated Ni-Cr-LDH NSs colloidal suspension.

4.2.3 Synthesis of Ni-Cr-LDH hybridized with POV anions

The nitrate form of Ni-Cr-LDH was synthesized by conventional co-precipitation method, as reported previously in chapter-3. The exfoliated Ni-Cr-LDH NSs colloidal suspension was achieved by the vigorous shaking of Ni-Cr-LDH powder (1 mg mL^{-1}) in formamide [24].

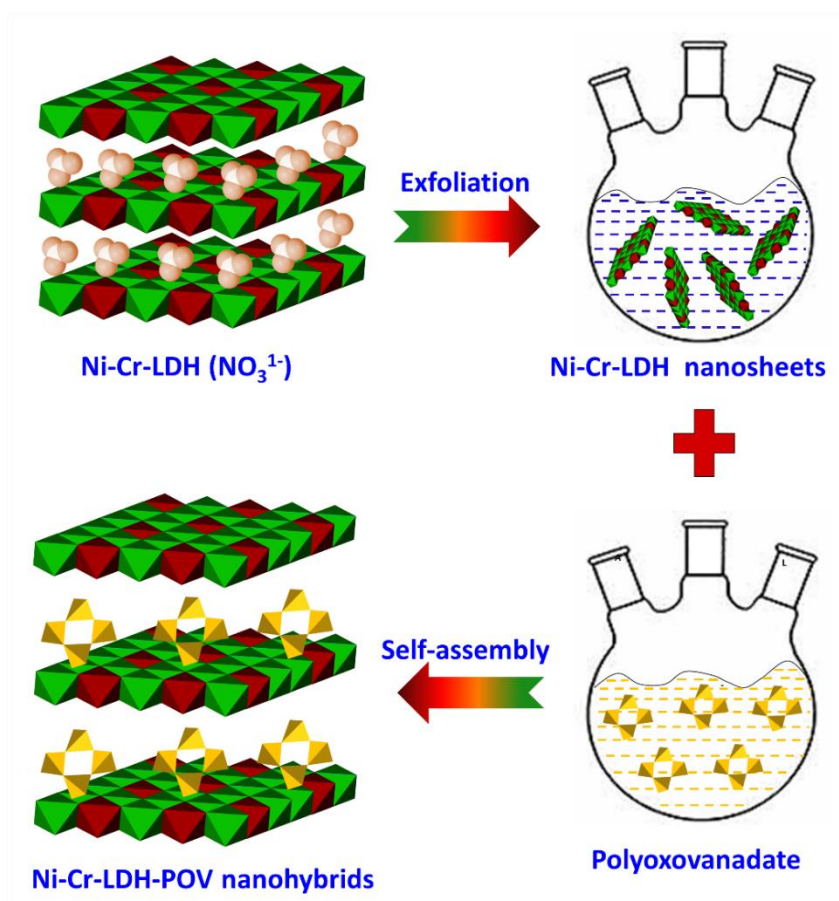


Fig. 4.2: Schematic experimental procedure for the preparation of NCV nanohybrids.

The pillared NCV nanohybrids were prepared by slow mixing of an aqueous solution of POV anions and exfoliated Ni-Cr-LDH NSs suspension with continuous stirring at ambient temperature (shown in Fig. 4.2). The spontaneous flocculation of cationic Ni-Cr-LDH NSs with POV anions occurred upon mixing, confirming the immediate formation of self-assembled NCV nanohybrids. The eventual flocculation products of NCV nanohybrid were collected by centrifugation, washed with absolute ethanol and formamide, and finally freeze-dried to ensure solid NCV nanohybrid product. To prevent contamination of the pristine Ni-Cr-LDH and NCV nanohybrids from atmospheric carbonate, all the experiments were carried out with decarbonized water and in a schlenk line, which was continuously supplied with the N_2 gas. Three different POV:Ni-Cr-LDH molar ratios of 1:1, 2:1, and 3:1 were employed to test the chemical composition effect on their physicochemical

properties. The obtained NCV nanohybrids are named NCV-1, NCV-2, and NCV-3, respectively.

4.3 Results and discussion

4.3.1 XRD study

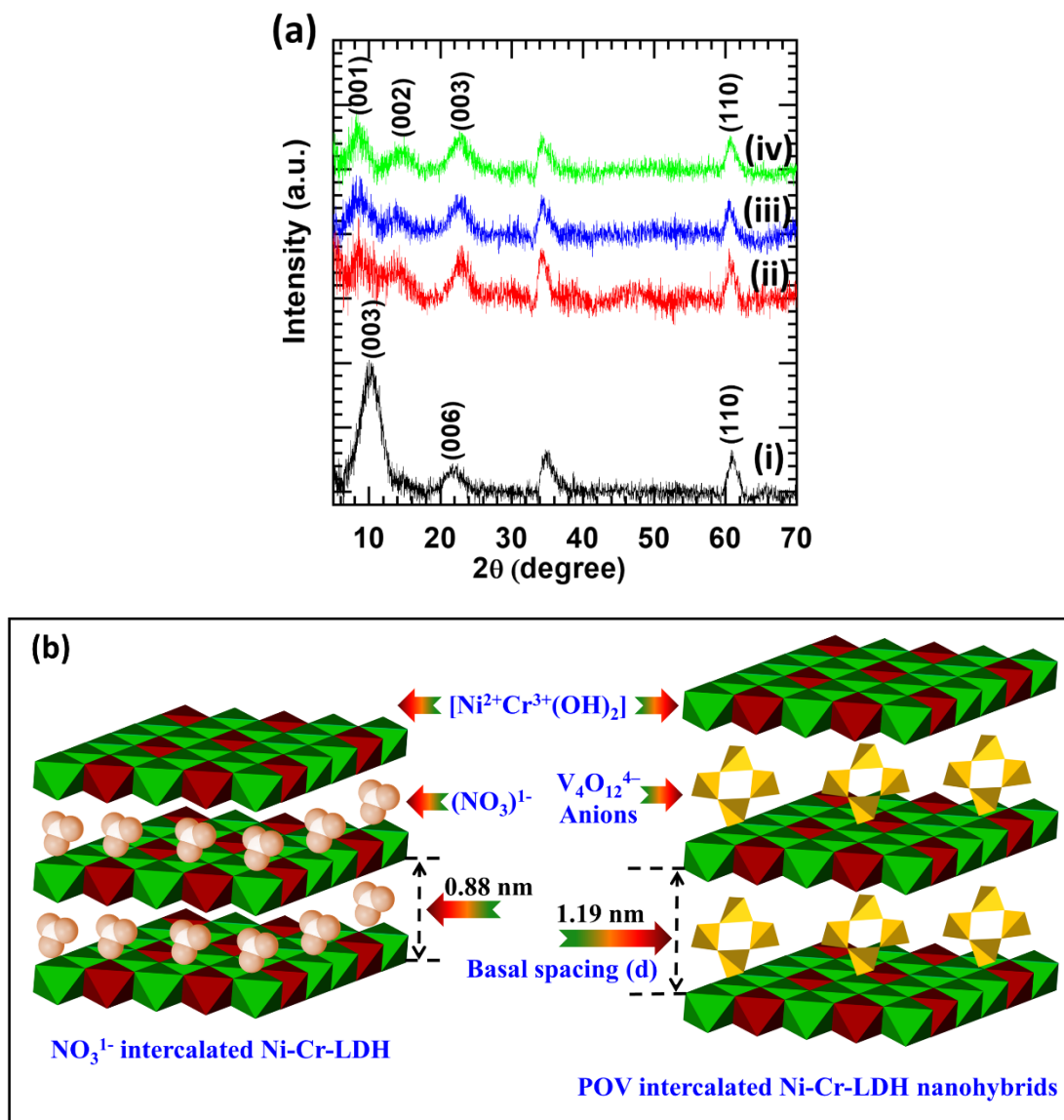


Fig. 4.3: (a) XRD patterns of (i) pristine Ni-Cr-LDH and (ii) NCV-1, (iii) NCV-2 and (iv) NCV-3 nanohybrids. (b) structural schematic model of the NCV nanohybrid.

The powder XRD patterns of NCV nanohybrids compared with the pristine Ni-Cr-LDH are presented in Fig. 4.3(a). The pristine Ni-Cr-LDH demonstrates a characteristic series of $(00l)$ Bragg reflections as evidence of hexagonal layered LDH structure with space group $R\bar{3}m$ and rhombohedral symmetry [25]. The estimated unit cell parameters $a=b=0.31$ nm and $c=0.88$ nm are well-matched with

the lattice parameters of NO_3^{1-} intercalated Ni-Cr-LDH phase [12,15]. Like pristine Ni-Cr-LDH, all the pillared NCV nanohybrids exhibit a series of (*00l*) reflections in the low 2θ region, indicating an excellent c-axis ordering due to layer-by-layer stratification of POV anions and Ni-Cr-LDH NSs, with notable enlargement of basal spacing upon hybridization. The standard thickness value of LDH NSs is 0.48 nm. Irrespective of the POV:Ni-Cr-LDH ratio, all pillared NCV nanohybrids exhibit an expanded gallery height of 0.61 to 0.74 nm, corresponding to the interplanar spacings $d_{(00l)}$ of 1.0 to 1.19 nm, respectively. The NCV nanohybrids display interplanar spacing of 1.0, 1.19 nm and 1.10 nm for NCV-1, NCV-2 and NCV-3 nanohybrids, respectively. The expanded interplanar spacing for NCV nanohybrids indicates the intercalation of high-nuclearity $\text{V}_4\text{O}_{12}^{4-}$ anions, as shown in Fig. 4.3(b). Along with *00l* peak shifting, all NCV nanohybrids show peak broadening, indicating only a few NCV crystallites stacked together in the c-axis direction. The average NCV crystallite thickness is estimated to be ~ 9 nm according to Scherrer's calculation for the (*00l*) reflections [26]. In addition, all the NCV nanohybrids and pristine Ni-Cr-LDH commonly exhibit the in-plane (*110*) peak of hexagonal LDHs phase at $2\theta = \sim 61^\circ$ and broad hump at $\sim 33\text{--}42^\circ$, indicating the maintenance of the in-plane structure of Ni-Cr-LDH NSs and distorted turbostratic stacking structure of the self-assembled NCV nanohybrids. The XRD pattern confirms the layer-by-layer stacking structure of NCV nanohybrids.

4.3.2 FTIR Study

The nature of chemical bonding and functional groups of pristine Ni-Cr-LDH and NCV nanohybrids is analyzed by FTIR analysis. The FTIR spectra of Ni-Cr-LDH and NCV nanohybrids are shown in Fig. 4.4. Ni-Cr-LDH displays the low-frequency absorption bands in $400\text{--}800\text{ cm}^{-1}$ (ν_1 (515 cm^{-1}), ν_2 (576 cm^{-1}), and ν_3 (670 cm^{-1})) which are associated with stretching and bending normal modes of metal-oxygen-hydrogen vibrations and oxygen-metal-oxygen of solitary brucite-like layers of Ni-Cr-LDH [27-29]. The strong and sharp peak at ν_4 (1384 cm^{-1}) can be assigned to the asymmetric stretching of NO_3^{1-} anions in the interlayer galleries of LDH [30]. All NCV nanohybrids show new bands at ν_7 (512 cm^{-1}), ν_8 (560 cm^{-1}), ν_9 (744 cm^{-1}) and ν_{10} (960 cm^{-1}). These bands are ascribed to the symmetric/antisymmetric stretching modes of the V–O–V POV chains and V=O

symmetric stretching mode of intercalated POV anions in the Ni-Cr-LDH gallery [31-33]. Interestingly, the nitrate and carbonate-related sharp bands (1382 cm^{-1}) are significantly quenched upon hybridization, emphasizing negligible contamination of NCV nanohybrids with adsorbed carbonate or nitrate anions. All the NCV nanohybrids and reference Ni-Cr-LDH show broad bands ν_6 (3460 cm^{-1}) and ν_5 (1630 cm^{-1}) ascribed to the stretching vibration of the O-H groups and bending vibrational mode of water molecule entrapped in Ni-Cr-LDH NSs [27, 30]. All the present NCV nanohybrids demonstrate distinct IR features related to POV intercalation in Ni-Cr-LDH and intactness of Ni-Cr-LDH monolayers after hybridization, underscoring the effective hybridization of Ni-Cr-LDH NSs pillared with POV anions.

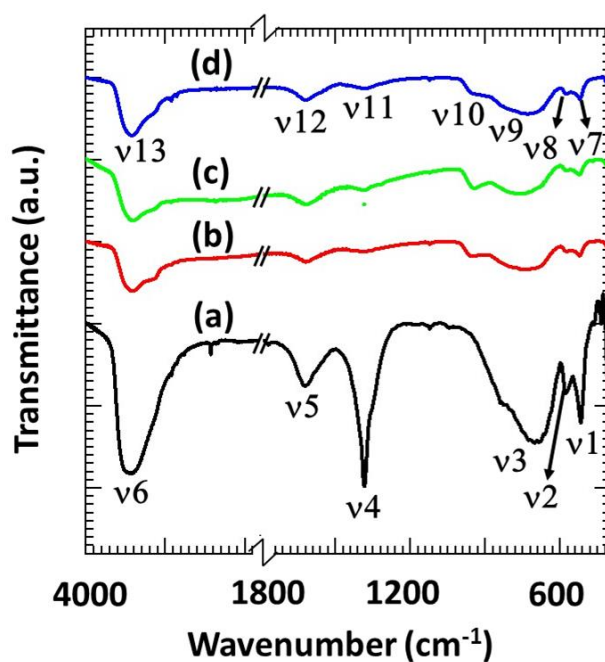


Fig. 4.4: FTIR spectra of the (a) pristine Ni-Cr-LDH (b) NCV-1, (c) NCV-2 and (d) NCV-3 nanohybrids.

4.3.3 Micro-Raman study

The microscopic structural bonding properties of the pillared NCV nanohybrid are studied using Raman spectroscopy, as presented in Fig. 4.5.

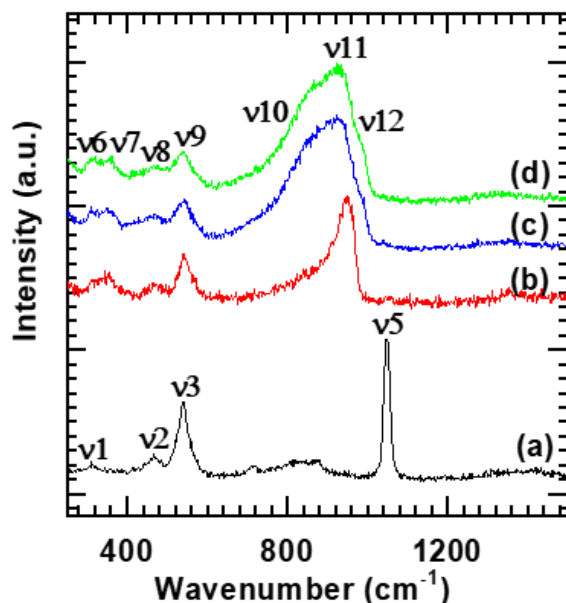


Fig. 4.5: Micro-Raman spectra of the (a) pristine Ni-Cr-LDH, (b) NCV-1, (c) NCV-2 and (d) NCV-3 nanohybrids.

The Raman spectrum of the reference Ni-Cr-LDH shows the peaks at v1 (311 cm^{-1}) and v2 (464 cm^{-1}), which are ascribed to the E_g and A_{1g} Raman-active vibrational modes of $\text{Ni}(\text{OH})_2$, respectively [34]. The broad and high-intensity peak v3 centered on 540 cm^{-1} is attributed to the superposition of Cr-O-H bending mode of $\text{Cr}(\text{OH})_3$ at 530 cm^{-1} and the second-order acoustic mode of $\text{Ni}(\text{OH})_2$ at 540 cm^{-1} [29, 30]. Moreover, the reference Ni-Cr-LDH shows the characteristic Raman bands at v4 (1050 cm^{-1}) owing to the symmetric stretching modes of NO_3^{1-} anions [34,35]. Similar to reference Ni-Cr-LDH, all NCV nanohybrids display characteristic Raman peaks at v5 (310 cm^{-1}), v7 (455 cm^{-1}), and v8 (546 cm^{-1}) which are ascribed to the Ni-Cr-LDH NS lattice vibrational modes [34, 36]. The observation of these Raman features indicates the intactness of Ni-Cr-LDH NSs after the hybridization with POV anions. NCV nanohybrids accompanied by additional mild and high-intensity broad Raman peaks at v6 (354 cm^{-1}), and v10 (931 cm^{-1}), respectively. The mild Raman peak v6 is attributed to the bending mode of VO_4^{3-} [37]. Raman peak centred at v10 (931 cm^{-1}) is formed by the superposition of v9 (790 cm^{-1}), v10 (931 cm^{-1}) and v11 (982 cm^{-1}) peaks which are attributed to the second-order vibrational mode of the $\text{NiCr}(\text{OH})_2$ lattice, V-O symmetric-stretching vibrational mode of the $[\text{V}_4\text{O}_{12}]^{4-}$ and symmetric-stretching vibrations of decavanadate $[\text{V}_{10}\text{O}_{28}]^{6-}$ anions, respectively [26, 38]. Interestingly, the characteristic Raman

peak related to stretching modes of NO_3^{1-} anions at 1050 cm^{-1} is completely quenched in the case of NCV nanohybrids, reflecting the absence of NO_3^- anions. The observed Raman features disclose the pillaring of $[\text{V}_4\text{O}_{12}]^{4-}$ anions in the Ni-Cr-LDH NSs.

4.3.4 FESEM study

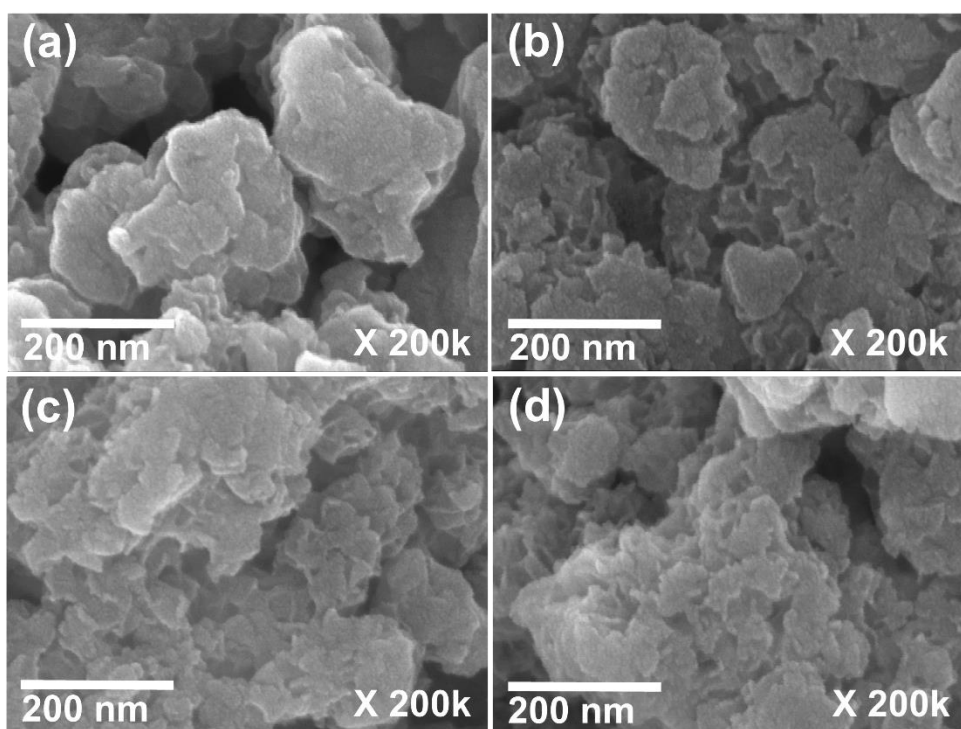


Fig. 4.6: FESEM images of (a) pristine Ni-Cr-LDH, (b) NCV-1, (c) NCV-2, and (d) NCV-3 nanohybrids.

The surface morphologies of the pristine Ni-Cr-LDH and NCV nanohybrids are studied using FESEM. The FESEM images of NCV-2 nanohybrid compared with the pristine Ni-Cr-LDH are shown in Fig. 4.6. The pristine Ni-Cr-LDH displays clusters of sheets like compact morphology with negligible porosity. Conversely, the porous morphology composed of randomly aggregated network of nanoplate crystallites is observed for the pillared NCV nanohybrids. The FESEM images of NCV nanohybrids (Fig. 4.6b-d) clearly show the randomly aggregated nanoplate network formed by the edge-to-face interaction of pillared LDH NSs that is quite effective for inducing the mesoporosity in NCV nanohybrids. In addition, a close examination of these micrographs discloses two regions where the restacked NCV crystallites aligned flat and vertical to the beam direction.

Judging from the flat alignment, the lateral size range of NCV NSs is estimated as ~50 to 160 nm. This type of mesoporous morphology is typically observed for the nanohybrid materials synthesized by exfoliation-reassembling of 2D inorganic NSs with various guest nanostructures [22, 23].

4.3.5 HRTEM Study

The localized nanostructure, morphology, crystal shape and crystal structure of the pillared NCV nanohybrids and pristine Ni-Cr-LDH are examined by the TEM, HRTEM, and the SAED analyses. As displayed in Fig. 4.7 (a, b) at low magnification, the TEM images of pristine Ni-Cr-LDH show the aggregated plate-shaped dense clusters with lateral sizes ranging between 150 to 400 nm. As shown in Fig. 4.7(c, d) at a high resolution, the top-view HRTEM images demonstrate the set of equidistant lines separated by a spacing of 0.15 nm that are well-matched with the (*110*) in-plane lattice fringes of Ni-Cr-LDH.

Alternatively, NCV-2 nanohybrid (Fig.4.7(e,f)) displays randomly interconnected thin sheet-like crystallites forming mesoporous structures. As shown in Fig. 4.7(h-j), at high resolution, two parallel sets of lattice fringes are observable for the NCV nanohybrid. One set is in the top view with an interplanar distance of 0.15 nm, and the other set is in the cross-sectional view with a higher interplanar distance of ~0.89 nm. The observed interplanar distances from the top (0.15 nm) and cross-sectional (0.89 nm) views can be indexed for the (*110*) and (*001*) planes of hexagonal Ni-Cr-LDH NSs pillared with POV anions, respectively. These values are well-matched with the lattice distances estimated from the XRD study. A long-range order of lattice fringes >20 nm can be observable for the top view, whereas cross-sectional view display only short-range order up to 6 nm. As judged from the c-axis lattice parameters, the NCV nanohybrid crystallite composed of 6 to 7 Ni-Cr-LDH monolayers pillared with POV anions which are well-matched with the Scherrer's calculations and FESEM analysis. The crystal structure is further confirmed by SAED analysis. The SAED pattern of NCV (See Fig. 4.8) shows diffused diffraction rings corresponding to 110 and 100 diffraction peaks of the NCV hexagonal structure [37, 38]. The development of such a crystal structure

with mesoporous morphology is commonly observed for the 2D NSs based nanohybrids [22, 23].

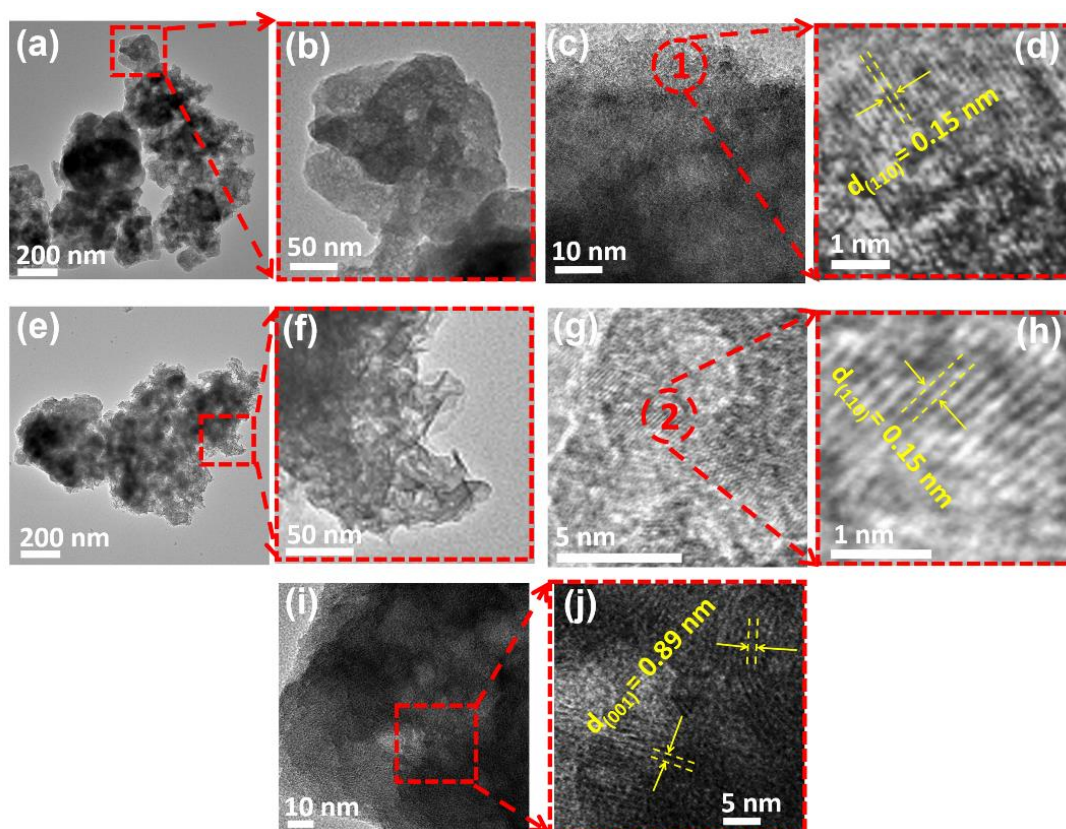


Fig. 4.7: (a, b) TEM images of pristine Ni-Cr-LDH, (c, d) top view HRTEM images of pristine Ni-Cr-LDH, (e, f) TEM images of NCV-2 nanohybrid, (g, h) top view HRTEM images of NCV-2 nanohybrid, (i, j) cross-sectional HRTEM images of the NCV-2 nanohybrid.

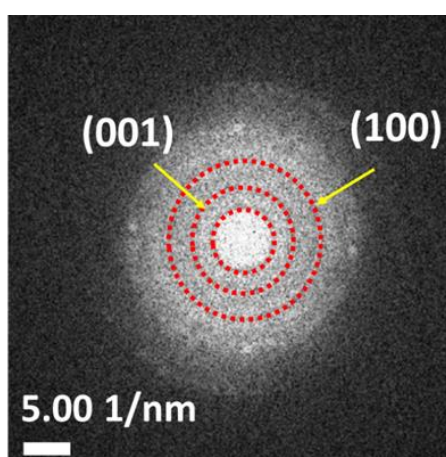


Fig. 4.8: The SAED pattern of NCV-2 nanohybrid.

4.3.6 Surface area study:

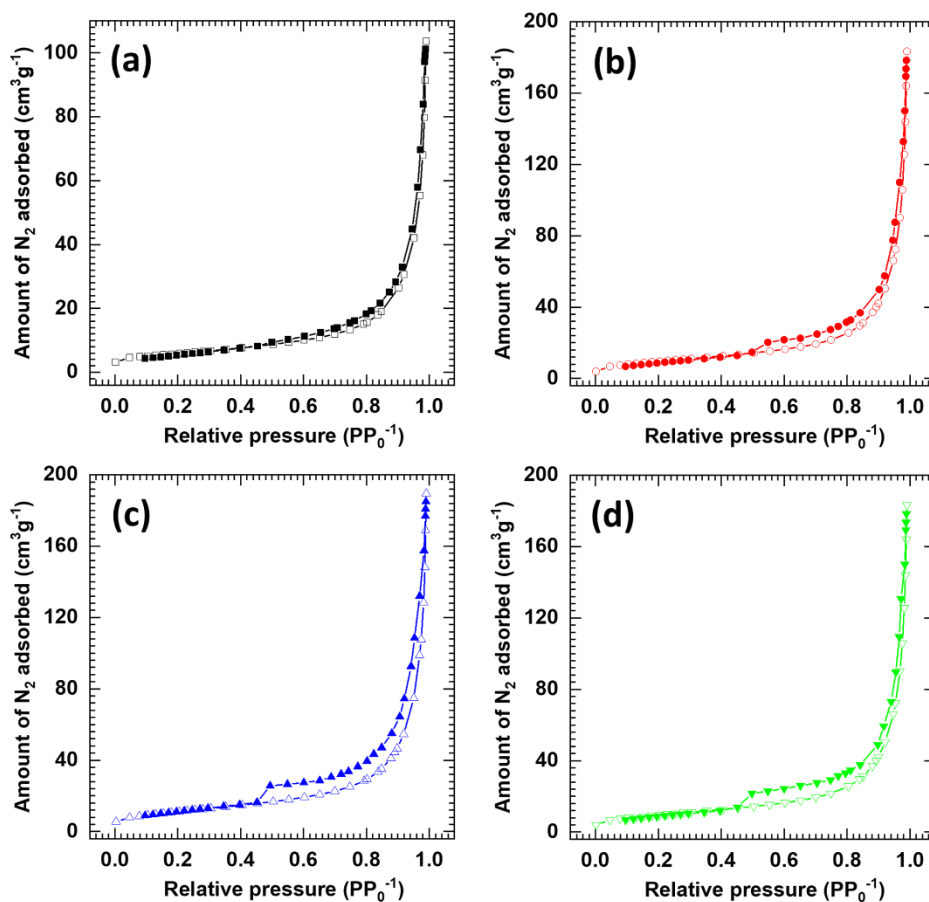


Fig. 4.9: N₂ adsorption-desorption isotherms of (a) pristine Ni-Cr-LDH, (b) NCV-1, (c) NCV-2 and (d) NCV-3 nanohybrids.

The surface area expansion and the mesoporous development via pillared hybridization is probed using N₂ adsorption-desorption isotherms analysis and pore size calculations. As shown in Fig. 4.9, a distinct hysteresis is observed in NCV nanohybrids at $pp_0^{-1} > 0.45$, indicating the presence of mesoporous structure. According to IUPAC and BDDT classifications, the shape of the isotherm is of type-IV with H3-type hysteresis loop, which can be ascribed to the well-ordered narrow slit-shaped mesopores having high energy of adsorption [26, 39]. Referring to the FESEM surface morphology, the observed porosity is originated from the mesopores formed by the randomly aggregated nanoplate network morphology of NCV nanohybrids. As per the fitting analysis based on the BET equation, the NCV-1, NCV-2 and NCV-3 nanohybrids possess the expanded surface areas of 34, 44, and 37 m²g⁻¹, respectively which are much higher than that of pristine Ni-Cr-LDH (14 m²g⁻¹). The decrease surface area of NCV-3 nanohybrid can be attributed to the

deposition of excess POV anions on the edges and surface of the nanohybrid. The present results underscore the role of optimum POV content in NCV-2 nanohybrid for enabling the maximum surface area of NCV nanohybrids. According to the BJH method, the pore size distribution of the NCV nanohybrids shows a wide distribution of the pores with an average pore diameter of 28 nm (Fig. 4.10). The present wide distribution of the pores is well-matched with mesoporous randomly aggregated nanoplate network morphology of NCV nanohybrids. The surface area expansion with mesopore formation highlighted the exfoliation-reassembling method's significant role in the pore structure modifications of NCV nanohybrids.

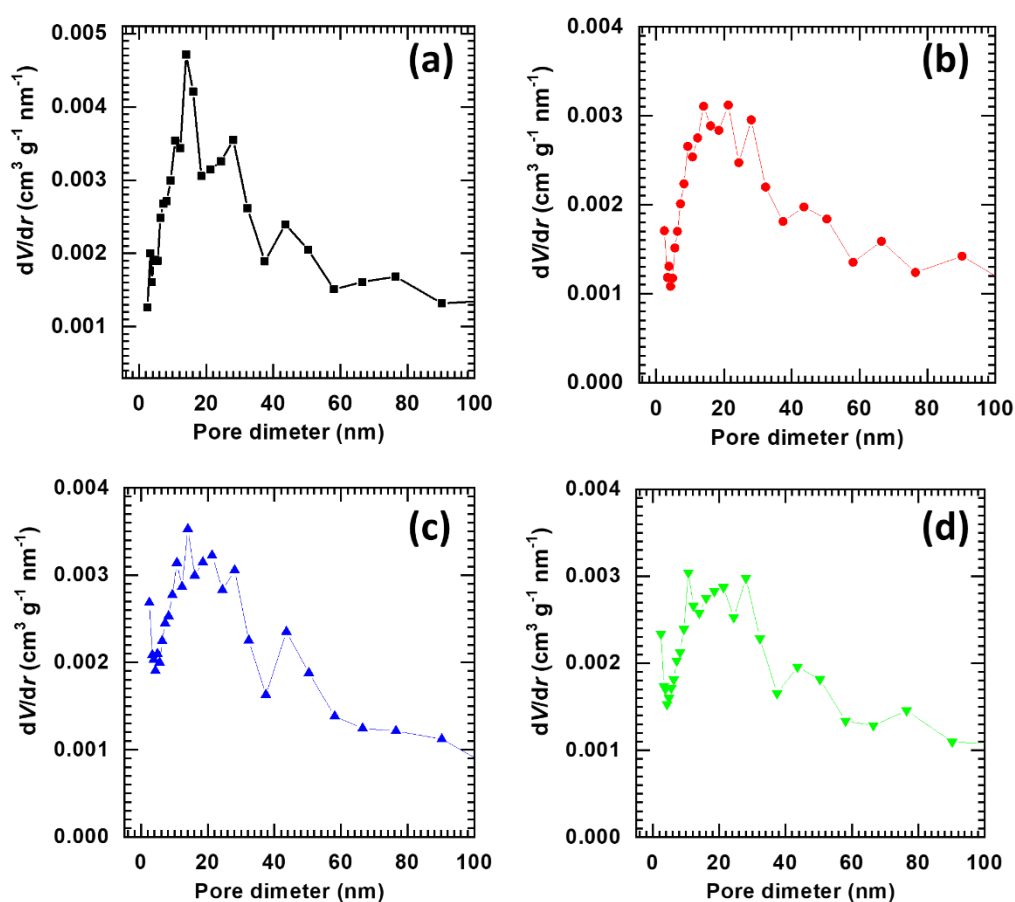


Fig. 4.10: Pore size distribution plots of the pristine (a) Ni-Cr-LDH, (b) NCV-1, (c) NCV-2, and (d) NCV-3 nanohybrids.

4.3.7 XPS Study

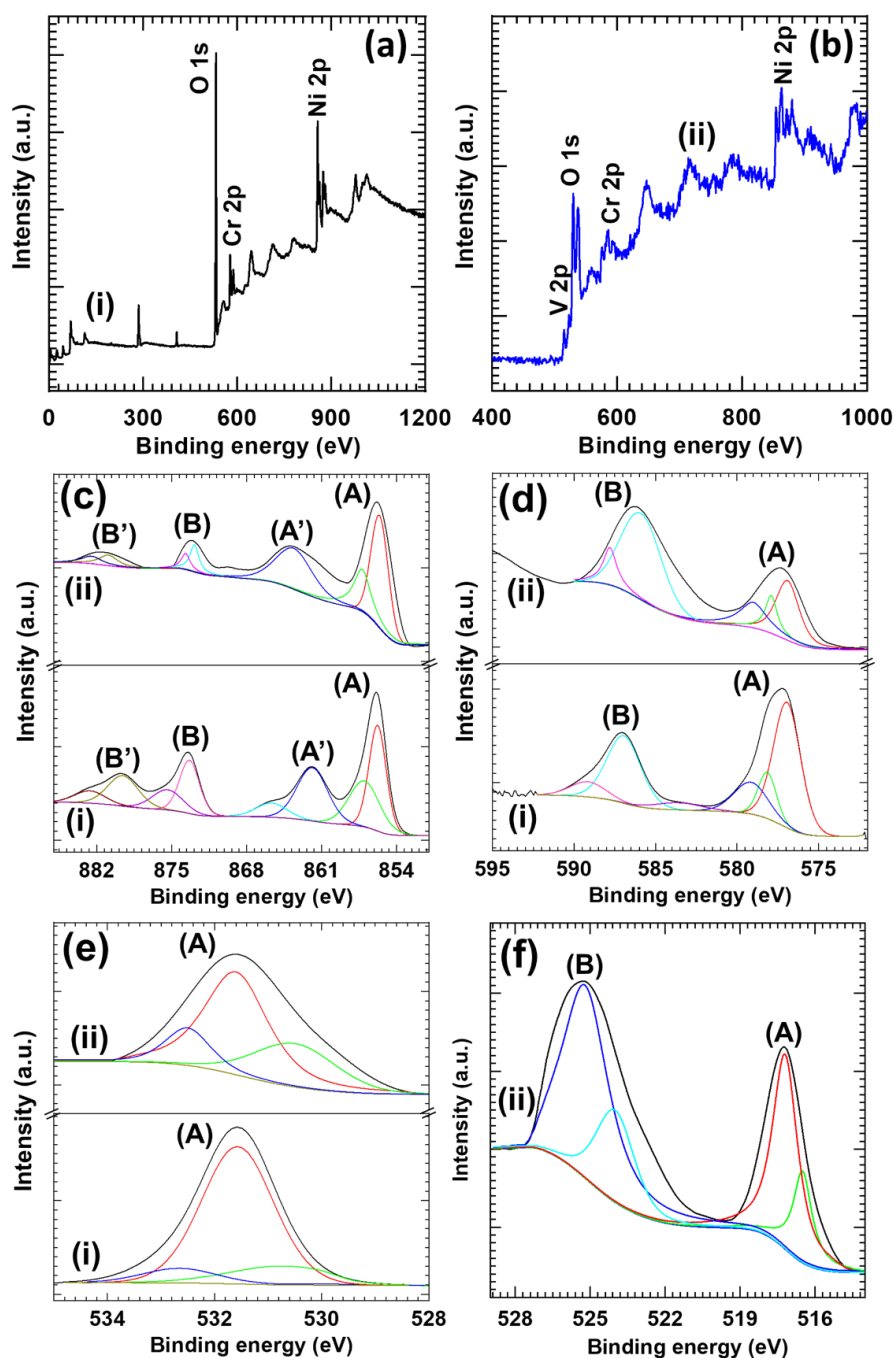


Fig. 4.11: (a,b) Survey, (c) Ni2p, (d) Cr2p, (e) O1s, and (f) V2p XPS spectra of (i) pristine Ni-Cr-LDH and, (ii) NCV-2 nanohybrid.

Further insight into the surface composition and chemical states of pillared POV anions and their influence on the host Ni-Cr-LDH structure is probed by XPS. The full survey XPS spectra for the pristine Ni-Cr-LDH and NCV-2 nanohybrid shows (Fig. 4.11(a,b)) the spectral features of the elements Ni, Cr, and O. The high resolution XPS spectra of the pristine Ni-Cr-LDH and NCV-2 nanohybrid for Ni, Cr, O and V are plotted in Fig. 4.11(c-f). The additional spectral features related to V

for the NCV nanohybrids confirm the pillaring of the POV anion between the Ni-Cr-LDH NSs. As shown in Fig. 4.11(c), pristine Ni-Cr-LDH and NCV-2 nanohybrid commonly exhibit two strong peaks at A (855.9 eV) and B (873.4 eV) with corresponding satellite peaks at A' (862.1 eV) and B' (880 eV), which are assigned to the Ni 2p_{3/2} and Ni 2p_{1/2} binding energies, respectively. The presence of Ni 2p_{3/2} and Ni 2p_{1/2} peaks separated by a spin-energy difference of 17.5 eV indicates the existence of Ni⁺² in Ni-Cr-LDH [40]. As plotted in Fig. 4.11 (d), the high-resolution Cr 2p spectra show two broad peaks at A (577.3 eV) and B (587.0 eV), corresponding to spin-orbit splitting into Cr 2p_{1/2} and Cr 2p_{3/2}, respectively. The binding energy of Cr 2p for pristine Ni-Cr-LDH and NCV-2 nanohybrid samples at 577.3 eV suggests the trivalent Cr in Ni-Cr-LDH [41]. Interestingly host Ni-Cr-LDH and NCV nanohybrid depicted identical XPS features underscoring the intactness of Ni-Cr-(OH)₂ NSs during the self-assembly. As plotted in Fig. 4.11(e), the O 1s spectra of pristine Ni-Cr-LDH and NCV-2 nanohybrid exhibit the broad peak centred at A (531.6 eV), which ascribed to the lattice oxygen (530.4 eV), hydroxyl group (531.5 eV) and bound water (532.6 eV) [42]. The XPS spectrum of NCV-2 nanohybrid shows negative skew ascribed to the metal-oxygen bonding in pillared POV anions [70]. As illustrated in Fig. 4.11 (f), the V 2p XPS spectra for the NCV-2 nanohybrid show two spectral features, A (517.1 eV) and B (525.2 eV), owing to the V 2p_{3/2} and V 2p_{1/2} spin-orbit splitting, respectively [34, 44, 45]. The characteristic peak at 517.1 eV highlighted the V⁺⁵ state in the pillared [V₄O₁₂]⁴⁻ anions. The present XPS results clearly indicate divalent and pentavalent states of Ni and V in NCV-2 nanohybrid, respectively, which confirms the maintenance of Ni-Cr-LDH NSs and intercalation of [V₄O₁₂]⁴⁻ anions during pillared hybridization.

4.4 Conclusions

In conclusion, mesoporous nanohybrids of 2D Ni-Cr-LDH NSs pillared with POV anions are prepared by the electrostatically driven exfoliation-restacking process at ambient temperature. XRD analysis confirms the formation of layer-by-layer NCV nanohybrid with expanded gallery space. FTIR features confirm the maintenance of Ni-Cr-LDH NSs and intercalation of POV anions into the interlayer spaces of the Ni-Cr-LDH. The Micro-Raman results confirm the intercalation of POV anions in Ni-Cr-LDH. FESEM analysis demonstrated the mesoporous house-of-

card-type morphology of NCV nanohybrids. HRTEM study clearly demonstrates the intercalative stabilization of POV anions into Ni-Cr-LDH with the formation of layer-by-layer stacking structure of Ni-Cr-LDH and POV anions. The XPS study confirms the formation of NCV-2 nanohybrid by observing oxidation states of Ni, Cr, O and V element. The observed surface area and pore size distribution analysis revealed the crucial importance of the self-assembly method for tuning the pore structure of the resulting NCV nanohybrids. The overall results indicate the formation of a well crystalline, mesoporous, and pillared structure of NCV nanohybrid.

4.5 Electrochemical performance evaluation of NCV nanohybrids

4.5.1 Preparation of NCV electrode

The working electrodes were prepared by mixing the active material (Ni-Cr-LDH, NCV), AC, and PVDF in a mass ratio of 85:15:5. The mixtures were stirred for 1 h in NMP to become homogeneous slurry. Then, a formed slurry is coated on SS substrate (1 cm × 1 cm) and dried at 80°C for 12 h. The NCV electrode prepared via the above protocol was used as a working electrode in a three-electrode cell for electrochemical study.

4.5.2 Results and discussion

4.5.2.1 CV study

The effects of pillared POV anions on the capacitive performance of the host Ni-Cr-LDH are studied using CV, GCD, and EIS analyses. The electrochemical properties of the pristine Ni-Cr-LDH and NCV nanohybrids are studied in an aqueous 2 M KOH electrolyte using a three-electrode system with Hg/HgO reference electrode and Pt mesh counter electrode. Fig. 4.12 shows the CV curves of the pristine Ni-Cr-LDH and NCV nanohybrid electrodes at a scan rate of 10 mV s⁻¹. The NCV nanohybrids and pristine Ni-Cr-LDH display a pair of apparent redox peaks corresponding to the quasi reversible redox transformation among Ni(OH)₂ and NiOOH according to the redox mechanism (equation 3.1).

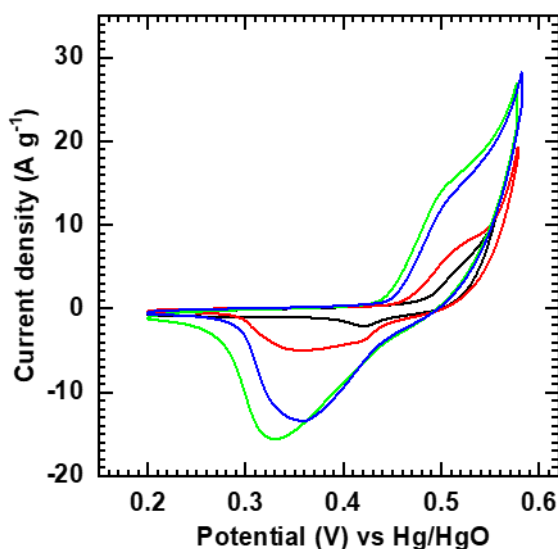


Fig. 4.12: The comparative CV curves of Ni-Cr-LDH and NCV nanohybrid electrodes at a scan rate of 10 mV s^{-1} . In this panel Ni-Cr-LDH (black), NCV-1 (red), NCV-2 (green) and NCV-3 (blue) nanohybrids.

The presence of these redox peaks highlights the hybrid electrochemical charge storage mechanism comprising diffusion-controlled (battery) and EDLC (capacitive) type charge storage. Compared with pristine Ni-Cr-LDH, the NCV nanohybrid electrodes enclose larger area under CV, reflecting their higher charge storing ability. The pillaring of Ni-Cr-LDH with POV anions leads to the partially shifting of cathodic peaks towards the negative potential and anodic peak towards the positive potential and broadening redox peaks. This effect elucidates the improved accessibility of NCV nanohybrid electrodes for the percolation of electrolyte ions and adequate current amplification upon the intercalation of POV anions. Moreover, a significant variation in the area enclosed by CV with pillared POV content is observable for NCV nanohybrids. NCV-2 nanohybrid with POV:Ni-Cr-LDH molar ratio of 2:1 displays the highest area under the CV amongst NCV nanohybrids. The NCV-3 nanohybrid with excess pillaring of POV anions shows a pernicious effect on its energy storing ability, which can be observed from the decrease area under CV. The advantages of NCV-2 nanohybrid over the other NCV nanohybrids indicate the crucial importance of optimum POV anions content for improving the electrode performance of NCV nanohybrids.

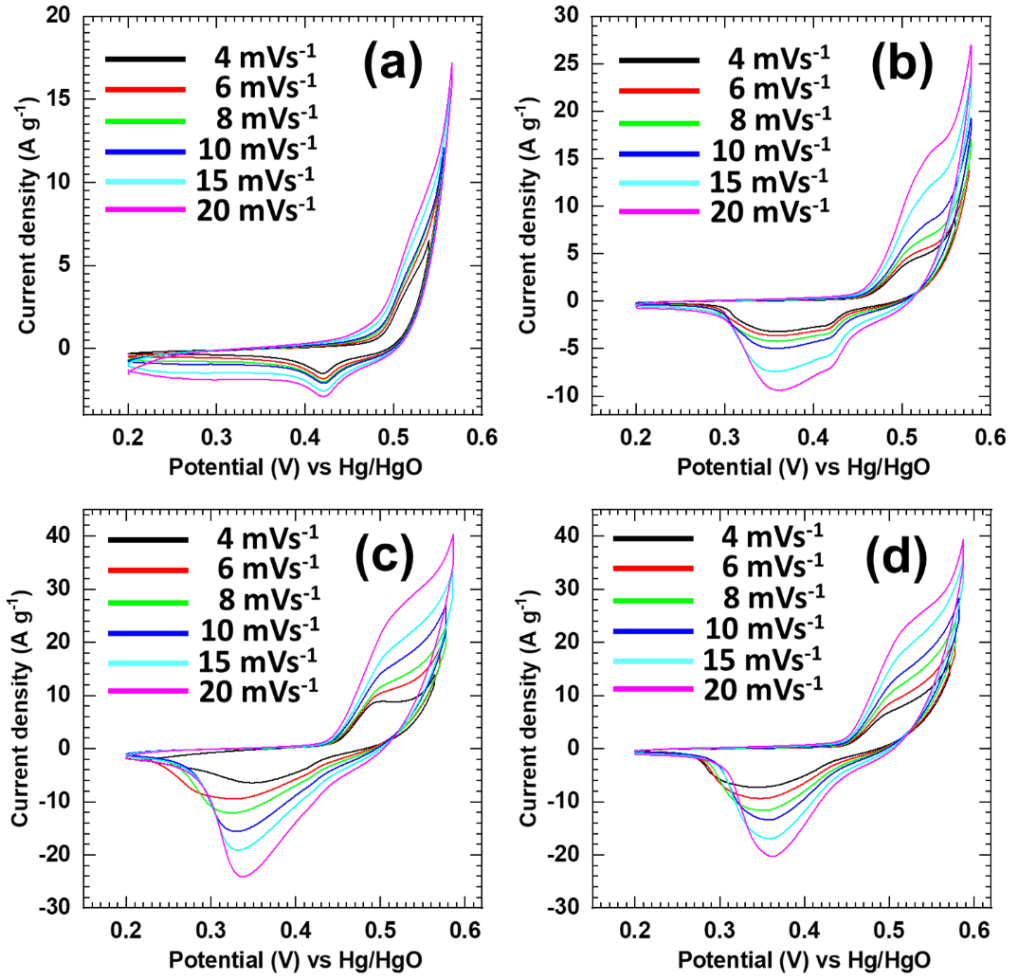


Fig. 4.13: CV curves of (a) pristine Ni-Cr-LDH, (b) NCV-1, (c) NCV-2, and (d) NCV-3 nanohybrid electrodes at various scan rates from 4 to 20 mV s⁻¹.

The variation of CV shape, current response and redox peak potentials with the scan rate for pristine Ni-Cr-LDH and NCV nanohybrids are plotted in Fig. 4.13. The redox peaks are shifted towards more positive potential with scan rate, highlighting the hybrid charge storage mechanism involving both capacitive and diffusion-controlled battery type charge storage. The capacitive and diffusion-controlled component can be resolved using the electrochemical kinetics study conferring to the following relation,

$$Q_t = Q_s + cv^{-1/2} \quad (4.1)$$

Where Q_t is the total voltammetric charge, Q_s is the capacitive surface charge, c is the constant, and v is the scan rate.

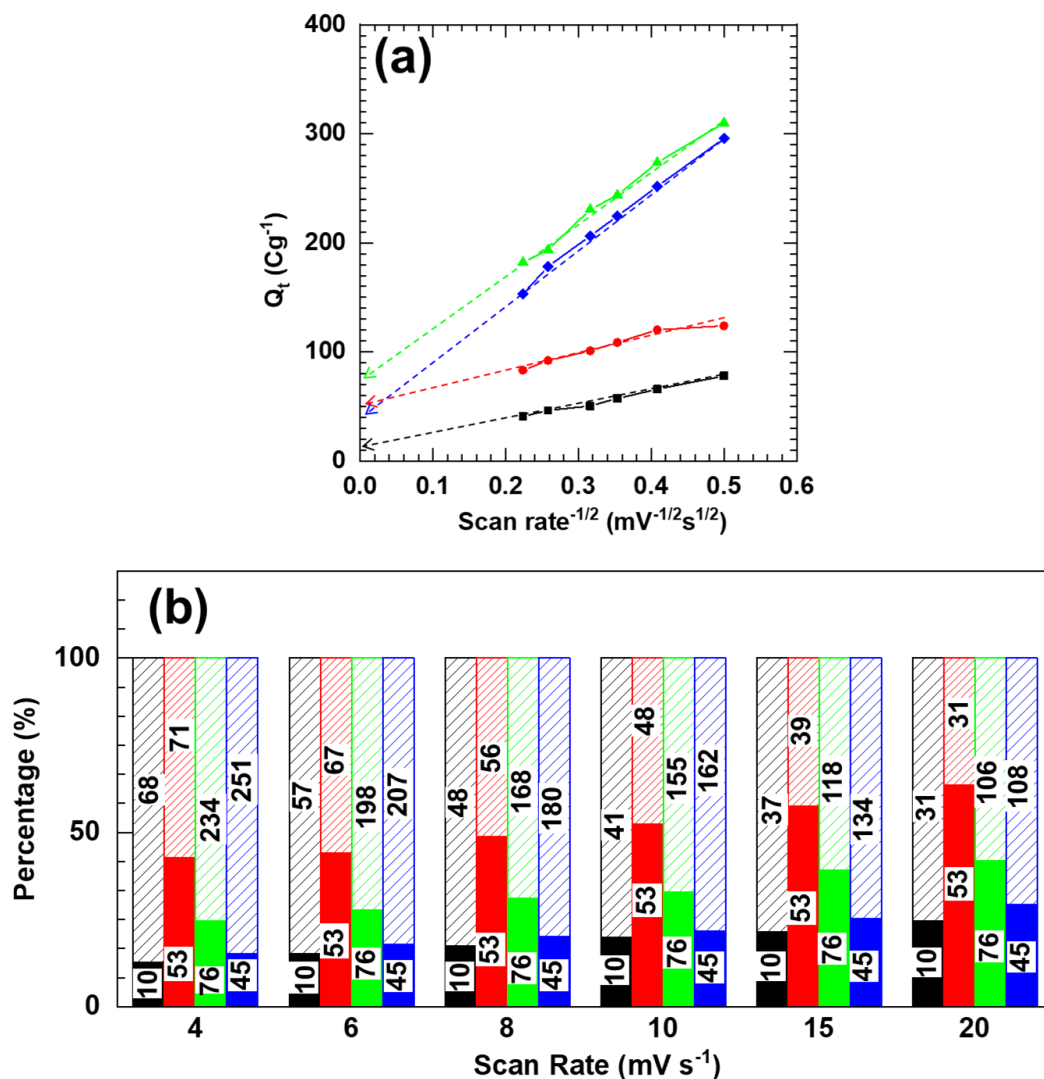


Fig. 4.14: (a) Plots of total charge (Q_t) enclosed under CV against the reciprocal of the square root of the potential scan rate. (b) The fraction of the capacitive (solid) and diffusion-controlled (pattern) contributions of Ni-Cr-LDH and NCV nanohybrids (values in bar assigned for the respective charge contributions), in a, and b panels Ni-Cr-LDH (black), NCV-1 (red), NCV-2 (green), and NCV-3 (blue) nanohybrids.

By plotting the Q_t vs $(v)^{-1/2}$ (Fig. 4.14 (a)) for the reasonable range of sweep rates (4 to 20 mV s⁻¹), the capacitive surface charge (Q_s) can be resolved by extrapolating v to infinity assuming semi-infinite linear diffusion. The estimated capacitive (solid columns) and diffusion-controlled (pattern columns) fractions of NCV nanohybrids compared to pristine Ni-Cr-LDH are plotted in Fig. 4.14 (b). At a high scan rate of 20 mV s⁻¹, pristine Ni-Cr-LDH, NCV-1, NCV-2, and NCV-3 nanohybrids display the high surface capacitive contribution of 25, 64, 42 and 30 %, respectively. In contrast, at a scan rate

of 4 mV s^{-1} , they show the low capacitive contribution of 13, 43, 25 and 15 %, respectively. Thus, all NCV nanohybrids, along with pristine Ni-Cr-LDH, display significant Q_s and Q_d charge contributions at high and low scan rates. Moreover, all the NCV nanohybrids demonstrate a substantial fraction of Q_s charge storage compared to the pristine Ni-Cr-LDH. This fraction increases with scan rate, suggesting easy intercalation of electrolyte ions in NCV nanohybrids. The significant Q_s charge storage contribution in NCV nanohybrids demonstrates faster charge transfer kinetics due to the expanded gallery height and surface area of NCV nanohybrids via pillared hybridization.

4.5.2.2 GCD study

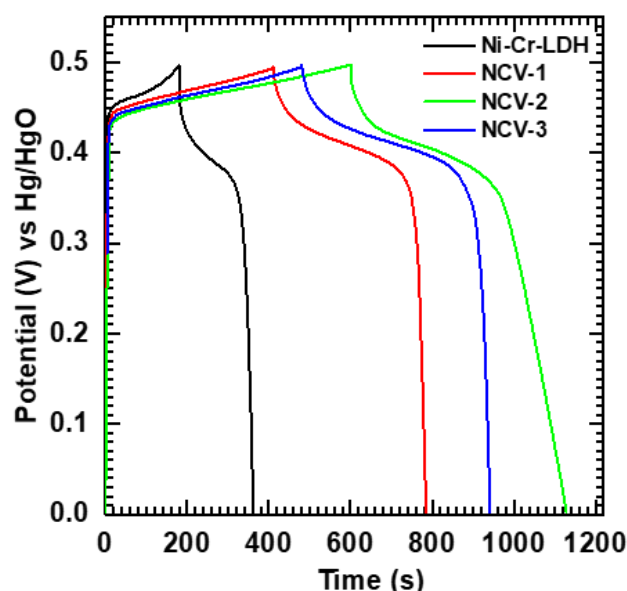


Fig. 4.15: GCD curves of pristine Ni-Cr-LDH and NCV-1, NCV-2, NCV-3 nanohybrids at current density of 1 A g^{-1} .

Additionally, the beneficial effect of the pillared hybridization of Ni-Cr-LDH monolayer with POV anions is tested by GCD measurements. The GCD profiles of NCV nanohybrids and Ni-Cr-LDH electrodes at the current density 1 A g^{-1} within an operating potential window of +0.0 to +0.5 V vs Hg/HgO are shown in Fig. 4.15. Pristine Ni-Cr-LDH electrode displays typical nonlinear GCD curve and vivid discharge plateau with specific capacity of 356 C g^{-1} at 1 A g^{-1} . The nonlinear GCD curve with vivid discharge plateau is assigned to the reversible faradaic reactions. Analogous to pristine Ni-Cr-LDH electrode, all NCV nanohybrids demonstrate

similar GCD curves with prolonged charging-discharging times, indicating enhanced charge storing capacities upon pillared hybridization.

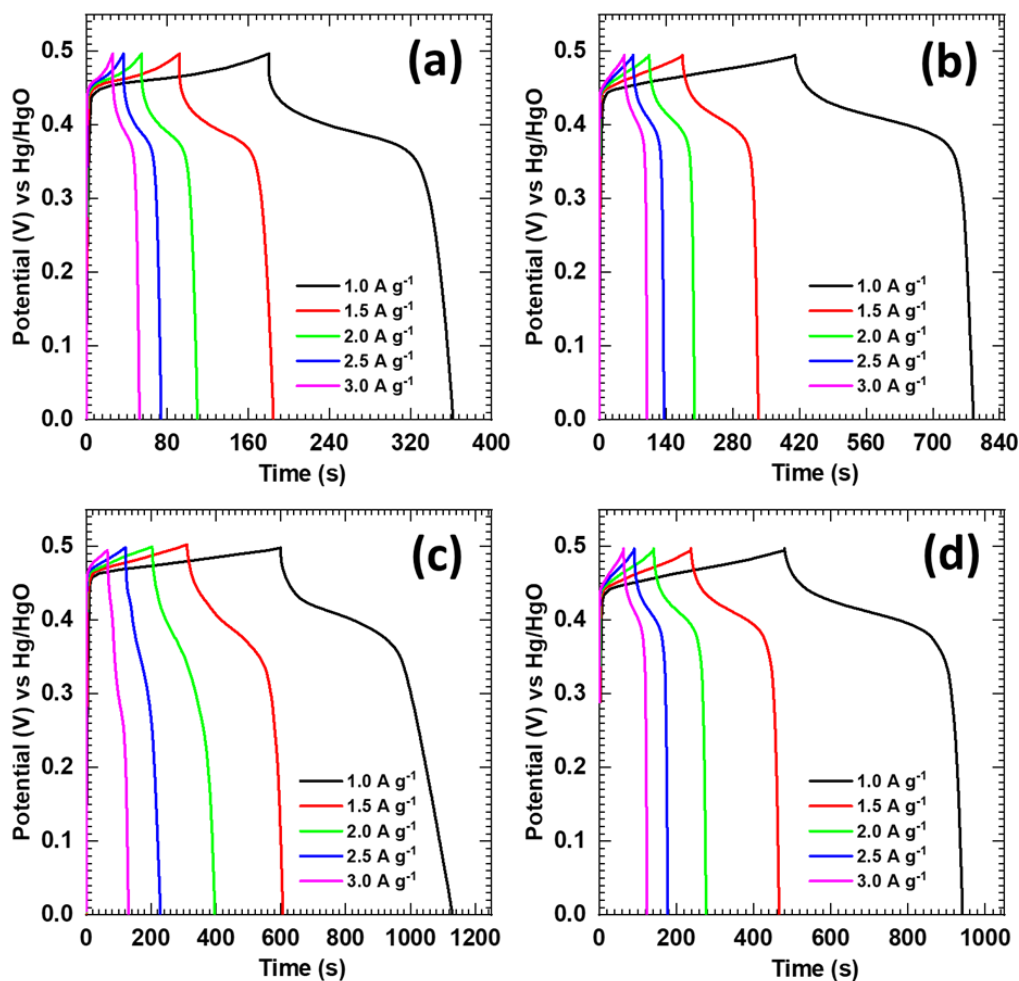


Fig. 4.16: The GCD curves of (a) pristine Ni-Cr-LDH and (b) NCV-1, (c) NCV-2, (d) NCV-3 nanohybrid electrode at different current densities (1-3 A g⁻¹).

The charge storing ability of pristine Ni-Cr-LDH and NCV-2 nanohybrid is further evaluated by performing GCD measurements at different current densities (1 to 3 A g⁻¹), depicted in Fig. 4.16. In contrast to pristine Ni-Cr-LDH, NCV-2 nanohybrid shows superior charge storage characteristics at distinct current densities.

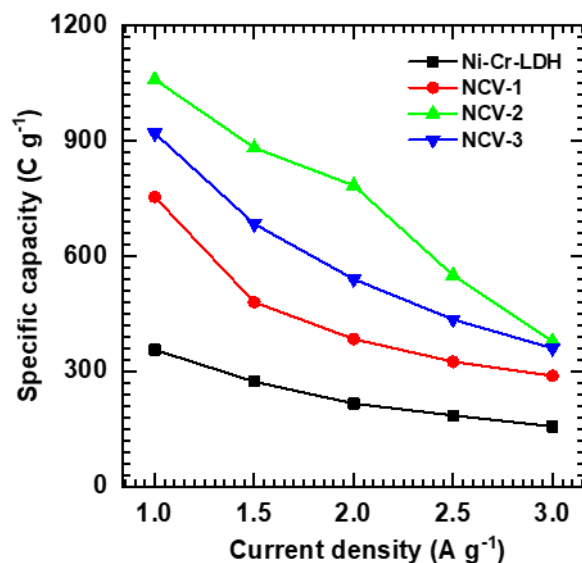


Fig. 4.17: Specific capacity of pristine Ni-Cr-LDH, NCV-1, NCV-2, and NCV-3 nanohybrids at different current densities (1 to 3 A g⁻¹).

The specific capacity vs current density (1 to 3 A g⁻¹) plot of Ni-Cr-LDH and NCV-2 nanohybrid (Fig. 4.17) displays decrement in specific capacity values with respect to increasing charge-discharge current densities. The specific capacity values of NCV-1, NCV-2, and NCV-3 nanohybrids are 754, 1060, and 920 C g⁻¹ respectively, as compare to pristine Ni-Cr-LDH electrode (356 C g⁻¹ at 1 A g⁻¹). The increased specific capacities of NCV nanohybrids are ascribed to the easy ion diffusion between the electrode and electrolyte due to expanded gallery height and formation of mesoporous randomly aggregated nanoplate network morphology of NCV nanohybrids. The pillaring of bulky tetra-charged POV anions (V₄O₁₂⁴⁻) with a high charge to size ratio in NCV nanohybrids occupy less gallery space than mono-charged NO₃¹⁻ anions in pristine Ni-Cr-LDH, leading free accessible interlayer gallery space in NCV nanohybrids for the accelerated ion diffusion and charge storage. The NCV-2 nanohybrid electrode delivered the highest specific capacity as compared to other NCV nanohybrids underscoring the crucial role of optimum POV content on the charge storing ability of NCV nanohybrids. Further increase of pillaring POV content in NCV-3 nanohybrid shows the pernicious effect on specific capacity as a result of cloaking deposition of excess POV anions at edges and surface of NCV-3 nanohybrid. The electrochemical performance of NCV nanohybrid is comparable to or better than the reported LDH-based materials, listed in Table

1.1 (see chapter 1). Therefore, the NCV-2 nanohybrid with optimum POV content is regarded as the best electrode composition to enhance electrochemical activity.

4.5.2.3 EIS study

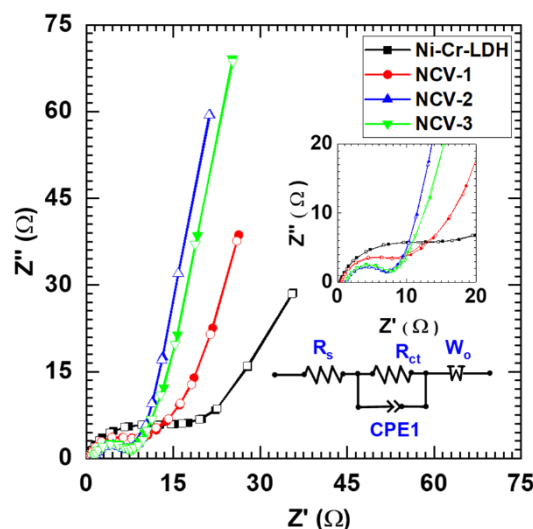


Fig. 4.18: Nyquist plots of pristine Ni-Cr-LDH, NCV-1, NCV-2 and NCV-3 nanohybrids (inset: fitted circuit and magnified view of Nyquist plots).

To examine the effect of POV pillared hybridization on the charge transport rate kinetics, EIS measurements are carried out, and resultant Nyquist plots, simulated equivalent circuit and their magnified views in the higher frequency region are shown in Fig. 4.18. All of the NCV nanohybrid electrodes and pristine Ni-Cr-LDH show partially overlapping semicircles and inclined lines in the high-frequency and low-frequency regions associated with the R_{ct} and R_s , respectively. In the Nyquist plot, the opening point of the semicircle and diameter of extrapolated semicircle represents the R_s and R_{ct} , respectively. The R_s and R_{ct} values are extracted using the curve simulation and fitting analysis. In contrast to the R_s and R_{ct} (0.46 & 14.18 Ω) of pristine Ni-Cr-LDH, the NCV nanohybrids show smaller R_s and R_{ct} values of (0.38 & 5.55 Ω), (0.34 & 4.9 Ω) and (0.37 & 5.15 Ω) for NCV-1, NCV-2 and NCV-3, respectively. As judged from the surface area analysis, all NCV nanohybrids displayed similar surface areas, consequently smaller values of R_s and R_{ct} , indicating improved electrical conductivity of the NCV electrodes upon pillaring of POV anions. Moreover, in the low frequency region, all the NCV nanohybrids display a steeper straight line than the reference Ni-Cr-LDH, demonstrating low

Warburg impedance that allows easy diffusion of electrolyte ions in NCV nanohybrids electrode.

4.5.2.4 Stability study

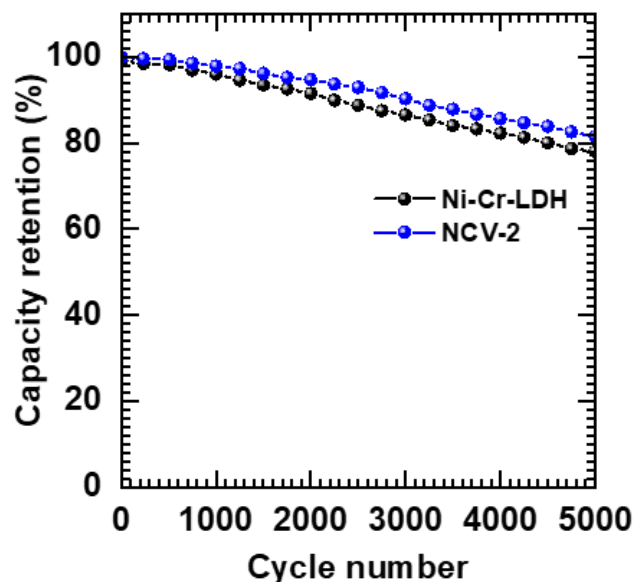


Fig. 4.19: The plot of capacity retention of pristine Ni-Cr-LDH and NCV-2 nanohybrid electrode at 5 A g^{-1} for 5000.

Also, the cycling stability of pristine Ni-Cr-LDH and NCV-2 nanohybrid electrodes is assessed at a current density of 5 A g^{-1} for 5000 GCD cycles (See Fig. 4.19). NCV-2 nanohybrid electrode exhibits superior cycling stability (82%) than the pristine Ni-Cr-LDH electrode (78%). Subsequently, the remarkable electrochemical performance improvement in NCV nanohybrids is attributed to the easy electrolyte ions diffusion and improved electrical conductivity. Present single electrode electrochemical performance of NCV nanohybrids vividly represents advantages of NCV nanohybrids as a redox electrode in HSC.

4.6. Electrochemical performance of hybrid supercapacitor device

4.6.1 Hybrid supercapacitor device fabrication

The HSC device was fabricated using the NCV nanohybrid coated SS foil as the positive electrode (cathode) and rGO coated on SS as the negative electrode (anode) in a 2M KOH aqueous electrolyte. Before making HSC, the mass ratio

between positive to negative electrodes were balanced using the following equation,

$$\frac{m_+}{m_-} = \frac{C_- \times \Delta V_-}{C_+ \times \Delta V_+} \quad (4.3)$$

In above equation m_+ , C_+ and, m_- , C_- are the masses and specific capacities of the positive (NCV) and negative (rGO) electrodes, respectively. ΔV_+ and ΔV_- are the working voltage windows of the positive and negative electrodes, respectively. Using this equation, the optimal mass ratio of Ni-Cr-LDH to rGO electrodes was calculated as 1:2.92.

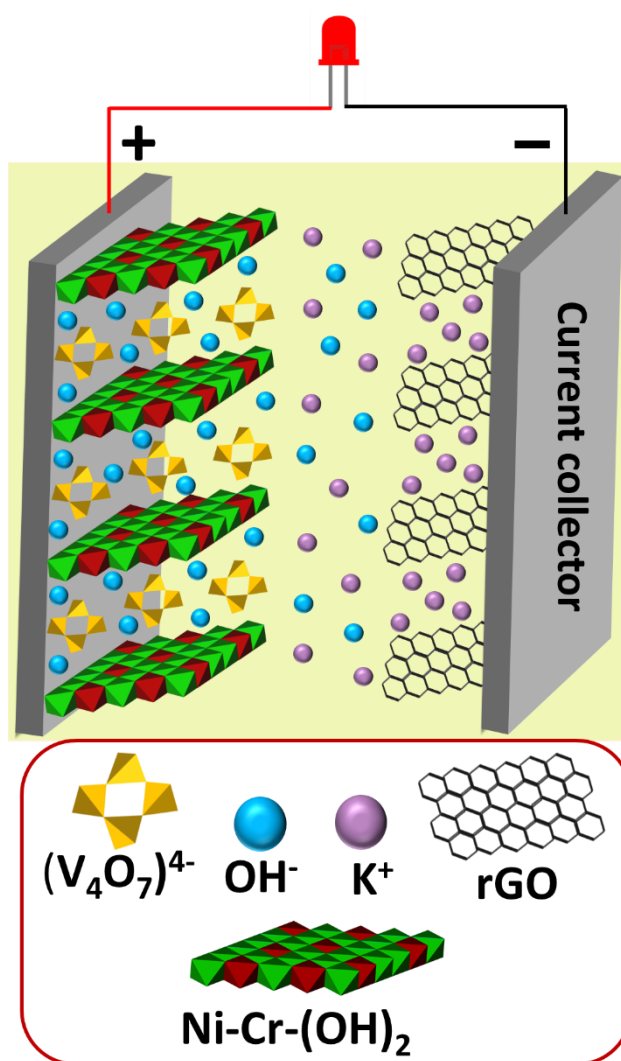


Fig. 4. 20: Schematic illustration of NCV-2||rGO HSC.

To estimate the potential of self-assembled nanohybrid electrodes for real-time applications, the full cell HSC was assembled that comprises NCV-2

nanohybrid and rGO as a cathode and anode, respectively, as presented in Fig. 4.20. An aqueous 2M KOH is used as an electrolyte.

4.6.2 CV study

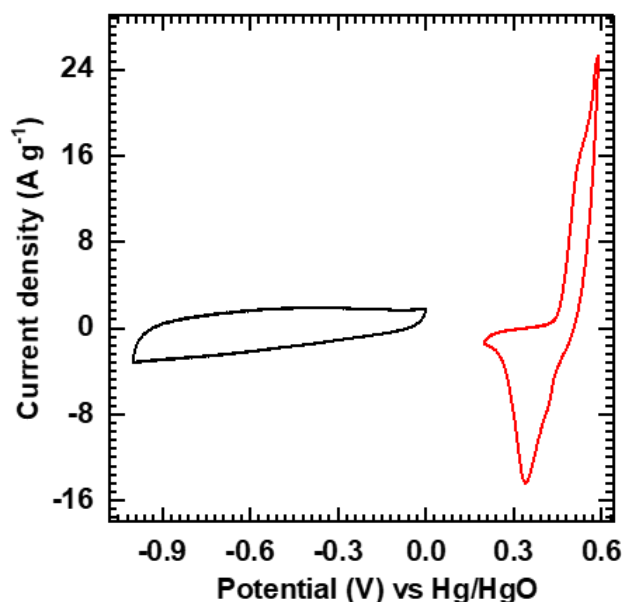


Fig. 4.21: CV curves of NCV-2 (red) nanohybrid electrode and rGO (black) at a scan rate of 20 mV s⁻¹.

As NCV nanohybrid and rGO electrodes have different specific charge capacities, to ensure the maximum specific capacity and voltage window of HSC, there is of utmost necessity to balance the charges between both electrode materials before assembling the HSC. The charge balance for both electrode materials while assembling NCV-2||rGO HSC can be achieved by adjusting the mass loading ratio of the cathode and an anode. Detail information about mass balancing is given in the previous section. NCV nanohybrid electrode demonstrates a battery type charge storage mechanism in the potential window of 0.2 to 0.6 V vs Hg/HgO. Hence, it is expected that full cell NCV-2||rGO HSC can be operated in the voltage window of +1.6 V. The CV graphs of NCV-2 nanohybrid and rGO NS electrode at a scan rate of 20 mV s⁻¹ in different potential windows are shown in Fig.4.21.

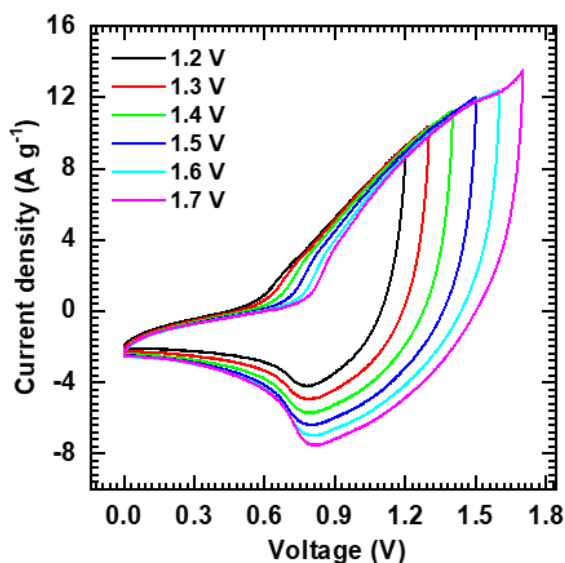


Fig. 4.22: CV curves of the HSC performed in different potential windows at 100 mV s^{-1} .

To ascertain the proper voltage window for assembled full cell NCV-2||rGO HSC, CV measurements are performed at varying potential windows at a constant sweep rate of 100 mV s^{-1} in aqueous 2M KOH electrolyte, and corresponding CV graphs are presented in Fig. 4.22. The CV profiles of NCV-2||rGO HSC within the voltage windows of 0-1.2 V to 0-1.6 V do not show any polarization phenomenon; thus, the potential window of 0 to 1.6 is selected for the proper operation of NCV-2||rGO HSC with optimum ED and without any operational distortions.

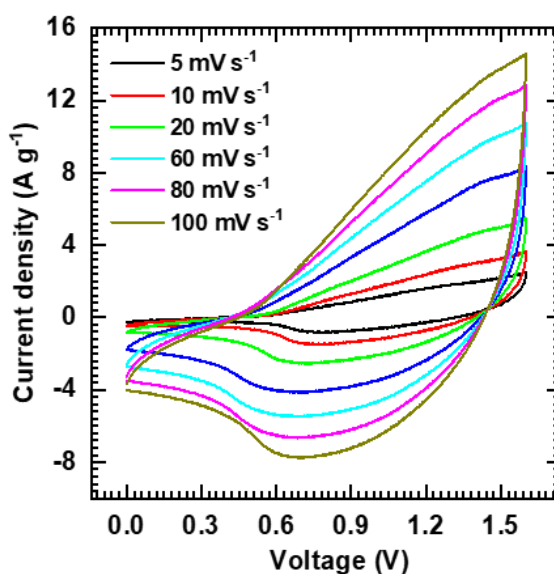


Fig. 4.23: CV curves of HSC device at different sweep rates from 5 to 100 mV s^{-1} .

Also, CV curves of NCV-2||rGO HSC are recorded at various scan rates (5 to 100 mV s^{-1}) within the potential window of 0-1.6 V, and obtained results are shown in Fig. 4.23. CV curves at various scan rates clearly validate involvement of both the battery and the EDLC type charge storage processes in NCV-2||rGO HSC. Moreover, the area under the CV curves and characteristic response current linearly increase with scan rates, strongly suggesting equal charge delivery by both electrodes, with superior reversibility.

4.6.3 GCD study

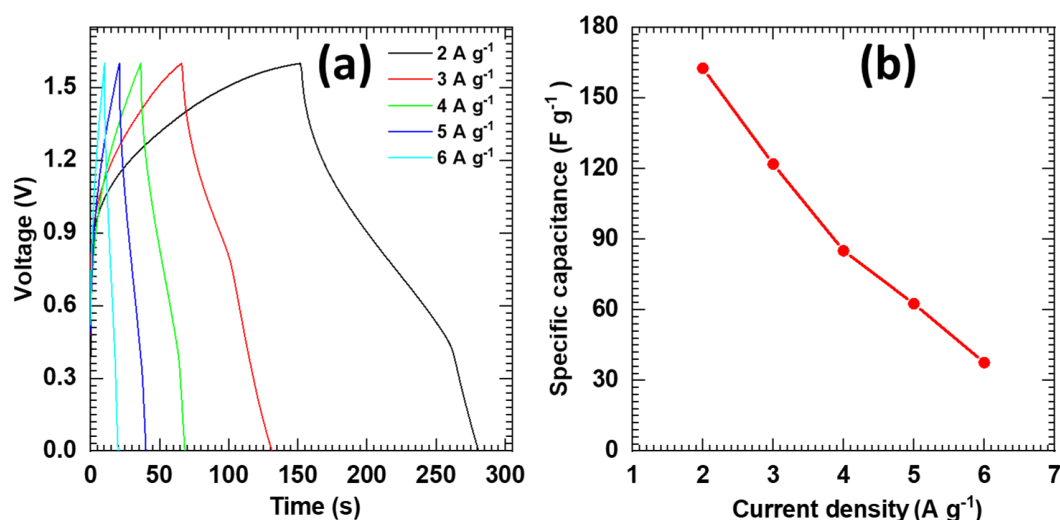


Fig. 4.24: (a) GCD curves at current densities 2-6 A g^{-1} , (b) the plot of C_s verses current densities.

To probe the charge storing capabilities and fast delivery of NCV-2||rGO HSC, GCD measurements are executed at different current densities (2 to 6 A g^{-1}), as shown in Fig. 4.24(a). Resultant GCD curves demonstrate the virtually linear and symmetric behavior of the charging-discharging curves, representing the excellent reversibility of the nanohybrid electrode materials. Additionally, NCV-2||rGO HSC exhibits discharge curves with longer charge-discharge times, indicating superior electrode-electrolyte interaction that enhances the charge storing ability of HSC. In addition, GCD curves do not exhibit any potential drop while discharging intercourse suggests superior electrical conductivity of the electrode and better electrolyte compatibility. As NCV-2||rGO HSC demonstrated capacitive characteristics, the performance is also calculated in terms of C_s . The NCV-2||rGO

HSC displays the highest Cs of 162.5 F g^{-1} at a current density of 2 A g^{-1} that decreased up to 37 F g^{-1} with higher current densities, as depicted in Fig. 4.24(b).

4.6.4 Ragone plot

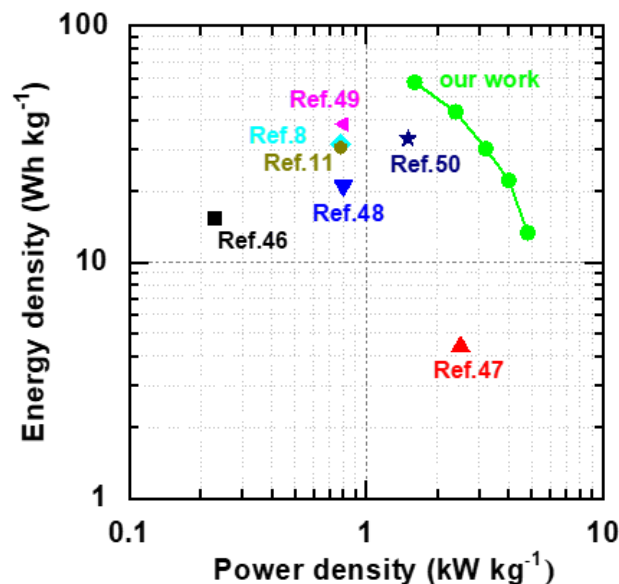


Fig. 4.25: Comparative Ragone plot related to the ED and PD of the HSC device with available literature.

Figure 4.25 shows the Ragone plot of the NCV-2||rGO HSC. The NCV-2||rGO HSC delivered the highest ED of 57.78 Wh kg^{-1} with a PD of 1.59 kW kg^{-1} . Obtained values are much superior as compared recently reported HSC, such as NiAl-LDHs/rGO||AC (ED: 15.4 Wh kg^{-1} ; PD: 230 W kg^{-1}) [46], CoMn-LDHs||AC (ED: 4.4 Wh kg^{-1} ; PD: 2500 W kg^{-1}) [47], NiAl-LDHs||AC (ED: 21 Wh kg^{-1} ; PD: 800 W kg^{-1}) [48], B-CoNi-LHSs||AC (ED: 31.7 Wh kg^{-1} ; PD: 780 W kg^{-1}) [8], NiCoO₂||AC (ED: 38.4 Wh kg^{-1} ; PD: 800 W kg^{-1}) [49], NiAl-LDH-NF||GNS-NF (ED: 30.2 Wh kg^{-1} ; PD: 800 W kg^{-1}) [10], NiV LDH||AC (ED: 30.6 Wh kg^{-1} ; PD: 0.78 kW kg^{-1}) [11], and ZIF-67-LDH-CNP-110||AC (ED: 33.29 Wh kg^{-1} ; PD: 0.15 kW kg^{-1}) [50]. The superior performance of NCV-2||rGO HSC can be attributed to the expanded surface area, high electrical conductivity and optimum charge balance of constituent NCV-2 and rGO electrodes. Moreover, expanded gallery height and mesoporous randomly aggregated nanoplate network morphology of NCV nanohybrids enables rapid diffusion of electrolyte ions in the interior of NCV-2 cathode and perform charge

storing redox reactions. Ultimately, the present NCV-2||rGO HSC display superior performance than the recently reported LDH based cathodes.

4.6.5 Cycling stability

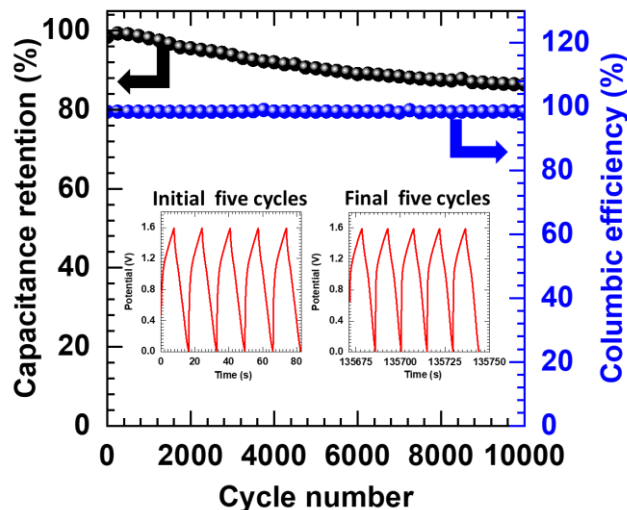


Fig. 4.26: Cycling stability plots for the HSC device, The inset shows the initial and final GCD cycles at a current density of 5 A g^{-1} .

The capacitance retention and Coulombic efficiency vs cycle number of NCV-2||rGO HSC subjected to 10,000 GCD cycles are shown in Fig. 4.26. NCV-2||rGO HSC exhibited superior electrochemical durability by showing remarkable capacitance retention of 87% and good Coulombic efficiency of 98% after being subjected to 10,000 GCD cycles at a current density of 5 A g^{-1} , underscoring its superior functionality for high-energy and power applications.

4.6.6 EIS study

Fig. 4.27 shows the Nyquist plot corresponding to the NCV-2||rGO HSC before and after 10,000 GCD cycles. The NCV-2||rGO HSC shows R_s values of 0.74Ω and 1.12Ω and R_{ct} values of 8.85Ω and 14.35Ω , before and after cycling, respectively. Superior conductivity and accelerated diffusion kinetics of electrolytic ions during electrochemical reactions are suggestive outcomes of low resistance values showed by NCV-2||rGO HSC. Moreover, EIS analysis also revealed a prominent role of POV intercalative hybridization in improving the charge transfer kinetics. The exceptional electrochemical characteristics of NCV-2||rGO HSC are not only attributable to the favourably expanded inter-gallery spacing and

randomly aggregated nanoplate network morphology but also to the considerably lower resistance value of the NCV-2||rGO HSC that is affirmed by the EIS analysis.

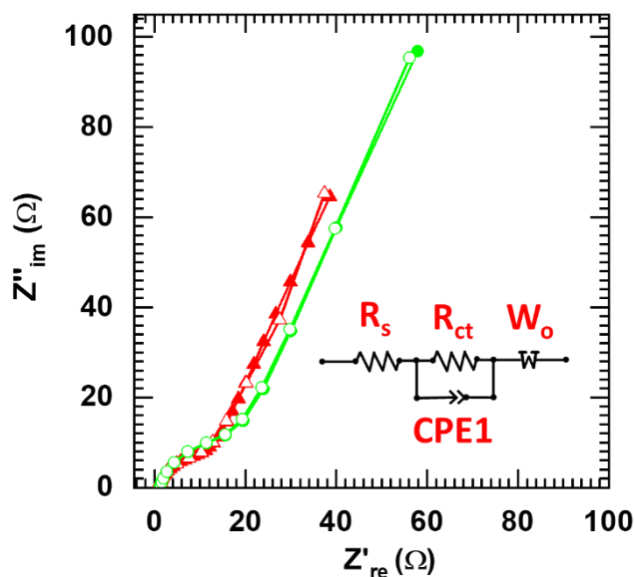


Fig. 4.27: Nyquist plots for the NCV-2||rGO HSC before (red) and after (green) stability (Inset: fitted circuit).

4.6.7 Practical demonstration of HSC

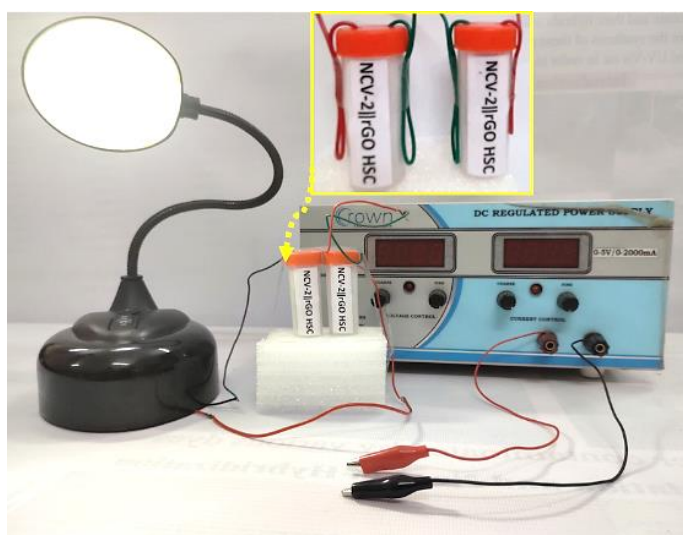


Fig. 4.28: Actual demonstration of the NCV-2||rGO HSC.

The practical application of the NCV-2||rGO HSC device is demonstrated by charging two serially linked devices for 30 seconds at a constant potential of +3.2 V and turning on an LED lamp, as shown in Fig. 4.28. The blazing intensity of white

LEDs, in particular, suggests that the NCV-2||rGo HSC device has a high power capacity, while the extended brightening time interval of LEDs suggests that it has a higher energy storing capacity. This demonstration clearly implies the enormous potential of the device as the most promising energy storage device in a verities of portable electronic application.

4.7 Conclusions

In summary, mesoporous nanohybrids of 2D Ni-Cr-LDH NSs pillared with POV anions were synthesized by electrostatically driven exfoliation-restacking process and investigated electrochemical activity. The highest specific capacity of 1060 C g^{-1} at a current density of 1 A g^{-1} was obtained for NCV nanohybrid electrode, which was much higher as compared to that of pristine Ni-Cr-LDH (356 C g^{-1}). The scalable enhancement of the EES capability of NCV nanohybrids is attributed to the mesoporous house-of-cards-type interconnected network morphology and increased freely accessible gallery space with high electrical conductivity and facilitated ions diffusion pathways. Also, the remarkable electrochemical performance improvement in NCV nanohybrids is attributed to the easy electrolyte ions diffusion and improved electrical conductivity thereof. Present single electrode electrochemical performance of NCV nanohybrids vividly represents the effectiveness of POV pillared hybridization as a redox electrode material in HSC.

The HSC with NCV as a positive electrode and rGO as a negative electrode delivered an outstanding Cs of 162.5 F g^{-1} at a current density of 2 A g^{-1} . Additionally, the HSC exhibited an ED of 57.78 Wh kg^{-1} at a PD of 1.59 kW kg^{-1} and efficient cycling stability for 10,000 charge-discharge cycles. The commercial applicability of NCV-2||rGO HSC is assessed by performing a demonstration to power up the LED lamp. The NCV-2||rGO HSC device exhibits excellent ED as well as PD, good rate capability with superior cyclic stability and these features suggest significant potential of NCV-2||rGO HSC for application in various portable and flexible electronic devices.

4.8 References

- [1] N. R. Chodankar, H. D. Pham, A. K. Nanjundan, J. F. S. Fernando, K. Jayaramulu, D. Golberg, Y-K. Han, D. P. Dubal, *Small* 16 (2020) 1-35.
- [2] J. Zhou, J. Yu, L. Shi, Z. Wang, H. Liu, B. Yang, C. Li, C. Zhu, J. Xu, *Small* 14 (2018) 1-9.
- [3] Y. Jiao, A. M. Hafez, D. Cao, A. Mukhopadhyay, Y. Ma, H. Zhu, *Small* 14 (2018) 1-20.
- [4] Y. Huang, F. Cui, J. Bao, Y. Zhao, J. Lian, T. Liu, H. Li, *J. Mater. Chem. A* 7 (2019) 20778-20789.
- [5] C. Prasad, H. Tang, W. Liu, *J. Nanostructure Chem.* 8 (2018) 393-412.
- [6] M. Shao, R. Zhang, Z. Li, M. Wei, D. G. Evans, X. Duan, *Chem. Commun.* 51 (2015) 15880-15893.
- [7] S. Chandra Sekhar, G. Nagaraju, B. Ramulu, S. Arbaz, D. Narsimulu, S. K. Hussain, J. S. Yu, *Nano Energy* 76 (2020) 105016.
- [8] Y. Li, Z. Luo, H. Qin, S. Liang, L. Chen, H. Wang, C. Zhao, S. Chen, *J. Colloid Interface Sci.* 582 (2020) 842-851.
- [9] W. Wang, Y. Lu, M. Zhao, R. Luo, Y. Yang, T. Peng, H. Yan, X. Liu, Y. Luo, *ACS Nano* 13 (2019) 12206-12218.
- [10] L. Zhang, K. N. Hui, K. S. Hui, H. Lee, *J. Power Sources* 318 (2016) 76-85.
- [11] A. Tyagi, M. C. Joshi, A. Shah, V. K. Thakur, R. K. Gupta, *ACS Omega* 4 (2019) 3257-3267.
- [12] A. S. Patil, J. L. Gunjekar, C. D. Lokhande, U. M. Patil, S. V. Sadavar, N. S. Padalkar, R. B. Shinde, M. M. Wagha, J. S. Bagi, *Synth. Met.* 264 (2020) 1-9.
- [13] L. Mohapatra, K. Parida, M. Satpathy, *J. Phys. Chem. C* 116 (2012) 13063-13070.
- [14] Y. Xiao, D. Su, X. Wang, S. Wu, L. Zhou, S. Fang, F. Li, *Sci. China Mater.* 61 (2018) 263-272.
- [15] D-H. Park, S-J. Hwang, J-M. Oh, J.-H. Yang, J-H. Choy, *Prog. Polym. Sci.* 38 (2013) 1442-1486.
- [16] D. G. Evans, X. Duan, *Chem. Commun.* (2006) 485-496.
- [17] S. Omwoma, W. Chen, R. Tsunashima, Y. F. Song, *Coord. Chem. Rev.* 258 (2014) 58-71.
- [18] C. F. Baes and R. E. Mesmer, *In The hydrolysis of cations*. Wiley, New York, 1976; p. 241.
- [19] J. Livage, *Coordin. Chem. Rev.* 178 (1998) 999-1018.
- [20] Y. Hayashi, *Coordin. Chem. Rev.* 255 (2011) 2270-2280.
- [21] T. Kwon, G. A. Tsigdinos, T. J. Pinnavaia, *J. Am. Chem. Soc.* 110 (1988) 3653-3654.
- [22] J. L. Gunjekar, T. W. Kim, I. Y. Kim, J. M. Lee, S. J. Hwang, *Sci. Rep.* 3 (2013) 2080.
- [23] J. L. Gunjekar, I. Y. Kim, S-J. Hwang, *Eur. J. Inorg. Chem.* 7 (2015) 1198-1202.
- [24] R. Z. Ma, Z. P. Liu, L. Li, N. Iyi, T. Sasaki, *J. Mater. Chem.* 16 (2006) 3809-3813.
- [25] Y. Zhao, S. Zhang, B. Li, H. Yan, S. He, L. Tian, W. Shi, J. Ma, M. Wei, D. G. Evans, X. Duan, *Chem. Eur. J.* 17 (2011) 13175-13181.
- [26] J. L. Gunjekar, B. Hou, A. I. Inamdar, S. M. Pawar, A. Talha, A. Ahmed, H. S. Chavan, J. Kim, S. Cho, S. Lee, Y. Jo, S. J. Hwang, T. G. Kim, S. N. Cha, H. Kim, H. Im, *Small* 14 (2018) 1-10.
- [27] S. Xia, T. Dai, Y. Meng, X. Zhou, G. Pan, X. Zhange, Z. Ni, *Phys. Chem. Chem. Phys.* 22 (2020) 12630-12643.
- [28] N. Baliarsingh, L. Mohapatra, K. Parida, *J. Mater. Chem. A* 1 (2013) 4236-4243.

- [29] R. A. Nyquist, R. O. Kagel, *Infrared spectra of inorganic compounds* (3800-450cm⁻¹), Academic Press, New York, 1971.
- [30] L. Zhang, J. Wang, J. Zhu, X. Zhang, K. S. Huib, K. N. Huic, *J. Mater. Chem. A* 2013, 1, 9046-9053.
- [31] F. Kooli, W. Jones, *Inorg. Chem.* 34 (1995) 6237-6238.
- [32] C. Barriga, W. Jones, P. Malet, V. Rives, M. A. Ulibarri, *Inorg. Chem.* 37 (1998) 1812-182.
- [33] M. A. Ulibani, F. M. Labajos, V. Rives, R. Trujillano, W. Kagunya, W. Jones, *Inorg. Chem.* 33 (1994) 2592-2599.
- [34] J. L. Gunjekar, A. I. Inamdar, B. Hou, S. Cha, S. M. Pawar, A. A. Abu Talha, H. S. Chavan, J. Kim, S. Cho, S. Lee, Y. Jo, H. Kim, H. Im, *Nanoscale* 10 (2018) 8953-8961.
- [35] A. S. O. Gomes, N. Yaghini, A. Martinelli, E. J. Ahlberg, *J. Raman Spectrosc.* 48 (2017) 1256-1263.
- [36] L. P. F. Benício, D. Eulálio, L. M. Guimarães, F. G. Pinto, L. M. da Costa, J. Tronto, *Mater. Res.*, 21 (2018) 1-13.
- [37] S. Mulkapuri, S. K. Kurapati, S. Mukhopadhyay, S. K. Das, *New J. Chem.* 43 (2019) 17670-17679.
- [38] M. Aureliano, C. A. Ohlin, M. O. Vieira, M. P. M. Marques, W. H. Casey, L. A. E. B. de Carvalho, *Dalton Trans.* 45(2016)7391-7399.
- [39] J. B. Condon, *Surface area and porosity determinations by physisorption: measurements and theory*, 1st ed. Elsevier: Amsterdam; Boston, 2006; p 274.
- [40] W. Ye, X. Fang, X. Chen, D. Yan, *Nanoscale* 10 (2018) 19484-19491.
- [41] Y. Yang, L. Dang, M. J. Shearer, H. Sheng, W. Li, J. Chen, P. Xiao, Y. Zhang, R. J. Hamers, S. Jin, *Adv. Energy Mater.* 8 (2018) 1-9.
- [42] T. Zhou, Z. Cao, P. Zhang, H. Ma, Z. Gao, H. Wang, Y. Lu, J. He, Y. Zhao, *Sci. Rep.* 7 (2017) 1-9.
- [43] J. Mendialdua, R. Casanova, Y. Barbaux, *XPS studies of V₂O₅, V₆O₁₃, VO₂ and V₂O₃* J. Electron Spectrosc 71 (1995) 249-261.
- [44] S. Wu, X. Yang, J. Hu, H. Ma, Z. Lin, C. Hu, *CrystEnComm* 17 (2015) 1625-1630.
- [45] G. Silversmit, D. Depla, H. Poelman, G. B. Marin, R. D. Gryse, *J. Electron. Spectrosc. Relat. Phenom.* 135 (2004) 167-175.
- [46] X. Ge, C. Gu, Z. Yin, X. Wang, J. Tu, J. Li, *Nano Energy* 20(2016) 185-193.
- [47] A. D. Jagadale, G. Guan, X. Li, X. Du, X. Ma, X. Hao, A. Abudula, *J. Power Sources* 306(2016) 526-534.
- [48] L. Zhang, H. Yao, Z. Li, P. Sun, F. Liu, C. Dong, J. Wang, Z. Li, M. Wu, C. Zhang and B. Zhao, *J. Alloys Compd.* 711(2017) 31-41.
- [49] B. Liu, J. Hou, T. Zhang, C. Xu, H. Liu, *J. Mater. Chem. A* 7 (2019) 16222-16230.
- [50] Z. Xiao, Y. Bao, Z. Li, X. Huai, M. Wang, P. Liu, L. Wang, *ACS Appl. Energy Mater.* 2 (2019) 1086-1092.



CHAPTER-5

**Synthesis, Characterization and
Electrochemical Performance
Evaluation of Ni-Cr-LDH
Hybridized with POW Anions and
HSC Device**

CHAPTER 5

Synthesis, Characterization and Electrochemical Performance Evaluation of Ni-Cr-LDH Hybridized with POW Anions and HSC

Sr. No.	Title		Page No.
5.1	Introduction		135-136
5.2	Experimental details		136-138
	5.2.1	<i>Chemicals</i>	136
	5.2.2	<i>Synthesis of Ni-Cr-LDH nanosheets hybridized with POW anions</i>	137-138
5.3	Results and discussion		138-149
	5.3.1	<i>XRD study</i>	138-139
	5.3.2	<i>FTIR study</i>	139-140
	5.3.3	<i>Micro-Raman study</i>	140-141
	5.3.4	<i>FESEM study</i>	141-142
	5.3.5	<i>EDS study</i>	142-144
	5.3.6	<i>HRTEM study</i>	144-145
	5.3.7	<i>BET surface area study</i>	146-147
	5.3.8	<i>XPS study</i>	147-149
5.4	Conclusions		149
5.5	Electrochemical performance evaluation of Ni-Cr-LDH nanosheets hybridized with POW anions		
5.5.1	Electrode preparation		150
5.5.2	Results and discussion		150-158
	5.5.2.1	<i>CV study</i>	150-153
	5.5.2.2	<i>GCD study</i>	153-156
	5.5.2.3	<i>EIS study</i>	156-157
	5.5.2.4	<i>Stability study</i>	157-158
5.6	Electrochemical performance evaluation of NCW-2 rGO hybrid supercapacitor device		
	5.6.1	<i>CV study</i>	159-160
	5.6.2	<i>GCD study</i>	161

	5.6.3	<i>Ragone plot</i>	161-162
	5.6.4	<i>Stability study</i>	162-163
	5.6.5	<i>EIS study</i>	163-164
	5.6.6	<i>Practical Demonstration of HSC</i>	164
5.7	Conclusions		164-165
5.8	References		165-167

5.1 Introduction

Hybridization of nanostructured inorganic materials with functional guest species can provide an effective synthetic strategy to design novel multifunctional nanohybrid materials with improved performances [1, 2]. 2D inorganic NSs derived from the exfoliation of layered inorganic crystals are excellent 2D platforms for hybridization with various guest species. Hybridization of exfoliated 2D inorganic NSs with high interfacial coupling is advantageous for fine-tuning of physicochemical properties, chemical bonding natures of hybridized components, surface features and electronic properties, which ensures the usefulness of resultant hybrid materials for multifunctional applications [3]. Among the various application areas, inorganic NS-based nanohybrid materials are highly advantageous as the electrode material in the EES devices specially in Li-ion batteries and supercapacitors [3-8]. The hybrid superstructures of host 2D inorganic NSs and functional guest nanoclusters prepared via electrostatically driven self-assembly based on intercalative hybridization route would likely propose some novel and efficient electrode materials for electrochemical energy storage devices.

LDH represents an important class of 2D layered materials that has been vividly explored for many applications [9]. Features like facile tunability of the chemical composition, unique anion intercalated layered structure, ion exchange properties, multiple redox states of constituent elements are some of the worth-mentioning properties of LDHs that ensures their huge potential as a battery-type electrode in HSC [10]. However, the performance of the LDH based electrodes is limited by the loss in the electroactive surface area affected by particle aggregation and compact layered structure [11]. To address these difficulties, substantial research has been conducted to synthesize LDHs with expanded surface area and enlarged interlayer gallery height via intercalation of a variety of bulky anionic inorganic and organic guest species [12-14]. Recently reported self-assembly strategy of exfoliation of LDH into cationic NSs and restacking them with anionic guest species provides excellent control over the chemical composition and more open porous structure of LDHs [15]. POMs are the anionic 0D metal-oxygen clusters that possesses multiple redox states and excellent electrochemical properties, which can be the best choice as a guest for intercalative hybridization

[16]. Moreover, they have the ability to act as a stable multielectron acceptor having tunable structures and properties as per particular demands with well-defined molecular dimensions [17, 18]. In order to develop advanced HSC devices, novel electrode materials are continuously explored that can deliver high ED with the desired PD. Therefore, the HSC device, which consists of battery and capacitive-type electrodes, is currently under development to overcome the energy gap restriction. A suitable combination of these two types of electrodes in terms of the charge balance can broaden the working potential window, resulting in a higher capacity as well as better ED [19, 20]. In this regard, HSC with the battery-type 2D LDH based nanohybrid cathode can provide a high ED. In contrast, the well-known carbonaceous anode can provide EDLCs with a high PD and long cycle life.

This work proposes a novel approach for preparing prospective electrode material for efficient HSC devices with high energy density. Layer-by-layer Ni-Cr-LDH-POW (NCW) nanohybrids are synthesized via electrostatic self-assembly between cationic Ni-Cr-LDH NSs and anionic polyoxotungstate (POW) nanoclusters through the exfoliation-reassembling method. The effects of POW hybridization on the electrochemical activity, crystal structure, and physicochemical properties of the pristine Ni-Cr-LDH are investigated. The proposed NCW nanohybrids deliver markedly superior electrochemical activity in aqueous electrolytes, suggesting their potential application as an electrode for the fabrication of HSCs. For validation, the aqueous HSC device is fabricated with the NCW nanohybrid and rGO NSs as a battery (cathode) and capacitive type (anode) electrodes, respectively and, their electrochemical properties are extensively evaluated. Moreover, the practical viability of the HSC device is also demonstrated by powering LED lamp.

5.2 Experimental details

5.2.1 Chemicals

Nickel nitrate $\text{Ni}(\text{NO}_3)_2$, chromium nitrate $\text{Cr}(\text{NO}_3)_3$, sodium tungstate (Na_2WO_4), sodium nitrate (NaNO_3), and sodium hydroxide (NaOH) purchased from Sigma-Aldrich were used without additional purification.

5.2.2 Synthesis of Ni-Cr-LDH hybridized with polyoxotungstate anions (NCW)

Pristine Ni-Cr-LDH in NO_3^{1-} form and its exfoliation was achieved according to previous Chapter-III [21]. The self-assembled NCW nanohybrids were synthesized by the drop-wise addition of the aqueous solution of POW anions to the formamide suspension of Ni-Cr-LDH NSs under constant stirring at ambient temperature. The flocculation product of NCW nanohybrid was restored by centrifugation at 7000 rpm. The resulting product was washed with formamide and absolute ethanol and, finally, freeze-dried to ensure a solid NCW nanohybrid product. To avoid carbonate contamination from solvents, all of the preparation processes in this study were carried out in an N_2 atmosphere and decarbonated water.

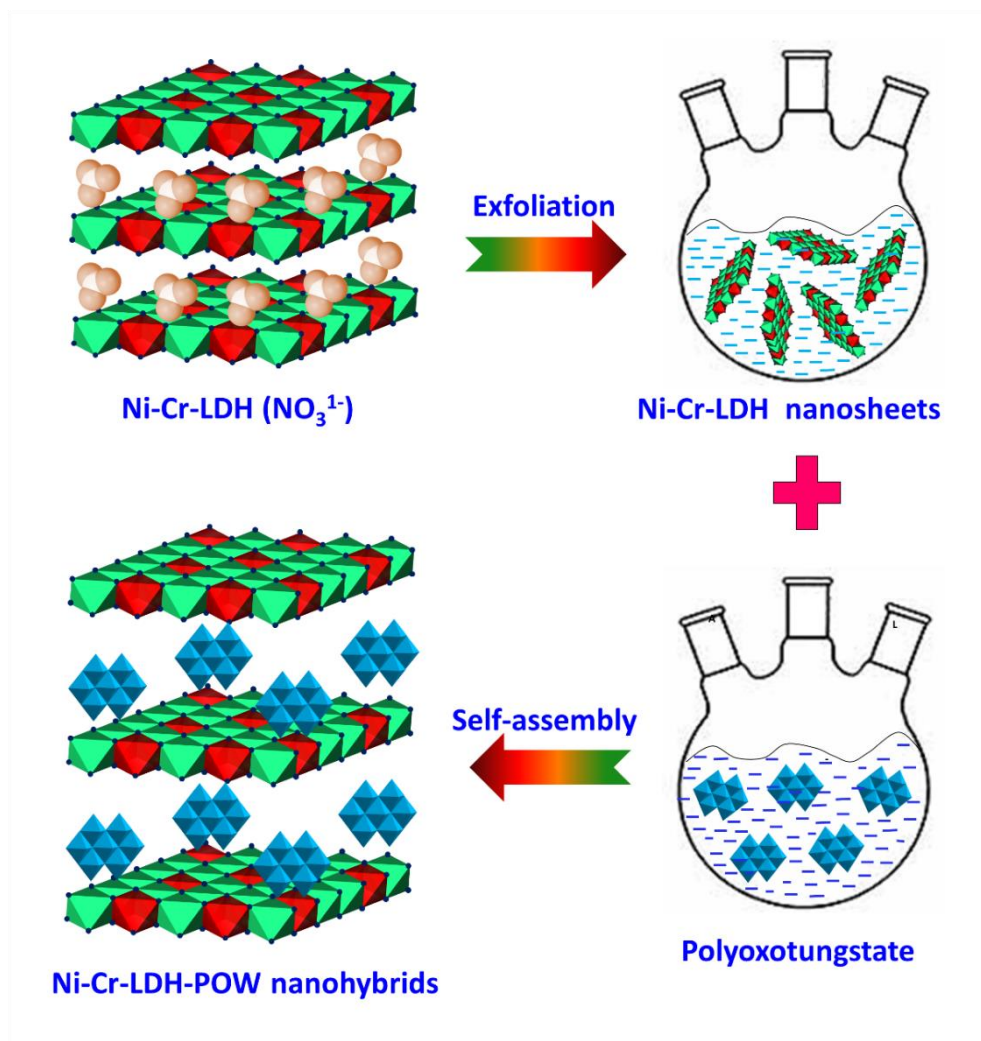


Fig. 5.1: Schematic of the exfoliation-reassembling route for the preparation of NCW nanohybrids.

The schematic representation of the exfoliation-restacking process is shown in Fig. 5.1. For the synthesis of NCW nanohybrids, three distinct POW: Ni-Cr-LDH molar fractions of 1:1, 2:1, and 3:1 were used to investigate the effect of chemical composition variation on their physicochemical properties. The prepared NCW nanohybrids are labeled as NCW-1, NCW-2, and NCW-3, correspondingly.

5.3 Results and discussion

5.3.1 XRD study

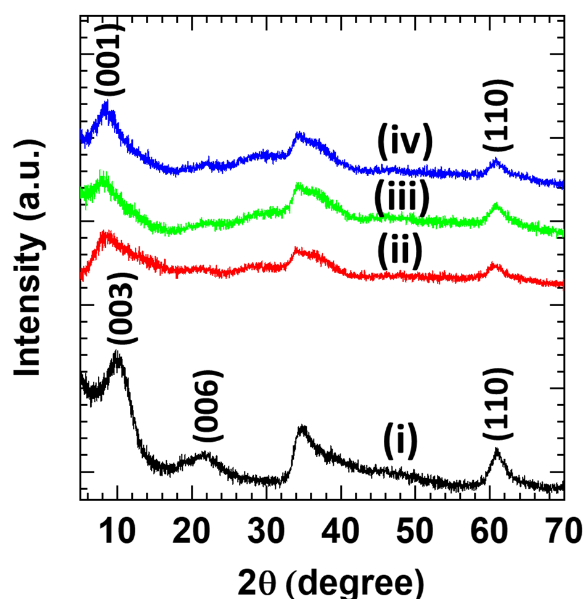


Fig. 5.2: XRD patterns of (i) pristine Ni-Cr-LDH, (ii) NCW-1, (iii) NCW-2, and (iv) NCW-3 nanohybrids.

The powder XRD patterns of the self-assembled NCW nanohybrids in comparison with pristine Ni-Cr-LDH are plotted in Fig. 5.2. The pristine Ni-Cr-LDH shows well-developed basal reflections ($00l$) with the hexagonal LDH phase having R-3m space group rhombohedral symmetry. The lattice constants of pristine Ni-Cr-LDH, $a = 0.31$ nm and $c = 0.88$ nm are estimated from least-squares fitting, which matches well with the NO_3^{1-} intercalated LDH structure [24]. All NCW nanohybrids show similar series of ($00l$) Bragg reflections. After self-assembly with POW, ($00l$) reflection series of the pristine Ni-Cr-LDH is shifted towards the low-angle region, demonstrating the intercalation of POW anions in-between the Ni-Cr-LDH NSs and expansion of interlayer spacing. The self-assembled NCW nanohybrids demonstrate c -axis parameters of 1.07, 1.14, and 1.05 nm, indicating expanded gallery heights of 0.62, 0.69, and 0.60 nm for NCW-1, NCW-2, and NCW-3

nanohybrids, respectively, higher than pristine Ni-Cr-LDH (0.43 nm). Interestingly, such expansion of gallery height is independent from POW/Ni-Cr-LDH fraction, indicating high tolerance of POW anions in NCW. The pristine Ni-Cr-LDH and NCW nanohybrids display the (110) peak at 61° and a broad hump peak extended over 32-43°, which underscore the conservation of the Ni-Cr-LDH NSs in-plane structure and turbostatic stacking structure.

5.3.2 FTIR study

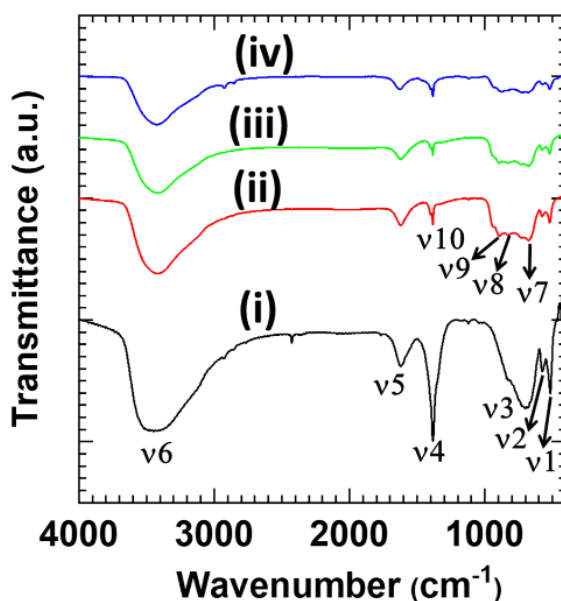


Fig. 5.3: FTIR spectra of the (i) pristine Ni-Cr-LDH (ii) NCW-1, (iii) NCW-2, and (iv) NCW-3 nanohybrids.

FTIR spectroscopy were used to study nature of chemical bonding, microscopic structural variations and the type of intercalated POW anions in NCW nanohybrids. As shown in Fig. 5.3, the pristine Ni-Cr-LDH and NCW nanohybrids commonly show characteristics absorption peaks at ν_1 (515 cm^{-1}), ν_2 (576 cm^{-1}), ν_3 (670 cm^{-1}), ν_4 (1384 cm^{-1}), ν_5 (1625 cm^{-1}), ν_6 (3451 cm^{-1}). The broad adsorption peaks at ν_6 and ν_5 are ascribed to the O-H stretching vibrations and bending vibrational modes of interlayer water molecules, respectively [27]. The intense absorption peak ν_4 is attributed to the N-O stretching vibrations of NO_3^{-1} ions which is significantly quenched in NCW nanohybrids, indicating negligible contamination of carbonate or nitrate anions in NCW nanohybrids [24]. The ν_1 , ν_2 , and ν_3 peaks in the low-frequency region (800-400 cm^{-1}) are ascribed to the lattice vibrational modes, the M-O-M vibrations and the M-O-H vibrations in the Ni-Cr-

LDH NS [28]. On the other hand, the NCW nanohybrids show additional absorption peaks at ν_7 (818 cm^{-1}) and ν_8 (894 cm^{-1}) assigned to symmetric and asymmetric stretching modes of W-O-W chains of intercalated POW anions, respectively [29]. The presence of these characteristic IR features confirms the intercalation of POW anions in the Ni-Cr-LDH.

5.3.3 Micro-Raman study

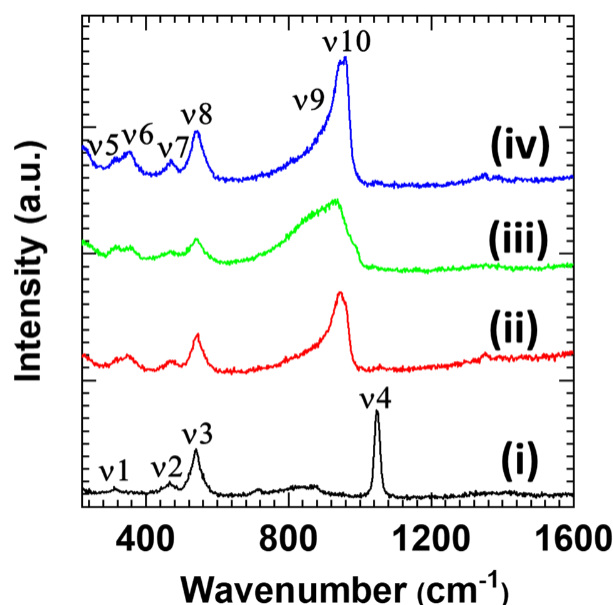


Fig. 5.4: Micro-Raman spectra of the (i) pristine Ni-Cr-LDH (ii) NCW-1, (iii) NCW-2, and (iv) NCW-3 nanohybrids.

As illustrated in Fig. 5.4, the pristine Ni-Cr-LDH and NCW nanohybrids exhibit characteristic Raman features ν_1 to ν_{10} corresponding to $\text{Ni}(\text{OH})_2$, $\text{Cr}(\text{OH})_3$, NO_3^- , and OD-POW species. The pristine Ni-Cr-LDH and NCW nanohybrids commonly exhibit characteristic Raman peaks at ν_1 (311 cm^{-1}), ν_2 (460 cm^{-1}), and ν_3 (540 cm^{-1}). The sharp peaks ν_1 and ν_2 are ascribed to the E_g and A_{1g} lattice vibrational mode of $\text{Ni}(\text{OH})_2$, respectively [17]. The characteristic peak of the symmetric stretching vibrational mode of NO_3^- at ν_4 clearly highlights the intercalation of the NO_3^- ions in the pristine Ni-Cr-LDH [30]. The broad peak ν_3 is attributed to the superposition of Cr-O-H bending mode of $\text{Cr}(\text{OH})_3$ at 530 cm^{-1} and the second-order acoustic mode of $\text{Ni}(\text{OH})_2$ at 540 cm^{-1} [17, 31]. All NCW nanohybrids show typical Raman peaks at ν_5 (313 cm^{-1}), ν_7 (461 cm^{-1}), and ν_8 (542 cm^{-1}), which attributed to the Ni-Cr-LDH NS lattice vibrational modes, similar to the pristine Ni-Cr-LDH [17, 31]. Moreover, NCW nanohybrids show mild Raman

peak ν_6 (356 cm^{-1}) ascribed to the bending mode of W-O of POW chains, confirming the intercalation of POW anions in NCW nanohybrids [32]. The broad high intense peak ν_{10} is formed by the superposition of peaks at 930 and 960 cm^{-1} , which are ascribed to the W=O vibrational-mode of $(\text{WO}_4)^{2-}$ and $(\text{W}_7\text{O}_{24})^{6-}$ anions, respectively [33]. The present Raman features clearly highlight the intercalation of $(\text{W}_7\text{O}_{24})^{6-}$ anions in NCW nanohybrids.

5.3.4 FESEM study

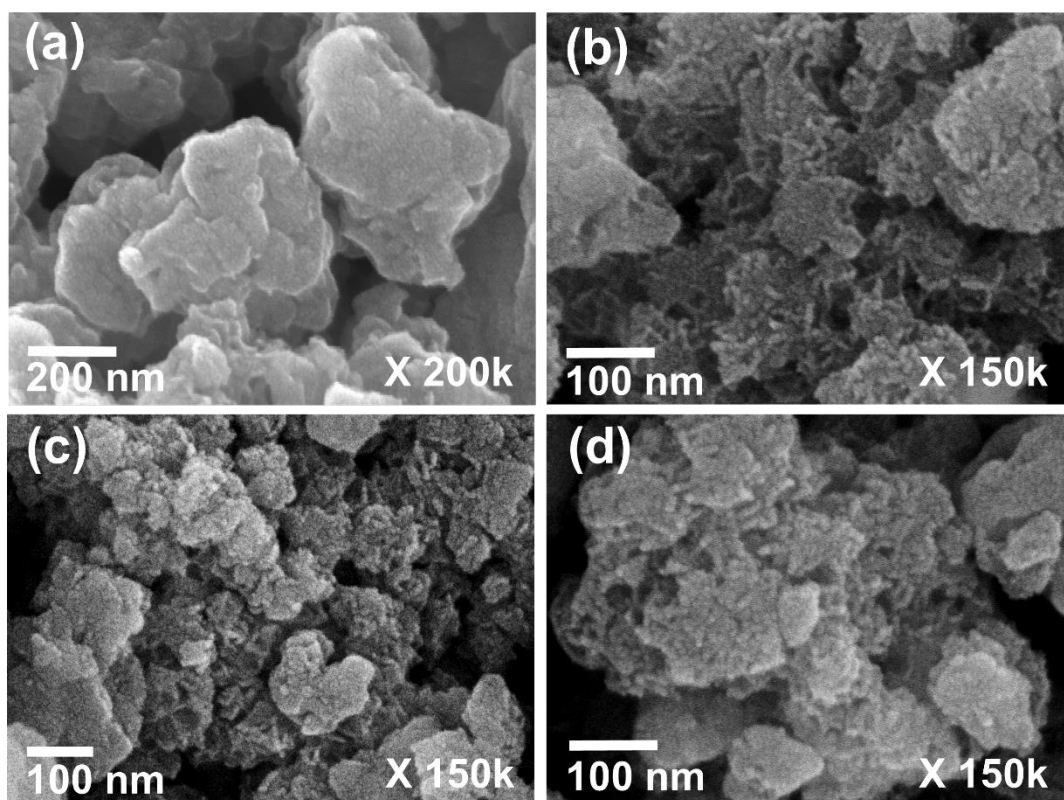


Fig. 5.5: FESEM images of the (a) pristine Ni-Cr-LDH, (b) NCW-1, (c) NCW-2, and (d) NCW-3 nanohybrids.

FESEM analysis was used to examine the topography of the pristine Ni-Cr-LDH and NCW nanohybrids. The pristine Ni-Cr-LDH shows (5.5a), compact sheet like non-porous morphology, which is commonly observed in LDH synthesized by coprecipitation method [24]. As shown in Fig. 5.5, NCW nanohybrids commonly demonstrate highly porous morphology composed of interconnected sheet-like crystallites formed by the edge-to-face interaction of reassembled LDH NSs. A close inspection of micrographs reveals that the estimated average lateral size of the NCW NSs is $\sim 45\text{ nm}$ and thickness $\sim 4\text{ nm}$, with small scrolling of edges to reduce

the surface energy. The estimated thickness of ~ 4 nm proposes the presence of about ~ 8 staked monolayers of Ni-Cr-LDH. The interconnected sheet-like crystallites connected by edge-to-face interaction, creating mesoporous spaces around 15 to 70 nm are shown in Fig. 5.5(b-d). This type of randomly interconnected sheet surface morphology is common for the self-assembled nanohybrids prepared via exfoliation-restacking of 2D nanoplates with various NSs [7, 25, 26].

5.3.5 EDS study

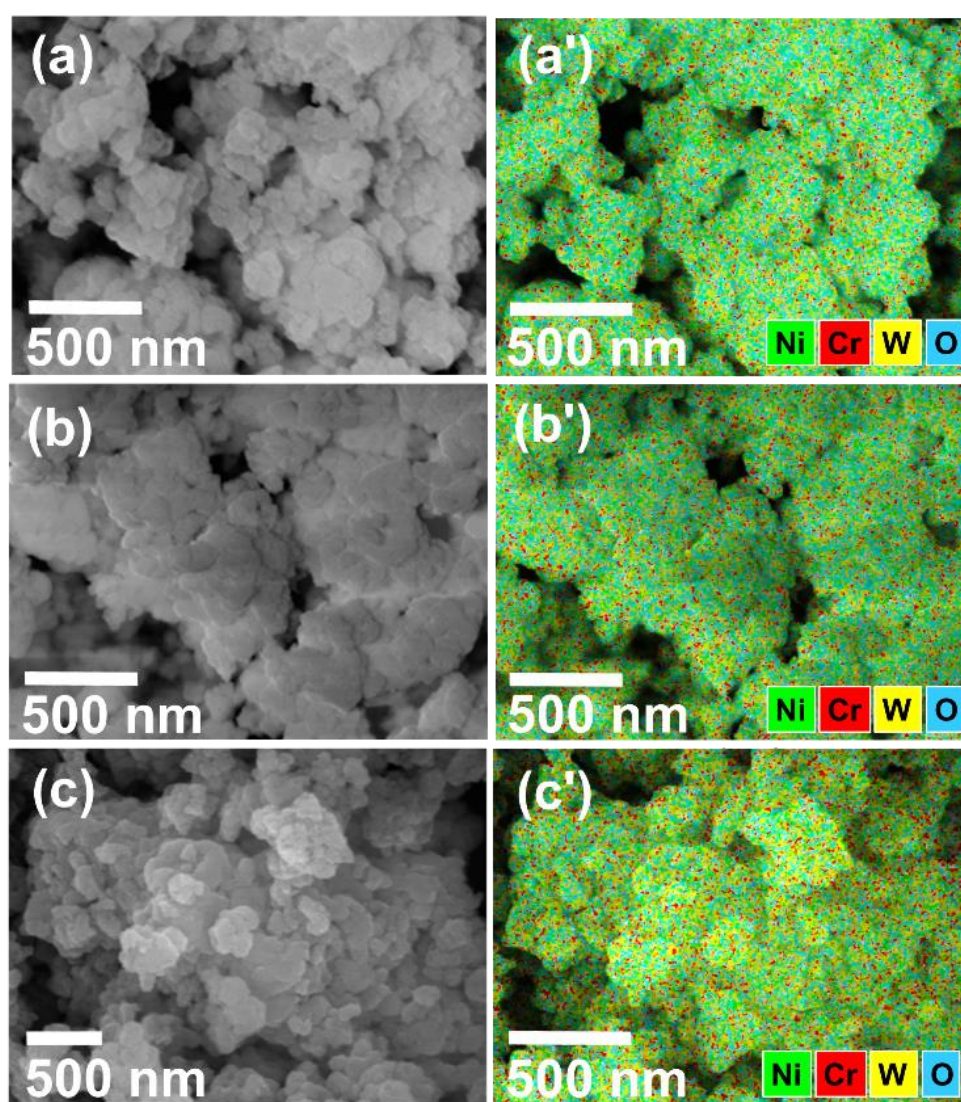


Fig. 5.6: (left) FE-SEM images and (right) EDS elemental maps of the (a) NCW-1, (b) NCW-2, and (c) NCW-3 nanohybrids.

The chemical composition and the distribution of constituent elements of NCW nanohybrids and Ni-Cr-LDH at the nanometer scale was examined by the EDS and elemental analyses (Fig. 5.6, 5.7, and 5.8). All nanohybrids display uniform distribution of nickel (Ni), chromium (Cr), tungsten (W), and oxygen (O) elements over the entire mapping area, confirming the homogeneous intercalation of the POW anions in the Ni-Cr-LDH without any phase separation. Based on the EDS and elemental mapping analyses, the chemical compositions of NCW nanohybrids along with pristine Ni-Cr-LDH are estimated as $\text{Ni}_{0.66}\text{Cr}_{0.34}(\text{OH})_2 \cdot 0.34(\text{NO})_3 \cdot y\text{H}_2\text{O}$, $\text{Ni}_{0.67}\text{Cr}_{0.33}(\text{OH})_2 \cdot 0.04(\text{W}_7\text{O}_{24}) \cdot y\text{H}_2\text{O}$, $\text{Ni}_{0.68}\text{Cr}_{0.32}(\text{OH})_2 \cdot 0.09(\text{W}_7\text{O}_{24}) \cdot y\text{H}_2\text{O}$, and $\text{Ni}_{0.70}\text{Cr}_{0.30}(\text{OH})_2 \cdot 0.12(\text{W}_7\text{O}_{24}) \cdot y\text{H}_2\text{O}$ for Ni-Cr-LDH, NCW-1, NCW-2, and NCW-3 nanohybrids, respectively.

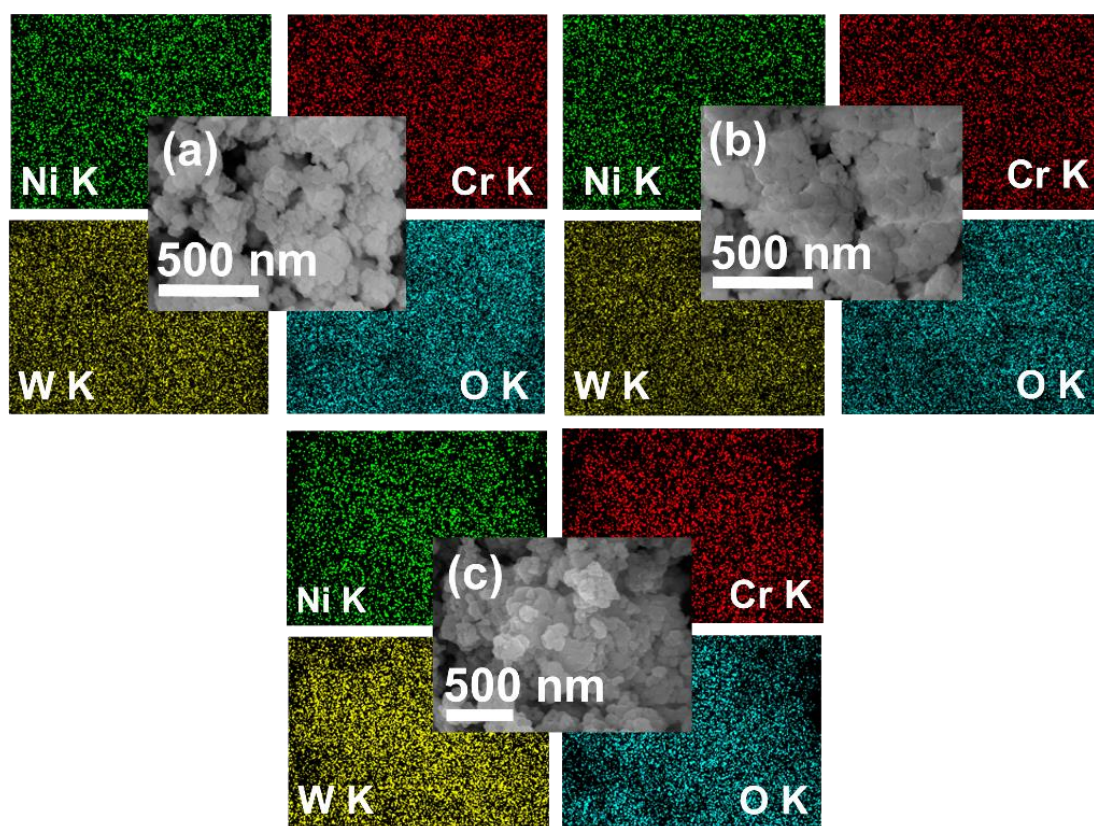


Fig. 5.7: EDS-elemental mapping and (centre) FESEM images of the (a) NCW-1, (b) NCW-2, and (c) NCW-3 nanohybrids.

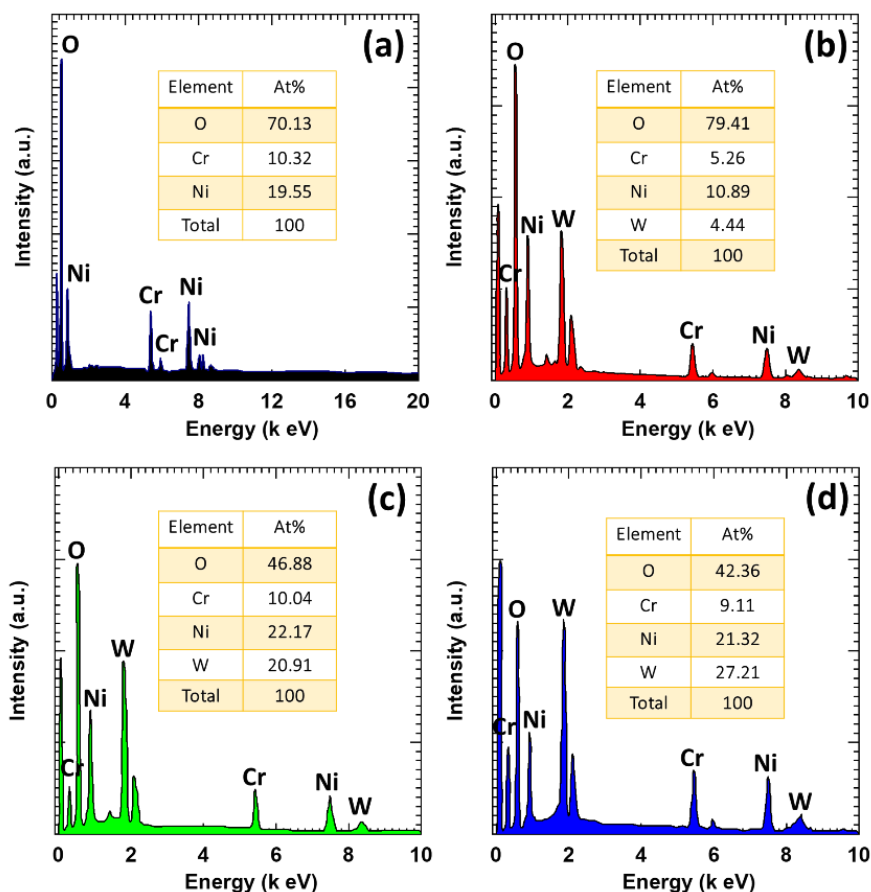


Fig. 5.8: EDS spectra of (a) pristine Ni-Cr-LDH, (b) NCW-1, (c) NCW-2, and (d) NCW-3 nanohybrids.

5.3.6 HRTEM study

The crystal morphology, and the layer-by-layer stacking structure of the pristine Ni-Cr-LDH and NCW nanohybrids at nanometer scale was studied by the TEM and HRTEM technique. The TEM images of pristine Ni-Cr-LDH display plate shaped dense clusters with lateral width ranging from 150 to 400 nm, as depicted in chapter 3, Fig. 3.8. As shown in Fig. 5.9a and b, the plane view TEM images of the NCW-2 nanohybrid clearly display thin NS crystallites forming an interconnected mesoporous structure. As illustrated in the Fig. 5.9 c and d, the plane view HRTEM images of the NCW-2 nanohybrid show the set of parallel lines separated by a distance of 0.15 nm which are well-matched with the (110) in-plane lattice parameters of Ni-Cr-LDH (JCPDS card, No.74-1057). At high resolution, two parallel zones of lattice fringes for the NCW-2 nanohybrid are clearly visible. One type is in the top view with a spacing of 0.15 nm and extended over the ~2.1 nm range. The observed fringe distance is in good agreement with the in-plane (110)

lattice parameters. Other zone extended over a distance of ~ 6 nm with larger separation distance of 0.9 nm is shown in Fig. 5.9e, f. The observed fringe distance of cross-sectional view is well matched with c-axis lattice parameter calculated from the XRD study. The cross-sectional HRTEM images display only short-range zone of lattice fringes up to ~ 5 nm, indicating that 5 to 6 Ni-Cr-LDH NS are restacked together with POW anions. These results clearly highlight the intercalation of POW anions within the Ni-Cr-LDH NSs gallery.

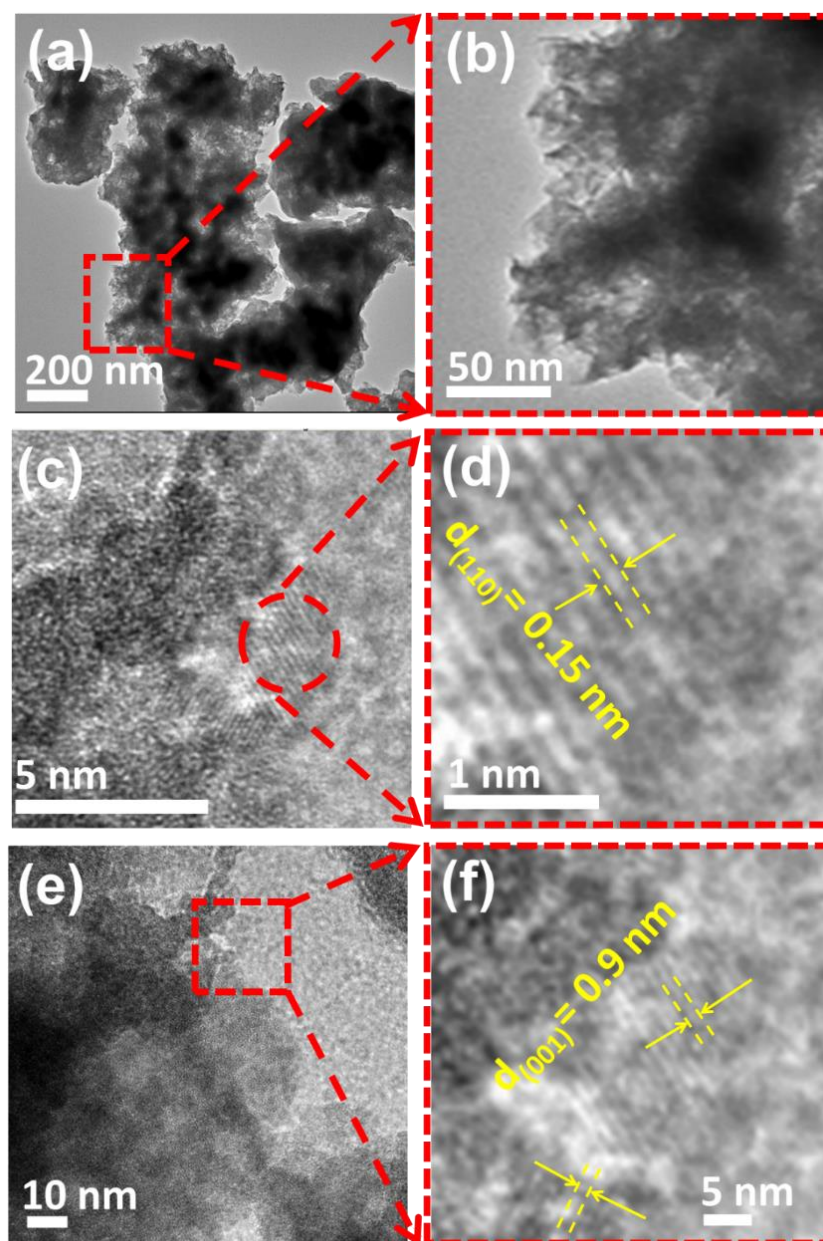


Fig. 5.9: (a, b) TEM images of NCW-2 nanohybrid, (c, d) top view HRTEM images of NCW-2 nanohybrid, (e, f) cross-sectional HRTEM images of the NCW-2 nanohybrid.

5.3.7 Surface area study

The porosity and surface area of the pristine Ni-Cr-LDH and NCW nanohybrids were probed by BET N_2 adsorption and desorption isotherms analysis. As plotted in Fig. 5.10, except pristine Ni-Cr-LDH, a distinct hysteresis is observed in all nanohybrids at $pp_0^{-1} > 0.45$, indicating the presence of mesoporous structure.

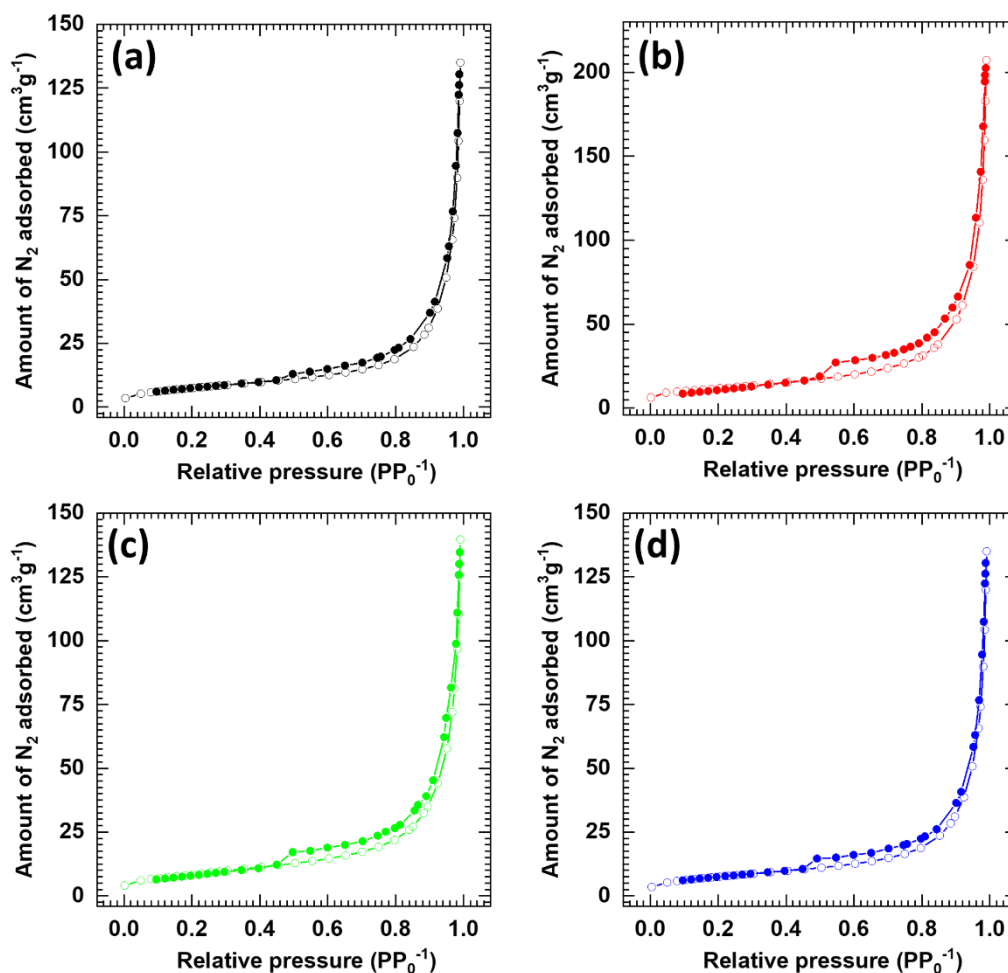


Fig. 5.10: N_2 adsorption-desorption isotherms of (a) pristine Ni-Cr-LDH, (b) NCW-1, (c) NCW-2, and (d) NCW-3 nanohybrids.

According to IUPAC classification, NCW nanohybrids display type IV isotherm with a H3 type hysteresis. The observed combination of type IV isotherm with a H3 type hysteresis is attributed to the presence of well-ordered slit-shaped mesopores having a high energy of adsorption with narrow and wide sections [38]. This highlights that most of the porosity is originated from the mesoporous nature formed by the interconnected stacking structure of LDH NSs [7, 25]. These results

are well-matched with the surface morphological results [7]. The specific surface areas for NCW-1, NCW-2, and NCW-3 nanohybrid are found to be, 24, 30, and 27 $\text{m}^2 \text{g}^{-1}$, respectively which are larger than that of the pristine Ni-Cr-LDH ($14 \text{ m}^2 \text{g}^{-1}$). According to the BJH analysis method, the NCW nanohybrids display the wide pore distribution in the 2 to 50 nm range of pores, as shown in Fig. 5.11. The wide pores in NCW nanohybrid indicate the multiple origin of pores from intercalative stacking structure as well as interconnected NS surface morphology of NCW nanohybrids.

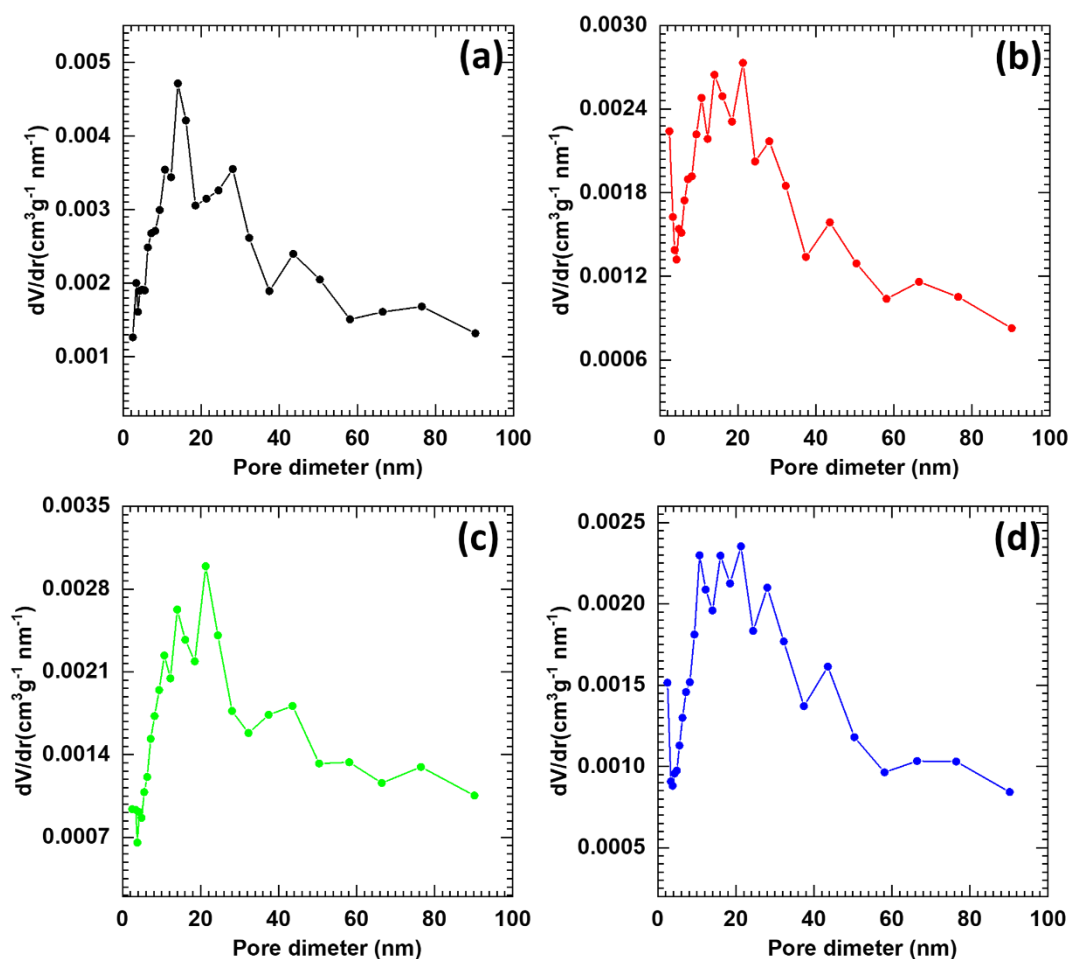


Fig. 5.11: Pore size distribution plots of the (a) pristine Ni-Cr-LDH (b) NCW-1, (c) NCW-2, and (d) NCW-3 nanohybrids.

5.3.8 XPS study

The XPS was used to probe chemical composition and characteristics within materials.

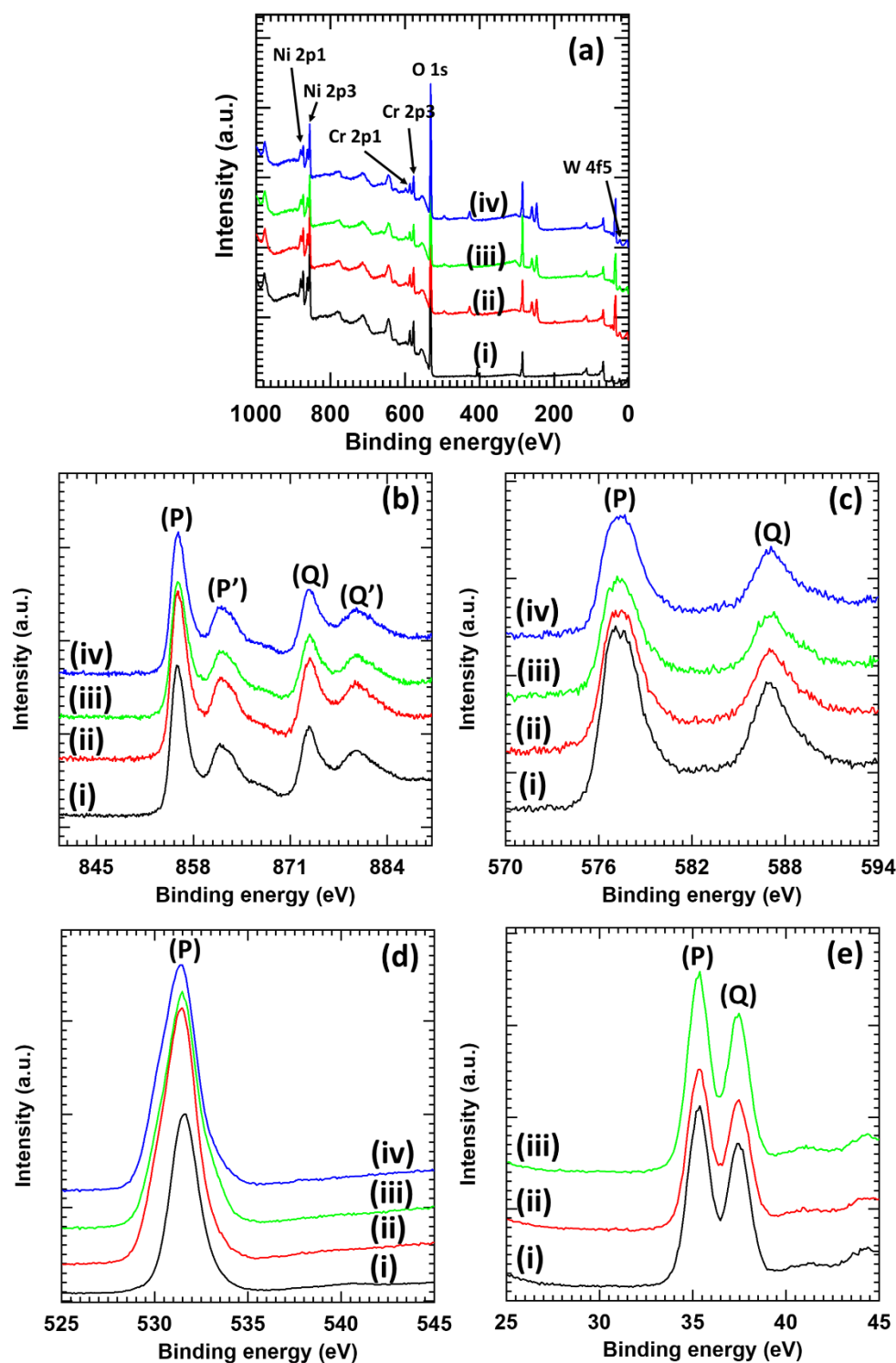


Fig. 5.12: (a) Survey, (b) Ni2p, (c) Cr2p, (d) O1s, and (e) W4f XPS spectra of pristine Ni-Cr-LDH, NCW-1, NCW-2, and NCW-3 nanohybrids.

The full survey XPS spectra of NCW nanohybrids (Fig. 5.12a) display characteristic XPS features at the binding energies of the elements Ni, Cr, O and, W. The high-resolution XPS spectra of the pristine Ni-Cr-LDH and NCW nanohybrids

for Ni, Cr, O and W are plotted in Fig. 5.12(b-e). As illustrated in Fig. 5.12b, Ni-Cr-LDH and NCW nanohybrids exhibit two strong peaks of Ni 2p_{3/2} (855.9 eV) and Ni 2p_{1/2} (873.4 eV), with a spin-energy difference of 17.5 eV and satellite peaks at P' (861.6 eV) and Q' (879.7 eV) which indicates the divalent Ni in the Ni-Cr-LDH NS [17, 34]. The Cr 2p spectra Ni-Cr-LDH and NCW nanohybrids (Fig. 5.12c) show two broad peaks corresponding to Cr 2p_{1/2} (P = 587.0 eV) and Cr 2p_{3/2} (Q = 577.3 eV). The binding energy (BE) of Cr 2p at 587.0 eV is attributed to Cr³⁺ in Ni-Cr-LDH NS [35]. The O 1s broad spectra of Ni-Cr-LDH and NCW nanohybrid samples (Fig. 5.12d) is centered at BE of P (531.4 eV), which is ascribed to the lattice oxygen (530.4 eV), hydroxyl group (531.5 eV) and bound water (532.6 eV) [36]. Furthermore, as shown in Fig. 5.12e, high-resolution W 4f core-level spectra which are only discernable for NCW nanohybrids, show doublet at P (35.3 eV) and Q (37.7 eV) due to the W 4f_{7/2} and W 4f_{5/2}. The presence of doublets at BE values of P and Q indicates W-O bond configuration and is observed typically for W⁶⁺ in the POW chains [37]. The observed XPS characteristic confirms the intercalation of the POW anions into the interlayer space of the Ni-Cr-LDH.

5.4 Conclusions

In conclusion, mesoporous nanohybrids of 2D Ni-Cr-LDH NSs hybridized with POW anions are prepared by the electrostatically driven exfoliation-restacking process at ambient temperature. Powder XRD and HRTEM analysis confirmed the formation of layer-by-layer stacking of Ni-Cr-LDH NSs and POW anions. FESEM microscopy and BET analysis revealed house-of-card type morphology and mesoporous structure of NCW nanohybrids. EDS mapping result shows the presence of all constituent elements (Ni, Cr, and W) which are uniformly distributed across the entire part of the elemental mapping area of NCW nanohybrids. Present elemental mapping results demonstrate the homogeneous hybridization of the Ni-Cr-LDH NSs and POW anions without any spatial phase separation. FTIR, Micro-Raman features, and XPS analysis indicate the maintenance of Ni-Cr-LDH NSs and intercalation of POW anions into the interlayer spaces of the Ni-Cr-LDH.

5.5 Electrochemical performance evaluation of NCW nanohybrids

5.5.1 Preparation of NCW electrodes

The active materials (Ni-Cr-LDH or NCW), AB, and PVDF were mixed together in an 80:15:5 mass ratio for fabrication of working electrodes. The mixtures were grounded for 1 h in NMP to become homogeneous slurry. Further, it was used to prepare the HSC electrode by simple doctor blade method on SS substrate, and finally dried in a vacuum oven at 80°C for 6h.

5.5.2 Results and discussion

5.5.2.1 CV study

To examine the potential application of the as-prepared pristine Ni-Cr-LDH and NCW nanohybrids, the samples were designed for EES electrodes and characterized by using CV, GCD, and EIS measurements. Fig. 5.13 displays CV curves of Ni-Cr-LDH and NCW nanohybrids electrodes at sweep rate of 20 mV s⁻¹. All the tested electrodes show well-defined redox peaks due to redox transition of Ni⁺²/Ni⁺³ between Ni(OH)₂ and NiOOH according to following reaction mechanism (equation 3.1).

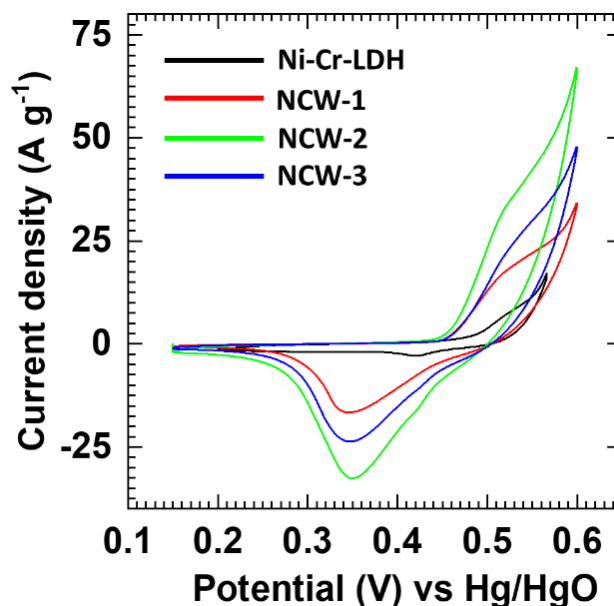


Fig. 5.13: The comparative CV curves of pristine Ni-Cr-LDH, NCW-1, NCW-2, and NCW-3 nanohybrid electrodes at a scan rate of 20 mV s⁻¹.

Interestingly, NCW nanohybrid electrodes show larger current distribution than the pristine Ni-Cr-LDH electrode, indicating the beneficial role of POW intercalation for improved charge storage in NCW nanohybrids. Improved electrode performance of NCW nanohybrids is attributed to the high surface area interconnected sheets morphology and high access of bulk electrode material due to expanded gallery space of NCW nanohybrids. Among the NCW nanohybrids, NCW-2 nanohybrid shows the highest current under CV highlighting the importance of optimum POW content for the improvement of electrochemical activity of NCW nanohybrids. The effect of scan rate on CV profiles for pristine Ni-Cr-LDH and NCW nanohybrids is examined by varying the scan rate from 4 to 20 mV s^{-1} , as shown in Fig. 5.14.

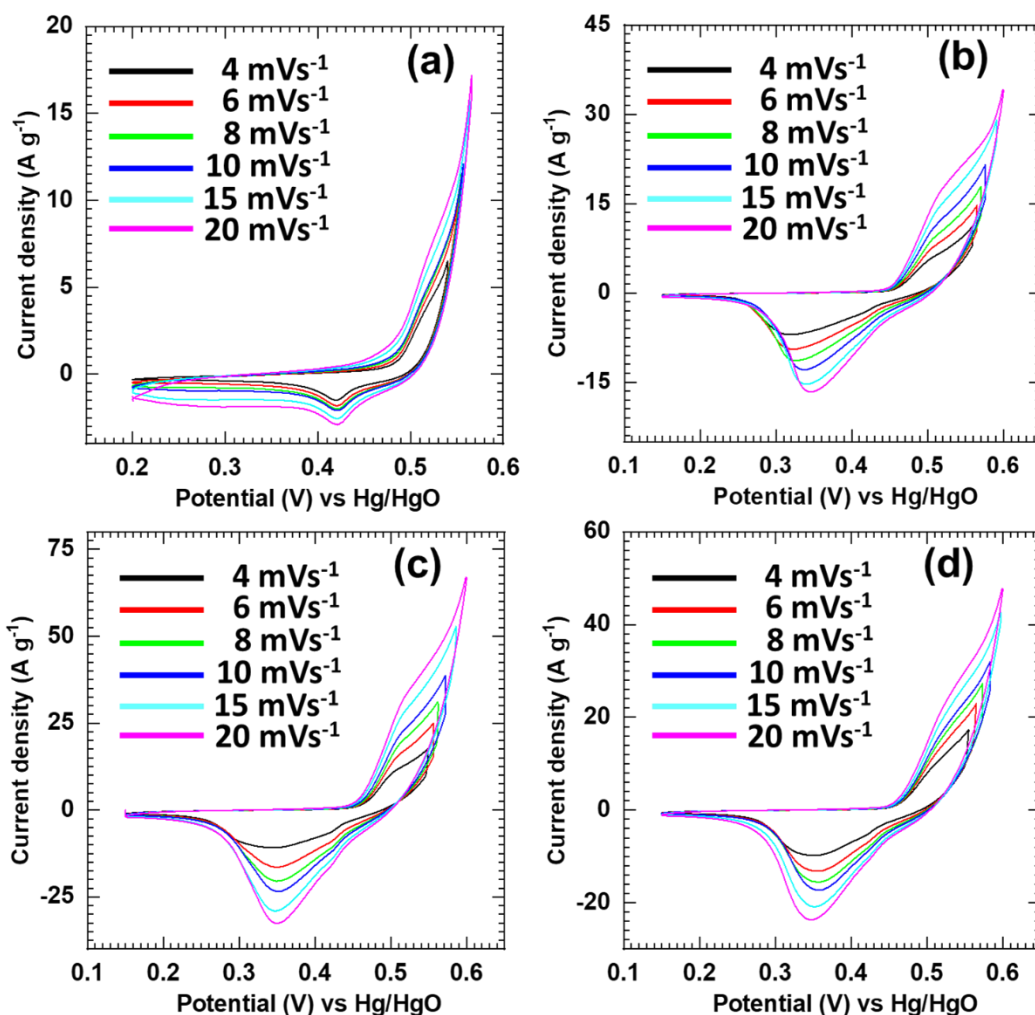


Fig. 5.14: CV curves of (a) pristine Ni-Cr-LDH (b) NCW-1, (c) NCW-2, and (d) NCW-3 nanohybrid electrodes at various scan rates from 4 to 20 mV s^{-1} .

The integral area under CV with shifting of cathodic peak towards positive potential and anodic peak towards negative potential can be clearly discernible with increasing scan rates. This further indicates the presence of both capacitive and diffusion-controlled battery-type charge storage mechanisms in pristine Ni-Cr-LDH and NCW nanohybrids. Further to explore the charge storage kinetics for all electrodes, an attempt was made to quantify the individual contribution of the diffusion-controlled Faradaic and the surface-dominant capacitive (non-Faradaic) responses to the total charge accumulated in these materials [39, 40]. Total charge (Q_t) stored by an electrode can be resolved as contribution from surface-capacitive (Q_s) and diffusion-controlled (Q_d) charges as shown in equation (4.2),

From a graph of Q_t versus $v^{-1/2}$ (Fig. 5.15), the fraction of outer Q_s can be judged by the Y-axis intercept at infinite scan rate. The high scan rates CV curves ($>20 \text{ mV s}^{-1}$) are not included in the fitting to avoid polarization effects [41].

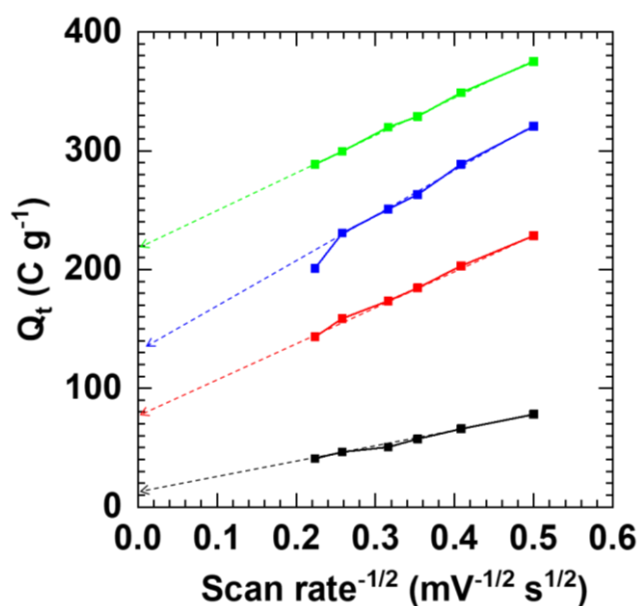


Fig. 5.15: The Plots of total gravimetric charge against the reciprocal of the square root of potential sweep rate for pristine Ni-Cr-LDH(black), NCW-1(red), NCW-2(green), and NCW-3(blue) nanohybrids.

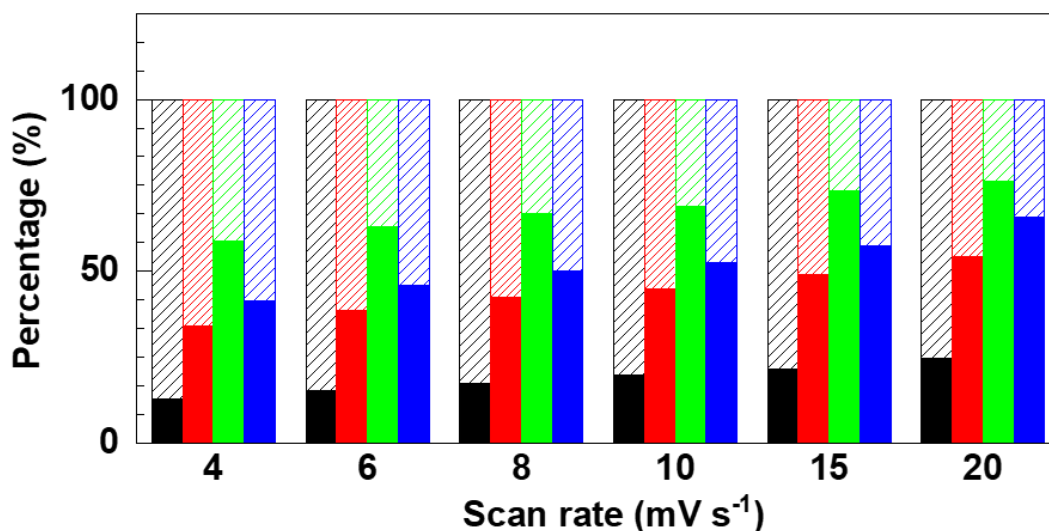


Fig. 5.16: The fraction of the capacitive (solid) and diffusion-controlled (pattern) contributions of pristine Ni-Cr-LDH (black), NCW-1(red), NCW-2(green), and NCW-3(blue) nanohybrids (values in bar assigned for the respective charge contributions).

Distinct contributions of Q_s and Q_d to the total charge stored in pristine Ni-Cr-LDH and NCW nanohybrid electrodes are illustrated in Fig. 5.16. At low scan rate of 4 mV s^{-1} , pristine Ni-Cr-LDH, NCW-1, NCW-2, and NCW-3 nanohybrids display a low surface capacitive contribution of 13, 26, 50, and 34%, respectively, while at higher scan rate of 20 mV s^{-1} they show high capacitive contribution of 25, 54, 76, and 65%, respectively. These results indicate dominance of diffusion controlled processes at lower scan rate and capacitive processes at higher scan rate. All the NCW nanohybrids display higher charge storage with increased capacitive charge contribution as compared to the pristine Ni-Cr-LDH indicating rapid charge storage and delivery kinetics in NCW nanohybrids. The superior charge transfer kinetics of NCW nanohybrids can be attributed to the high surface area interconnected sheet morphology with expanded interlayer space of NCW nanohybrids.

5.5.2.2 GCD study

Further, GCD measurement was used to investigate the charge storage performance of the pristine Ni-Cr-LDH and NCW nanohybrid samples (Fig. 5.17).

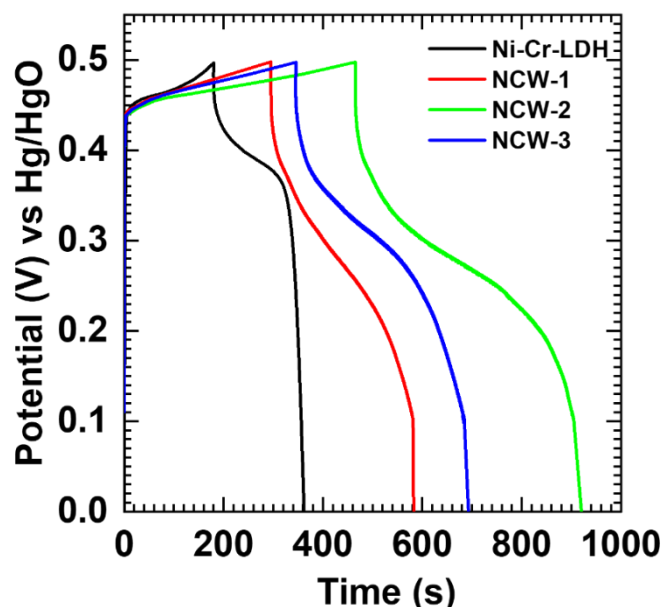


Fig. 5.17: GCD curves of pristine Ni-Cr-LDH, NCW-1, NCW-2, and NCW-3 nanohybrids at current density of 1 A g^{-1} .

The pristine Ni-Cr-LDH shows a non-linear charge-discharge profile with characteristic plateau and sudden potential drop, indicating battery-type charge storage mechanism [20]. On the other hand, all the NCW nanohybrids exhibit non-linear charge-discharge profile with longer charging and discharging times, revealing the pseudocapacitive charge storage behavior of NCW nanohybrids. The specific capacities of tested electrodes were calculated from equation 2.9. The specific capacities of 476 , 736 , and 570 C g^{-1} were estimated for NCW-1, NCW-2, and NCW-3 nanohybrids, respectively, which are significantly higher than that of the pristine Ni-Cr-LDH (356 C g^{-1}). The NCW-2 nanohybrids with optimum POW exhibit a maximum specific capacity of 736 C g^{-1} which is consistent with the CV analysis.

In addition, the GCD performance of pristine Ni-Cr-LDH and NCW nanohybrid electrode at various current densities was measured to study the charge transfer kinetics and results are shown in Fig. 5.18. The specific capacities for all electrodes decrease with charging-discharging current density, indicating the less utilization of active material at fast charging-discharging rates. In contrast to the pristine Ni-Cr-LDH with decrease of specific capacity from 296 C g^{-1} at 1 A g^{-1} to 75 C g^{-1} at 5 A g^{-1} , the NCW-2 nanohybrid displays the specific capacity of 736

C g^{-1} at 1 A g^{-1} that decreases to 416 C g^{-1} at 5 A g^{-1} , indicating high-rate capability of NCW nanohybrids (Fig. 5.19).

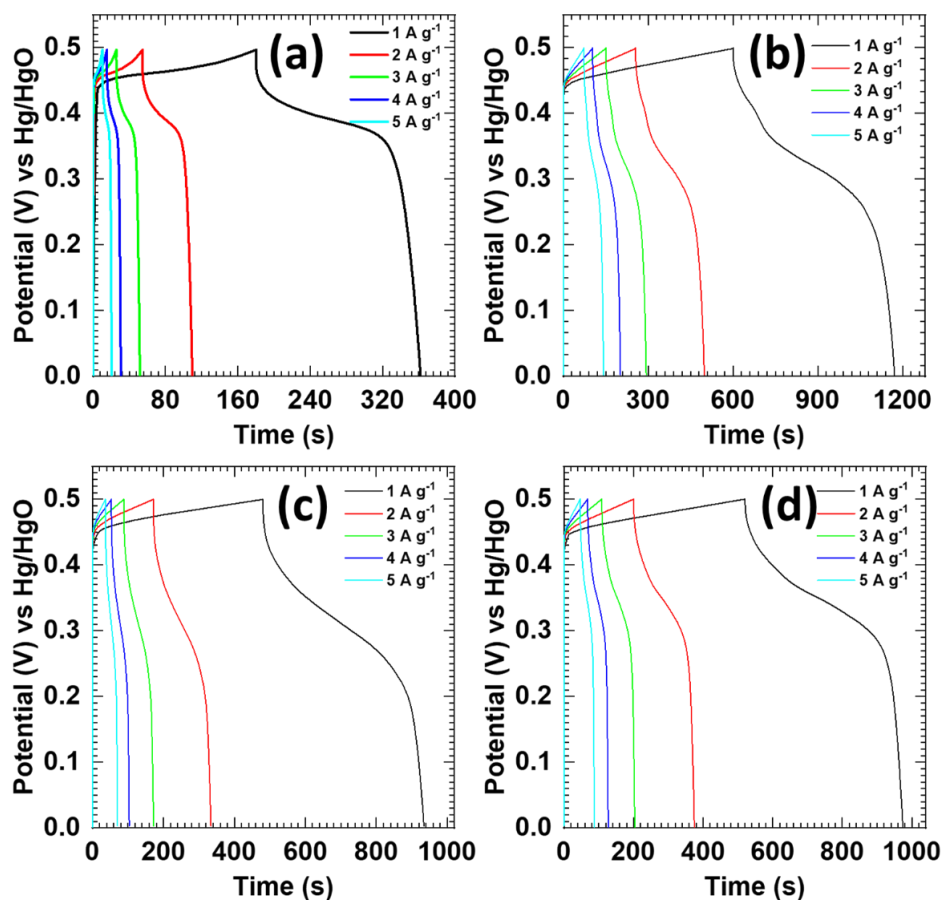


Fig. 5.18: The GCD curves of (a) pristine Ni-Cr-LDH, (b) NCW-1, (b) NCW-2, and (c) NCW-3 nanohybrid electrode at different current densities ($1\text{--}5 \text{ A g}^{-1}$).

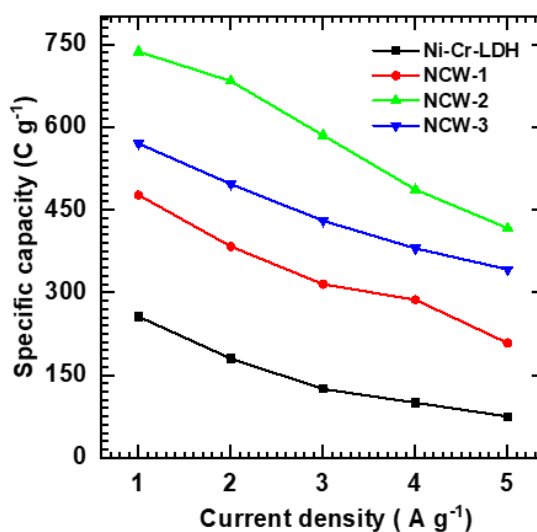


Fig. 5.19: Specific capacity of pristine Ni-Cr-LDH, NCW-1, NCW-2, and NCW-3 nanohybrids at different current densities ($1\text{--}5 \text{ A g}^{-1}$).

The high rate capability of NCW nanohybrids is ascribed to the increase gallery space upon the POW intercalation, together with the formation high surface area interconnected sheet morphology as they are expected to enable the easy diffusion of electrolyte ions at the interior of Ni-Cr-LDH. Present electrode performance of NCW nanohybrids underscores the advantage of exfoliation-restacking strategy for the enhancement of electrochemical performance.

Further, the comparative study reveals that the electrochemical performance of NCW nanohybrid is far superior to that of the previously reported Ni-based LDH and their hybrid materials (listed in chapter 1-Table 1.3. and 1.4). This novel nanohybrid demonstrates its applicability as a potentially appealing electrode material for high performance electrochemical energy storage system. Considering the obtained results, it is concluded that the enhancement in the electrochemical performance of pristine LDH material can be achieved by rational intercalation of POW anions in Ni-Cr-LDH. The unique integrated architectures obtained by above strategy substantially expand freely accessible interlayer gallery space of the Ni-Cr-LDH lattice, leading accelerated redox-reactions and facilitated diffusion of electrolytic ions. Electrostatically driven self-assembly between monolayer host LDH NSs and guest POW anions induces superstructures with interconnected sheet-like structured morphology, having plenty of redox-active sites that further contribute to superior electrode performance nanohybrid materials.

5.5.2.3 EIS study

The charge transport features of pristine Ni-Cr-LDH and NCW-2 nanohybrid were investigated using the EIS analysis and corresponding Nyquist plots with curve simulation fitting analysis are displayed in Fig. 5.20. Both pristine Ni-Cr-LDH and NCW-2 nanohybrid display characteristic semicircle and a straight line at high and low frequency regions, respectively. The diameter of semicircle and its intercept on Z_{re} axis at high frequency side signifies the R_{ct} and R_s , respectively. In contrast to Ni-Cr-LDH with higher R_s (0.46 Ω) and R_{ct} (14.20 Ω), the NCW-2 nanohybrid shows lower R_s (0.42 Ω) and R_{ct} (8.18 Ω) with steeper slope of the straight line in low frequency region. The observed low values of R_s and R_{ct} , with steeper slope of the straight line in low frequency region in NCW-2 nanohybrids

clearly indicate higher electrical conductivity of the nanohybrids electrodes with lower resistance (Warburg impedance) for electrolyte ion diffusion. These features are attributed to the expanded gallery height and porous interconnected morphology of NCW nanohybrid that enables easy charge transfer into nanohybrid lattice.

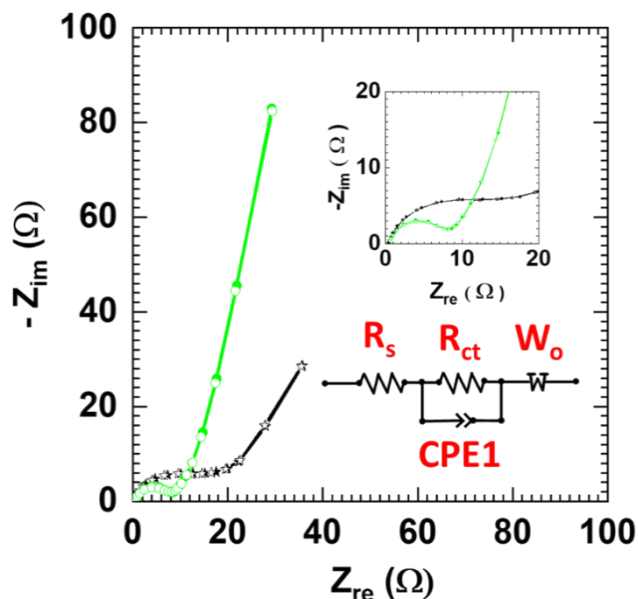


Fig. 5.20: Nyquist plots of pristine Ni-Cr-LDH (black) and NCW-2 (green) nanohybrid (inset: fitted circuit).

5.5.2.4 Stability study

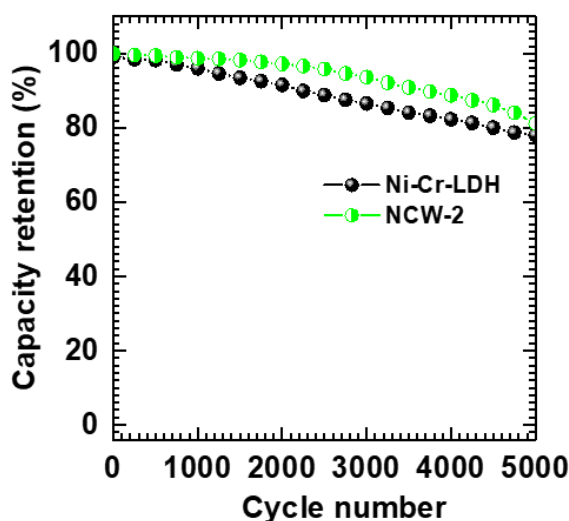


Fig. 5.21: GCD stability graph of pristine Ni-Cr-LDH and NCW-2 nanohybrid electrode for 5000 cycles.

The cycling stability of pristine Ni-Cr-LDH and NCW-2 nanohybrid is estimated by performing GCD tests at a 5 A g^{-1} , as presented in Fig. 5.21. The NCW-2 nanohybrid exhibits a good capacity retention of 81% over 5000 continuous GCD cycles as compared to the pristine Ni-Cr-LDH (capacity retention of 78% over 5000 cycles) electrode.

5.6. Electrochemical performance evaluation of hybrid supercapacitor device

To validate the capability of NCW nanohybrids at real-time device, the HSC device with a full cell configuration was fabricated using rGO as the anode and NCW-2 nanohybrid as the cathode in aqueous 2 M KOH solution, the corresponding HSC cell is denoted NCW-2||rGO HSC as shown in Fig. 5.22.

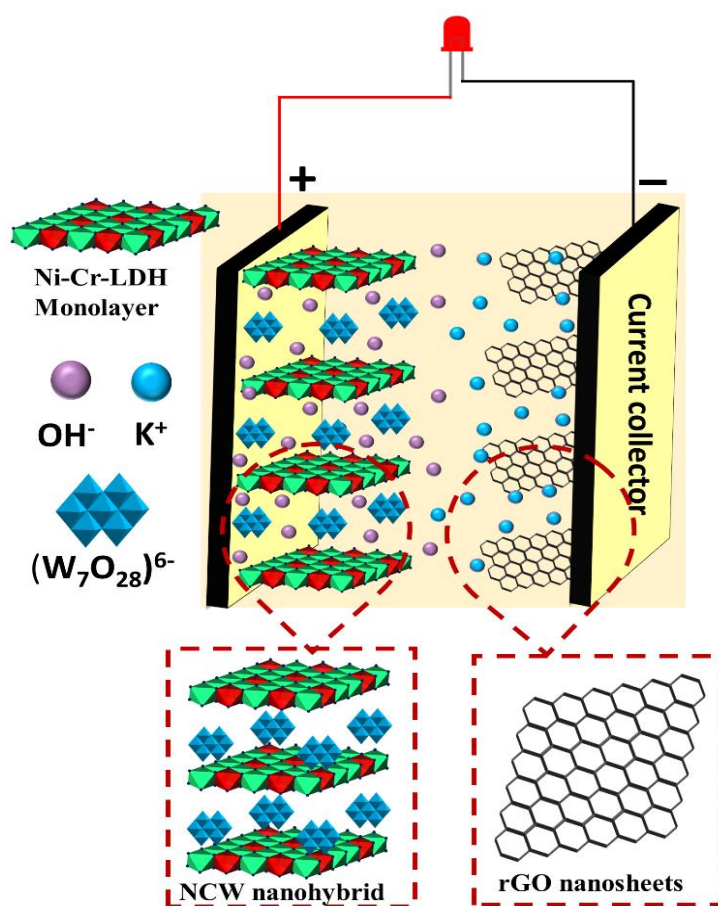


Fig. 5.22: Schematic illustration of NCW-2||rGO HSC device.

Considering excellent performance, NCW-2 nanohybrid was used for the HSC cathode. Prior to construction of HSC, the electrochemical performance of rGO was evaluated with a half-cell configuration by CV, GCD, and EIS tests. The electrochemical capacitive performance of rGO is provided in chapter 3rd. For stable and efficient working of HSC device, the charge balance between anode and cathode was attained by adjusting the active electrode mass of respective electrodes using equation 4.3.

5.6.1 CV study

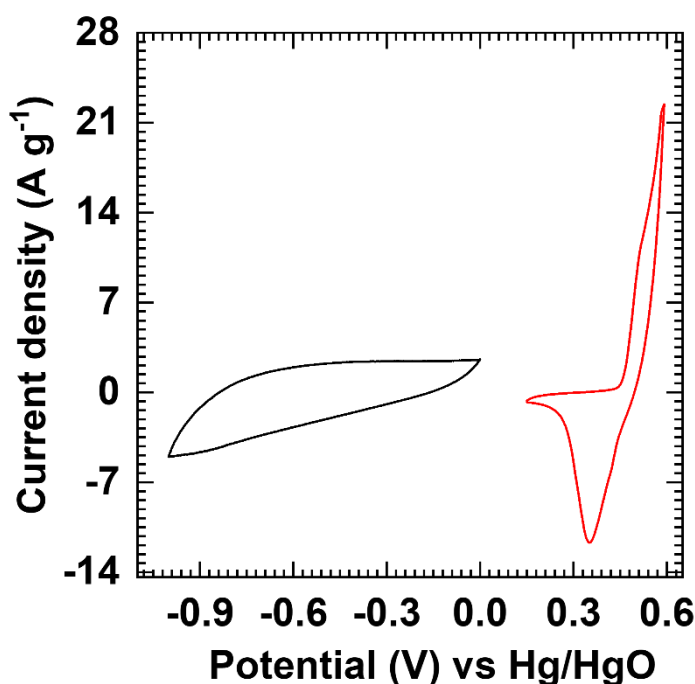


Fig. 5.23: The CV curves of rGO (black) and NCW-2 (red) nanohybrid electrode at a scan rate of 10 mV s⁻¹.

As shown in Fig. 5.23, judging from the individual working potential windows of (0 to -1 V versus Hg/HgO) rGO and (0.15 to 0.6 V versus Hg/HgO) NCW-2 nanohybrid electrodes, the NCW-2||rGO HSC can expect to operate up to 1.6 V. The operating voltage limit for NCW-2||rGO HSC was fixed by measuring CV curves within various voltage windows between 0 and 1.7 at 100 mV s⁻¹ (Fig. 5.24).

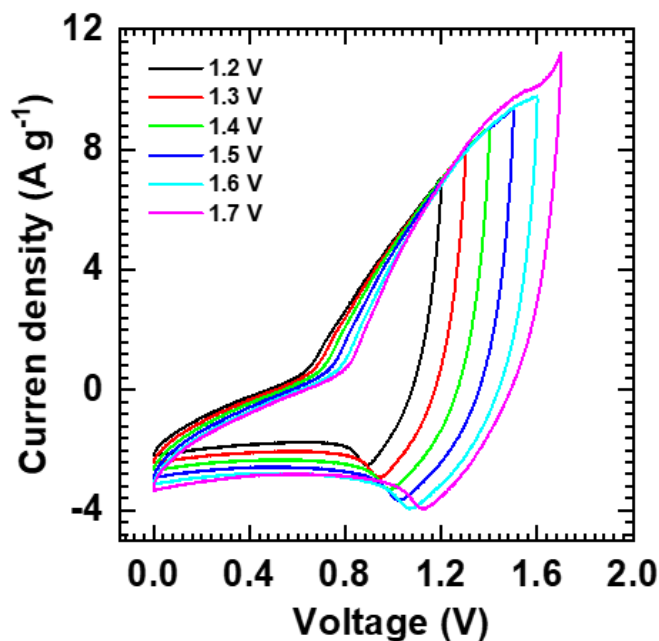


Fig. 5.24: CV curves of the HSC performed in different potential windows at 100 mV s^{-1} .

The NCW-2||rGO HSC operates between 0 to 1.6 V CV without any polarization of electrolyte. The effect of scan rate on CV shape and current response is shown in Fig. 5.25. The current under CV curves increases with scan rate without any shape alteration and redox peak positions, indicating the rapid charge storage and delivery with good reversibility of NCW-2||rGO HSC [42].

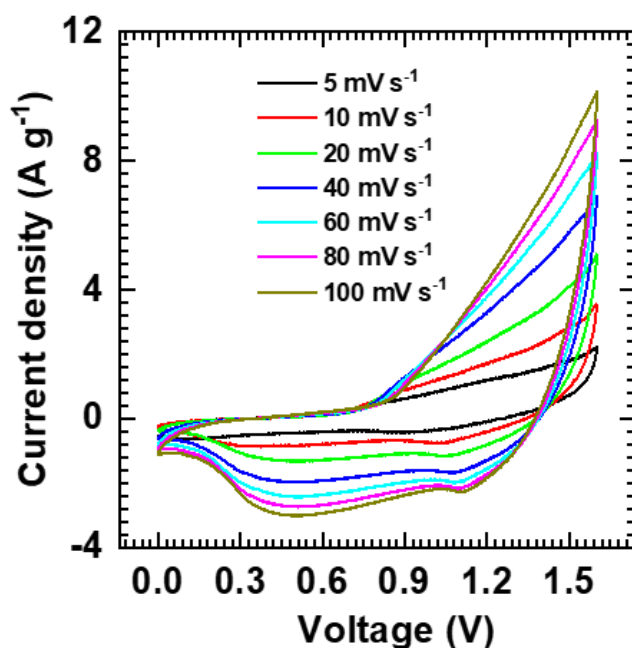


Fig. 5.25: The CV curves of HSC at different sweep rates from 5 to 100 mV s^{-1} .

5.6.2 GCD study

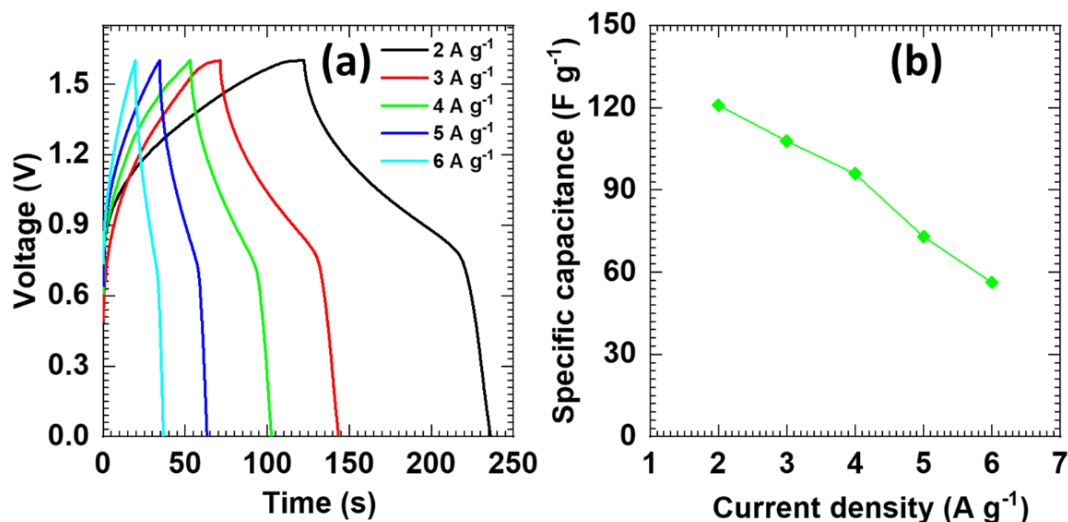


Fig. 5.26: (a) GCD curves at current densities 2-6 A g⁻¹, (b) The plot of Cs verses current densities of HSC device.

The Cs, ED and PD of NCW-2||rGO HSC were assessed by measuring the GCD curves at various current densities, as shown in Fig. 5.26(a, b). The NCW-2||rGO HSC delivers a Cs of 120 F g⁻¹ at a current density of 2 A g⁻¹ with maximum ED of 43 Wh kg⁻¹ at PD of 1.3 kW kg⁻¹.

5.6.3 Ragone plots

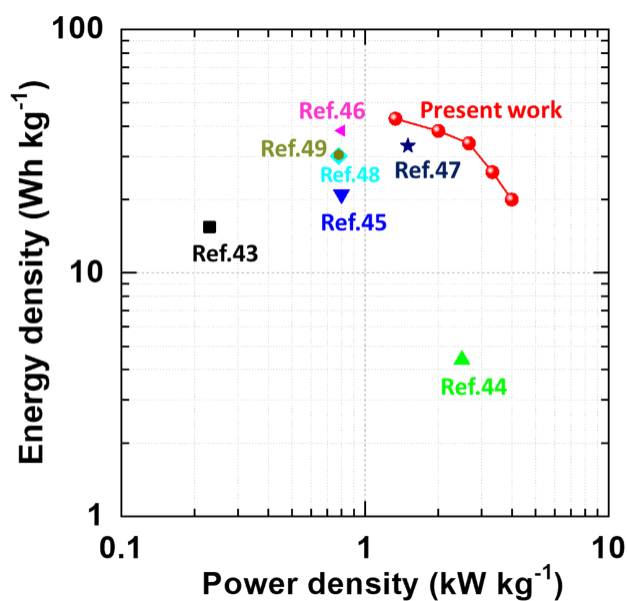


Fig. 5.27: Comparative Ragone plot the NCW-2||rGO HSC device with available literature.

The electrochemical performance of this device is competitive or even superior to recently reported HSCs such as NiAl-LDH-rGO||AC (15.4 Wh kg^{-1} @ 0.23 W kg^{-1}) [43], CoMn-LDHs||AC (4.4 Wh kg^{-1} @ 2.5 kW kg^{-1}) [44], NiAl-LDHs||AC (21 Wh kg^{-1} @ 0.8 kW kg^{-1}) [45], NiCoO₂||AC (38.4 Wh kg^{-1} @ 0.8 kW kg^{-1}) [46], ZIF-67-LDH-CNP-110||AC (33.29 Wh kg^{-1} @ 0.15 kW kg^{-1}) [47], NiAl-LDH-NF||GNS-NF (30.2 Wh kg^{-1} @ 0.8 kW kg^{-1}) [48], and NiV LDH||AC (30.6 Wh kg^{-1} @ 0.78 kW kg^{-1}) [49], which are represented in Ragone plot, Fig. 5.27.

5.6.4 Stability study

Moreover, the rate capability, cycling stability of HSC is shown in Fig. 5.28 and 5.29. As plotted in Fig. 5.28 even after subjecting to high charge-discharge current densities, the NCW-2||rGO HSC retains the high-capacity with negligible capacity fading.

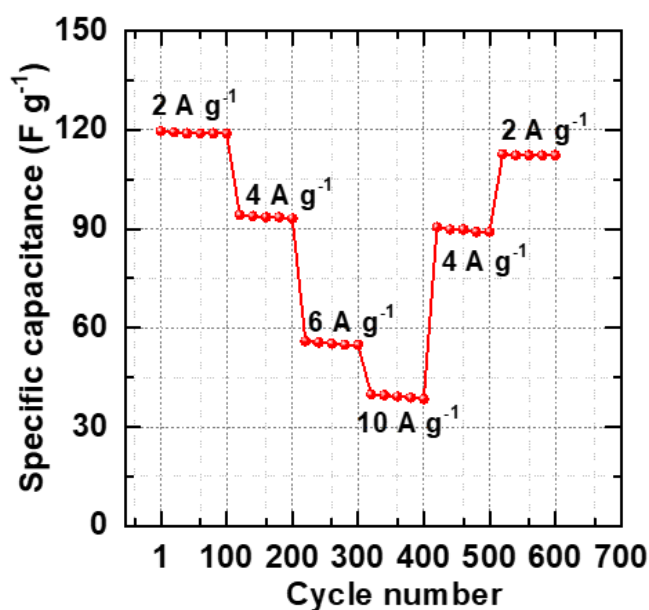


Fig. 5.28: The capacity rate capability of the HSC device with lower to higher and reverse back to the different current density.

The cycling stability and coulombic efficiency of NCW-2||rGO HSC monitored over 10000 GCD cycles at 5 A g^{-1} are shown in Fig. 5.29 (inset shows initial and final five GCD cycles). The NCW-2||rGO HSC retains 84% of the initial specific capacity and $\sim 97\%$ coulombic efficiency after 10000 GCD cycles, indicating excellent cycling stability and reversibility of both NCW-2 and rGO electrodes.

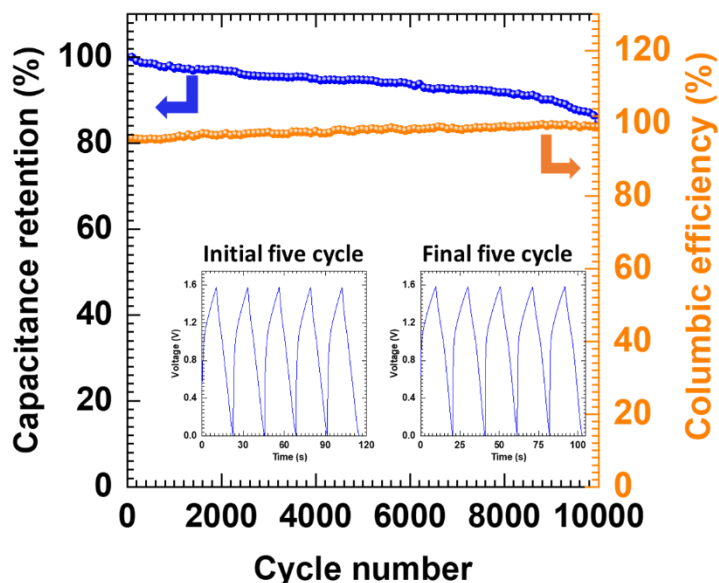


Fig. 5.29: Cycling stability/coulombic efficiency plots for the HSC device. The inset shows the initial and final five GCD cycle at a high current density of 5 A g^{-1} .

5.6.5 EIS study

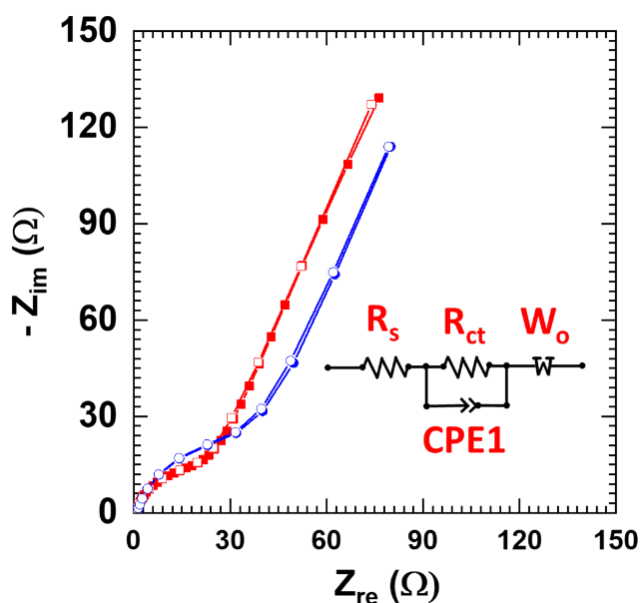


Fig. 5.30: Nyquist plot (Inset: fitted circuit) for the HSC before (red) and after (blue) stability.

The EIS plots of NCW-2||rGO HSC device before and after 10000 GCD cycles are shown in Fig. 5.30 (Inset: best fitted circuit). Based on the fitting analysis before cycling NCW-2||rGO HSC exhibits R_s and R_{ct} of 0.53 and $19.5 \text{ } \Omega$, respectively. Moreover, after cycling the NCW-2||rGO HSC upholds the R_s and R_{ct} of $0.58 \text{ } \Omega$ and

31.2 Ω , respectively. The lower values of R_s and R_{ct} indicate a high electrical conductivity and fast charge transfer reaction, respectively.

5.6.6 Practical demonstration of HSC

Practical application of NCW-2||rGO HSC device prototype was tested by lightening up LED lamp (Fig. 5.31). All of these findings emphasize the potential of this simple and straightforward technique for next-generation eco-friendly sustainable energy storage with power output device using nanohybrid materials.

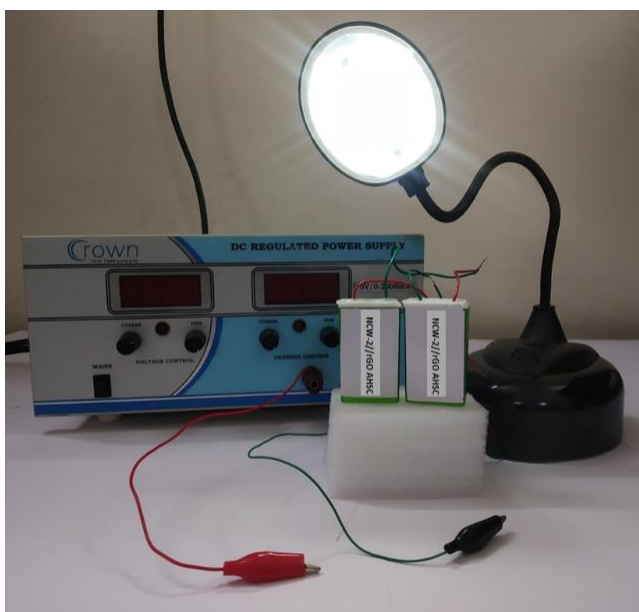


Fig. 5.31 Photograph of practical demonstration of HSC device.

5.7 Conclusions

In summary, we demonstrated the preparation of a novel NCW nanohybrid electrode material via exfoliation-reassembling based electrostatic self-assembly strategy for high ED HSCs. We have successfully fabricated aqueous HSC device comprising mesoporous NCW nanohybrid as a cathode and rGO as an anode with KOH electrolyte. The 2D intercalative layered nanohybrids exhibited enhanced electrode activity, thereby underscoring the beneficial influence of controlled POW intercalation on the electrochemical performance of pristine Ni-Cr-LDH. The optimized NCW-2 nanohybrid electrode delivered the highest specific capacity of 736 C g⁻¹. The synergetic enhancement in the electrochemical activity of Ni-Cr-LDH upon POW intercalation is not only attributed to the formation of highly

mesoporous interconnected network microstructure, but also to the expansion of freely accessible large interlayer space for effective intercalation-deintercalation of electrolytic ions. The NCW-2||rGO HSC device exhibited the highest Cs of 120 F g⁻¹ at 2 A g⁻¹ current density, a high ED of 43 Wh kg⁻¹ while delivering 1.33 kW kg⁻¹ PD, and long-term cycling stability (over 84% after 10000 GCD cycles). Based on the outstanding electrochemical performance delivered by HSC device, it is proposed that the highly mesoporous nanohybrid materials obtained by above synthetic strategy could pave a new way to fabricate efficient energy storage devices with both high ED and PD.

5.8 References

- [1] X. Jin, S-J. Shin, J. Kim, N-S. Lee, H. Kim, S-J. Hwang, *J. Mater. Chem. A* 6 (2018) 15237-15244.
- [2] H. Jin, C. Guo, X. Liu, J. Liu, A. Vasileff, Y. Jiao, Y. Zheng, S-Z. Qiao, *Chem. Rev. Chem. Rev.* 118 (2018) 6337-6408.
- [3] J. L. Gunjekar, I. Y. Kim, J. M. Lee, Y. K. Jo, S-J. Hwang, *J. Phys. Chem. C* 118 (2014) 3847-3863.
- [4] S. M. Oh, S. B. Patil, X. Jin, S-J. Hwang, *Chem. Eur. J.* 24 (2018) 4757-4773.
- [5] L. Zhang, P. Cai, Z. Wei, T. Liu, J. Yu, A. A. Al-Ghamdi, S. Wageh, *J. Colloid Interface Sci.* 588 (2021) 637-645.
- [6] X. Jin, M. Park, S-J. Shin, Y. Jo, M. G. Kim, H. Kim, Y-M. Kang, S-J. Hwang, *Small* 16 (2020) 1903265.
- [7] J. L. Gunjekar, T. W. Kim, I. Y. Kim, J. M. Lee, S-J. Hwang, *Sci. Rep.* 3 (2013) 2080.
- [8] H. Niu, Y. Zhang, Y. Liu, N. Xin, W. Shi, *J. Colloid Interface Sci.* 539 (2019) 545-552.
- [9] Q. Wang, D. O'Hare, *Chem. Rev.* 112 (2012) 4124-4155.
- [10] M. Shao, R. Zhang, Z. Li, M. Wei, D. G. Evans, X. Duan, *Chem. Commun.* 51 (2015) 15880-15893.
- [11] R. Z. Ma, Z. P. Liu, L. Li, N. Iyi, T. Sasaki, Sasaki, *J. Mater. Chem.* 16 (2006) 3809-3813.
- [12] D. H. Park, S-J. Hwang, J. M. Oh, J. H. Yang, J. H. Choy, *Prog. Polym. Sci.* 38 (2013) 1442-1486.
- [13] L. Mohapatra, K. Parida, M. Satpathy, *J. Phys. Chem. C* 1163 (2012) 13063-13070.
- [14] L. Li, R. Z. Ma, Y. Ebina, K. Fukuda, K. Takada, T. J. Am. Chem. Soc. 129 (2007) 8000-8007.
- [15] Y. Xu, W. Huang, X. Chen, F. Ge, R. Zhu, L. Sun, *Appl. Catal. A* 550 (2018) 206-213.
- [16] D. P. Dubal, N. R. Chodankar, A. Vinu, D. H. Kim, P. Gomez-Romero, *ChemSusChem* 10 (2017) 2742-2750.
- [17] J. L. Gunjekar, A. I. Inamdar, B. Hou, S. N. Cha, S. M. Pawar, A. A. A. Talha, H. S. Chavan, J. Kim, S. Cho, S. Lee, Y. Jo, H. Kim, H. Im, *Nanoscale* 10 (2018) 8953-8961.

- [18] M. R. Horn, A. Singh, S. Alomari, S. Goberna-Ferrón, R. Benages-Vilau, N. Chodankar, N. Motta, K. Ostrikov, J. MacLeod, P. Sonar, P. Gomez-Romero, D. Dubal, *Energy Environ. Sci.* 14 (2021) 1652-1700.
- [19] D. P. Dubal, O. Ayyad, V. Ruiz, P. Gómez-Romero, *Chem. Soc. Rev.* 44 (2015) 1777-1790.
- [20] N. R. Chodankar, H. D. Pham, A. K. Nanjundan, J. F. S. Fernando, K. Jayaramulu, D. Golberg, Y.-K. Han, D. P. Dubal, *Small* 16 (2020) 2002806.
- [21] W.T. Reichle, *Solid State Ion.* 22 (1986) 135-141.
- [22] D. Marcano, D. Kosynkin, J. Berlin, A. Sinitskii, Z. Sun, A. Slesarev, L. Alemany, W. Lu, J. Tour, *ACS Nano* 4 (2010) 4806-4814.
- [23] S. J. Marje, P. K. Katkar, S. S. Pujari, S. A. Khalate, A. C. Lokhande, U. M. Patil, *Synth. Met.* 259 (2020) 116224.
- [24] A. S. Patil, J. L. Gunjekar, C. D. Lokhande, U. M. Patil, S. V. Sadavar, N. S. Padalkar, R. B. Shinde, M. M. Wagh, J. S. Bagi, *Synth. Met.* 264 (2020) 116371.
- [25] J. L. Gunjekar, I. Y. Kim, S.-J. Hwang, *Eur. J. Inorg. Chem.* 7 (2015) 1198-1202.
- [26] M. Qin, S. Li, Y. Zhao, C.-Y. Lao, Z. Zhang, L. Liu, F. Fang, H. Wu, B. Jia, Z. Liu, W. Wang, Y. Liu, X. Qu, *Adv. Energy Mater.* 9 (2019) 1803060.
- [27] R. A. Nyquist, R. O. Kagel, *Infrared spectra of inorganic compounds (3800-450cm⁻¹)*, Academic Press Inc, New York 1971, p. 3.
- [28] N. Baliarsingh, L. Mohapatra, K. Parida, *J. Mater. Chem. A* 1 (2013) 4236-4243.
- [29] V. B. Kumar, D. Mohanta, *Bull. Mater. Sci.* 34 (2011) 435-442.
- [30] L. P. F. Benício, D. Eulálio, L. M. Guimarães, F. G. Pinto, L. M. da Costa, J. Tronto, *Mater. Res.* 6 (2018) 1-13.
- [31] A. S. O. Gomes, N. Yaghini, A. Martinelli, E. J. Ahlberg, *J. Raman Spectrosc.* 48 (2017) 1256-1263.
- [32] F. D. Hardcastle, I. E. Wachs, *J. Raman Spectrosc.* 26 (1995) 397-405.
- [33] A. F. Redkin, G. V. Bondrenko, *J. Solution Chem.* 39 (2010) 1549-1561.
- [34] W. Ye, X. Fang, X. Chen, D. Yan, *Nanoscale* 10 (2018) 19484-19491.
- [35] Y. Yang, L. Dang, M. J. Shearer, H. Sheng, W. Li, J. Chen, P. Xiao, Y. Zhang, R. J. Hamers, S. Jin, *Adv. Energy Mater.* 8 (2018) 1703189.
- [36] T. Zhou, Z. Cao, P. Zhang, H. Ma, Z. Gao, H. Wang, Y. Lu, J. He, Y. Zhao, *Sci. Rep.* 7 (2017) 46154.
- [37] T. Li, Z. Wang, W. Chen, H. N. Miras, Y.-F. Song, *Chem. Eur. J.* 23 (2017) 1069-1077.
- [38] J. B. Condon, *Surface area and porosity determinations by physisorption: measurements and theory* 1st ed. Elsevier: Amsterdam; Boston, 2006; p 274.
- [39] C. L. Hill, *Chem. Rev.* 98 (1998) 1-2.
- [40] L. Zhang, K. N. Hui, K. S. Hui, H. Lee, *J. Power Sources* 318 (2016) 76-85.
- [41] S. D. Perera, X. Ding, A. Bhargava, R. Hovden, A. Nelson, L. F. Kourkoutis, R. D. Robinson, *Chem. Mater.* 27 (2015) 7861-7873.

- [42] Y. Li, Z. Luo, H. Qin, S. Liang, L. Chen, H. Wang, C. Zhao, S. Chen, J. Colloid Interface Sci. 582 (2020) 842-851.
- [43] X. Ge, C. Gu, Z. Yin, X. Wang, J. Tu, J. Li, Nano Energy 20 (2016) 185-193.
- [44] A. D. Jagadale, G. Guan, X. Li, X. Du, X. Ma, X. Hao, A. Abudula, J. Power Sources 306 (2016) 526-534.
- [45] L. Zhang, H. Yao, Z. Li, P. Sun, F. Liu, C. Dong, J. Wang, Z. Li, M. Wu, C. Zhang, B. Zhao, J. Alloys Compd. 711 (2017) 31-41.
- [46] B. Liu, J. Hou, T. Zhang, C. Xu, H. Liu, J. Mater. Chem. A 7 (2019) 16222-16230.
- [47] Z. Xiao, Y. Bao, Z. Li, X. Huai, M. Wang, P. Liu, L. Wang, ACS Appl. Energy Mater. 2 (2019) 1086-1092.
- [48] W. Wang, Y. Lu, M. Zhao, R. Luo, Y. Yang, T. Peng, H. Yan, X. Liu, Y. Luo, ACS Nano 13 (2019) 12206-12218.
- [49] A. Tyagi, M. C. Joshi, A. Shah, V. K. Thakur, R. K. Gupta, ACS Omega 4 (2019) 3257-3267.
- [50] P. K. Katkar, Supriya J. Marje, S. S. Pujari, S. A. Khalate, A. C. Lokhande, U. M. Patil, ACS Sustainable Chem. Eng. 7 (2019) 11205-11218.



CHAPTER-6

**Synthesis, Characterization and
Electrochemical Performance
Evaluation of Ni-Cr-LDH
Hybridized with GO and HSC
Device**

CHAPTER 6

Synthesis, Characterization and Electrochemical Performance Evaluation of Ni-Cr-LDH Hybridized with GO and HSC

Sr. No.	Title		Page No.
6.1	Introduction		169-170
6.2	Experimental details		170-171
	6.2.1	<i>Chemicals</i>	170
	6.2.2	<i>Synthesis of Ni-Cr-LDH nanosheets hybridized with GO</i>	171
6.3	Results and Discussion		171-181
	6.3.1	<i>XRD study</i>	171-173
	6.3.2	<i>FTIR study</i>	173-174
	6.3.3	<i>Micro-Raman study</i>	174-175
	6.3.4	<i>FESEM study</i>	175-176
	6.3.5	<i>HRTEM study</i>	176-178
	6.3.6	<i>BET surface area study</i>	178-179
	6.3.7	<i>XPS study</i>	179-181
6.4	Conclusions		181-182
6.5	Electrochemical performance evaluation of Ni-Cr-LDH nanosheets hybridized with GO		
6.5.1	Preparation of electrode		182
6.5.2	Results and discussion		182-190
	6.5.2.1	<i>CV study</i>	182-186
	6.5.2.2	<i>GCD study</i>	186-188
	6.5.2.3	<i>Stability study</i>	189
	6.5.2.4	<i>EIS study</i>	189-190
6.6	Electrochemical performance evaluation of NCG-2 rGO hybrid supercapacitor device		
	6.6.1	<i>CV study</i>	191-193
	6.6.2	<i>GCD study</i>	193
	6.6.3	<i>Ragone plot</i>	193-194

	6.6.4	<i>Stability study</i>	194-195
	6.6.5	<i>EIS study</i>	196
	6.6.6	<i>Practical demonstration of HSC</i>	196-197
6.7	Conclusions		197
6.8	References		198-200

6.1 Introduction

Energy storage via batteries and SC focuses on an enormous amount of research activity due to their usefulness in new-generation electric automobiles, portable electronics, healthcare, and defense equipment [1–3]. SCs or electrochemical capacitors garnered colossal attention because of their advantages like high power delivery, extended cycle life, good operational safety, and high rate characteristic [4]. However, the lower ED associated with commercially available carbon-based SCs cannot meet the requirement of advanced applications, especially hybrid electric vehicles [5]. Thus, numerous efforts are put forward on the HSCs with one pseudocapacitor or battery-type and other EDLC-type electrode [6–11]. As SCs electrode materials design significantly impacts its performance, exploration of the novel electrode materials possessing characteristics of high ED, PD and electrochemical stability is the key to achieving desired electrochemical performance. The expanded surface area carbon-based materials perform exceptionally well as an EDLC-type electrode in HSC [12]. However, materials like transition metal oxide, hydroxides, and conducting polymers are potential pseudocapacitive or battery-type electrode materials in HSC [13–16].

LDHs are a class of 2D lamellar compounds, which comprise stacking of positively charged brucite-like metal hydroxide monolayers and charge-balancing anions sandwiched between the monolayers. LDHs are regarded as high-performance pseudocapacitive or battery-type SCs electrodes due to their unique properties like flexible chemical composition, anions intercalated layered structure, and tunable interlayer space [17,18]. Though many efforts have been taken to improve the electrochemical activity of LDHs-based electrodes, their performances are far below theoretical capacity due to their compact stacking structure, low surface area, and conductivity [19]. Consequently, several attempts have been made to hybridize LDHs with carbonaceous materials to enable high conductivity and electrochemical stability [20–22]. These research efforts mainly included direct growth or anchoring of LDHs on carbonaceous materials, in which control of chemical composition, particle size, surface area, morphology, and stacking structure are critical factors.

Recently explored exfoliation routes for LDHs leading a positively charged 2D monolayer LDH NSs [23]. On the other hand, GO, synthesized by the chemical oxidation of graphene, possess exfoliation capability in water and leads to negatively charged GO NSs [24–26]. Thus, exfoliation of these NSs with opposite electrostatic charges opens up a window of opportunity to design and develop a unique kind of 2D-2D LDH-GO nanohybrids by simply mixing two kinds of NSs (self-assembling). Such a 2D-2D LDH-GO nanohybrids can enable expanded surface area by random restacking of constituent NSs, high electrical conductivity via intimate coupling between NSs, tunable chemical composition, and stacking structure [27,28]. Consequently, such self-assembling provides better control over chemical composition, particle size, surface area, morphology, and stacking structure. Furthermore, these self-assembled LDH-GO nanohybrids can demonstrate enhanced electrochemical activity when used as SCs electrodes. On a few instances, self-assembled LDH-GO nanohybrids were explored as photocatalysts, SCs electrodes, CO₂ capture and Li-ion battery electrodes [29–32].

Herein, we prepared 2D-2D layered nanohybrids of Ni-Cr-LDH wrapped by GO NSs (NCG nanohybrids) via electrostatic self-assembly between cationic Ni-Cr-LDH NSs and anionic GO NSs. The NCG nanohybrids are tested for their application in HSC electrodes. Additionally, we explored the effect of GO on the physicochemical properties and electrochemical performance of the NCG nanohybrid electrodes. Further, the HSC device is developed using the NCG nanohybrids as a positive electrode and hydrothermally rGO as the negative electrode. This is the first report on a synthesis of NCG nanohybrid and their use as an HSC electrode.

6.2. Experimental details

6.2.1 Chemicals

Graphite flakes, nickel nitrate Ni(NO₃)₂, chromium nitrate Cr(NO₃)₃, sodium nitrate (NaNO₃), and sodium hydroxide (NaOH) were purchased from Sigma-Aldrich and used without further purification. The SS (304 grade) was used as a substrate.

6.2.2 Synthesis of Ni-Cr-LDH hybridized with graphene oxide

The colloidal suspension of GO NSs was obtained by ultrasonic shaking of GO in water. As another precursor, the colloidal suspension of the exfoliated Ni-Cr-LDH monolayer was prepared by vigorous shaking of Ni-Cr-LDH (1mg ml^{-1}) in formamide solution [33].

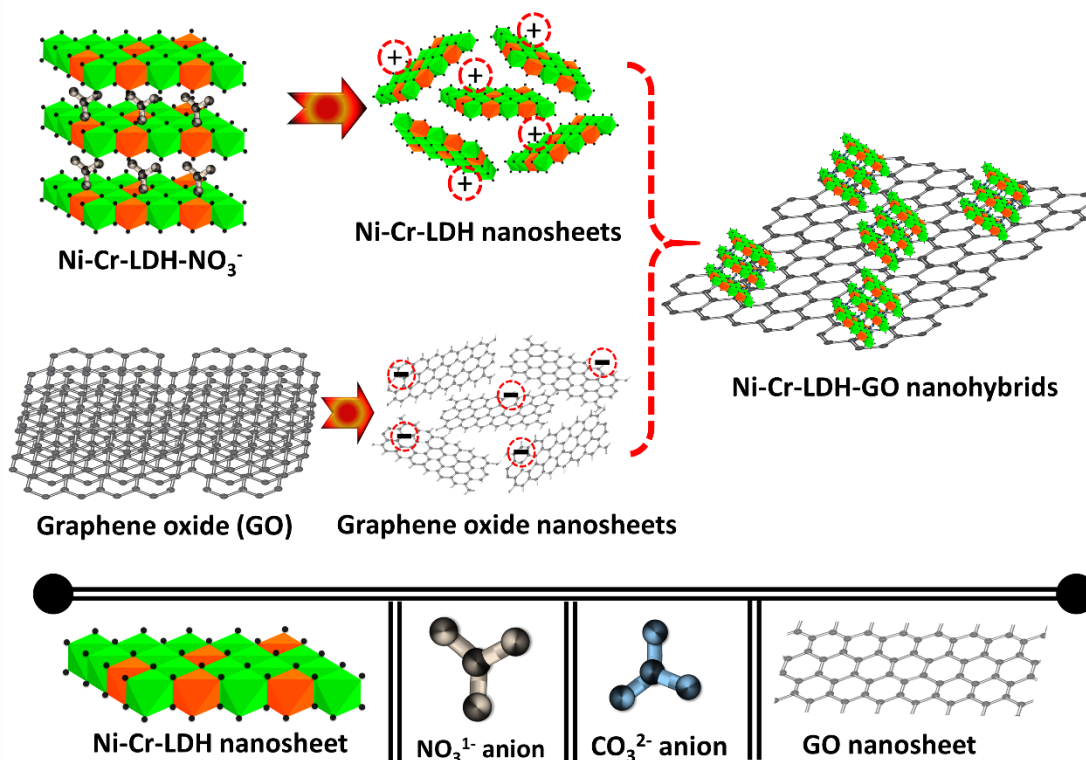


Fig. 6.1: The schematic for the synthesis of self-assembled NCG nanohybrids.

The self-assembled NCG nanohybrids (Fig. 6.1) were synthesized by mixing the NSs suspensions of Ni-Cr-LDH and GO under constant stirring at ambient temperature. Instantaneous flocculation was observed just after mixing the two NSs suspensions. Subsequently, the flocculated NCG nanohybrids product was collected by centrifugation at 7000 rpm, washed with absolute ethanol and water three times, and then freeze-dried to ensure solid powder of NCG nanohybrids. Additionally, the various chemical compositions of NCG were obtained by varying Ni-Cr-LDH to GO weight % (wt%). The NCG nanohybrids prepared at GO wt% of 2, 4, and 6 are denoted as NCG-1, NCG-2 and NCG-3, respectively.

6.3 Results and discussion

6.3.1 XRD study

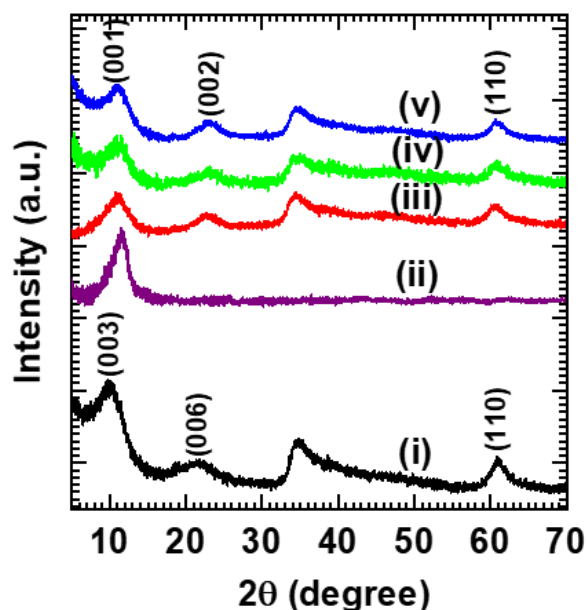


Fig. 6.2: XRD patterns of (i) pristine Ni-Cr-LDH, (ii) GO, (iii) NCG-1, (iv) NCG-2, and (v) NCG-3 nanohybrids.

Powder XRD analysis is performed to elucidate the crystal structure of pristine Ni-Cr-LDH, GO NSs, and NCG nanohybrids, as shown in Fig. 6.2. The observed Bragg reflections of pristine Ni-Cr-LDH can be indexed to hexagonal lattice having an $R\text{-}3m$ space group with rhombohedral symmetry [34]. The presence of $(00l)$ Bragg reflection series corresponds to the basal spacing of 0.88 nm, which indicates the nitrate anions intercalated Ni-Cr-LDH structure [34]. The formation of nitrate intercalated Ni-Cr-LDH enables its exfoliation capability in formamide. Further dispersion of the nitrate intercalated Ni-Cr-LDH in formamide yields a colloidal suspension of exfoliated Ni-Cr-LDH NSs. The zeta potential measurement reveals the positive zeta potential (43 mV), indicating the formation of positively charged exfoliated Ni-Cr-LDH NSs (Chapter 4, Fig. 4.1(b)). The lattice dimensions $a=b=0.3$ nm and $c=0.88$ nm are calculated for pristine Ni-Cr-LDH. The GO sample shows a typical XRD pattern with the intense $(00l)$ reflection at $2\theta = 11.5^\circ$, confirming the formation of GO with exfoliation capability [35]. All the NCG nanohybrids commonly show well-developed $(00l)$ Braggs reflections corresponding to the basal spacing of ~ 0.78 nm. The decreased basal spacing of NCG nanohybrids is attributed to the intercalation of divalent carbonate ions into the restacked LDH crystals [36]. The intercalation of carbonate ions can be understood from the high solvation of CO_2 during the synthesis and washing

process of GO suspension [36]. In addition, all nanohybrid materials exhibit a broad hump at $2\theta \sim 30\text{--}40^\circ$, which is attributable to the disordered stacking structure of NSs. Also, all the nanohybrids display characteristic inplane Braggs reflection at 61° assigned to the (110) plane. This peak indicates the retention of the in-plane structure of the LDH NSs upon hybridization with anionic GO NSs. Interestingly, the absence of any peak associated with GO indicates the homogeneous distribution of GO without agglomeration or phase separation.

6.3.2 FTIR study

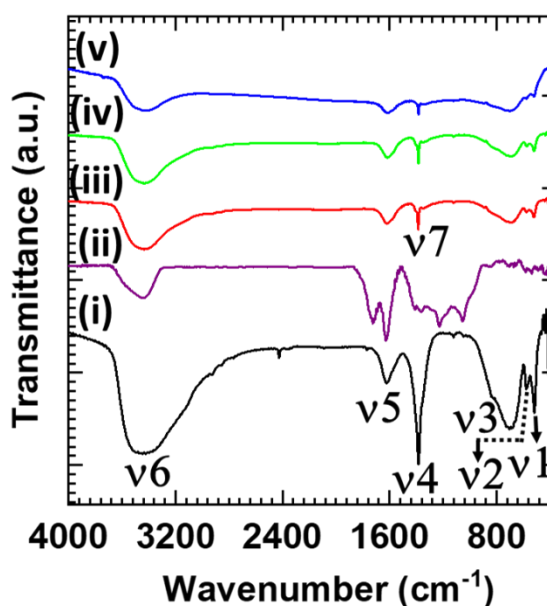


Fig. 6.3: FTIR spectra of the (i) pristine Ni-Cr-LDH (ii) GO (iii) NCG-1, (iv) NCG-2 and (v) NCG-3 nanohybrids.

The nature of chemical bonding and grafted functional groups present in the NCG nanohybrids are probed using FTIR and Micro-Raman spectroscopy. Fig. 6.3 shows the FTIR spectra of pristine Ni-Cr-LDH and NCG nanohybrids. Ni-Cr-LDH and NCG nanohybrid commonly show low-frequency peaks v_1 (515 cm^{-1}), v_2 (576 cm^{-1}), and v_3 (670 cm^{-1}) which are associated with metal-oxygen and metal-oxygen-metal lattice vibrational modes of Ni-Cr-LDH lattice [37,38]. The intense peak v_4 (1384 cm^{-1}) is assigned to the intercalated NO_3^{1-} anions in Ni-Cr-LDH [39]. The reference GO displays IR peaks in the $1800\text{--}900\text{ cm}^{-1}$, which are ascribed to the carbon-oxygen functional groups attached to the GO during the chemical oxidation of graphene [36]. All NCG nanohybrid and pristine Ni-Cr-LDH exhibit a broad peak at v_6 (3334 cm^{-1}) and v_5 (1645 cm^{-1}), which are ascribed to the O-H stretching

mode and bending mode of adsorbed water molecules, respectively [39,40]. All NCG nanohybrids exhibit sharp peaks at ν_7 (1390 cm^{-1}), which is assigned to the stretching mode of intercalated carbonate anions. The presence of peak ν_7 indicates the intercalation of carbonate anions in LDH crystals during the self-assembly process [40,41]. Similarly, all NCG nanohybrids display only weak intensity for these IR peaks related to the carbon-oxygen bonds due to the probable reduction of GO during the hybridization with Ni-Cr-LDH NSs.

6.3.3 Micro-Raman study

Fig. 6.4 shows Micro-Raman spectra of NCG nanohybrid as compared to pristine Ni-Cr-LDH and GO. The pristine Ni-Cr-LDH display characteristic Raman peaks at 311 cm^{-1} and 460 cm^{-1} , assigned to the E_g and A_{1g} vibration mode of Ni(OH)_2 , respectively [42]. The broad and high-intensity peak at 560 cm^{-1} formed by the superposition of two peaks at 530 cm^{-1} and 557 cm^{-1} are assigned to the Cr-O-H bending mode and second-order acoustic mode of Ni(OH)_2 in Ni-Cr-LDH lattice, respectively [43]. Moreover, the pristine Ni-Cr-LDH display a sharp peak at 1050 cm^{-1} , attributed to the symmetric vibrations of intercalated NO_3^- anions in pristine Ni-Cr-LDH [44,45]. All NCG nanohybrids show characteristic peaks at 351 cm^{-1} and 560 cm^{-1} , assigned to the A_{1g} Ni-O stretching and lattice vibrational mode of $\alpha\text{-Ni(OH)}_2$, respectively [46]. The Raman peak at 790 cm^{-1} observed for Ni-Cr-LDH and NCG nanohybrids is assigned to the second-order lattice mode of Ni-Cr-LDH [47]. In addition to the LDH related peaks, the NCG nanohybrids additionally show characteristic peaks related at 1350 cm^{-1} and 1600 cm^{-1} corresponding to the D (breathing mode of A_{1g}) symmetry and G band (E_{1g} symmetry of SP^2 of carbon atom) of GO, respectively [35]. Interestingly, the NCG nanohybrids show a higher D/G intensity ratio than pristine Ni-Cr-LDH, reflecting the significant reduction of GO after hybridization.

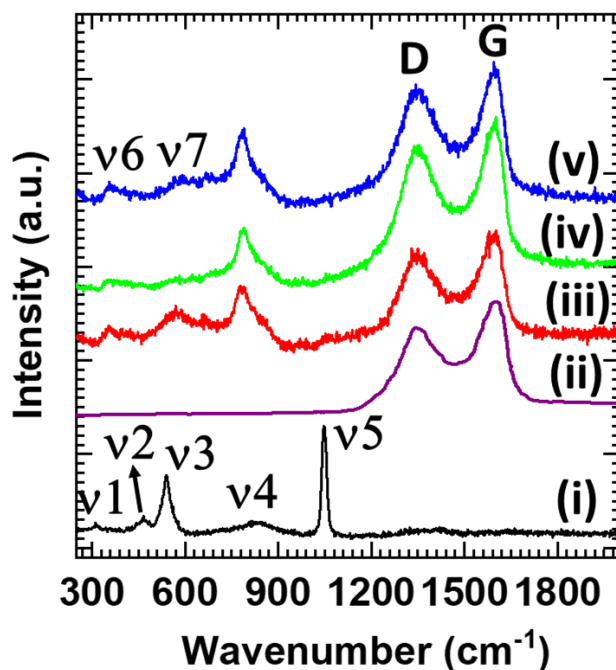


Fig. 6.4: Micro-Raman spectra of the (i) pristine Ni-Cr-LDH, (ii) GO (iii) NCG-1, (iv) NCG-2 and (v) NCG-3 nanohybrids.

6.3.4 FESEM study

The surface morphology of the NCG nanohybrids, GO and pristine Ni-Cr-LDH is examined by the FESEM technique. As shown in Fig. 6.5(c-e), all NCG nanohybrids display highly porous morphology composed of restacked Ni-Cr-LDH NSs crystallites wrapped by the ultrathin GO NSs. As seen from the micrographs of Ni-Cr-LDH and GO NSs (Fig. 6.5a,b), the lateral crystallite size of pristine Ni-Cr-LDH is ~ 50 - 150 nm, and that of GO NSs is ~ 5 - 10 μm . Such ultralong lateral dimensions of GO establish conducting channels among the restacked Ni-Cr-LDH crystallites upon the self-assembly. Eventually, NCG nanohybrids are expected to display high electrical conductivity. This type of porous morphology is commonly observed in nanohybrid materials prepared by exfoliating-reassembling 2D inorganic NSs with GO or rGO NSs [17,20,36]. Moreover, this type interconnected restacked Ni-Cr-LDH crystallites wrapped by GO NSs morphology can provide large contact area between redox-active sites and electrolyte, and efficient charge transport when used as an electrode in the electrochemical cell [17,20].

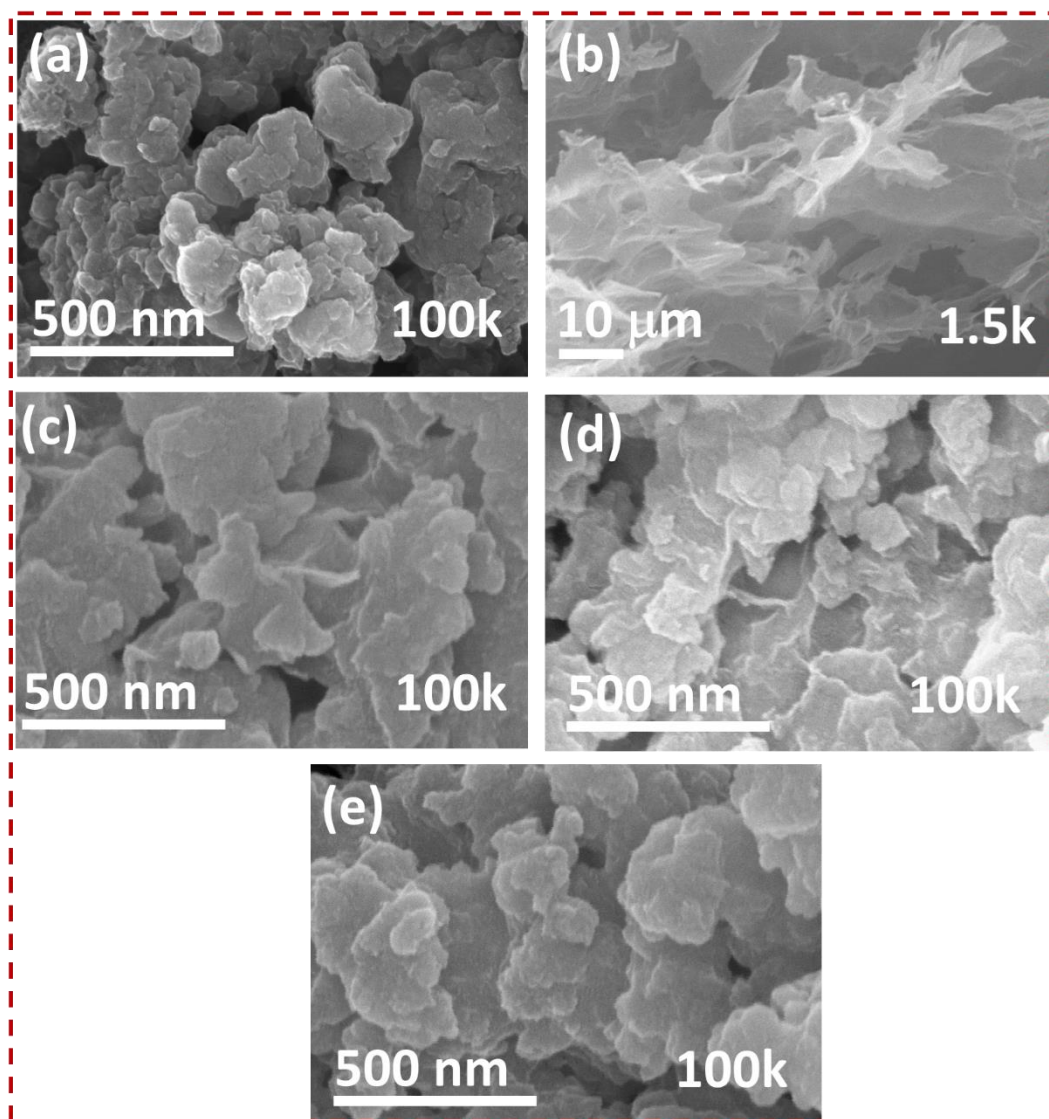


Fig. 6.5: FESEM images of the (a) pristine Ni-Cr-LDH, (b) GO, (c) NCG-1, (d) NCG-2, and (e) NCG-3 nanohybrids.

6.3.5 HRTEM study

The local crystal structure and crystal shape of the as-prepared NCG-2 nanohybrid at the nanometer scale are examined by TEM and cross-sectional HRTEM. The pristine Ni-Cr-LDH shows (Chapter 3, Fig. 3.6) compact sheet-like non-porous morphology, frequently observed in LDH synthesized by the coprecipitation method [39].

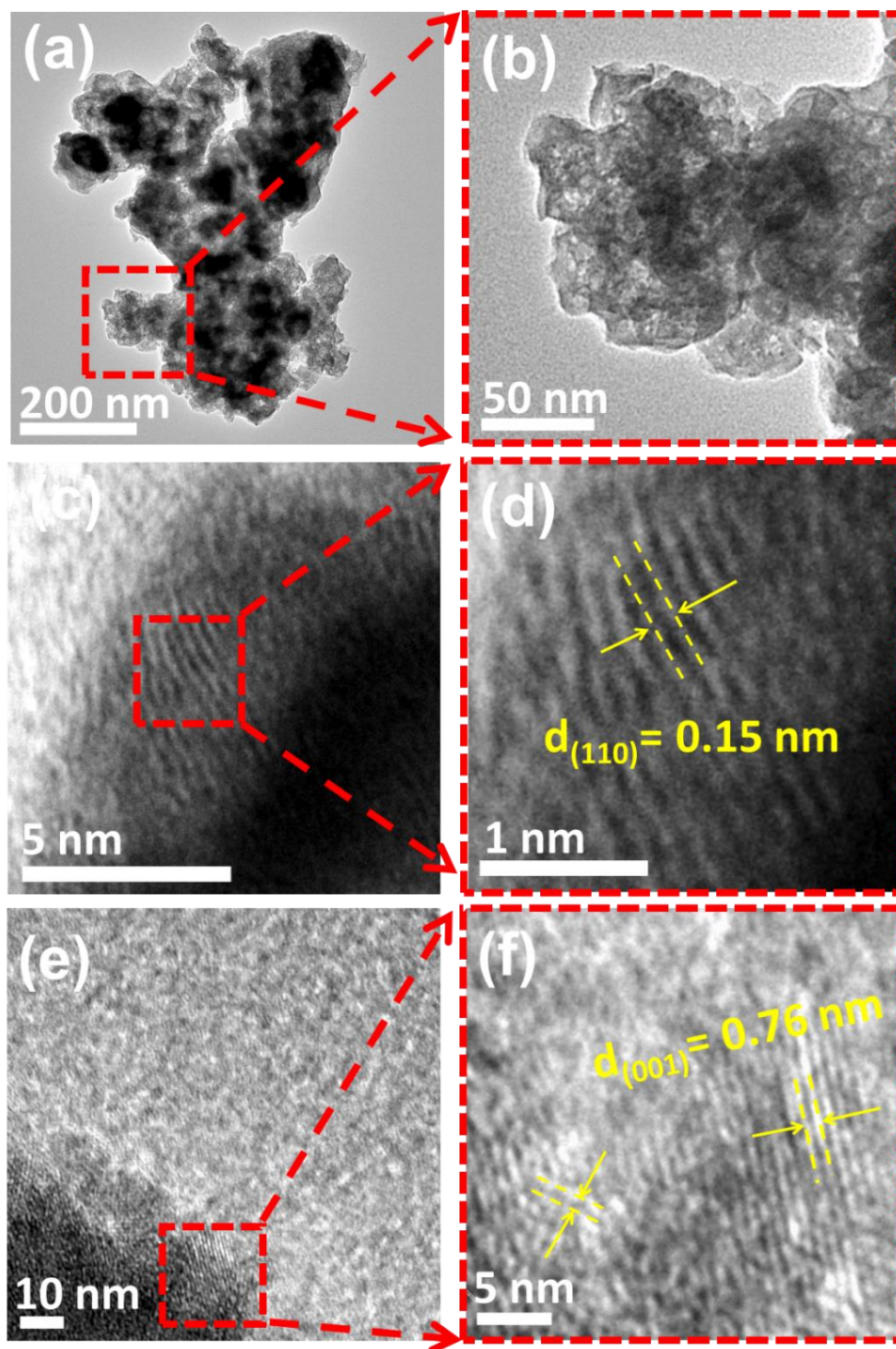


Fig. 6.6: (a, b) TEM images of NCG-2, (c, d) top view HRTEM images of NCG-2, (e, f) cross-sectional HRTEM images of the NCG-2 nanohybrid.

As presented in Fig. 6.6(a) and (b) the NCG-2 nanohybrid vividly displays randomly aggregated clusters composed of restacked Ni-Cr-LDH nanosheet crystallites wrapped by the ultrathin GO NSs. In addition, a highly porous structure

made up of edge-to-face interaction of aggregated Ni-Cr-LDH and GO NSs is clearly visible. As illustrated in Fig. 6.6(c-f), the NCG nanohybrid shows two high-resolution sets of parallel lattice fringes. One set with the fringe spacing of 0.15 nm corresponds to the in-plane lattice distance of Ni-Cr-LDH. The other set with the fringe spacing of 0.76 nm well matches with the c-axis parameter of the Ni-Cr-LDH lattice calculated from the XRD study. However, no fringes for GO are observed in HR-TEM analysis due to the high dispersion of GO NSs throughout the nanohybrid. This observation clearly demonstrates the advantages of the self-assembled NCG nanohybrids for forming layer-by-layer stacked porous structures and wrapping effect of Ni-Cr-LDH by GO NSs.

6.3.6 Surface area study

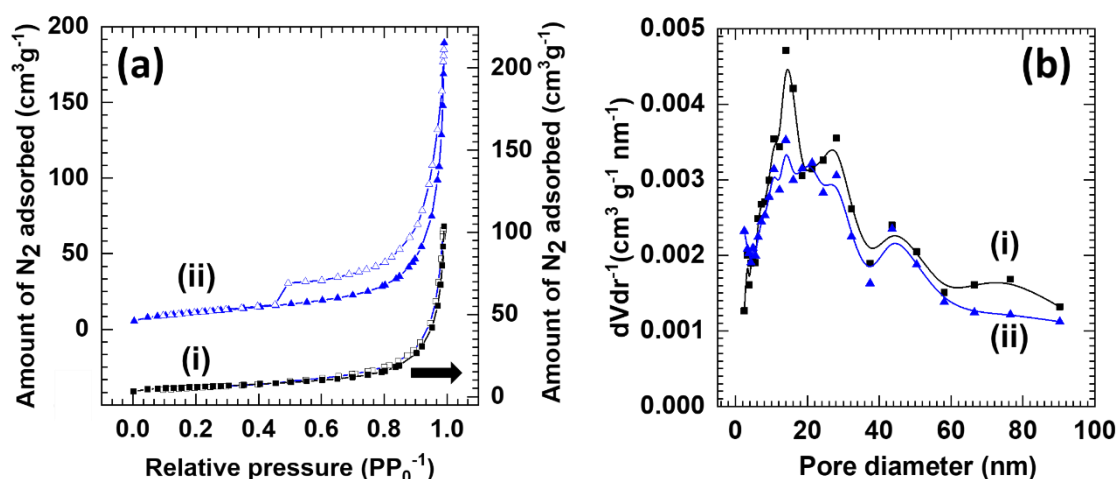


Fig. 6.7: (a) N₂ adsorption-desorption isotherms, (b) pore size distribution plot of NCG-2 nanohybrid.

N₂ adsorption-desorption isotherm analysis is used to investigate the pore architectures and surface area of pristine Ni-Cr-LDH and NCG-2 nanohybrid. N₂ adsorption-desorption isotherms of pristine Ni-Cr-LDH and NCG-2 nanohybrid are presented in Fig. 6.7(a). As compared to the pristine Ni-Cr-LDH, NCG-2 nanohybrid displays significant N₂ adsorption in the PP₀⁻¹ < 0.45 region and vivid hysteresis in the PP₀⁻¹ > 0.45 region [48]. The observed isotherm is classified as BDDT type-IV isotherms and H3-type hysteresis loop, which is the characteristics of mesoporous materials, open slit-shaped capillaries with wide bodies and narrow short necks

[23]. In contrast, pristine Ni-Cr-LDH displays only minute N_2 adsorption and the absence of hysteresis, a typical characteristic of non-porous materials. According to the surface area measurements based on the BET equation, NCG-2 nanohybrid exhibit remarkably expanded surface areas of $49 \text{ m}^2 \text{ g}^{-1}$, which is greater than that of pristine Ni-Cr-LDH ($14 \text{ m}^2 \text{ g}^{-1}$). The corresponding distribution of the pore size is analyzed using the BJH method. The NCG-2 nanohybrids display an average pore diameter of 15 nm (Fig. 6.7b). This result provides strong evidence for the beneficial role of GO matrix in expanding the surface area of NCG-2 nanohybrids.

6.3.7 XPS study

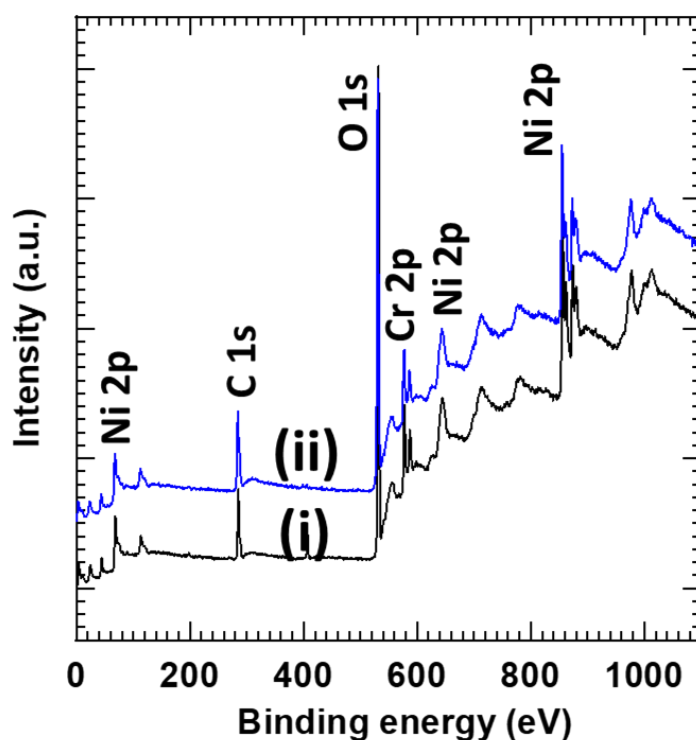


Fig.6.8: Full survey of XPS spectra of (i) pristine Ni-Cr-LDH, (ii) NCG-2 nanohybrid.

XPS study is used to probe the surface electronic states of NCG nanohybrids, pristine Ni-Cr-LDH and GO. The full survey of XPS spectra for the pristine Ni-Cr-LDH and NCG-2 nanohybrid in Fig. 6.8 shows spectral features of the Ni, Cr, O, and C elements. As shown in Fig. 6.9(a), the pristine Ni-Cr-LDH and NCG-2 nanohybrids show two sharp peaks at BE P (856 eV) and Q (873.5 eV), which correspond to the spin-orbit splitting of $Ni 2p_{1/2}$ and $Ni 2p_{3/2}$. In addition, two shakeup-type peaks at

P' (861 eV) and Q' (879.8 eV) are separated by BE difference of 15 eV. This BE difference indicates Ni²⁺ oxidation state in Ni-Cr-LDH and NCG-2 nanohybrid [49]. The High-resolution Cr 2p spectrum of pristine Ni-Cr-LDH and NCG-2 nanohybrid in Fig. 6.9(b) show two broad peaks at P (577 eV) and Q (587 eV) ascribed to the spin-orbit doublet of Cr 2p_{1/2} and Cr 2p_{3/2}, respectively. The broad peak P at BE of 577 eV is attributed to the Cr³⁺ hydroxide [50]. The O 1s XPS spectra of NCG-2 nanohybrid, pristine Ni-Cr-LDH and GO are plotted in Fig. 6.9(c). The pristine Ni-Cr-LDH displays a broad peak at P (531.5 eV) due to the presence of oxygen from metal hydroxide (530.4 eV), surface hydroxyl group (531.5 eV) and bound water (532.6 eV) [51]. On the other hand, the pristine GO displays a broad peak at 532.07 eV due to O=C bonds in carbonyl C=O and carboxyl O=C-OH groups (531.0 eV), O-C bonds in hydroxyl C-OH and epoxy C-O-C moieties (532.07 eV) and O-H bonds in adsorbed water (533.2 eV) [52]. Similar to pristine Ni-Cr-LDH, the NCG-2 nanohybrid exhibits a broad peak P (531.5 eV) ascribed to the major contribution of the LDH related O 1s features of metal hydroxide (530.4 eV), surface hydroxyl group (531.5 eV) and bound water (532.6 eV). The C 1s XPS spectra of NCG-2 nanohybrid and pristine GO are plotted in Fig. 6.9(d). The pristine GO shows characteristic C 1s peaks at BE of 284.4 eV, 285.33 eV, and 286.8 eV, which are assigned to the C-C (non-oxygenated ring), C-O (hydroxyl C-OH and epoxy C-O-C moieties), C=O (carbonyl) functional groups [36]. Remarkably, the NCG-2 nanohybrid shows an intense peak at BE of 284.5 and a low-intensity peak at 285.8 eV, which are ascribed to the C-C (non-oxygenated ring) and (hydroxyl C-OH and epoxy C-O-C moieties). Moreover, NCG-2 nanohybrid also displays one broad peak at 288.25 eV, assigned to the intercalated carbonate anions [53]. The C 1s XPS feature of C-O (hydroxyl C-OH and epoxy C-O-C moieties) and C=O (carbonyl) functional groups are observed to be quenched in nanohybrids underscoring the reduction of GO. A similar reduction of GO was observed for the self-assembled ZnCr-LDH-GO nanohybrids [36].

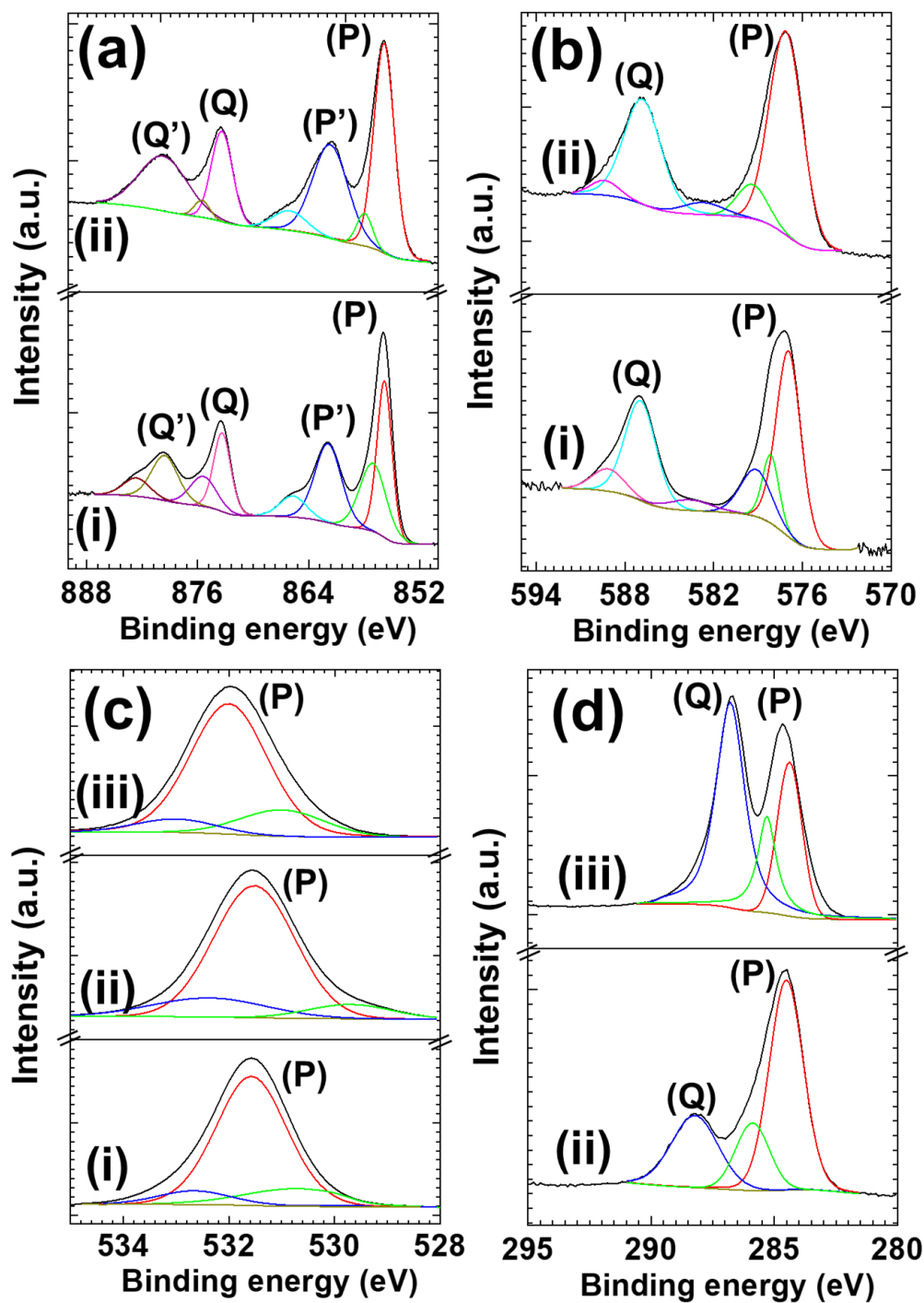


Fig. 6.9: (a) Ni 2p, (b) Cr 2p, (c) O 1s and (d) C 1s core-level XPS spectra of (i) pristine Ni-Cr-LDH and (ii) NCG-2 nanohybrid (in panel c and d, (iii) corresponds to pristine GO).

6.4 Conclusions

In the present work, mesoporous Ni-Cr-LDH-GO nanohybrids were successfully synthesized by the electrostatically derived self-assembly of positively

charged (cationic) Ni-Cr-LDH nanoplates with negatively charged (anionic) GO NSs. Structural study of NCG revealed the formation anchored assembly of Ni-Cr-LDH and GO NSs. Interestingly, the absence of any peak associated with GO indicates the homogeneous distribution of GO without agglomeration or phase separation. All NCG nanohybrids display highly porous morphology composed of restacked Ni-Cr-LDH NSs crystallites wrapped by the ultrathin GO NSs. FTIR and Micro-Raman analysis indicate the incorporation of carbonate ions into the interlayer space of the Ni-Cr-LDH component upon the self-assembly process. Surface area study clearly indicates the exfoliation-hybridization process remarkably enhanced the surface area of pristine Ni-Cr-LDH. In summary nanohybrids of 2D Ni-Cr-LDH wrapped by GO NSs (NCG) are successfully prepared by electrostatic self-assembly between cationic Ni-Cr-LDH NSs and anionic GO NSs.

6.5 Electrochemical performance evaluation of Ni-Cr-LDH hybridized with GO nanosheets

6.5.1 Preparation of NCG electrodes

The electrochemical tests of NCG nanohybrids and Ni-Cr-LDH were conducted using a three-electrode electrochemical cell in a 2M KOH electrolyte. Hg/HgO electrode and pt mesh (2 cm × 2 cm) were used as the reference and counter electrodes, respectively. The working electrodes of Ni-Cr-LDH/NCG were prepared by making slurry with a composition of 85 wt% of active materials, 10 wt% of AB and 5 wt% of PVDF binder, dissolved in NMP. The slurry was coated on SS substrate (1cm × 1cm in area) and dried under a vacuum oven at 70°C for 10 h.

6.5.2 Results and discussion

6.5.2.1 CV study

The electrochemical performance of the Ni-Cr-LDH and NCG nanohybrids electrodes is evaluated by CV, GCD, and EIS tests in an aqueous 2 M KOH solution using a three-electrode electrochemical cell. Fig. 6.10 presents the comparative CV profiles of the Ni-Cr-LDH and NCG nanohybrid electrodes at a scan rate of 20 mV s⁻¹. All the electrodes display characteristic CV shapes with pairs of redox peaks

ascended due to quasi-reversible redox transformation between $\text{Ni}^{2+}/\text{Ni}^{3+}$ based on the equation 3.1.

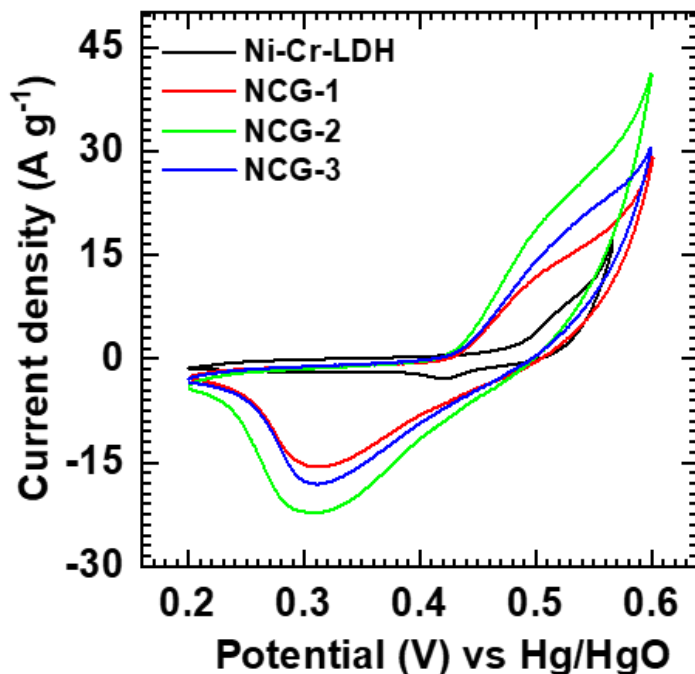


Fig. 6.10: The CV curves of pristine Ni-Cr-LDH, NCG-1, NCG-2, and NCG-3 nanohybrid electrodes at a scan rate of 20 mV s^{-1} .

The integral area enclosed by the CV curve relates to the capacity of electrode material. Interestingly, all NCG nanohybrid electrodes display significantly increased integral area enclosed by the CV curves than pristine Ni-Cr-LDH, indicating higher charge storing ability of nanohybrids. Moreover, the integral area enclosed by the CV curves varies with the GO Wt %. The NCG-1 nanohybrids prepared at 2 wt % GO display the smallest area that increases to a maximum for NCG-2 at 4 wt % GO. Further increase in GO to 6 wt % (NCG-3) leads to a decrease in integral area. The present result underscores the beneficial effect of optimum GO content in NCG-2 nanohybrids for increased electrode performance. Moreover, excess GO incorporation in NCG-3 nanohybrid negatively affects its charge storing ability, as seen by reducing the area under CV.

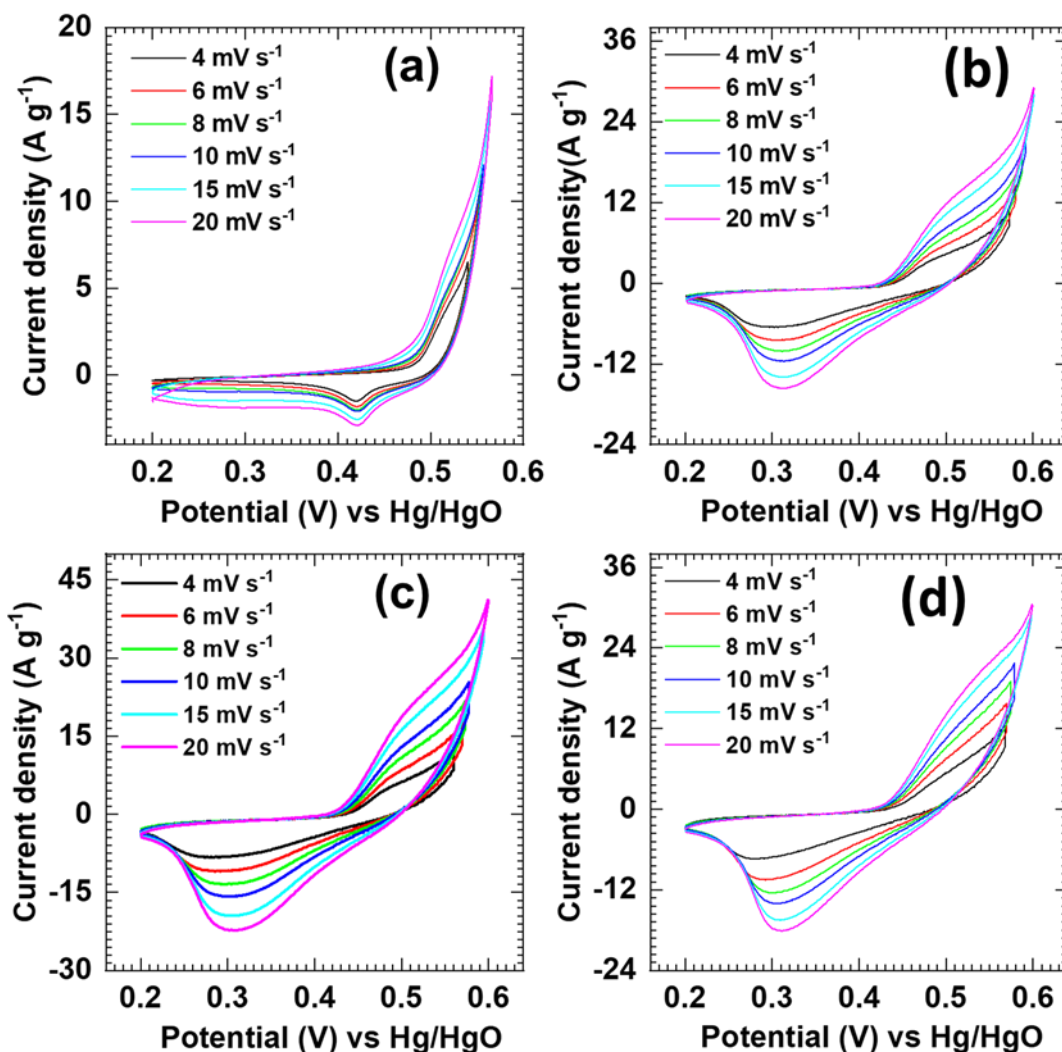


Fig. 6.11: The CV curves of (a) Ni-Cr-LDH, (b) NCG-1, (c) NCG-2, and (d) NCG-3 nanohybrid electrodes at various scan rates (4-20 mV s^{-1}).

The effect of scan rate on CV profile for all the samples is shown in Fig. 6.11. The positive cathodic peak shift, peak broadening, and increased area under CV with the scan rate are clearly observable, which indicates a hybrid charge storage mechanism involving capacitive and battery-type charge storage in all samples. Consequently, the electrochemical kinetics analysis determines the contribution of capacitive (Q_s) and battery-type (Q_d) charge storage. The total charge (Q_t) stored by the electrode can be expressed by equation 4.2.

According to equation 4.2, the Q_s contribution is determined by plotting the graph of total charge stored versus the reciprocal of the square root of the scan rate

and extrapolating Q_t to infinity by assuming semi-infinite linear diffusion (Fig.6.12) [54].

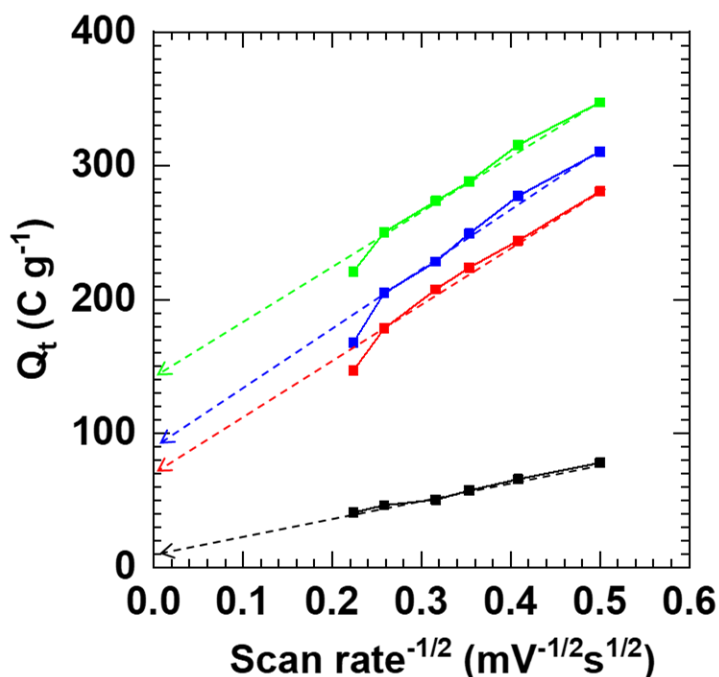


Fig. 6.12: Plots of total charge (Q_t) enclosed under CV against the reciprocal of the square root of the potential scan rate for pristine Ni-Cr-LDH (black) and NCG-1 (red), NCG-2 (green), NCG-3 (blue) nanohybrids.

Fig. 6.13 displays the capacitive and diffusion-controlled contributions of NCG nanohybrids and Ni-Cr-LDH electrodes at various scan rates (4 to 20 mV s^{-1}). All the samples display predominant diffusion-controlled and capacitive contributions at lower and higher scan rates, respectively. Interestingly, NCG-2 nanohybrid exhibits increased charge storage than Ni-Cr-LDH. Moreover, at each scan rate, all NCG nanohybrids demonstrated higher capacitive contributions than the Ni-Cr-LDH, indicating more capacitive-dominant reactions in nanohybrids. Present results are attributed to the unique GO-wrapped structure of NCG nanohybrids that enables faster charge transfer kinetics by expanded surface area interconnected morphology and higher electrical conductivity provided by the wrapped GO channels.

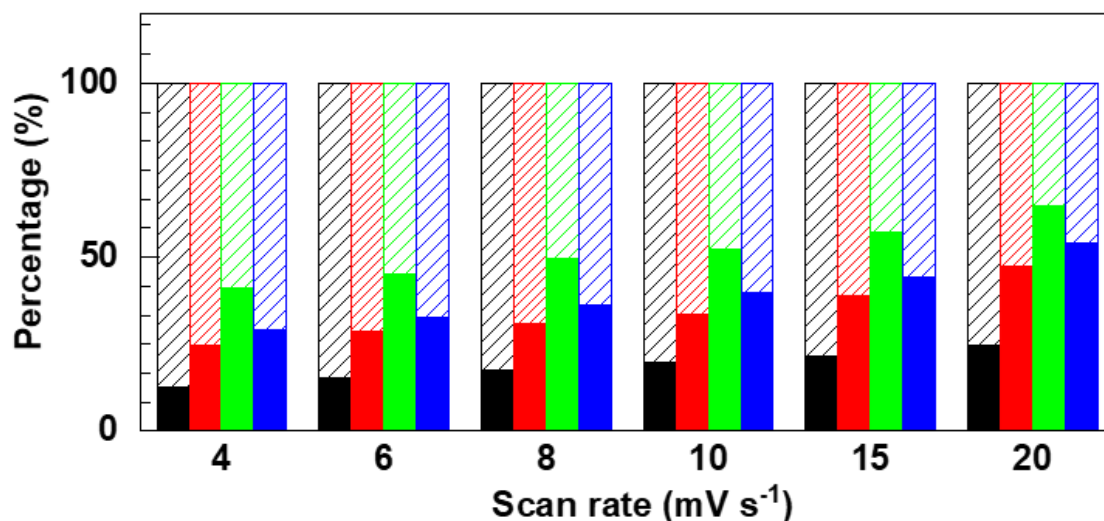


Fig. 6.13: The fraction of the capacitive (solid) and diffusion-controlled (pattern) contributions of Ni-Cr-LDH (black) and NCG-1(red), NCG-2(green), NCG-3(blue) nanohybrids (values in bar assigned for the respective charge contributions).

6.5.2.2 GCD study

The beneficial role of GO incorporation on the electrode performance and charge transport rate kinetics of LDH is additionally examined by galvanostatic charge-discharge (GCD) cycling and EIS analysis. Fig. 6.14 showed the comparative GCD curves of pristine Ni-Cr-LDH and NCG nanohybrids with a potential range of 0 to 0.5 V at a fixed current density of 1 A g^{-1} .

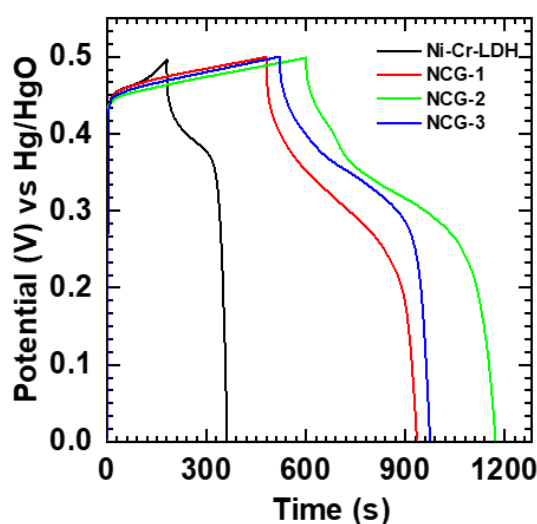


Fig. 6.14: The GCD curves of pristine Ni-Cr-LDH, NCG-1, NCG-2, and NCG-3 nanohybrids at current density of 1 A g^{-1} .

Pristine Ni-Cr-LDH shows typical charge-discharge curves with a characteristic plateau at the middle, followed by a sudden potential drop suggesting the battery-type behavior of the material. All NCG nanohybrids demonstrated characteristic non-linear GCD curves with extended charge-discharge periods indicating an improved charge storing ability upon GO incorporation and significant contribution of the reversible Faradaic reactions therein. In addition, the NCG nanohybrids exhibit specific capacities of 645, 815, and 660 C g⁻¹ for NCG-1, NCG-2 and NCG-3, respectively, which are significantly larger than pristine Ni-Cr-LDH (356 C g⁻¹). GCD performances of pristine Ni-Cr-LDH and NCG nanohybrids are tested at higher current densities from 1 to 5 A g⁻¹, as shown in Fig. 6.15. The corresponding specific capacities are plotted in Fig. 6.16. At the high charging-discharging rate of 5 A g⁻¹, all NCG nanohybrids maintain higher specific capacities than pristine Ni-Cr-LDH, indicating quick charge-discharge ability (high rate capabilities) of NCG nanohybrids. The high rate capability of NCG nanohybrids can be ascribed to the unique porous morphology composed of restacked Ni-Cr-LDH crystallites wrapped by the ultrathin conducting GO NSs, which enables rapid diffusion of electrolyte ions and facilitates quick charge transport through nanohybrid electrodes. NCG-2 nanohybrid displays the highest specific capacity of 815 C g⁻¹ (at 1 A g⁻¹), which is attributed to the more conducting channels for the charge transport via optimum GO incorporation.

Conversely, in comparison to NCG-2, low specific capacities are observed for NCG-1 and NCG-3 nanohybrids due to insufficient and excess GO incorporation, respectively. Excess incorporation of GO decreases the active mass of Ni-Cr-LDH in NCG nanohybrids and may lead to pores-blocking masking effect due to more wrapping of restacked Ni-Cr-LDH NSs. The present NCG nanohybrids electrochemical performance is superior to the recent LDH-GO hybrid electrode materials listed in previous Table 1.3 and 1.4.

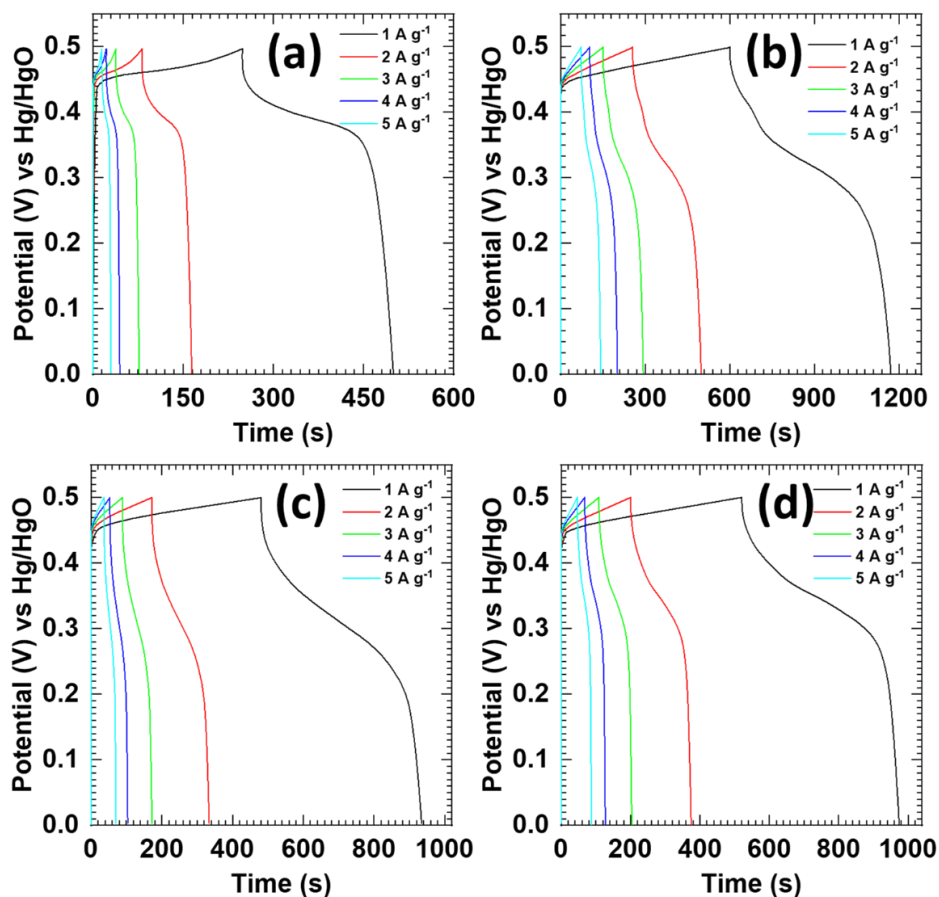


Fig. 6.15: The GCD curves of (a) Ni-Cr-LDH (b) NCG-1, (c) NCG-2, and (d) NCG-3 nanohybrid electrode at different current densities (1-5 A g⁻¹).

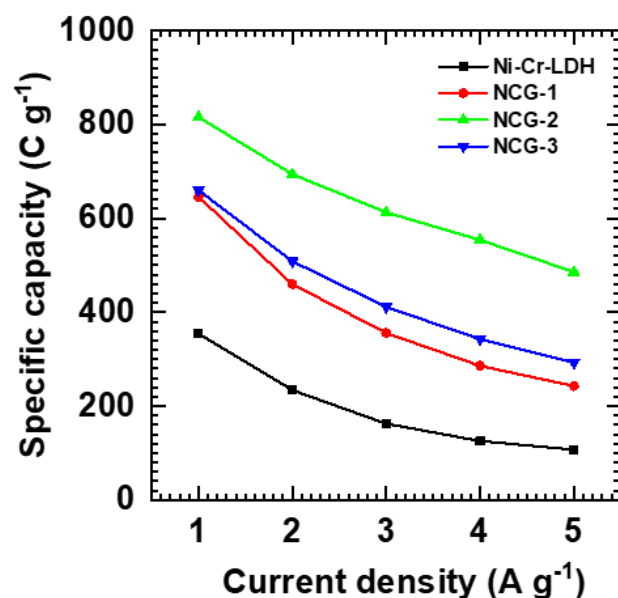


Fig. 6.16: specific capacity of pristine Ni-Cr-LDH and NCG-1, NCG-2, NCG-3 nanohybrids at different current densities (1 to 5 A g⁻¹).

6.5.2.3 Stability study

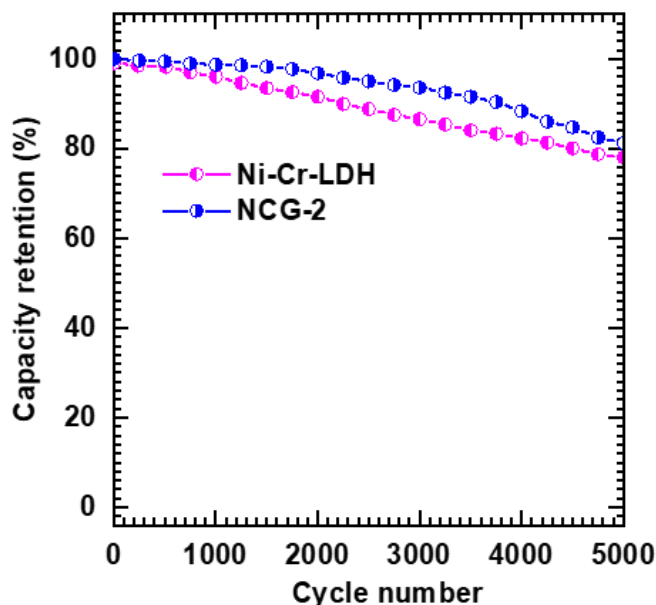


Fig. 6.17: GCD stability graph of pristine Ni-Cr-LDH (pink) and NCG-2(blue) nanohybrid electrode for 5000 cycles.

The cycling stability of pristine Ni-Cr-LDH and NCG-2 nanohybrid electrodes were tested at a constant current density of 5 A g^{-1} , as shown in Fig. 6.17. NCG-2 nanohybrid retain 80% of the initial capacity even after 5000 GCD cycles which is much better than Ni-Cr-LDH (78%). The improvement of the cyclic stability for NCG-2 nanohybrid material is attributed to the anionic GO NSs provide charge-transporting conducting channels by wrapping restacked Ni-Cr-LDH.

6.5.2.4 EIS study

EIS analysis was used to probe the charge transport rate kinetics of NCG nanohybrids, and the corresponding Nyquist plots are shown in Fig. 6.18. All the tested electrodes display typical Nyquist plots characterized by semicircles in the high-frequency region and straight lines in the low-frequency region. The semicircle diameter corresponds to the R_{ct} and the x-axis intercept at high frequency relates to the R_s . The NCG nanohybrids show smaller R_s and R_{ct} of 0.30 and 3.15Ω for NCG-1, 0.27 and 2.18Ω for NCG-2, and 0.28 and 2.84Ω for NCG-3, as compared to pristine Ni-Cr-LDH (0.46 and 15.5Ω). Moreover, NCG nanohybrids display steeper straight lines in the low-frequency region than the pristine Ni-Cr-

LDH, which indicates lower electrolyte diffusion resistance (Warburg impedance) in nanohybrid samples.

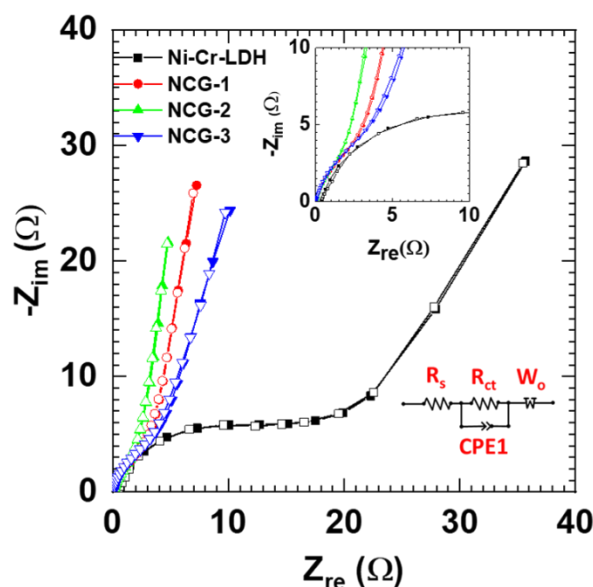


Fig. 6.18: EIS spectra of pristine Ni-Cr-LDH and NCG nanohybrids (Inset: magnified view and fitted electronic circuit).

6.6 Electrochemical performance evaluation of hybrid supercapacitor device

The usefulness of NCG nanohybrid as a high-ED electrode material is tested by fabricating HSC using optimized NCG nanohybrid (NCG-2) as a positive electrode and rGO as a negative electrode. 2 M KOH is employed as an electrolyte. The schematic representation of HSC is shown in Fig. 6.19 and denoted by NCG-2||rGO. The hydrothermally rGO was employed due to its excellent EDLC-type charge storage performance (see chapter 3, section 3.9). So, prior to assembling HSC, the electrochemical performance of rGO was measured with a three-electrode system by CV, GCD, and EIS tests (See chapter 3, section 3.9). The balanced charge delivery is essential to achieve maximum electrode performance and cell stability of HSC. It is achieved by adjusting the masses of respective electrodes in HSC. Thus, the NCG-2||rGO mass ratio of 0.33 is calculated from the charge balance calculations (equation 4.4).

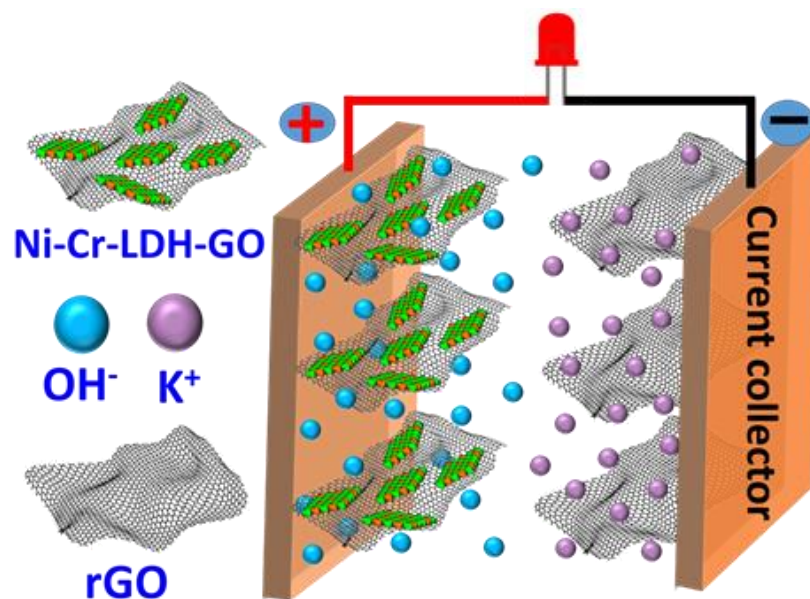


Fig. 6.19: Schematic representation of HSC device.

6.6.1 CV study

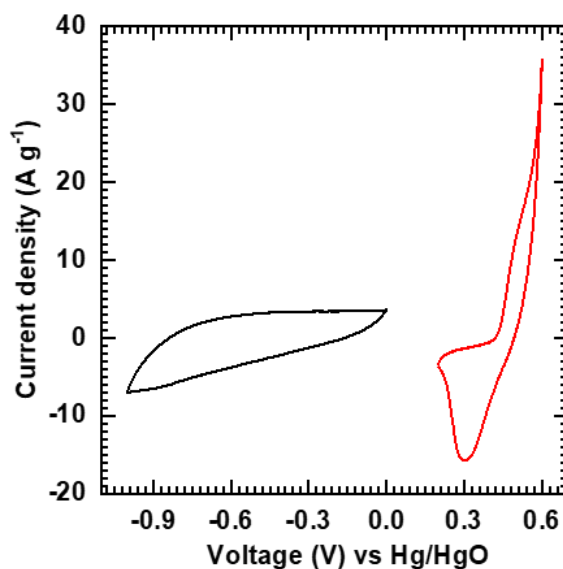


Fig. 6.20: CV curves of rGO (black) and NCG-2 (red) at a scan rate of 10 mV s⁻¹.

As reflected from the half-cell electrochemical performance of NCG-2 and rGO electrodes, these electrodes worked in separate potential windows, which is beneficial for boosting the potential window of the HSC device. As illustrated in Fig.

6.20, the NCG-2 electrode operates in a positive potential window of 0 to 0.6 V (vs Hg/HgO) while the rGO electrode operates in a negative potential window of -1 to 0 V (vs Hg/HgO). Thus, in-principle operational potential window of the HSC device can be extended up to 1.6V.

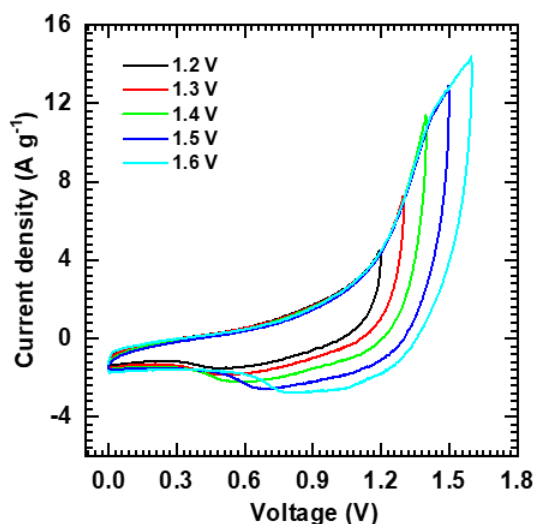


Fig. 6.21: CV curves of the HSC performed in different potential windows at 100 mV s⁻¹.

The actual operating potential window of HSC is judged by measuring the CV curves of HSC within different potential windows (0 to 1.3-1.7V) at scan rate of 100 mV s⁻¹ (Fig. 6.21). The HSC exhibit stable CV curves without any abrupt current response up to a potential window of 1.6 V. Consequently, the electrochemical performance of HSC is tested within a potential window of 0 to 1.6 V.

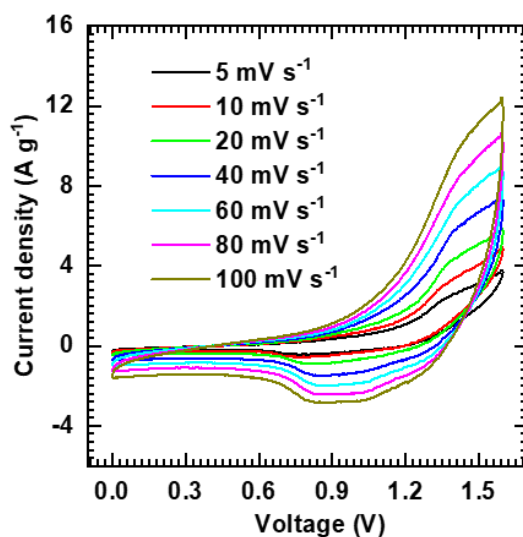


Fig. 6.22: CV curves of the HSC device at 5-100 mV s⁻¹.

Fig. 6.22 displays the typical CV profiles of the HSC device at various scan rates (5 to 100 mV s^{-1}). The HSC device exhibits a non-rectangular CV shape and linearly increased current responses with scan rate without any significant change in redox peak positions. These results reflected both battery and EDLC-type charge storage in the device and good compatibility between the electrode and electrolyte.

6.6.2 GCD study

Fig. 6.23(a) illustrate the GCD curves of HSC device at different current densities of 2, 3, 4, 5, and 6 A g^{-1} within a potential window of 0 to +1.6 V. The GCD curves exhibit non-linear charging-discharging characteristic and mild plateau at the middle reflecting pseudo-triangular GCD profiles. Present results reflect a typical characteristic of HSC devices involving both battery and EDLC-type charge storage. Also, the HSC device exhibits extended charging-discharging periods indicating the high energy storage capacity of the HSC device. The C_s of the HSC device is calculated from GCD curves and represented in Fig. 6.23(b). The HSC device demonstrates maximum C_s of 145 F g^{-1} at 2 A g^{-1} that decreased to 53 F g^{-1} for 6 A g^{-1} suggesting better rate capability (36%) of the HSC device.

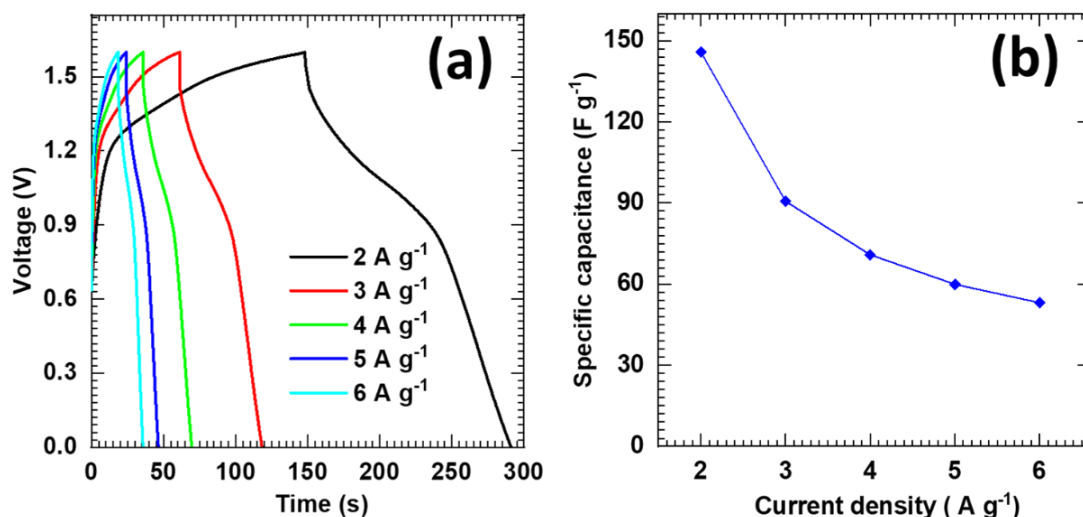


Fig. 6.23: (a) The GCD curves of HSC device at 2-6 A g^{-1} , (b) The plot of C_s at various current densities (2-6 A g^{-1}) for HSC device.

6.6.3 Ragone plot

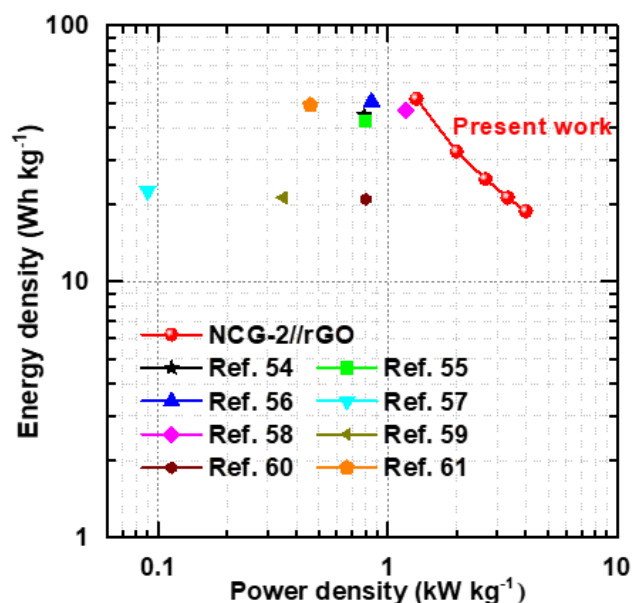


Fig. 6.24: Ragone plots of HSC device in comparison with previously reported devices.

The PD and ED are two crucial factors in HSC performance evaluation. As presented in Fig. 6.24 (Ragone plot), the HSC device possess a high ED (51.85 Wh kg⁻¹) and PD (1.34 kW kg⁻¹) at 2 A g⁻¹, which are comparable to other graphene-based LDH hybrids reported previously such as, Co-Al LDH/rGO||AC (44.6 Wh kg⁻¹ at 0.79 kW kg⁻¹) [54], NiCoAl-LDH||AC (42.25 Wh kg⁻¹ at 0.8 kW kg⁻¹) [55], ZIF-LDH/GO||ZIF-C/F (50.5 Wh kg⁻¹ at 0.85 kW kg⁻¹) [56], rGO/CoAl-LDH||rGO (22.6 Wh kg⁻¹ at 0.09 kW kg⁻¹) [57], CoAl-LDH/PG-4||NPCF (46.8 Wh kg⁻¹ at 1.2 kW kg⁻¹) [58], Ni-Fe LDH/GHA||AC (21.3 Wh kg⁻¹ at 0.35 kW kg⁻¹) [59], NiAl-LDH-GO(LG9)||AC (21 Wh kg⁻¹ at 0.8 kW kg⁻¹) [60], NiCo LDH@NG/CC||NG/CC (49 Wh kg⁻¹ at 0.46 kW kg⁻¹) [61].

6.6.4 Cycling stability

Furthermore, the long-term cycling stability of HSC over 10000 GCD cycles is tested by GCD at 5 A g⁻¹. As shown in Fig. 6.25, the HSC displays 85% of capacitance retention and 94 % of Coulombic efficiency after 10000 GCD cycles, suggesting a long operational life of the device without significant performance degradation.

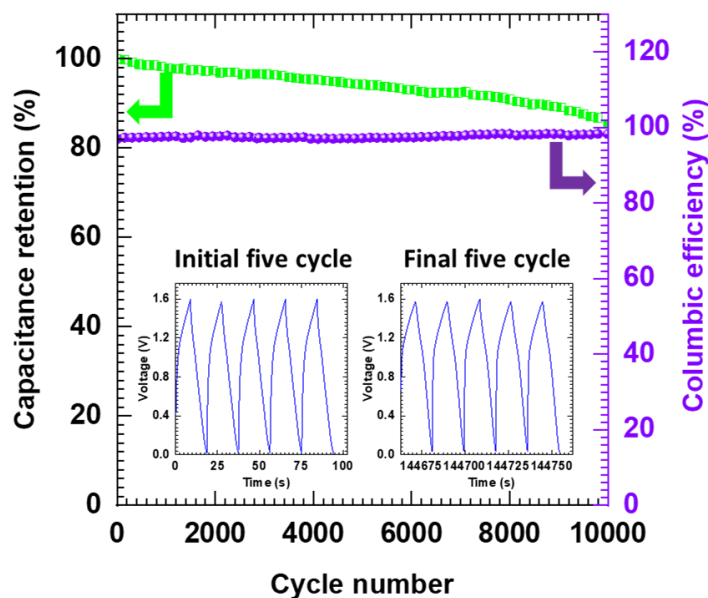


Fig. 6.25: Prolonged cyclic performance and Coulombic efficiency of HSC device at 5 A g^{-1} (inset: initial and final five cycles).

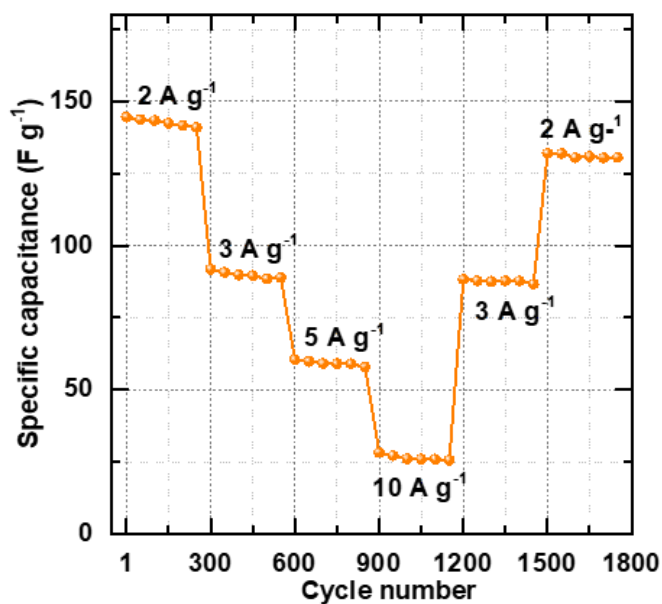


Fig. 6.26: The rate capability plot of HSC device.

The rate capability of HSC device was assessed by testing the performance of the device by applying various charging-discharging current densities and reversing the sequence, as shown in Fig. 6.26. At every current density, the HSC recovers its original C_s with minor alterations, which suggests the excellent rate capability of the device.

6.6.5 EIS study

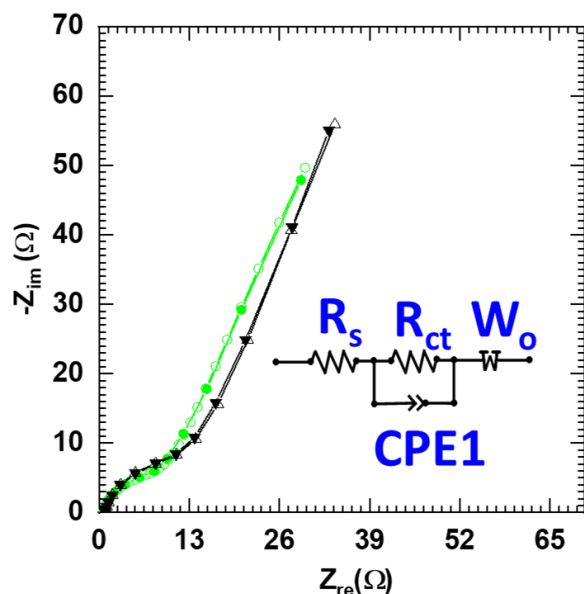


Fig. 6.27: Nyquist plots (Inset: fitted circuit) for the HSC before (green) and after (black) stability.

Additionally, the rate kinetics of HSC is probed using EIS analysis, and the corresponding Nyquist plot and the simulated equivalent electric circuit are shown in Fig. 6.27. The HSC device shows low R_s (0.62Ω) and R_{ct} (6.3Ω) indicating superior capacitive behavior and good electric conductivity of NCG-2||rGO electrodes.

6.6.6 Practical demonstration of HSC

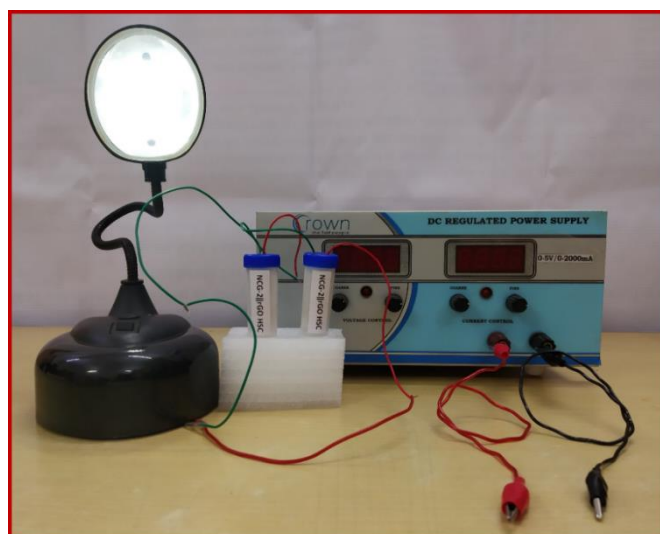


Fig. 6.28: Digital photograph of the demonstration of HSC to light a LEDs lamp.

To further evaluate the practical application of the HSC device, two HSC devices are connected in series to achieve a total potential of 3.2 V. These serially connected HSC devices are used to power commercial LED lamp, as shown in Fig. 6.28.

6.7 Conclusions

This report develops an exfoliation-restacking strategy to design 2D-2D nanohybrids of Ni-Cr-LDH wrapped by GO NSs for HSC electrodes. The resultant NCG nanohybrids possess high electrical conductivity due to the wrapping of 2D Ni-Cr-LDH by GO NSs and expanded surface area due to interconnected porous morphology. Fine-tuning of chemical composition (GO wt %) is an effective method for enhancing the electrochemical performance of NCG nanohybrids. The enhanced electrochemical performance of NCG nanohybrids is attributed to the high electrical conductivity, expanded surface area, ample active electrochemical sites, and fast charge-transporting channels. Consequently, the best optimized NCG-2 nanohybrid exhibits outstanding electrochemical performance with a high specific capacity of 815 at 1 A g⁻¹, superior to pristine Ni-Cr-LDH (356 C g⁻¹). Furthermore, HSC is fabricated using the best optimized NCG-2 nanohybrid as a cathode and *h*-rGO as an anode. As a result, the HSC demonstrates excellent electrochemical performance with high ED of 51.85 Wh kg⁻¹ and PD of 1.34 kW kg⁻¹. Furthermore, HSC device display good cycling stability of 85% capacitance retention after 10000 GCD cycles. The present exfoliation-restacking strategy provides a useful method for 2D-2D GO-wrapped LDH structure for a highly active next-generation hybrid-type SC. This exfoliation-reassembling strategy can be readily applicable to develop numerous nanohybrids based on cationic 2D LDH NSs and GO NSs. Moreover, LDH-GO nanohybrids with the above unique physicochemical properties might have numerous excellent functionalities for other applications such as electrocatalysts, biosensors, and Li-ion batteries.

6.8 References

- [1] N.R. Chodankar, H.D. Pham, A.K. Nanjundan, J.F.S. Fernando, K. Jayaramulu, D. Golberg, Y. Han, D.P. Dubal, *Small*. 16 (2020) 2002806.
- [2] D.P. Dubal, N.R. Chodankar, D.-H. Kim, P. Gomez-Romero, *Chem. Soc. Rev.* 47 (2018) 2065–2129.
- [3] X. Zhang, X. Cheng, Q. Zhang, *J. Energy Chem.* 25 (2016) 967–984.
- [4] G. Wang, L. Zhang, J. Zhang, *Chem. Soc. Rev.* 41 (2012) 797–828.
- [5] L. Miao, Z. Song, D. Zhu, L. Li, L. Gan, M. Liu, *Mater. Adv.* 1 (2020) 945–966.
- [6] J. Yan, Z. Fan, W. Sun, G. Ning, T. Wei, Q. Zhang, R. Zhang, L. Zhi, F. Wei, *Adv. Funct. Mater.* 22 (2012) 2632–2641.
- [7] D. Kumar, A.K. Tomar, G. Singh, R.K. Sharma, *Electrochimica Acta* 363 (2020) 137238.
- [8] Y. Li, Z. Luo, H. Qin, S. Liang, L. Chen, H. Wang, C. Zhao, S. Chen, *J. Colloid Interface Sci.* 582 (2021) 842–851.
- [9] S. C. Sekhar, G. Nagaraju, B. Ramulu, S. J. Arbaz, D. Narsimulu, S. K. Hussain, J. S. Yu, *Nano Energy*. 76 (2020) 105016.
- [10] A. Tyagi, M. C. Joshi, A. Shah, V. K. Thakur, R. K. Gupta, *ACS Omega* 4 (2019) 3257–3267.
- [11] L. Zhang, K. N. Hui, K. San Hui, H. Lee, *J. Power Sources* 318 (2016) 76–85.
- [12] S. Bose, T. Kuila, A. K. Mishra, R. Rajasekar, N. H. Kim, J. H. Lee, *J. Mater. Chem.* 22 (2012) 767–784.
- [13] V. C. Lokhande, A. C. Lokhande, C. D. Lokhande, J. H. Kim, T. Ji, *J. Alloys Compd.* 682 (2016) 381–403.
- [14] Y. Liu, X. Peng, *Appl. Mater. Today* 8 (2017) 104–115.
- [15] S. J. Patil, N. R. Chodankar, R. B. Pujari, Y. -K. Han, D. W. Lee, *J. Power Sources*. 466 (2020) 228286.
- [16] F. Wang, X. Wu, X. Yuan, Z. Liu, Y. Zhang, L. Fu, Y. Zhu, Q. Zhou, Y. Wu, W. Huang, *Chem. Soc. Rev.* 46 (2017) 6816–6854.
- [17] Q. Du, L. Su, L. Hou, G. Sun, M. Feng, X. Yin, Z. Ma, G. Shao, W. Gao, *J. Alloys Compd.* 740 (2018) 1051–1059.
- [18] J. Yang, C. Yu, X. Fan, C. Zhao, J. Qiu, *Adv. Funct. Mater.* 25 (2015) 2109–2116.
- [19] L. Zhang, M. Ou, H. Yao, Z. Li, D. Qu, F. Liu, J. Wang, J. Wang, Z. Li, *Electrochim. Acta* 186 (2015) 292–301.
- [20] J. Fang, M. Li, Q. Li, W. Zhang, Q. Shou, F. Liu, X. Zhang, J. Cheng, *Electrochim. Acta* 85 (2012) 248–255.
- [21] M. He, L. Kang, C. Liu, Z. Lei, Z.-H. Liu, *Mater. Res. Bull.* 68 (2015) 194–202.
- [22] F. He, Z. Hu, K. Liu, S. Zhang, H. Liu, S. Sang, *J. Power Sources* 267 (2014) 188–196.

- [23] J.L. Gunjekar, T.W. Kim, H.N. Kim, I.Y. Kim, S.-J. Hwang, *J. Am. Chem. Soc.* 133 (2011) 14998–15007.
- [24] F. Li, X. Jiang, J. Zhao, S. Zhang, *Nano Energy* 16 (2015) 488–515.
- [25] J. L. Shi, H. F. Wang, X. Zhu, C. M. Chen, X. Huang, X. D. Zhang, B. Q. Li, C. Tang, Q. Zhang, *Carbon* 103 (2016) 36–44.
- [26] S. L. Candelaria, Y. Shao, W. Zhou, X. Li, J. Xiao, J.-G. Zhang, Y. Wang, J. Liu, J. Li, G. Cao, *Nano Energy*. 1 (2012) 195–220.
- [27] R. Ma, X. Liu, J. Liang, Y. Bando, T. Sasaki, *Adv. Mater.* 26 (2014) 4173–4178.
- [28] Y. Zhong, Y. Liao, A. Gao, J. Hao, D. Shu, Y. Huang, J. Zhong, C. He, R. Zeng, *J. Alloys Compd.* 669 (2016) 146–155.
- [29] S. Nayak, K.M. Parida, *Chem. Asian J.* 16 (2021) 1–39.
- [30] M.-Q. Zhao, Q. Zhang, J. -Q. Huang, F. Wei, *Adv. Funct. Mater.* 22 (2012) 675–694.
- [31] J. Wang, X. Mei, L. Huang, Q. Zheng, Y. Qiao, K. Zang, S. Mao, R. Yang, Z. Zhang, Y. Gao, Z. Guo, Z. Huang, Q. Wang, *J. Energy Chem.* 24 (2015) 127–137.
- [32] J. Hu, G. Lei, Z. Lu, K. Liu, S. Sang, H. Liu, *Chem. Commun.* 51 (2015) 9983–9986.
- [33] R. Ma, Z. Liu, L. Li, N. Iyi, T. Sasaki, *J. Mater. Chem.* 16 (2006) 3809.
- [34] Y. Zhao, S. Zhang, B. Li, H. Yan, S. He, L. Tian, W. Shi, J. Ma, M. Wei, D.G. Evans, X. Duan, *Chem. Eur. J.* 17 (2011) 13175–13181.
- [35] J. Chen, Y. Li, L. Huang, C. Li, G. Shi, *Carbon* 81 (2015) 826–834.
- [36] J. L. Gunjekar, I. Y. Kim, J. M. Lee, N. -S. Lee, S. -J. Hwang, *Energy Environ. Sci.* 6 (2013) 1008.
- [37] S. Nayak, L. Mohapatra, K. Parida, *J. Mater. Chem. A* 3 (2015) 18622–18635.
- [38] N. Baliarsingh, L. Mohapatra, K. Parida, *J. Mater. Chem. A* 1 (2013) 4236.
- [39] A. S. Patil, J. L. Gunjekar, C. D. Lokhande, U. M. Patil, S. V. Sadavar, N. S. Padalkar, R. B. Shinde, M. M. Wagh, J. S. Bagi, *Synthetic Metals*. 264 (2020) 116371.
- [40] R. A. Nyquist, R. O. Kagel. *Infrared spectra of inorganic compounds*, Academic Press, Inc., New York, 1st edn, 1971.
- [41] I. Y. Kim, J. M. Lee, T. W. Kim, H. N. Kim, H. Kim, W. Choi, S.-J. Hwang, *Small*. 8 (2012) 1038–1048.
- [42] J. L. Gunjekar, A. I. Inamdar, B. Hou, S. Cha, S. M. Pawar, A. A. Abu Talha, H. S. Chavan, J. Kim, S. Cho, S. Lee, Y. Jo, H. Kim, H. Im, *Nanoscale* 10 (2018) 8953–8961.
- [43] A.S.O. Gomes, N. Yaghini, A. Martinelli, E. Ahlberg, *J Raman Spectrosc.* 48 (2017) 1256–1263.
- [44] D. S. Hall, D. J. Lockwood, S. Poirier, C. Bock, B. R. MacDougall, *ACS Appl. Mater. Interfaces*. 6 (2014) 3141–3149.

- [45] L. P. F. Benício, D. Eulálio, L. de M. Guimarães, F. G. Pinto, L. M. da Costa, J. Tronto, *Mat. Res.* 21 (2018) 1.
- [46] J. Desilvestro, D.A. Corrigan, M.J. Weaver, *J. Electrochem. Soc.* 135 (1988) 885–892.
- [47] D. S. Hall, D. J. Lockwood, S. Poirier, C. Bock, B. R. MacDougall, *J. Phys. Chem. A* 116 (2012) 6771–6784.
- [48] J. B Condon, *Surface area and porosity determinations by physisorption: measurements and theory*, 1st ed. Elsevier: Amsterdam; Boston, 2006; p 274.
- [49] W. Ye, X. Fang, X. Chen, D. Yan, *Nanoscale*. 10 (2018) 19484–19491.
- [50] Y. Yang, L. Dang, M. J. Shearer, H. Sheng, W. Li, J. Chen, P. Xiao, Y. Zhang, R. J. Hamers, S. Jin, *Adv. Energy Mater.* 8 (2018) 1703189.
- [51] T. Zhou, Z. Cao, P. Zhang, H. Ma, Z. Gao, H. Wang, Y. Lu, J. He, Y. Zhao, *Sci Rep.* 7 (2017) 46154.
- [52] V. Rebutini, E. Fazio, S. Santangelo, F. Neri, G. Caputo, C. Martin, T. Brousse, F. Favier, N. Pinna, *Chem. Eur. J.* 21 (2015) 12465–12474.
- [53] M. K. Rabchinskii, A. T Dideikin, D. A. Kirilenko, M. V. Baidakova, V. V. Shnitov, F. Roth, S. V. Konyakhin, N. A. Besedina, S. I. Pavlov, R. A. Kuricyn, N. M. Lebedeva, P. N. Brunkov, A. Y. Vul, *Sci. Rep.* 8 (2018) 14154.
- [54] J. Li, P. Zhang, X. Zhao, L. Chen, J. Shen, M. Li, B. Ji, L. Song, Y. Wu, D. Liu, *J. Colloid Interface Sci.* 549 (2019) 236–245.
- [55] X. Wang, X. Li, C. Huang, C. Hao, C. Ge, Y. Guo, *Appl. Surf. Sci.* 527 (2020) 146891.
- [56] D. Yu, L. Ge, X. Wei, B. Wu, J. Ran, H. Wang, T. Xu, *J. Mater. Chem. A* 5 (2017) 16865–16872.
- [57] R. Zhang, H. An, Z. Li, M. Shao, J. Han, M. Wei, *Chem. Eng. J.* 289 (2016) 85–92.
- [58] Y. Zhang, D. Du, X. Li, H. Sun, L. Li, P. Bai, W. Xing, Q. Xue, Z. Yan, *ACS Appl. Mater. Interfaces.* 9 (2017) 31699–31709.
- [59] X. Gao, H. Lv, Z. Li, Q. Xu, H. Liu, Y. Wang, Y. Xia, *RSC Adv.* 6 (2016) 107278–107285.
- [60] L. Zhang, H. Yao, Z. Li, P. Sun, F. Liu, C. Dong, J. Wang, Z. Li, M. Wu, C. Zhang, B. Zhao, *J. Alloys Compd.* 711 (2017) 31–41.
- [61] B. Mehrabimatin, E. P. Gilshteyn, M. E. Melandsø Buan, O. Sorsa, H. Jiang, A. Irajizad, S. Shahrokhian, A. G. Nasibulin, T. Kallio, *Energy Technol.* 7 (2019) 1801002.



CHAPTER-7

Summary and Conclusions

Summary and conclusions

With the impending energy crisis, efforts are undertaken to find alternative sustainable and green energy sources that are renewable. Efficient utilization and efficient energy storage from renewable sources are heavily dependent on storing the harvested energy in energy storage devices and retrieves when needed. Thus there is an impetus to the research on the development of charge storage devices such as batteries, capacitors, and supercapacitors in recent times. The conventional rechargeable batteries with high ED are very expensive, with limited cycle life and not suitable for high power applications. Out of these different energy storage devices, the HSCs that combine high power capability, short charging/discharging periods, ED comparable to the batteries, and long cycle life are attractive devices for the next-generation energy storage appliances. These advantages performance make the HSC act as a supplement or alternative to batteries in portable electronic devices, memory backup systems, long-time constant circuits, flash cameras, hybrid electric vehicles etc. Moreover, the performance of the HSC device is highly reliable on the electrode activity of comprising electrodes. Thus efforts are put forward to find efficient electrode materials that fulfilled the desired characteristics. Ni-Cr-LDH is one of the potential candidates as a redox-type (cathode) electrode in HSC. However, its performance is restricted by the compact structure, nonporous morphology, limited interlayered gallery space and low conductivity. Thus, the present study focused on improving electrode performance of Ni-Cr-LDH via expanding surface area and interlayer gallery space by hybridizing exfoliated Ni-Cr-LDH NS with POM anions (POV anions and POW anions). Also, analogous efforts are taken to tune the electrical conductivity and surface area by hybridizing exfoliated Ni-Cr-LDH NS with GO NSs. Further, preparative parameters such as the chemical composition, surface area and gallery space are optimized to get the optimum electrochemical performance of Ni-Cr-LDH-based nanohybrid electrodes. In addition, the Ni-Cr-LDH-POV, Ni-Cr-LDH-POW and Ni-Cr-LDH-GO redox-type electrodes with higher electrochemical performance are used to fabricate HSC devices. The rGO prepared by the hydrothermal method was used as an EDLC-type electrode in HSCs. Thus, the three types of HSCs are fabricated with cell configuration Ni-Cr-LDH-POV||rGO, Ni-Cr-LDH-POW||rGO and Ni-Cr-LDH-GO||rGO. Also, a practical demonstration of LED

lamp illumination is carried out using HSC devices. The present thesis work has been distributed in eight chapters.

Chapter 1 discusses the general introduction, energy demands of the future generation, and overview of various energy storage systems. Furthermore, it describes the historical background, current status, working principle, salient features and classification of SCs based on the charge storage mechanism are discussed in detail. The fundamental requirements of electrode, electrolyte and current collector properties are discussed briefly. Furthermore, the literature review on the usage of LDHs and LDH-based nanohybrid electrodes for HSC is summarized. Ultimately, the orientation and purpose of the dissertation with existed a research gap indicating an immediate urge to investigate LDH-based hybrids electrodes are stated at the end of chapter 1.

In **Chapter 2**, an introduction of layered material, synthesis strategies, and applications of 2D NSs and their hybrids are briefly presented. Moreover, the various characterization techniques and instruments with their theoretical background are described in this chapter, such as Zeta potential, powder PXRD, FTIR, Micro-Raman spectroscopy, FE-SEM with EDS, HR-TEM/SAED, XPS and BET. Finally, the theoretical background of electrochemical techniques (CV, GCD and EIS) used to evaluate HSC electrode performance is explained briefly.

Chapter 3 focused on the synthesis, characterization and electrochemical performance evaluation of pristine Ni-Cr-LDH and rGO materials. The results of various physicochemical characterizations of pristine Ni-Cr-LDH and rGO are presented in this chapter. The pristine Ni-Cr-LDH demonstrated nitrate intercalated hexagonal layered nonporous structure. The rGO prepared by hydrothermal methods displayed characteristic features that validates the formation of the rGO NSs sponge with high conductivity and surface area. The pristine Ni-Cr-LDH demonstrates the highest specific capacity of 356 C g^{-1} at 1 A g^{-1} with 78% capacity retention over 5000 GCD cycles. The present electrochemical performance of pristine Ni-Cr-LDH is limited due to the compact plate-like nonporous morphology and restricted gallery heights. On the other hand, the rGO electrode exhibits a maximum C_s of 258 F g^{-1} at 3 A g^{-1} with better capacitance retention of 76% over 4000 GCD cycles. So, the rGO electrode is used as a negative (anode) electrode for HSC device fabrication.

Chapter 4 mainly focuses on the synthesis, characterization and electrochemical performance evaluation of pillared Ni-Cr-LDH-POV nanohybrids. The exfoliated Ni-Cr-LDH NSs colloidal suspension was achieved by the vigorous shaking of Ni-Cr-LDH powder (1 mg mL^{-1}) in formamide. In this chapter, the synthesis process for mesoporous layer-by-layer self-assembled Ni-Cr-LDH-POV nanohybrids by the electrostatically-driven self-assembly of exfoliated Ni-Cr-LDH NSs and POV anions is described. The Tyndale effect, Zeta potential, XRD, FTIR, Micro-Raman, FE-SEM, HR-TEM/SEAD, BET, and XPS analysis are used to confirm prepared nanohybrid material. The formation of the colloidal suspension of positively charged exfoliated Ni-Cr-LDH NSs is evidenced by the observation of a clear Tyndall light scattering effect and Zeta potential measurements. The Ni-Cr-LDH-POV nanohybrids demonstrate layer-by-layer stacking of Ni-Cr-LDH and POV anions, mesoporous interconnected surface morphology, and expanded surface area.

Part 4.5 describes the electrochemical performance evaluation of pillared Ni-Cr-LDH-POV nanohybrid. The electrochemical measurements demonstrate that the NCV-2 nanohybrid electrode shows a high specific capacity of 1060 C g^{-1} at 1 A g^{-1} . Moreover, it displays excellent capacity retention of 82% after 5000 GCD cycles. In addition, NCV-2 nanohybrid exhibits small values of R_s (0.34Ω) and R_{ct} (4.9Ω) as compared to other samples. The enhancement in electrochemical performance is ascribed due to mesoporous house of card surface morphology, which provides more efficient pathways for easy penetration of electrolyte into the interior of active material. Hence, the present single electrode electrochemical performance of NCV nanohybrids vividly represents the effectiveness of POV pillared hybridization as a redox electrode material in an HSC. In part 4.6 describes the fabrication and electrochemical performance of HSC comprising Ni-Cr-LDH-POV as a positive electrode and rGO as a negative electrode which delivered an outstanding C_s of 162.5 F g^{-1} at a current density of 2 A g^{-1} , ED of 57.78 Wh kg^{-1} at a PD of 1.59 kW kg^{-1} and cycling stability of 87% for 10,000 charge-discharge cycles.

Chapter 5 deals with the synthesis, characterization and electrochemical performance evaluation of Ni-Cr-LDH hybridized with POW anions. The exfoliation-reassembling process for synthesizing porous nanohybrids of cationic

Ni-Cr-LDH 2D NSs and anionic POW 0D nanoclusters is described in detail. The analysis of various physicochemical characterization techniques indicates a highly porous layer-by-layer ordered pillared structure with an expanded basal spacing and surface area of Ni-Cr-LDH-POW nanohybrid.

Part 5.5 describes the electrochemical performance evaluation of the Ni-Cr-LDH-POW nanohybrid electrode. The optimized Ni-Cr-LDH-POW nanohybrid electrode delivers a maximum specific capacity of 736 C g^{-1} at 1 A g^{-1} with capacity retention of 81% over 5000 GCD cycles. The HSC is developed using NCW-2 nanohybrid and rGO used as positive and negative electrodes, respectively in two electrode system with 2 M KOH electrolyte. Part 5.6 describes the electrochemical performance evaluation of HSC device. The fabricated NCW-2||rGO HSC device works well up to 1.6 V and delivers high energy of 43 Wh kg^{-1} at 1.3 kW kg^{-1} with the stability of 84% after 10000 GCD cycles.

Chapter 6 encloses the synthesis, characterization, and electrochemical performance evaluation of Ni-Cr-LDH hybridized with GO. In this chapter, the synthesis process of restacked Ni-Cr-LDH is anchored on negatively charged GO NSs via exfoliation-restacking strategy. The Ni-Cr-LDH-GO nanohybrids display formation of carbonate intercalated Ni-Cr-LDH, which is anchored on negatively charged GO NSs. The Ni-Cr-LDH-GO nanohybrids enable expanded surface area, homogeneous hybridization of Ni-Cr-LDH and GO NSs and high electrical conductivity.

The part 6.5 discusses the electrochemical performance evaluation of Ni-Cr-LDH-GO nanohybrids. Ni-Cr-LDH-GO nanohybrids exhibits the outstanding specific capacity of 815 C g^{-1} at 2 A g^{-1} with superior capacity retention after 5000 cycles. The HSC device based on NCG-2 and rGO delivers an ED 52 Wh kg^{-1} and PD of 1.4 kW kg^{-1} at a 2 A g^{-1} with capacity retention of 85% over 10000 GCD cycles. This assembly design strategy suggests that Ni-Cr-LDH-GO nanohybrid are promising electrode materials for high-performance HSC device. Finally, for an actual demonstration of the HSC device, LEDs are lightened up using a series combination of two aqueous devices.

In **Chapter 7** all the results are summarized from the above chapters and conclusions are made on the analysis. It is concluded that exfoliation-restacking strategy is useful for synthesizing high surface area layer-by-layered Ni-Cr-LDH-

POV, Ni-Cr-LDH-POW, and Ni-Cr-LDH-GO nanohybrids and highly effective to improve the electrode performance of nanohybrid electrodes. The high performance HSCs are made by Ni-Cr-LDH-based redox-type and rGO-based EDLC-type electrodes in KOH electrolytes. Therefore, it is concluded that Ni-Cr-LDH-POV, Ni-Cr-LDH-POW, and Ni-Cr-LDH-GO nanohybrids are beneficial as a redox-type electrode in HSC. From the analysis of physicochemical characterizations, it is concluded that high surface area morphology, expanded gallery space and high electrical conductivity of Ni-Cr-LDH-based hybrids are beneficial for the HSC performance increment. The comparative of electrochemical performance of NCV-2||rGO, NCW-2||rGO and NCG-2||rGO HSC devices are presented in Table 7.1. From the analysis of Table 7.1, it is clear that NCV-2||rGO HSC device displays maximum electrode performance. Thus the conclusion is drawn that among the tested Ni-Cr-LDH-based hybrids, the POV anions are the best choice for hybridizing with Ni-Cr-LDH.

Table 7.1

Sr. No.	Device configuration	Cs (F g^{-1} at 2 A g^{-1})	ED (Wh kg^{-1})	PD (kW kg^{-1})	No. of Cycles & Stability (%)
1	NCV-2 rGO	162.5	57.78	1.59	10000 (87)
2	NCW-2 rGO	120	43	1.3	10000 (84)
3	NCG-2 rGO	145	52	1.4	10000 (85)

CHAPTER-8

80-Recommendation

8.1 Recommendations

Ni-Cr-LDH is one of the potential electrode materials for the SC. Though Ni-Cr-LDH demonstrated battery-type charge storage behavior, its electrode performance is highly limited by the low surface area morphology, compact layered structure, and high electrical conductivity. Thus, with the aim to enhance electrode performance of the Ni-Cr-LDH, Ni-Cr-LDH hybridized with POM (POV and POW) and GO via exfoliation-restacking route are prepared and tested as electrodes for SCs. The exfoliation-restacking route offers advantages like forming a highly mesoporous structure, controlled chemical composition, flexibility to choose the type of hybridized species, and high electronic coupling between the hybridized components. Several recommendations are proposed based on the findings and conclusion of the synthesis, characterization, and electrochemical performance of Ni-Cr-LDH-based HSC. The Ni-Cr-LDH hybridized with POV (Ni-Cr-LDH-POV) and that hybridized with POW (Ni-Cr-LDH-POW) exhibited layer-by-layer stacking of Ni-Cr-LDH NSs and POV/POW anions. As a result, Ni-Cr-LDH-POV and Ni-Cr-LDH-POW nanohybrids displayed expanded gallery height and high surface area mesoporous interconnected NS morphology.

Similarly, Ni-Cr-LDH hybridized with GO NSs (Ni-Cr-LDH-GO) displayed anchored assembly of restacked Ni-Cr-LDH anchored on GO NSs. In addition, the Ni-Cr-LDH-GO possessed high electrical conductivity due to the wrapping of restacked Ni-Cr-LDH by GO NSs and expanded surface area due to interconnected porous morphology. All the Ni-Cr-LDH-based nanohybrid electrodes displayed enhanced electrode performance with a redox-type charge storage mechanism. Thus, the HSC devices are formed using either Ni-Cr-LDH-POV or Ni-Cr-LDH-POW or Ni-Cr-LDH-GO nanohybrids as redox-type electrodes and rGO as an EDLC-type electrode in KOH electrolyte. The three types of HSCs are fabricated with cell configuration Ni-Cr-LDH-POV||rGO, Ni-Cr-LDH-POW||rGO and Ni-Cr-LDH-GO||rGO. All of the Ni-Cr-LDH-POV||rGO, Ni-Cr-LDH-POW||rGO and Ni-Cr-LDH-GO||rGO HSC devices performed outstandingly. Among the tested HSC devices, the Ni-Cr-LDH-POV||rGO device displayed the highest electrode performance with Cs of 162.5 F g^{-1} , ED of 57.78 Wh kg^{-1} , and PD of 1.59 kW kg^{-1} , thus recommending POV as the best pillaring anions choice to improve electrode performance of Ni-Cr-LDH.

Consequently, an exfoliation-restacking strategy is recommended to achieve high surface area porous Ni-Cr-LDH-based nanohybrid electrodes with tunable chemical composition and electrical properties. Furthermore, this synthesis method enables expanded gallery space of nanohybrids when hybridized with POV or POW anions. Also, an exfoliation-restacking strategy is recommended to attain 2D-2D nanohybrids of Ni-Cr-LDH wrapped by GO NSs for HSC electrodes.

8.2 Conclusions of the research work

The conclusions from the present research work are listed as follows:

1. Conclusion made from the first two chapters (literature survey) : As SCs suffer from low Cs and limited cycle life, exploring pseudocapacitive-type electrode materials is necessary. Though Ni-Cr-LDH exhibited a redox-type charge storage mechanism, its electrode performance is limited by the low surface area morphology, compact layered structure, and high electrical conductivity. Accordingly, efforts are needed to address these issues via hybridization with other guest species to improve electrode performance and related characteristics.
2. The coprecipitation method is useful for synthesizing nitrate anions intercalated the Ni-Cr-LDH. Nitrate anions intercalated Ni-Cr-LDH exhibited exfoliation ability in formamide. Hydrothermally prepared rGO was successfully prepared. The electrochemical properties of Ni-Cr-LDH and rGO electrodes displayed redox-type and EDLC-type charge storage mechanisms. The maximum specific capacity of 356 C g^{-1} at 1 A g^{-1} with capacity retention of 78 % (5000 GCD cycles) is observed for Ni-Cr-LDH electrodes. The rGO electrode showed excellent electrochemical performance with a maximum specific capacitance of 258 F g^{-1} at of 3 A g^{-1} with capacity retention of 76 % over 4000 GCD cycles.
3. Mesoporous nanohybrids of 2D Ni-Cr-LDH NSs pillared with POV anions (Ni-Cr-LDH-POV nanohybrids) are successfully prepared by the electrostatically driven exfoliation-restacking process. The physicochemical characterizations confirmed the intercalation of POV anions in Ni-Cr-LDH, high surface area mesoporous house-of-card-type morphology, tunable pore distribution and flexible chemical composition of Ni-Cr-LDH-POV nanohybrids. The highest specific capacity of 1060 C g^{-1} at a 1 A g^{-1} was obtained for the NCV-2 nanohybrid electrode, which was much higher as compared to that of pristine Ni-Cr-LDH (356 C g^{-1}). Present single

electrode electrochemical performance of NCV nanohybrids vividly represents the effectiveness of POV pillared hybridization as a redox-type electrode in HSC. The HSC with NCV nanohybrid as a positive electrode and rGO as a negative electrode (NCV-2||rGO HSC device) delivered an outstanding Cs of 162.5 F g^{-1} at a current density of 2 A g^{-1} . Additionally, the HSC exhibited an ED of 57.78 Wh kg^{-1} at a PD of 1.59 kW kg^{-1} and capacitance retention of 87% after 10,000 charge-discharge cycles. The NCV-2||rGO HSC device exhibits excellent ED, PD, good rate capability, and superior cyclic stability. These features suggest the significant potential of NCV-2||rGO HSC for application in various portable and flexible electronic devices.

4. Mesoporous nanohybrids of 2D Ni-Cr-LDH NSs hybridized with POW anions (NCW nanohybrids) are prepared by the electrostatically driven exfoliation-restacking process. The physicochemical characterizations confirmed the intercalation of POW anions in Ni-Cr-LDH, high surface area mesoporous house-of-card-type morphology, tunable pore distribution, and flexible chemical composition of NCW nanohybrids. The optimized NCW-2 nanohybrid electrode displayed a maximum specific capacity of 736 C g^{-1} at a 1 A g^{-1} , which was much higher as compared to that of pristine Ni-Cr-LDH (356 C g^{-1}). The obtained electrochemical performance of NCW nanohybrids vividly signifies the efficacy of POV pillared hybridization as a redox-type electrode in HSC. The HSC with NCW-2 nanohybrid as a positive electrode and rGO as a negative electrode (NCW-2||rGO HSC device) delivered an enhanced Cs of 120 F g^{-1} at a current density of 2 A g^{-1} . Additionally, the NCW-2||rGO HSC device exhibited an ED of 43 Wh kg^{-1} at a PD of 1.33 kW kg^{-1} and capacitance retention of 84 % after 10,000 charge-discharge cycles. These electrochemical features suggest the significant potential of NCW-2||rGO HSC for application in various portable and flexible electronic devices.

5. Mesoporous Ni-Cr-LDH-GO (NCG) nanohybrids were successfully synthesized by the electrostatically derived self-assembly of positively charged (cationic) Ni-Cr-LDH NSs with negatively charged (anionic) GO NSs. The physicochemical characterizations confirmed the formation anchored assembly of Ni-Cr-LDH and GO NSs, high surface area porous morphology composed of restacked Ni-Cr-LDH NSs crystallites wrapped by the ultrathin GO NSs, tunable pore distribution, and flexible chemical composition of NCG nanohybrids. The best optimized NCG-2 nanohybrid exhibited enhanced electrochemical performance with a high specific

capacity of 815 at 1 A g^{-1} , superior to pristine Ni-Cr-LDH (356 C g^{-1}). Furthermore, HSC is fabricated using the best optimized NCG-2 nanohybrid as a cathode and rGO as an anode (NCG-2||rGO). As a result, the NCG-2||rGO HSC demonstrates excellent electrochemical performance with high ED of 51.85 Wh kg^{-1} and PD of 1.34 kW kg^{-1} with 85% capacitance retention after 10000 GCD cycles. The present exfoliation-restacking strategy provides a useful method for 2D-2D GO-wrapped LDH structure for a highly active next-generation hybrid-type SC.

It is concluded that exfoliation -restacking strategy is useful for synthesizing high surface area layer-by-layered NCV, NCW and NCG nanohybrids and highly effective to improve the electrode performance of nanohybrid electrodes. The high-performance HSCs are made by Ni-Cr-LDH-based redox-type and rGO-based EDLC-type electrodes in KOH electrolytes. Therefore, it is concluded that NCV, NCW and NCG nanohybrids are beneficial as a redox-type electrode in HSC. From the analysis of physicochemical characterizations, it is concluded that high surface area morphology, expanded gallery space and high electrical conductivity of Ni-Cr-LDH-based hybrids are beneficial for the HSC performance increment. The comparative electrochemical performance of NCV-2||rGO, NCW-2||rGO and NCG-2||rGO HSC devices indicates that the NCV-2||rGO HSC device displays maximum electrode performance. Thus the conclusion is drawn that among the tested Ni-Cr-LDH-based hybrids, the POV anions are the best choice for hybridizing with Ni-Cr-LDH.

8.3 Summery

1. Coprecipitation methods was used to synthesize nitrate intercalated Ni-Cr-LDH.
2. The Ni-Cr-LDH showed redox-type electrode activity in 2 M KOH electrolyte and exhibited a maximum specific capacity of 356 C g^{-1} at a 1 A g^{-1} .
3. The GO was synthesized by modified Hummers method. Further, rGO was prepared by reduction of GO through the hydrothermal method.
4. The rGO electrode showed excellent EDLC-type electrode activity in 2 M KOH electrolyte and exhibited maximum Cs of 258 F g^{-1} at a current density of 3.0 A g^{-1} .
5. An electrostatically driven exfoliation-restacking strategy was successfully synthesized Ni-Cr-LDH-POV (NCV) nanohybrid.

6. The best optimized NCV-2 nanohybrid exhibited the highest specific capacity of 1060 C g^{-1} at 1 A g^{-1} with capacitance retention of 82 % after 5,000 GCD cycles in 2 M KOH electrolyte.
7. HSC device was successfully fabricated using NCV-2 as a positive electrode and rGO as a negative electrode in 2M KOH electrolyte (NCV-2||rGO).
8. The NCV-2||rGO HSC delivered a Cs of 162.5 F g^{-1} at a 2 A g^{-1} , ED of 57.78 Wh kg^{-1} at a PD of 1.59 kW kg^{-1} and capacitance retention of 87% after 10,000 GCD cycles.
9. An electrostatically driven exfoliation-restacking strategy was successfully synthesized the Ni-Cr-LDH-POW (NCW) nanohybrids.
10. The best optimized NCW-2 nanohybrid exhibited the highest specific capacity of 736 C g^{-1} at 1 A g^{-1} with electrochemical stability up to 81% after 5,000 GCD cycles in 2 M KOH electrolyte.
11. HSC device was successfully fabricated using NCW-2 as a positive electrode and rGO as a negative electrode in 2M KOH electrolyte (NCW-2||rGO).
12. The NCW-2||rGO HSC delivered a Cs of 120 F g^{-1} at a 2 A g^{-1} , ED of 43 Wh kg^{-1} at a PD of 1.3 kW kg^{-1} and capacitance retention of 84% after 10,000 GCD cycles.
14. An electrostatically driven exfoliation-restacking strategy was successfully synthesized the Ni-Cr-LDH-GO (NCG) nanohybrids.
15. The best optimized NCG-2 nanohybrid exhibited the highest specific capacity of 815 C g^{-1} at 1 A g^{-1} current density with electrochemical stability up to 80 % after 5,000 GCD cycles in 2 M KOH electrolyte.
16. HSC device was successfully fabricated using NCW-2 as a positive electrode and rGO as a negative electrode in 2M KOH electrolyte (NCG-2||rGO).
17. The NCW-2||rGO HSC delivered Cs of 145 F g^{-1} at 2 A g^{-1} , ED of 52 Wh kg^{-1} at a PD of 1.4 kW kg^{-1} with capacitance retention of 85% after 10000 GCD cycles.

8.4 Future findings:

This research work successfully enhanced the electrode performance of Ni-Cr-LDH by making NCV, NCW and NCG nanohybrids and applied them as positive electrodes in HSC. This research work opens up new horizons for exploring LDH-based electrodes for EES. The specific capacity and cycling stability of LDH-based electrodes need to be further increased for their applications in hybrids electric vehicles and power tools. The present exfoliation-restacking

strategy can be applicable for numerous other LDHs and various guest species to further enhance the electrode performance of LDH-based electrodes.

Though this research work established state-of-the-art achievements for Ni-Cr-LDH-based hybrid electrodes, some challenges remained to further increase SCs Cs and ED without affecting its PD and safety.

- ❖ Transition metal doping in Ni-Cr-LDH to design novel nanohybrids can further enhance electrode performance of Ni-Cr-LDH-based electrodes.
- ❖ The asymmetric cell can be developed using organic electrolyte or redox electrolyte, so that operating potential reaches up to 4V, which leads to high ED of LDH-based HSC.
- ❖ Negative electrode materials other than rGO can be employed to achieve higher PD and electrochemical stability.